Selected Topics of Semiconductor Physics and Technology

Ausgewählte Probleme der Halbleiterphysik und Technologie

Vol. 141

Narayan Sircar

Group IV all-semiconductor spintronics: Materials aspects and optical spin selection rules

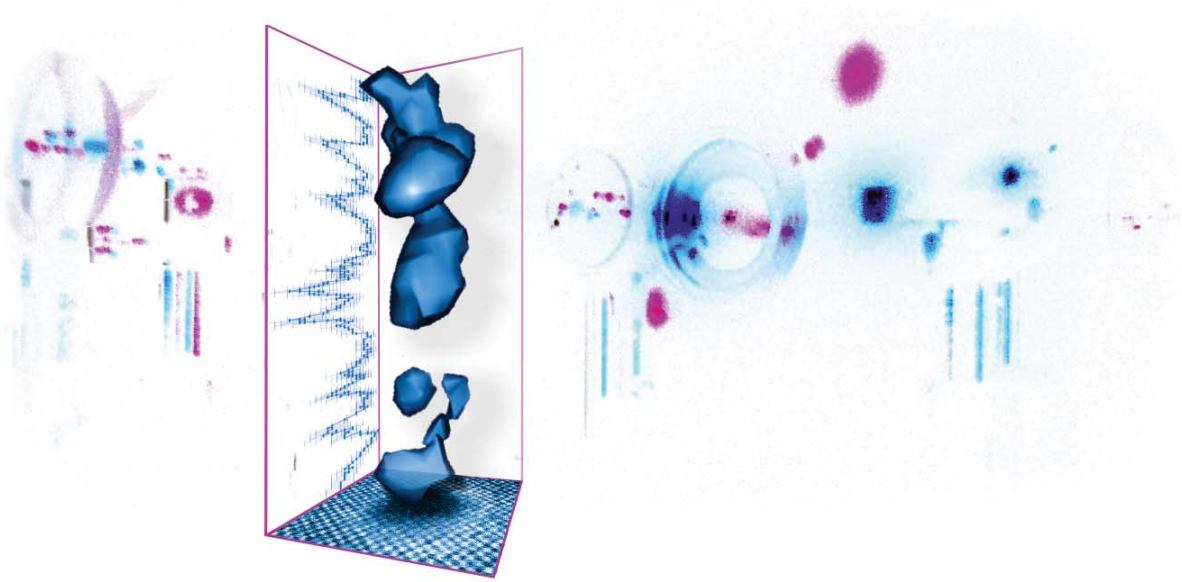

Editors:

G. Abstreiter, M.-C. Amann, M. Stutzmann, P. Vogl

Walter Schottky Institut, Technische Universität München

TECHNISCHE UNIVERSITÄT MÜNCHEN
Lehrstuhl für Experimentelle Halbleiterphysik I E24
Walter Schottky Institut

Group IV all-semiconductor spintronics: Materials aspects and optical spin selection rules

Narayan Sircar

Vollständiger Abdruck der von der Fakultät für Physik der Technischen Universität München zur Erlangung des akademischen Grades eines

Doktors der Naturwissenschaften

genehmigten Dissertation.

Vorsitzender: Univ.-Prof. Dr. Harald Friedrich

Prüfer der Dissertation:
1. Univ.-Prof. Dr. Gerhard Abstreiter
2. Univ.-Prof. Dr. Rudolf Gross
3. Univ.-Prof. Dr. Dominique Bougeard, Universität Regensburg

Die Dissertation wurde am 23.11.2011 bei der Technischen Universität München eingereicht und durch die Fakultät für Physik am 03.04.2012 angenommen.

1. Auflage Juni 2012

Titelbild:

3D reconstruction of the 8% Mn isoconcentration surfaces in a typical GeMn thin film obtained with atom probe tomography evidencing a string-of-pearls-like stacking of GeMn clusters. The frame on the left contains the measured Mn concentration profile along the string of clusters, while that on the bottom depicts a scanning electron microscopy plan-view image of the cluster nanostructure. In the background, an inverted-color photograph of the setup employed in the optical experiments part of this thesis is shown.

Druck: Printy Digitaldruck, München (http://www.printy.de)

ISBN: 978-3-941650-41-1

Abstract

In the scope of the present thesis various aspects for the realization of spintronic applications based on group IV semiconductors are discussed, with an emphasis on the injection and detection of charge carrier spins. This work comprises a refined material characterization of the magnetic semiconductor GeMn, for which promising ferromagnetism with a high Curie temperature was found in the past. We furthermore present efforts to utilize this material as spin injector for a Si-based optical spintronic device, which include the detailed discussion of key questions concerning the optical injection and detection of spins in Si and Si-based heterostructures.

The GeMn thin films that are subject to this thesis were fabricated by low-temperature molecular beam epitaxy in a prior study, in which a self-assembly process of roughly spherical Mn-rich GeMn clusters embedded in a single-crystalline Ge-rich matrix was observed. Applying transmission electron microscopy and atom probe tomography, we are able to resolve a vertical anisotropy in the self-assembly, leading to the stacking of well-defined clusters in the growth direction. Three-dimensional atom distribution maps confirm that clusters are built from a nonstoichiometric GeMn alloy and exhibit a high-Mn-concentration core with a decreasing Mn concentration toward a shell.

An amorphous nature of the cluster cores as well as the crystallinity of the shells, coherent with the surrounding Ge lattice, are revealed in scanning transmission electron microscopy. The quantification of Mn atoms incorporated within the amorphous and the crystalline GeMn phase is achieved by channeling ion beam experiments. From the comparison of the structural information about the present GeMn thin films with their magnetic properties we find that the structural core-shell picture has a correspondence in a magnetic core-shell picture: The large part of Mn atoms within the cluster cores is magnetically inactive, whereas ferromagnetically coupled, diluted Mn atoms in the shells conform the superparamagnetic moments of the GeMn clusters.

We localize a strain field surrounding each GeMn cluster by scanning transmission electron microscopy. The importance of strain to the stacking phenomenon of the clusters becomes clear in studies of Ge/GeMn superlattice structures, where a vertical spatial correlation of clusters over 30 nm-thick Ge spacer layers is observed.

We present evidence that electrical transport properties of the *p*-type GeMn thin films fabricated on high-resistivity Ge substrates are severely influenced by parallel conduction through the substrate. Anomalous Hall measurements and large mag-

netoresistance effects are completely understood by taking a dominating substrate contribution into account. It is shown that substrate conduction persists also for well-conducting degenerate *p*-type reference thin films, giving rise to an effective two-layer conduction scheme. Using *n*-type Ge substrates, parallel conduction through the substrate can be reduced for the *p*-type thin films, as a consequence of the emerging *pn*-interface junction. GeMn thin films fabricated on these substrates exhibit only a negligible magnetoresistance effect.

Before integrating GeMn in an optical spintronic device, some key aspects important for an understanding of the optical injection and detection of carrier spins in Si and Si-based heterostructures are clarified in the second part of this thesis. In particular, by including recent theory on spin-dependent selection rules for radiative transitions in bulk Si, we adapt an expression for the magnetic-field-induced photoluminescence polarization of direct band gap semiconductor materials of GaAs-type to Si. This opens the possibility to a direct experimental verification of the selection rules. Measurements within an applied magnetic field of the degree of circular polarization of phonon-assisted photoluminescence of bulk Si for different doping are presented and compared to the theory. We find an overall good agreement between the measured and calculated results.

Similar experiments on the photoluminescence of Ge quantum dot ensembles evidence a peculiarity for the spin-dependent selection rules for phononless radiative recombinations. We propose a connection between this – *a priori* puzzling – finding and the confined character of electrons that are involved in the transitions.

Furthermore, we try to optically inject and detect confined carrier spins in Ge quantum dot ensembles. For nonresonant excitation these efforts are unsuccessful, which we attribute to a hole spin relaxation that happens faster than the combined capture of the hole by the quantum dot and the radiative decay of the hole. Experiments employing quasi-resonant excitation are also discussed.

Finally, we employ the *p*-type GeMn thin film layers presented in the first part of this work as spin-polarizing contacts for Si/SiGe-based light-emitting diodes with the aim to inject spin-polarized holes. Preliminary results of a circularly polarized electroluminescence of these devices propose the possibility of a successful hole spin injection near liquid helium temperatures.

Zusammenfassung

Im Rahmen der vorliegenden Dissertation werden verschiedene Aspekte für die Realisierung von spintronischen Anwendungen diskutiert, die auf Halbleitern der Gruppe IV basieren, mit Schwerpunkt auf der Injektion und Detektion von Ladungsträgerspins. Diese Arbeit umfasst zunächst eine genaue Materialanalyse des magnetischen Halbleiters GeMn, bei dem zuvor potentiell interessanter Ferromagnetismus mit hoher Curie Temperatur nachgewiesen wurde. Im Zusammenhang mit Bemühungen, dieses Materialsystem als Spininjektor für ein siliziumbasiertes optisches Bauteil zu nutzen, werden weiterhin grundlegende Fragestellungen zur optischen Injektion und Detektion von Spins in Si und siliziumbasierten Heterostrukturen untersucht.

In einer vorangegangenen Studie wurden die hier untersuchten dünnen GeMn Schichten mittels Molekularstrahlepitaxie bei tiefen Temperaturen hergestellt und die Selbstorganisation von annähernd kugelförmigen manganreichen GeMn Anhäufungen beobachtet, welche in eine monokristalline germaniumreiche Umgebung eingebettet sind. Durch Transmissionselektronenmikroskopie und Atomsondentomographie wird in dieser Arbeit eine in Wachstumsrichtung ausgeprägte Anisotropie der Selbstorganisation aufgedeckt, die zum Stapeln von wohldefinierten GeMn Anhäufungen entlang dieser Richtung führt. Dreidimensionale Atomverteilungskarten zeigen, dass die Anhäufungen aus einem nicht stöchiometrischen Gemisch von Ge und Mn bestehen und weiterhin einen Kern mit hoher Mn Konzentration aufweisen. Dieser läuft in eine Schale mit abnehmender Konzentration aus.

Eine amorphe Phase in den Kernen der Anhäufungen sowie die Kristallinität der Schalen in Kohärenz zur umgebenden Ge Matrix werden mit Rastertransmissionselektronenmikroskopie nachgewiesen. Mit Hilfe von kanalisierten Ionenstrahlen wird zudem die genaue Konzentration von Mn im amorphen und kristallinen Bereich bestimmt. Der quantitative Vergleich der verschiedenen strukturellen Informationen über die GeMn Schichten mit ihren magnetischen Eigenschaften zeigt, dass sich das Kern-Schale Bild der Struktur einer Anhäufung in ihrem magnetischen Verhalten widerspiegelt: Der größte Teil der Mn Atome in den Kernen ist magnetisch nicht aktiv, wohingegen ferromagnetisch gekoppelte, in den Schalen gelöste Mn Atome die superparamagnetischen Momente der Anhäufungen ausbilden.

Rastertransmissionselektronenmikroskopie wird ebenso dazu eingesetzt, ein Verspannungsfeld zu lokalisieren, das jede GeMn Anhäufung umgibt. Die Verspannung ist eng mit dem Phänomen der gestapelten GeMn Anhäufung verknüpft, wie weiterfüh-

rende Studien an Ge/GeMn Übergitterstrukturen belegen. Dort umspannt die vertikale räumliche Korrelation von einzelnen GeMn Anhäufungen Ge Zwischenschichten mit bis zu einigen zehn Nanometern Dicke.

Es werden mehrere Anzeichen dafür präsentiert, dass die elektrischen Transporteigenschaften der *p*-artigen GeMn Schichtproben erheblich von paralleler Leitung durch die hochohmschen Ge Substrate beeinflusst werden, die bei der Herstellung der Schichtproben verwendet wurden. Ungewöhnliche Ergebnisse bei Messungen des Hallwiderstandes und der sehr große Magnetwiderstand können vollumfänglich durch einen überwiegenden Beitrag des Substrats zur elektrischen Leitung erklärt werden. Diese Substratleitung besteht auch bei sehr gut leitenden *p*-artigen Referenzschichten, was zu einem System von Leitung in zwei Schichten führt. Durch *n*-artige Substrate ist es möglich, die parallele Leitung für *p*-artige Schichten als Folge einer sich ausbildenden *pn*-Sperrschicht zu reduzieren. GeMn Schichten, die auf solchen Substraten hergestellt wurden, weisen nur einen sehr geringen Magnetwiderstand auf.

Vor der Anwendung von GeMn in einem optischen spintronischen Bauteil werden zunächst im zweiten Teil dieser Arbeit einige Kernpunkte für das Verständnis von optischer Injektion und Detektion von Ladungsträgerspins in Si und siliziumbasierten Heterostrukturen erörtert. Unter anderem wird ausgehend von der Beschreibung von magnetfeldinduzierter zirkularer Polarisation von Photolumineszenz in galliumarsenidartigen Halbleitern ein entsprechender Formalismus für Volumensilizium abgeleitet. Dabei werden die spinabhängigen Auswahlregeln bei strahlenden Übergängen in Si berücksichtigt. Dies eröffnet die Möglichkeit, die Auswahlregeln experimentell nachzuprüfen. Messungen des zirkularen Polarisationsgrades phononenassistierter Photolumineszenz von Volumensilizium mit verschiedener Dotierung werden innerhalb eines angelegten Magnetfeldes durchgeführt und mit der Theorie verglichen. Insgesamt ergibt sich dabei eine recht gute Übereinstimmung.

Ähnliche Experimente an der Photolumineszenz, die in Ge Quantenpunkten auftritt, zeigen eine Besonderheit für die Auswahlregeln der phononenlosen strahlenden Übergänge auf. Ein möglicher Zusammenhang zwischen diesem – zunächst unerwarteten – Verhalten und dem Einschlusscharakter der an den Übergängen beteiligten Elektronen wird aufgestellt.

Des Weiteren werden Versuche präsentiert, eingeschlossene Ladungsträgerspins optisch in Ge Quantenpunkte zu injizieren und detektieren. Bei nichtresonanter Anregung bleiben diese Versuche erfolglos. Dies wird auf eine Lochspinrelaxationszeit zurückgeführt, die kürzer ist als die Summe der Zeiten für den Einfang des Loches durch den Quantenpunkt und die anschließende strahlende Rekombination. Experimente zur quasiresonanten Anregung werden ebenfalls diskutiert.

Schließlich werden die im ersten Teil dieser Arbeit näher diskutierten *p*-artigen GeMn Schichten als elektrische Spininjektionskontakte für Si/SiGe-basierte Leuchtdioden verwendet mit dem Ziel, die Injektion von polarisierten Löcherspins zu realisieren. Erste Ergebnisse der zirkularen Polarisation der Elektrolumineszenz dieses Bauteils lassen auf eine erfolgreiche Lochspininjektion bei Flüssigheliumtemperaturen hoffen.

Contents

Part I

Nanostructural and electrical transport investigations of GeMn thin films

1

Introduction to magnetic GeMn semiconductors

THE modern globalized world owes its during the past sixty years grown and still increasing prosperity to the rapid and continuing progress in the development of novel technologies in the fields of transportation, telecommunication, information storage and processing, medical science, and, not to forget, consumer electronics, which particularly has come to the fore in the turn of the past century. These developments could not have been done without the invention of Si-based integrated circuits, most importantly the milestone realization of a Si metal-oxide-semiconductor field effect transistor (MOSFET), which still is the backbone of today's billion-dollar semiconductor industry. To this day, the demand for faster and less power-consuming computation devices has resulted in their extreme miniaturization down to the twenty nanometer scale, essentially obeying Moore's well-known empiric law. Clever device architectures, such as Intel's three-dimensional MOSFET, which recently has gone into mass production, will keep up this pace for some time and allow to further utilize the controlled motion of electric charges for logic operations. Eventually, however, entering the world of quantum-effects, the development of novel concepts seems inevitable.

This is where the idea of manipulating the spin-degree of freedom of a charge carrier instead of or in addition to the charge-degree of freedom comes into play. Stimulated by the impact of the finding of the giant magnetoresistance effect in metallic multilayer systems by the groups of Grünberg[1] and Fert[2] and the following, outstandingly successful commercial application of the associated spin-valves in hard disk drives, the so-called spintronics, short for spin-based electronics, have been an active field of fundamental research in the past two decades. Reviews illustrating the progress that was made in this versatile field may be found in Refs. 3–7.

In hard disk drives spins are essentially the units of information storage, while spin-associated effects are exploited to read-out the information by electrical currents. The processing of information using spins, which demands the initialization, manipulation, transportation and detection of spin-states, however, is so far not realized and would be a major achievement in the field of spintronics. The integration of spintronic concepts into the existing semiconductor-based complementary logic technologies is highly desirable. Thus, in large parts the focus of material research in the field of spintronics was kept on realizing semiconductors exhibiting a nonvolatile spin polarization of their charge carriers. Exotic material combinations have long been known to exhibit semiconducting and ferromagnetic properties at the same time, yet, the technologically relevant semiconductors Si, Ge, and GaAs are all diamagnetic. The straightforward approach to make these materials ferromagnetic was to literally introduce the magnetism by doping with elements of the periodic table that possess a permanent magnetic moment, such as the transition metals Mn, Fe, or Co. Semiconductors doped in such way are addressed as diluted magnetic semiconductors (DMS) in literature.[8] It was concordant opinion that in a DMS ferromagnetic coupling between the magnetic moments would happen for sufficiently large concentrations of the incorporated transition metal ions, similarly as the Curie temperature of the resulting ferromagnet should scale with the concentration. This held out the prospect of room temperature ferromagnetism, which is attractive for realistic applications. In contrast to this requirement, however, was the experimental fact of a low solubility of transition metals in the technologically relevant semiconductors in their solid-state. Thus, a milestone achievement was Ohno *et al.*'s[9] demonstration of a ferromagnetic (Ga,Mn)As solid-solution by low-temperature molecular beam epitaxy (LT-MBE). Its promising Curie temperature of 110 K and hole-mediated, and with that gateable, ferromagnetism made it the most intensively studied and best understood DMS so far.

The successful research on (Ga,Mn)As also promoted the application of LT-MBE to other material classes. Park *et al.*[10] were the first to claim the realization of ferromagnetic GeMn, with a Curie temperature of up to 116 K and a hole-mediated mechanism of magnetic coupling. Whereas the community undoubtedly profited from this first and the successive early studies,[10–14] some aspects of these pioneering works seem arguable from today's point of view. A major point of criticism is that the nanostructure of GeMn thin films fabricated by LT-MBE was not investigated and therefore completely ignored in the interpretation of the magnetization and magnetotransport measurements. With the intense studies of recent years, it has now become clear that epitaxial GeMn, although fabricated free of intermetallic secondary phases, in striking difference to (Ga,Mn)As is far from being a DMS in the sense of a homogeneous solid-solution of Mn with Ge.[15–17] A prominent feature of GeMn thin films is the self-assembly of nanometer-scale clusters with increased Mn concentration that are embedded in a single-crystalline Ge-rich matrix. Depending on the epitaxy conditions, the shapes of these clusters range from spheres of a few nanometers in diameter to columnar objects extending over a few ten nanometer. The exact understanding of the nature of these clusters, their formation mechanism and its driving forces is still in progress.

Other magnetic semiconductor materials with similar self-assembly phenomena,[18,19] for which GeMn can be considered as prototypical, might benefit from the deeper investigation of these aspects.

The magnetism in GeMn thin films is directly related to their nanostructure because the Mn-rich clusters act as single-domain ferromagnetic supermoments, each with a Curie temperature lying close to or even above room temperature.[15] Coupling of these supermoments to a global ferromagnetism has been convincingly shown only in rare cases,[16,20] what leads to the question of the physical origins of ferromagnetism in this material system, which is still not satisfactorily answered. Up to date, theoretical models of magnetic coupling in semiconductors have mostly assumed a perfect DMS structure and thus do not account for the actual conditions of GeMn.

It is a common observation that Mn incorporation in Ge has a *p*-type doping effect. However, again in contrast to (Ga,Mn)As, the doping does not lead to as many free holes as expected from the nominal Mn concentration values. Accordingly, a rather insulator- and not metalliclike resistance is often observed for thin films of GeMn. In a scenario of hole-mediated ferromagnetism the absence of free holes may be related to the absence of global ferromagnetism. In turn, local magnetic coupling within the GeMn clusters may be related to a scenario of an enhancement of itinerant holes locally confined to the clusters. Both scenarios, the validity of which is by far not proven, display only examples of the possible origins of magnetism in GeMn and illustrate the importance to account for the nanostructure in investigating, interpreting, and modeling transport properties of GeMn, including the effective bandstructure of this compound material. This process has started with the later studies of the past few years, and, still being in progress, no unanimous picture can be drawn so far.[16,17,21,22]

In **Chapter 2**, some generic properties of GeMn thin films will be addressed in more detail. Recent work of the research group of the Walter Schottky Institut and competing groups are displayed, whereas the focus will lie on those properties that will be of interest in the course of the present thesis.

In **Chapter 3** and **Chapter 4**, some key questions raised by these past investigations concerning the morphology, nanostructure, and self-assembly of the GeMn clusters will then be elucidated. We will report our results from state-of-the-art material characterization methods.

In **Chapter 5**, we will show that the difficulties in learning more about the interconnection of magnetic and electrical transport properties of GeMn thin films and a reason for the ambiguity of the results in literature can partly be traced back to a peculiarity inherent to the epitaxy of Ge-related thin films on commercially available Ge substrates.

Given the number of sparsely illuminated aspects and unanswered questions indicated above, it is not surprising that despite almost ten years of research on GeMn no implementation of this material system in any devices has been reported so far. Here, in a first step we attempt to integrate a thin film layer of GeMn into a Si-based light-emitting diode. We will come back to the results of this study in **Chapter 11** of **Part II** of this thesis.

2

Progress toward a magnetic GeMn semiconductor

In recent years, the search for technologically relevant magnetic semiconductors brought considerable progress to the research on the GeMn material system. The work group at the Walter Schottky Institut (WSI) finds itself among the leading research groups to investigate the structural and magnetic properties of epitaxial GeMn thin films completely free of any known Mn_nGe_m phases. The hitherto outcome of our past investigations on these thin films is summarized in Section 2.1 because Part I of the thesis at hand is based on that work. Additionally, in Section 2.2 and Section 2.3 an overview on similar and related studies that were reported in literature is given with the intention to put the findings of the present thesis in a more general context.

2.1 State of research at the WSI

The research on the GeMn material system at the WSI was taken up by S. Ahlers essentially with the beginning of his dissertation in 2005. His thesis[23] comprehensively documents first results obtained in our research group, some of which we have published in literature.[15,24–26] The topics that are subject to the present thesis have to be understood as complementary to the results reported by us so far, with the aim to highlight key question raised by our previous research in more detail.

The fabrication of GeMn thin films was realized by the simultaneous deposition of Ge and Mn on Ge substrates via solid-source LT-MBE in ultrahigh vacuum conditions. Details on our molecular beam epitaxy (MBE) machine and growth of GeMn thin films are described in Refs. 23 and 27. It was found that for a substrate tempera-

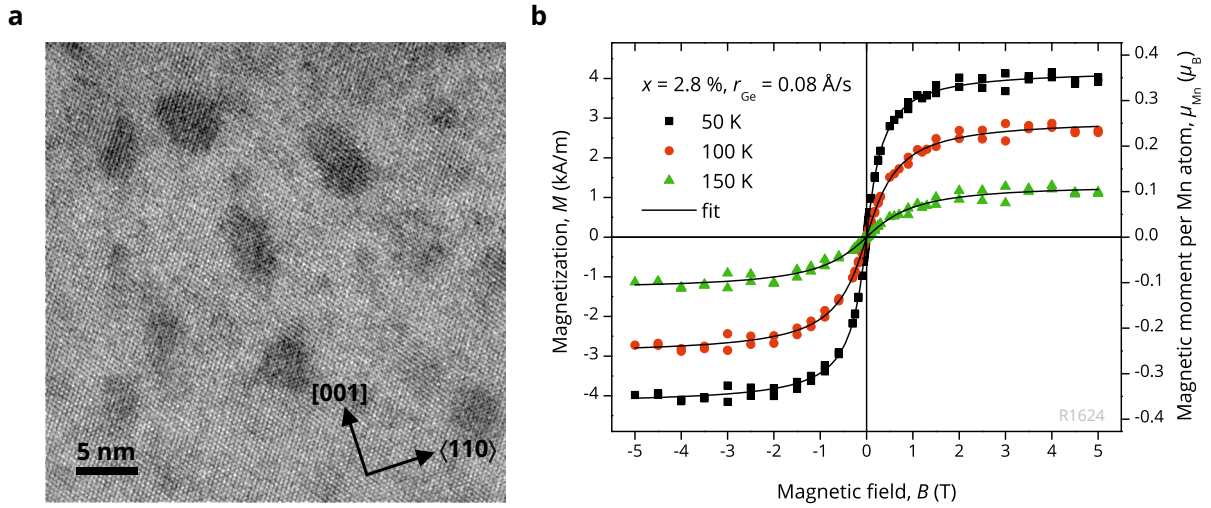

Figure 2.1 | a, HRTEM image of a GeMn thin film with $x = 2.8\,\%$ and $r_{\mathrm{Ge}} = 0.08\,\text{Å}\,\text{s}^{-1}$. GeMn clusters (dark contrast) exhibit a slight elongation along the [001] growth direction. **b**, In-plane magnetization of the same thin film as a function of an external magnetic field for different measurement temperatures. The symbols correspond to experimental data, whereas the solid lines are fits of the Langevin function to the data, assuming log-normal-distributed supermoment sizes. From Ref. 23.

ture of $T_{\mathrm{S}} = 60\,^{\circ}\mathrm{C}$ the precipitation of intermetallic secondary phases – Mn_5Ge_3 and $Mn_{11}Ge_8$ being the most important in the equilibrium binary phase diagram of Ge and Mn – can be completely suppressed.[15] As the possibility to employ growth rates r_{Ge} between $0.08\,\text{Å}\,\text{s}^{-1}$ and $0.25\,\text{Å}\,\text{s}^{-1}$, and Mn concentrations x up to 11.7 % has shown, this suppression is stable for a broad range of fabrication parameters.[23] Transmission electron microscopy (TEM) characterization showed a uniform and dislocation-free diamond-lattice-type crystal structure for the GeMn thin films.

Although Mn_nGe_m precipitates are absent for these fabrication parameters, Mn is nevertheless inhomogeneously dispersed. A self-assembly process leads to the formation of Mn-rich regions on the nanometer scale, which are coherently bound to an otherwise undisturbed Ge-rich matrix. The Mn-rich regions are always of circular shape in the growth plane with typical diameters of 3 nm to 5 nm but, depending on the fabrication parameters, can be elongated along the growth direction, leaving a slightly nonspherical, elliptical shape. As an example, the nanostructure of a sample with $x = 2.8\,\%$ and $r_{\mathrm{Ge}} = 0.08\,\text{Å}\,\text{s}^{-1}$ as obtained in high resolution transmission electron microscopy (HRTEM) is depicted in Fig. 2.1a. For large x or r_{Ge} structural investigations gave the impression that the elongation of the Mn-rich regions is seemingly as large as a few ten nanometers leading to an almost cylindrical shape.[23] We use the term *GeMn clusters* in the framework of this thesis to describe the Mn-rich regions irrespective of their shape, noting, however, that this must not be understood as a fixed stoichiometry of Ge_1Mn_1 for the composition of Ge and Mn in the clusters. In Section 3.1 we present our efforts to determine the nature of the slightly elliptical and elongated clusters by three-dimensional mapping of the chemical composition of GeMn thin films.

Ahlers[23] observed that the self-assembly phenomenon of GeMn clusters is anisotropic in the sense that it favors a short-ranged hexagonal order of GeMn clusters in the epitaxy plane and a correlated vertical stacking of clusters parallel to the [001] growth direction. Furthermore, X-ray diffraction evidenced that the formation of GeMn clusters imposes a strain of about 2 % to the surrounding Ge matrix.[25] Chapter 4 will elucidate the connection between strain and the self-assembly process in more detail.

It was also demonstrated that the nanostructure of the GeMn thin film samples is directly connected to their magnetic properties. Each GeMn cluster is a single-domain ferromagnet with a Curie temperature close to or exceeding room temperature.[15] The magnetic moment of each cluster is of the order of a few hundred Bohr magnetons in the whole fabrication parameter window. These supermoments are not blocked in any direction and are essentially freely rotating. The magnetism of GeMn thin films is thus described by superparamagnetism, whereas fitting the experimental magnetization data with the corresponding Langevin function yields best results assuming a narrow log-normal distribution of the supermoment sizes,[23] as can exemplary be seen in Fig. 2.1b. Surprisingly, it was found that irrespective of the growth conditions the magnetic moment per Mn atom is only of the order of $\mu_{\mathrm{Mn}} = 0.3\,\mu_{\mathrm{B}}$ to $0.45\,\mu_{\mathrm{B}}$,[23] see the right axis scale of Fig. 2.1b for example, and thus considerably smaller than the $3\,\mu_{\mathrm{B}}$ expected for the substitutional incorporation of Mn in Ge. X-ray absorption spectroscopy suggested that the diamond-lattice-type coordination of Mn in Ge is actually disturbed on a local scale. In a preliminary conjecture, the magnetic inactivity of Mn was connected to this local structural disorder.[23,26] Thus, disorder in GeMn thin films was one subject of particular interest to us and has been examined more closely in the course of this thesis. Our findings are outlined in Section 3.2.

In the straightforward electrical characterization of GeMn thin films, Ahlers[23] encountered difficulties when these were grown on high-resistivity Ge substrates. These difficulties were related to parallel conduction through the substrate. By using modified *n*-type buffer layers or *n*-type substrates, the problem of parallel conduction was diminished, but at the same time the underlying concept of electrical insulation by a *pn*-barrier limited the experimental and growth parameter range that could be investigated with magnetotransport measurements. These studies raised the question to what extent the epitaxy on Ge substrates of any kind whatsoever is suited for the investigation of the intrinsic magnetotransport properties of GeMn thin films. Thus, we will highlight the peculiar transport phenomena of Ge-based epitaxial thin films that are related to parallel substrate conduction in more detail in Chapter 5 and discuss the consequences on the interpretation of magnetotransport measurements from a general point of view.

2.2 Overview on competing research

In the recent years, multiple synthesis methods, such as sputtering,[28–30] solid-phase epitaxy,[31,32] furnace melting,[33,34] ion-implantation,[35–44] and MBE,[10,45–61] have been

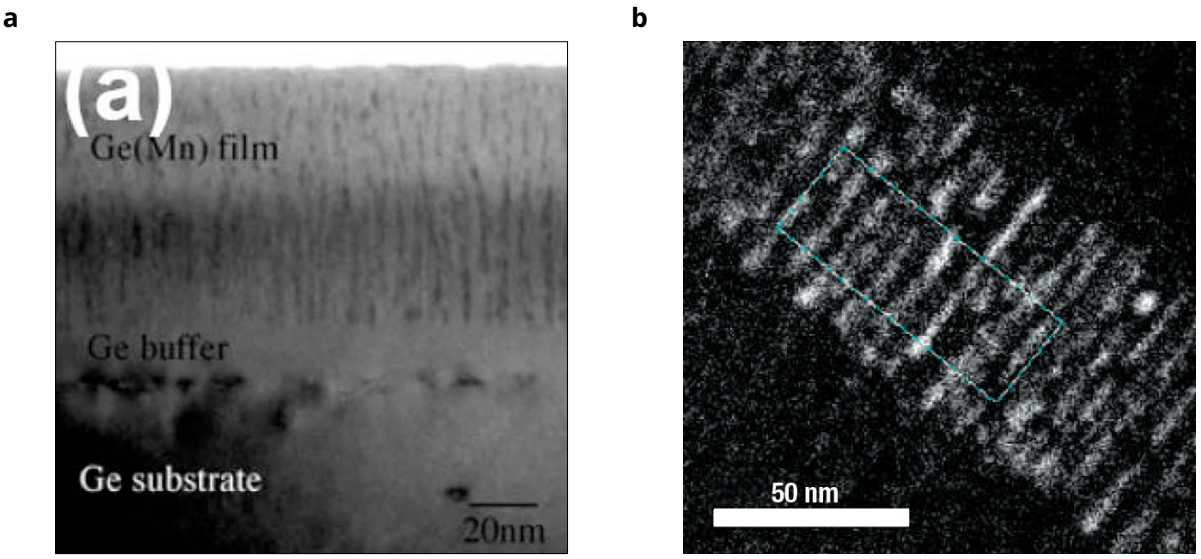

Figure 2.2 | a, TEM micrograph of a $Ge_{0.95}Mn_{0.05}$ thin film. The columnar features were attributed to strings of vertically elongated GeMn clusters. From Ref. 17. **b**, Mn chemical map of a $Ge_{0.94}Mn_{0.06}$ thin film derived from electron energy-loss spectroscopy showing the formation of Mn-rich nanocolumns. From Ref. 16.

tried to provide a ferromagnetic GeMn semiconductor. Accordingly, the GeMn material system exhibits a vast variety of structural and resulting magnetic and electrical properties. Especially in studies lacking the information on the nanostructure, the magnetism was often prematurely attributed to a DMS phase, i.e. the homogeneous dilution of the magnetic impurity atom, exhibiting Curie temperatures about room temperature, whereas the magnetization experiments in fact pointed to the presence of well-known intermetallic, magnetic Mn_nGe_m precipitates. Up to date, LT-MBE seems to be the most reliable method to completely suppress the precipitation of these secondary phases. Aside our group, the groups at the Oak Ridge National Laboratory in cooperation with the University of Tennessee, Knoxville, USA[13,14,17,20] and the group at the Commissariat à l'énergie atomique et aux énergies alternatives, Grenoble, France[16,62–65] have repeatedly demonstrated the capability to provide GeMn thin films by LT-MBE free of known intermetallic Mn_nGe_m phases.

Despite these successes, it has now become clear that the agglomeration of Mn impurity atoms into nanometer-scale GeMn clusters seems to be an inherent property of GeMn thin films fabricated by LT-MBE. The anisotropy in the shape of these clusters and their vertical correlation, as observed by us, have been independently reproduced. Some examples of the nanostructure of GeMn thin film samples published in literature are depicted in Fig. 2.2. Figure 2.2a depicts a TEM micrograph of a GeMn thin film sample, where the columnar features were attributed to the stacking of vertically elongated GeMn cluster,[17] very similar to the observations of Ahlers.[23] The finding of Ref. 17 of a Langevin superparamagnetism of individual, uncoupled ferromagnetic GeMn clusters each exhibiting a high Curie temperature is also in close agreement. Figure 2.2b shows an energy-filtered TEM image of another example of a GeMn thin

film for which the formation of well-defined nanocolumns, spanning the entire film thickness, with a composition close to stoichiometric $MnGe_2$ was claimed. Thin films containing these nanocolumns exhibited remarkable magnetic properties with a global ferromagnetic order and Curie temperatures exceeding 400 K.[16]

So far, the realization of a DMS as such via MBE seems to be elusive unless the special growth technique of ultracold, subsurfactant epitaxy[20] is employed. For thin films fabricated by this method, containing a homogeneously dispersed effective Mn concentration of only about 0.25 %, global ferromagnetic coupling of the Mn magnetic moments with a Curie temperature above 400 K was reported,[20] similar to the observations in Ref. 16. Whereas above mentioned studies in general support the results of our group that it is possible, at least on the local scale, to realize ferromagnetic GeMn, they at the same time raise the question of what triggers the global coupling of magnetic moments in GeMn thin films and what is the connection between the magnetism and the nanostructure. Hence, in the effort to shed more light on the nature of the self-assembled nanostructures observed in GeMn epitaxy and by that presumably on their magnetic properties, a thorough compositional analysis, the determination of the morphology, and the investigation of the driving forces for the self-assembly phenomenon in GeMn thin films have been pursued by us and are laid out in Chapter 3 and Chapter 4.

In the groundbreaking work on ferromagnetic GeMn semiconductors it was claimed that the magnetism could directly be controlled through electrical gating, suggesting that holes mediate the magnetic exchange interactions.[10] Hence, every now and then magnetotransport measurement have been employed for the purpose to investigate the coupling of holes with the magnetic moments of diluted Mn atoms or GeMn clusters. The magnetoresistance (MR) and the anomalous Hall effect (AHE) are considered an important fingerprint of a magnetic semiconductor. In the same degree as a consistent picture of the nanostructure of GeMn thin films has evolved, the interpretation of the MR and AHE in this material system remains manifold and lacks such a coherent description in literature. For example, MR effects reaching from several thousand percent being positive[16] to a few percent being negative[14,17,42] have been reported. Similarly, Hall effect measurements sometimes yield a large contribution of the AHE on the one hand,[14,66] but also a diminishing contribution washed out by the ordinary Hall effect on the other.[67] In many cases the interpretation of these results interestingly is not correlated to the sample magnetization, particularly regarding its saturation and hysteresis effects, which are often absent in transport measurements. In a recent article by Yu *et al.*,[21] a more detailed listing of the most relevant literature on transport studies of GeMn thin films and the key points of their respective interpretations can be found. Some of these studies come to the common conclusion that the transport phenomena in GeMn thin films are not necessarily related to the magnetic nature of the thin films in itself but are only a consequence of the doping of Ge with Mn impurities. In Chapter 5 of this thesis, we highlight the alternative possibility that the peculiar transport properties observed in some GeMn transport studies might not only be caused by the alloying of Ge with Mn but by parallel conduction through the employed substrates.

2.3 Origins of phase separation

The observation of an inhomogeneous dispersion of Mn in Ge has brought up the question of the growth mechanisms and driving forces responsible for the characteristic nanostructure of GeMn thin films fabricated by epitaxial methods. For the (Zn,Cr)Te and (Ga,Mn)N magnetic semiconductor systems Monte Carlo simulations of a static Ising model of pair interactions between different atom species at neighboring crystal sites have shown that the nanoscale agglomeration of the magnetic impurity atoms to clusters is favored, because the effective chemical pair interaction between the magnetic impurity atoms is attractive.[68] For the restriction that only surface diffusion can take place, as it is the prevalent case in MBE, the Monte Carlo simulations also predicted a distinct elongation of the clusters in growth direction leading to the formation of columnar structures,[68] a result which was recently reproduced by taking also kinetic effects into account.[69] So far, such simulations have not explicitly been carried out for the GeMn material system, but the theoretical finding of an attractive effective chemical pair interaction for Mn atoms in Ge[70,71] suggests that a simulation of the nanostructure of GeMn would yield similar results to (Zn,Cr)Te and (Ga,Mn)N. The attractive pair interaction, i.e. the fact that chemical bonds between two Mn atoms in a Ge lattice are favored over bonds between one Ge host atom and one Mn atom, can thus be expected to be one key factor in the formation of GeMn clusters. Indeed, the tendency for agglomeration of deposited Mn impurity atoms on Ge surfaces was experimentally observed.[20]

The authors of the early Monte Carlo studies used the term *spinodal decomposition* to describe the observed phase separation,[68] which in the following has been widely adapted in publications on magnetic semiconductor alloys with similar phase separation phenomena[18,19,72] including studies of GeMn.[65,73,74] Strictly, however, spinodal decomposition demands that for the given concentration x_0 of the magnetic impurity species in the alloy the Helmholtz free energy F of the alloy as a function of impurity concentration x has a negative curvature, i.e. $\frac{\partial^2 F}{\partial x^2}\big|_{x_0} < 0$. Contrary, for nucleation – the other possible mechanism for phase separation – the relation $\frac{\partial^2 F}{\partial x^2}\big|_{x_0} > 0$ holds.[75] The knowledge of the dependence of the Helmholtz free energy on the magnetic ion concentration under realistic experimental conditions is thus necessary to distinguish between spinodal decomposition and nucleation as relevant phase separation process. In a recent attempt, a phase separation diagram for (Ga,Mn)As has been determined, which allows to calculate the Helmholtz free energy and make predictions on the separation process.[76] Up to date, for the GeMn material system a similar study is not at hand, which makes it rather speculative to ascribe the formation of GeMn clusters in GeMn thin films to a spinodal decomposition process. The observed nanostructure of GeMn thin films reflects only the final state of a phase separation process whatsoever and is thus not very well suited to distinguish between nucleation or spinodal decomposition.[77] In fact, the investigation of the nanostructure may only then be helpful to the experimental determination of the phase separation process of solid solutions

if carried out time-dependently, i.e. at different stages of the spinodal decomposition or nucleation process.[77] Such an investigation, however, is inherently difficult for epitaxial fabrication methods. As long as one is only interested in determination of the parameters influencing the phase separation from a fundamental point of view, the exact nature of phase separation is not really of importance because both processes rely on the reduction of the Helmholtz free energy.[77] This is, determining the parameters contributing to the free energy is actually more useful in order to tailor physical properties of epitaxial GeMn thin films. One of these parameters, as stated above, is the energetics of the Ge-Ge, Ge-Mn and Mn-Mn chemical bonds. Due to the consistent observation of strain in epitaxial GeMn thin films, the accumulation of strain energy during the formation of GeMn clusters is apparently of importance as an additional factor.

3 Morphology of epitaxial GeMn

ALTHOUGH the characterization of GeMn thin films made tremendous progress in past years, the nature of the Mn-rich GeMn clusters is still under debate. Their chemical composition, structural configuration and the driving forces leading to their formation in the first place are three issues of particular interest because they determine parameters important for the spintronic utilization of GeMn thin films and will thus path the direction of future GeMn research. To gain deeper insight into these topics, we employed state-of-the-art material characterizations methods. The results of these studies are presented in this chapter and in Chapter 4. We will also relate them to the magnetic properties of GeMn thin films. Our findings have been partly published in Ref. 78.

3.1 Nanometer-sized GeMn clusters as smallest entities

3.1.1 String-of-pearls-like self-assembly of GeMn clusters

In the past, our group employed TEM in cooperation with A. Trampert from the Paul-Drude-Institut für Festkörperelektronik, Berlin, as imaging method for the structural analysis of GeMn thin films.[15,24] Conventional and in particular analytical[①] TEM in general allow to gain not only spatially resolved structural but also chemical information on samples. This is achieved with conventional dark field TEM (DFTEM) by selection of a chemically sensitive diffracted beam, for example. In the pure Ge lattice, the (002) diffraction spot is kinematically forbidden because the corresponding

[①] Under analytical TEM one comprises TEM-related techniques, like electron energy-loss spectroscopy or energy-dispersive X-ray spectroscopy, using special detectors for the sample analysis.

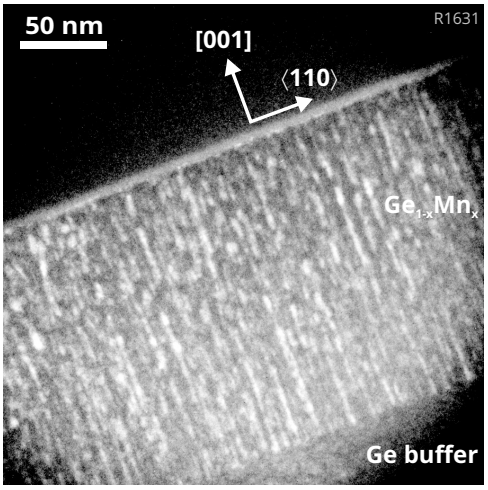

Figure 3.1 | Cross-sectional (002) DFTEM image of a GeMn thin film sample with $r_{\mathrm{Ge}} = 0.08\,\text{Å}\,\mathrm{s}^{-1}$ and $x = 7.3\,\%$. Bright contrast indicates the formation of GeMn clusters.

structure factor vanishes. For the presence of Mn atoms in the Ge lattice, however, this restriction is lifted.

Figure 3.1 depicts such a chemically sensitive (002) DFTEM micrograph for the $\langle 110 \rangle$ cross section of a GeMn thin film with $x = 7.3\,\%$ and $r_{\mathrm{Ge}} = 0.08\,\text{Å}\,\mathrm{s}^{-1}$. Bright spots correspond to the characteristic self-assembled GeMn clusters,[15] while dark areas with little intensity of the diffracted electron beam are obtained for the Ge-rich matrix. A strong anisotropy of the self-assembly leads to an alignment of GeMn clusters into a *string of pearls* pattern in the [001] growth direction. Furthermore, while the diameter of the GeMn clusters varies only between 3 nm to 5 nm in the (001) plane, there is a wide range of length in the [001] direction. One can observe both roughly spherical objects with dimensions of only a few nanometers as well as columnar objects with an elongation along the growth direction of several tens of nanometers. The characteristic string of pearls pattern is found within the entire fabrication parameter window of $r_{\mathrm{Ge}} = 0.08\,\mathrm{nm}$ to 0.4 nm and $x = 2\,\%$ to 11.7 %, whereas the self-assembly of columnar shaped objects is suppressed for a combination of both small r_{Ge} and x.[23]

DFTEM was in the first place useful to get an impression of the spatial variation of the chemical composition of our GeMn samples but did not allow for the quantification of the local Mn concentration. For composite materials that exhibit local variations of the chemical composition on a nanoscale, like epitaxial GeMn, the accuracy and informative value of analytical TEM techniques, however, is limited, too. This is due to the fact that the two-dimensional information provided by TEM is actually a down-projection of information from the three-dimensional (3D) volume of the TEM foil crossed by the electron beam. That is, depending on the specimen thickness one might get varying results by a TEM characterization. We note that it might be possible that the observation of columnar objects in the DFTEM micrograph stems from the 3D overlap of spherical GeMn clusters in projection, too. Atom probe tomography is a complementary technique to provide a chemical analysis with atomic resolution.[79,80]

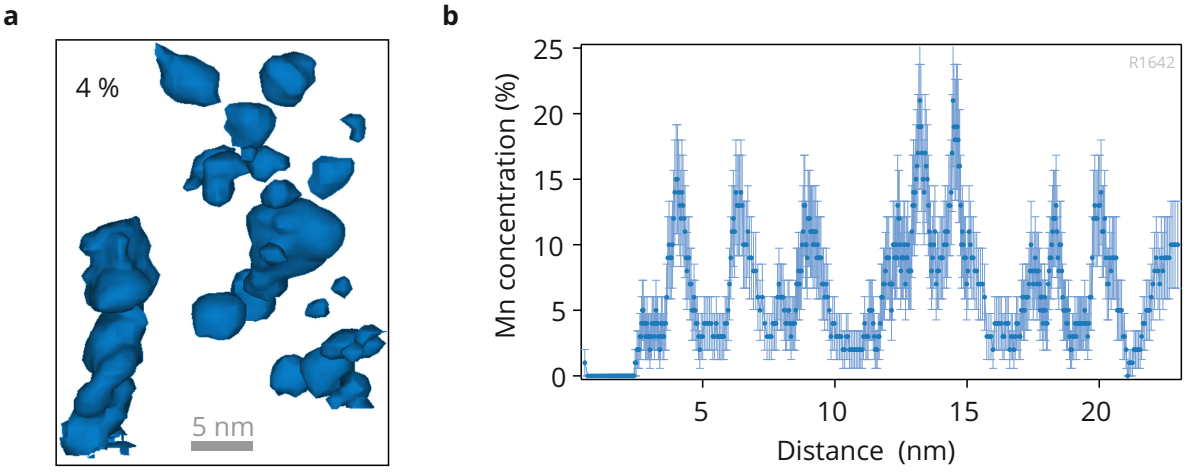

Figure 3.2 | APT data from a GeMn thin film sample with $r_{Ge} = 0.25\,\text{Å}\,\text{s}^{-1}$ and $x = 2.0\,\%$. **a**, 4 % Mn isoconcentration surfaces of a pane of the 3D APT reconstruction. Growth direction is bottom to top, analysis direction is top to bottom. **b**, 1D Mn concentration profile along the Mn-rich columnar feature in the lower left of **a**. The profile is generated by counting the number of atoms of each species within a slice of the reconstructed data. The error bars represent the uncertainty resulting from counting statistics.

3.1.2 3D chemical composition analysis

Atom probe tomography (APT) was conducted in collaboration with A. Cerezo and D. W. Saxey from the Department of Materials, University of Oxford. Experimental details on the APT studies are given in Appendix A.2. Here, we only want to emphasize that APT, other than analytical TEM, is able to produce a true 3D map of the distribution of different atom species. This unique ability of APT gives access to an accurate quantification of the chemical composition of the GeMn clusters observed in TEM. APT is thus well suited to determine their real morphology.

Figure 3.2a shows 4 % Mn isoconcentration surfaces of a GeMn thin film with $x = 2.0\,\%$ and $r_{Ge} = 0.25\,\text{Å}\,\text{s}^{-1}$, which were extracted from the 3D reconstruction of the Mn and Ge atom distributions. The Mn is clearly incorporated in both isolated GeMn clusters with dimensions of a few nanometers in all three spatial directions and in columnar objects reaching several tens of nanometers in elongation. The isoconcentration surfaces of columnar objects are not of perfect cylindrical but instead of irregular and corrugated shape.

Figure 3.2b displays a one-dimensional (1D) Mn concentration profile along the axis of such a columnar object, which is more than 20 nm in length. We observe large variations in the Mn content of the column on the scale of 2 nm to 3 nm. This variation demonstrates that columnar objects are in fact built from individual, nanometer-sized GeMn clusters, which are closely stacked in growth direction. Each GeMn cluster appears as a peak in Fig. 3.2b. Despite the close stacking, a low Mn content between individual GeMn clusters is clearly resolved. The close stacking of individual clusters also explains the very irregular shape of columnar objects which have been observed

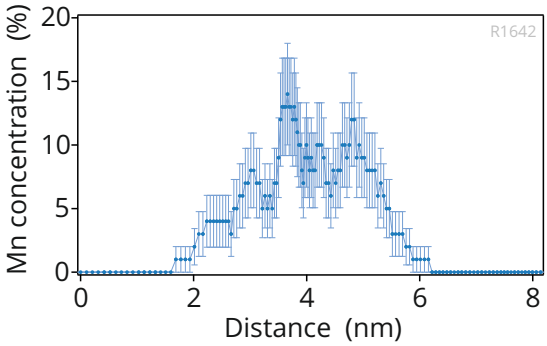

Figure 3.3 | APT data from a GeMn thin film sample with $r_{Ge} = 0.25\,\text{Å}\,\text{s}^{-1}$ and $x = 2.0\,\%$. 1D Mn concentration profile through a single GeMn cluster along a direction in the (001) epitaxial plane. The error bars represent the uncertainty resulting from counting statistics.

in the 3D reconstruction in Fig. 3.2a. Thus, the APT analysis confirms the string-of-pearls-like self-assembly of GeMn clusters along the growth direction, which has been indicated by TEM. Moreover it reveals that columnar objects can in fact neither be considered as homogeneous nor continuous.

APT furthermore shows that the average Mn content varies from cluster to cluster. We found the peak concentration to vary between 10 % and 20 % within the studied clusters of the present sample. The concentration of Mn that is incorporated into the Ge matrix is below $x_{\text{matrix}} = 0.7\,\%$.

Figure 3.3 shows a typical 1D Mn concentration profile, coplanar with the (001) growth plane, through a single GeMn cluster. Starting from the matrix level below 0.7 %, the Mn concentration steeply rises within 1 nm to 2 nm toward the cluster center. While it may be possible that ion trajectory aberrations and surface diffusion have some effect on these profiles, similar results are generated when taking concentration profiles along the direction of field evaporation. This suggests that a real Mn concentration gradient is present. This presence of a Mn concentration gradient is further illustrated in the 3D-reconstructed APT data by extending the isoconcentration surface plot of Fig. 3.2a to a series, as depicted in Fig. 3.4a–c. Upon plotting increasing Mn isoconcentration thresholds, we decrease the diameter of the GeMn cluster reconstructions. At high concentration thresholds, only the cores of the clusters are visible.

The presence of a Mn concentration gradient as well as the fact that the Mn content of the cluster cores noticeably fluctuates from cluster to cluster leads to the conclusion that the clusters are formed of a random $Ge_{1-\alpha}Mn_\alpha$, $0 < \alpha < 1$, solid-solution rather than an intermetallic compound with fixed stoichiometry.

In summary, the APT analysis confirms the TEM implication of a string-of-pearls-like self-assembly of GeMn clusters along the growth direction, while in the observed columnar regions individual, roughly spherical GeMn clusters seem to be retained as the smallest entities. APT also demonstrates that Ge and Mn assemble into random alloy $Ge_{1-\alpha}Mn_\alpha$ clusters. These can either be very closely stacked or isolated. Irrespective of their configuration, they always exhibit a high Mn concentration in the core with a steep concentration gradient.

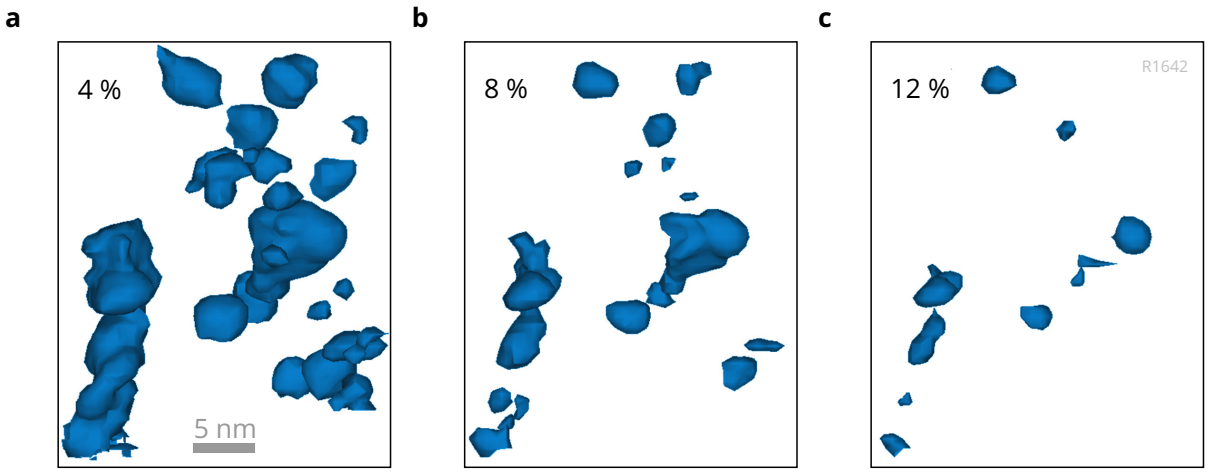

Figure 3.4 | APT data from a GeMn thin film sample with $r_{Ge} = 0.25\,\text{Å}\,\text{s}^{-1}$ and $x = 2.0\,\%$. **a**, 4 %, **b**, 8 % and **c**, 12 % Mn isoconcentration surfaces of the same pane of the 3D APT reconstruction illustrating the increasing Mn concentration gradient toward the cluster cores.

3.2 Amorphous GeMn cluster cores

3.2.1 Localization of disorder

As mentioned previously, we expect the results of structural TEM characterizations of GeMn thin films to depend on the thickness of the examined specimens. In well-prepared specimens suitable for high-quality HRTEM studies, one can scarcely achieve a specimen thickness smaller than 10 nm. Given the fact that the diameter of the GeMn clusters according to the APT data is of the order of 3 nm to 5 nm in the epitaxy plane, a cross-sectional specimen has a higher risk of containing a large portion of the Ge-rich matrix surrounding the clusters. The structure of the matrix will consequently contribute to the projected TEM image. For a plan view specimen, however, the fact of the string-of-pearls-like self-assembly of clusters in growth direction enhances the chance to increase the cluster-to-matrix volume ratio in a given specimen thickness. To study the structural properties of the GeMn clusters in more detail, we therefore conducted plan view TEM along the [001] growth direction of the GeMn thin films, in collaboration with S. Stemmer and J. M. LeBeau from the Materials Department, University of California, Santa Barbara. Experimental details on these TEM studies are given in Appendix A.1.

Figure 3.5a and 3.5b show a comparison of HRTEM micrographs from thicker and thinner parts, respectively, of the identical specimen of the GeMn sample with $r_{Ge} = 0.08\,\text{Å}\,\text{s}^{-1}$ and $x = 7.3\,\%$. The micrograph of the thicker part seems to indicate perfect crystal coherence between cluster strings and the surrounding Ge-rich matrix. On the other hand, in the thinner part we observe that the centers of the GeMn cluster strings are in fact amorphous. The seeming crystal coherence in the thick part of the

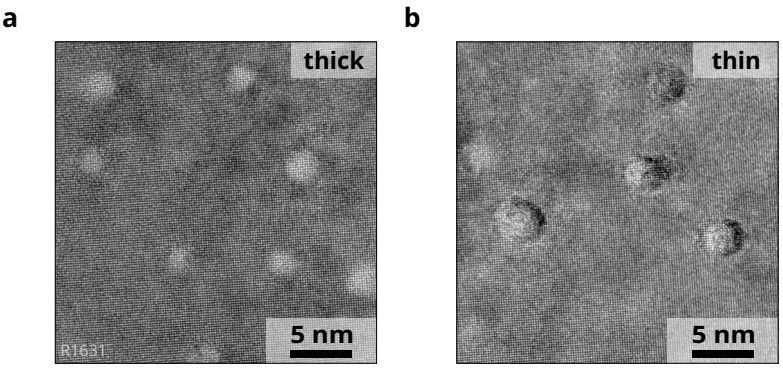

Figure 3.5 | a, HRTEM image of a GeMn sample with $r_{Ge} = 0.08\,Å\,s^{-1}$ and $x = 7.3\,\%$ recorded on a thick part of the specimen. **b**, HRTEM image of the same specimen as in **a** but for a thinner part.

specimen in Fig. 3.5a is due to the above described overlap of the amorphous clusters with the crystalline Ge matrix in projection. The thickness of the specimen at this part is presumably of the order of 40 nm and more. Unambiguous interpretation of TEM micrographs for this system thus requires plan view TEM foils with a thickness below 20 nm, as analyzed in Fig. 3.5b.

In addition to the HRTEM, we investigated a single cluster string with high-angle annular dark field (HAADF) scanning TEM (STEM). It was conducted in high resolution mode in order to resolve individual atomic columns. HAADF, also known as Z-contrast, is sensitive to chemical fluctuations in the specimen. HAADF micrographs thus allow a direct qualitative interpretation of bright-dark contrast variations of the observed crystal structure, in contrast to the HRTEM micrographs depicted above, for which in general simulations are necessary.

HAADF imaging, depicted in Fig. 3.6, shows a decreasing brightness of the scattered electron beam from the Ge matrix toward the center of the string. The onset of this decreasing brightness is marked with a dashed circle in the right panel of the Fig. 3.6. The low brightness in the center indicates the presence of an increasing amount of the lighter element Mn. Within the solid circle drawn in the right panel of Fig. 3.6, the crystalline arrangement of the atomic columns of the Ge matrix cannot be observed anymore. Instead, amorphous GeMn is clearly dominant. Note that while the amorphization of GeMn, as observed in Fig. 3.5, might have been caused by beam damage during HRTEM, such electron-beam-induced amorphization is essentially ruled out for the STEM mode because of the short and only punctual exposure of the material to the beam during the scanning process.[81]

The decrease of contrast between the two circles in the HAADF image can be induced both by strained crystalline material as well as a progressive increase of the Mn content toward the center of the cluster string. The latter would corroborate the observation of a Mn concentration gradient through APT. This situation would be indicative of a core-shell structure of GeMn clusters, revealing an amorphous core that contains most of the Mn and spreads out into a crystalline, probably strained shell with

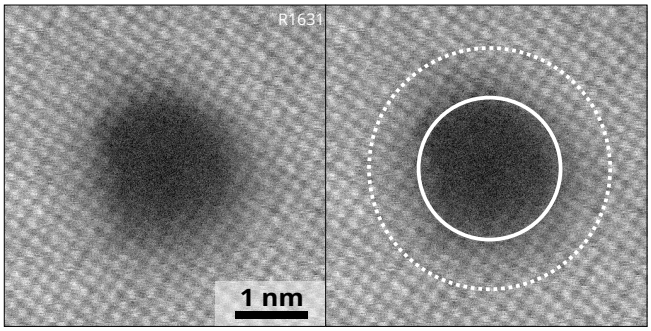

Figure 3.6 | High resolution plan view STEM image of a sample with $r_{Ge} = 0.08\,Å\,s^{-1}$ and $x = 7.3\,\%$ in HAADF. The right panel is a copy of the left panel containing white circles to mark regions with contrast that differs from the Ge matrix contrast.

moderate Mn content. We note that the diameter of the larger, dashed circle is within the range of the typical diameters of GeMn clusters as determined in APT and TEM.

3.2.2 Quantification of disorder

From the STEM study it is not feasible to quantify the fraction of Mn atoms in either GeMn phase, that of the core and that of the shell, with respect to the nominal Mn concentration of the whole thin film. This task can be fulfilled by employing channeling Rutherford backscattering (RBS) and the related channeling particle-induced X-ray emission (PIXE). RBS and PIXE were kindly performed by K. M. Yu from the Materials Sciences Division, Lawrence Berkeley National Laboratory. The measurement principle of the channeling experiments is further explained in Appendix A.3. With channeling RBS or PIXE one can determine, on the one hand, the fraction of so-called nonrandom Mn atoms f_{nr}, i.e. Mn atoms incorporated on substitutional and interstitial lattice sites of the Ge host crystal. On the other hand, Mn atoms sitting in neither of these lattice sites give the random fraction of Mn, $f_r = 1 - f_{nr}$, which we use as the measure for the degree of structural disorder.

For the GeMn thin film sample with $r_{Ge} = 0.08\,Å\,s^{-1}$ and $x = 7.3\,\%$, which was presented in Fig. 3.6, $f_r = 0.88$. Thus, a vast majority of Mn is indeed incorporated in a random manner within the Ge crystal during the epitaxy. This is in agreement with the combined STEM and APT observations because they accordingly show that most of the Mn forms an amorphous GeMn phase within the high-Mn-concentration GeMn clusters. For amorphous GeMn one would also expect a random fraction of Ge atoms. We note that the channeling measurements, however, did not indicate random Ge in a substantial portion. We relate this to the fact that, firstly, the amorphous clusters occupy only a volume fraction of about $v_{clusters} = 15\,\%$ of the thin film[23] and, secondly and more importantly, this thin film with a thickness of only 200 nm in turn makes out only a small portion of the total volume that is probed by the channeling beam because the beam penetrates deeply into the Ge substrate. Detecting the randomly placed Ge atoms is thus beyond the resolution limit of the channeling analysis.

The nonrandom fraction of Mn is quantified as $f_{\mathrm{nr}} = 0.12$. Recalling the HAADF implication of crystalline shells that enclose the amorphous cores of the GeMn clusters and apparently contain diluted Mn atoms, it is reasonable to attribute the nonrandom Mn atoms to these shells. We cannot completely rule out that nonrandom Mn atoms also sit within the Ge matrix. It is, however, unlikely that these make out the larger part of the observed nonrandom fraction f_{nr}, as an estimate shows: The global concentration of nonrandom Mn is $x_{\mathrm{nr}} = f_{\mathrm{nr}} x = 0.9\,\%$. Under the assumption that all nonrandom Mn atoms are located within the matrix and considering the volume fraction of the Ge matrix of about $v_{\mathrm{matix}} = 1 - v_{\mathrm{clusters}} = 85\,\%$, an atomic Mn concentration in the matrix of $x_{\mathrm{matrix}} = \frac{x_{\mathrm{nr}}}{v_{\mathrm{matix}}} = 1.1\,\%$ is obtained. This is clearly higher than the upper bound of x_{matrix} as given by the APT measurements. The crystalline shells of the GeMn clusters thus have to house a substantial amount of substitutional or interstitial Mn atoms.

So far, the combined results of APT, STEM and channeling RBS/PIXE provide strong arguments for a structural core-shell layout of GeMn clusters: High-Mn-concentration, randomly ordered cores are surrounded by low-Mn-concentration, crystalline shells.

3.3 Discussion of results regarding magnetic properties

3.3.1 Magnetic entities in GeMn thin films

The magnetic properties of the GeMn thin films that are subject to this thesis have been previously reported[15,23] and are not detailed here. We recall two facts at this stage: The magnetic field response of the GeMn thin film samples is described by superparamagnetism of mostly noninteracting, ferromagnetic single-domains with supermoments in the range of $\mu_{\mathrm{sp}} = 150\,\mu_{\mathrm{B}}$ to $400\,\mu_{\mathrm{B}}$. The density n_{sp} of these supermoments, as derived by magnetization measurements, implies that the typical line density of supermoments has to be 15 to 50 per thin film layer thickness, which is of the order of 80 nm to 200 nm for our samples. Previously, both observations led to the conjecture that in average the spatial size of the smallest magnetic entity is always of the order of a few nanometer and are in contradiction with a magnetic entity that spans a few ten nanometers or even the complete thin film layer thickness.[23] This interpretation of magnetometry is now directly supported with our findings: It is indeed nanometer-sized, roughly spherical GeMn clusters that are, on the one hand, stacked in a string-of-pearls-like pattern along the growth direction and, on the other, retained as individual units in objects of seemingly columnar shape. Consequently, we identify these units as the noninteracting, ferromagnetic single-domain particles.

3.3.2 Magnetic activity of Mn in GeMn thin films

Another interesting magnetic property of the present GeMn thin films is the measured magnetic moment per Mn atom μ_{Mn}. For the example of the thin film with $r_{\mathrm{Ge}} = 0.08\,\mathrm{\AA\,s^{-1}}$ and $x = 7.3\,\%$, $\mu_{\mathrm{Mn}} = 0.3\,\mu_{\mathrm{B}}$.[23] This is substantially smaller than

the value of $\mu_{\mathrm{Mn}} = 3\,\mu_{\mathrm{B}}$ that has so far been multiply predicted by independent theories for substitutional or interstitial Mn in Ge[10,70,71,82–88] and has been observed in experiment,[20] too. From the channeling experiments we know, however, that only the fraction of 12 % of the Mn atoms is incorporated on such lattice sites. Assuming that the remaining Mn atoms do not exhibit a net magnetic moment would yield an average magnetic moment per Mn atoms of $\mu_{\mathrm{Mn}} = 0.12 \cdot 3\,\mu_{\mathrm{B}} = 0.36\,\mu_{\mathrm{B}}$, which is in fair agreement with the measured value.

This observation establishes an evident connection between the magnetic inactivity of Mn atoms and the structural properties of the GeMn thin films. We expect the absence of structural order in combination with the high Mn content in the cores of the GeMn clusters to be the origin of magnetic disorder. This disorder causes the observed magnetic inactivity, for instance through a canting of magnetic moments of randomly distributed Mn or antiferromagnetic (AFM) coupling of subensembles of the Mn moments in the amorphous cluster cores. A strong AFM coupling between Mn atoms is indeed predicted by theory for two Mn atoms occupying substitutional nearest-neighbors sites in a Ge-lattice-type GeMn alloy.[71,85,87,89–91] This general trend may still hold for disordered GeMn, as its building blocks exhibit a similar, although only short-ranged tetrahedral configuration.[63] Under the high-Mn-concentration conditions present in the cluster cores, the formation of n such AFM, nearest-neighbors Mn-Mn dimers, where n is any natural number, is particularly favored over the corresponding formation of $2n$ Mn-Ge bonds.[88] In turn, uncompensated magnetic moments at the surface of an AFM cluster core[92–95] or small volumes of dispersed, ferromagnetically ordered Mn atoms in the crystalline shell of a cluster lead to the observed superparamagnetic behavior.

If this core-shell picture is plausible, it has to account, at least roughly, for the measured values of different magnetic (μ_{sp}, n_{sp}) and structural (x, f_{r}, f_{nr}, core radius r_{c}, shell radius r_{s}) properties as well as their interrelation. We check this in a simple model assuming a spherically shaped cluster with a Mn concentration profile $x(r)$ as depicted in the schematic of Fig. 3.7, in resemblance of the measured profile of Fig. 3.3. In Fig. 3.7, x_{c} is the atomic Mn concentration at the center of the cluster, while x_{s} is that at the core-shell interface. $x(r)$ is thus parameterized as

$$x(r) = \begin{cases} \dfrac{x_{\mathrm{s}} - x_{\mathrm{c}}}{r_{\mathrm{c}}} r + x_{\mathrm{c}} & \text{if } 0 \le r \le r_{\mathrm{c}}, \\ \dfrac{x_{\mathrm{s}}}{r_{\mathrm{c}} - r_{\mathrm{s}}} (r - r_{\mathrm{s}}) & \text{if } r_{\mathrm{c}} \le r \le r_{\mathrm{s}}, \\ 0 & \text{if } r_{\mathrm{s}} \le r. \end{cases} \tag{3.1}$$

By integration, we derive an expression for the amount of Mn atoms in the core

$$N_{\mathrm{c}} = 4\pi n_{\mathrm{Ge}} \int_0^{r_{\mathrm{c}}} r^2 x(r)\, \mathrm{d}r, \tag{3.2}$$

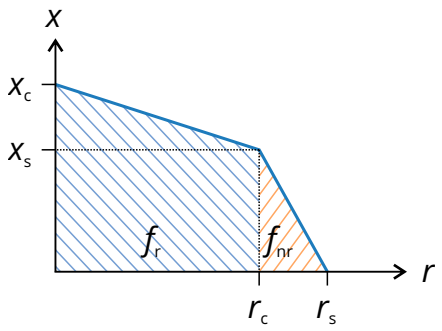

Figure 3.7 | Schematic of the radial concentration profile of a GeMn cluster in the core-shell picture. The core with radius r_c and center concentration x_c contains the fraction f_r of Mn atoms, while the shell, ranging from r_c to r_s, with core-shell interface concentration x_s contains the nonrandom fraction f_{nr}.

where n_{Ge} is the atomic density of Ge. The total amount of Mn in the cluster is

$$N_0 = 4\pi n_{Ge} \int_0^{r_s} r^2 x(r)\, \mathrm{d}r. \tag{3.3}$$

The condition that the core contains the random fraction f_r of all Mn atoms in the cluster imposes limitations to the value r_s. We set $r_c = a r_s$ and $x_s = b x_c$ for simplicity and get by equating

$$f_r \equiv \frac{N_c}{N_0} = \frac{(1+3b)a^3}{a^3 + b(1+a+a^2)}. \tag{3.4}$$

This equation has only one physical solution for a as a function of f_r and b. We now choose some parameters in our calculations to be fixed and some to be free in order to reproduce the properties of the GeMn sample with $r_{Ge} = 0.08\,\text{Å}\,\text{s}^{-1}$ and $x = 7.3\,\%$. f_r shall be fixed, with a value of 0.88 as determined by the channeling experiments. Furthermore, we set $x_c = 60\,\%$, which seems a reasonable estimate if we extrapolate the value found by APT for the sample with $r_{Ge} = 0.25\,\text{Å}\,\text{s}^{-1}$ and $x = 2.0\,\%$. The concentration gradient in the core shall be described by $b = \frac{2}{3}$. A value of $0\,\mu_B$ and $3\,\mu_B$ is ascribed to the magnetic moment per Mn atom for the core and shell, respectively. Fixing all these values, in order to get the measured average supermoment of one cluster of $\mu_{sp} = 360\,\mu_B$,[23] now a core radius of approximately $r_c = 2.2\,\text{nm}$ is needed. Employing Eq. (3.4) then results in a shell radius of $r_s = 2.4\,\text{nm}$. In this core-shell picture, the core radius of an average cluster has thus a reasonable magnitude, whereas it is a factor of two larger than what the specific cluster depicted in the HAADF micrograph of Fig. 3.6 would imply. Keeping in mind, however, that the supermoment sizes follow a log-normal distribution and thus not every cluster has to exhibit the average value μ_{sp}, the width of this distribution[23] suggests that also smaller clusters with smaller supermoment sizes would be described properly by the core-shell picture. More surprising is fact that the shell radius is not as much larger than the core radius, other than indicated by the HAADF image. Probably, the contrast variations surrounding the specific cluster string in the HAADF image are in parts also

due to the variations in the diameter along the string, which causes an overlap with the Ge matrix in the TEM projection.

The volume fraction of the GeMn clusters v_{clusters} can also be calculated in this model by

$$v_{\text{clusters}} = n_{\text{sp}} V_{\text{cluster}}, \tag{3.5}$$

where $V_{\text{cluster}} = \frac{4}{3}\pi r_{\text{s}}^3$ is the volume of one cluster. The supermoment density n_{sp} was determined with the help of magnetization measurements as $2.4 \times 10^{18}\,\text{cm}^{-3}$.[23] This yields $v_{\text{clusters}} = 15\,\%$, in good agreement with the estimates from structural investigations.[23] At last, also the nominal average Mn concentration of the whole thin film of $x = 7.3\,\%$ is reasonably described in this core-shell model by

$$x_{\text{average}} = \frac{v_{\text{clusters}} N_0}{V_{\text{cluster}} n_{\text{Ge}}} = 5.4\,\%. \tag{3.6}$$

Hence, from the plausible agreement between various values given by the APT and STEM analyses, the magnetometry data, and the calculated values in the framework of the core-shell model, we infer that the magnetically active part of Mn is located at the surfaces, in the shells of the GeMn clusters, whereas theirs cores remain magnetically inactive.

It is worthwhile to add that different concentration profiles than the one depicted in Fig. 3.7 deliver overall worse agreement between the calculated and the observed parameters. For example, assuming the concentration gradient to be uniform throughout the core and the shell would either demand $x_{\text{c}} = 120\,\%$ or $r_{\text{c}} = 2.8\,\text{nm}$ while keeping $r_{\text{c}} = 2.2\,\text{nm}$ and $x_{\text{c}} = 60\,\%$ fixed, respectively, in order to reproduce the same average magnetic supermoment of one cluster and the average Mn concentration of the thin film. Both values seem quite unlikely. Assuming a constant Mn concentration in the core while maintaining the linear gradient in the shell, which is equivalent to setting $b = 1$ in Eq. (3.4), would allow to reduce the core radius down to $r_{\text{c}} = 2.0\,\text{nm}$, however, such a profile would not be in line with the observation of a nonstoichiometric GeMn alloy within the GeMn clusters.

4

Strain-driven stacking of GeMn clusters

In the previous chapter, we concentrated on finding connections between the structural and magnetic properties of GeMn thin films. Here, we want to shed more light on the characteristic string-of-pearls-like pattern of GeMn clusters that forms during the self-assembly process. For this purpose, we first revisit properties of the previously shown GeMn thin films, which were fabricated by the continuous codeposition of Ge and Mn. Moreover, we will introduce samples with a Ge/GeMn superlattice structure in Section 4.2.

4.1 Localization of strain in GeMn thin films

Extending the STEM investigation of the previous chapter, we examined a GeMn cluster string of the GeMn sample with $r_{\mathrm{Ge}} = 0.08\,\text{Å}\,\mathrm{s}^{-1}$ and $x = 7.3\,\%$ by low-angle annular dark field (LAADF) STEM. Due to the low-angle deflection, this STEM mode is not as sensitive to chemically induced contrast variations as HAADF but instead more sensitive to strain-induced fluctuations.

In the LAADF micrograph, shown in Fig. 4.1a, the previously discussed dark image contrast indicative of an amorphous phase in the center of the string is reproduced. This is marked with the solid circle in the right panel of Fig. 4.1a. For comparison, we once more depict in Fig. 4.1b the HAADF image of the very same cluster string, already shown in the previous chapter. In addition to the amorphous core, the LAADF micrograph exhibits a distinct, bright halo surrounding the center of the string. For clarity, we marked this halo by the delimiting dashed circle in the right panel of Fig. 4.1a. The halo indicates the occurrence of strain in the matrix material in the direct vicinity of the GeMn clusters.

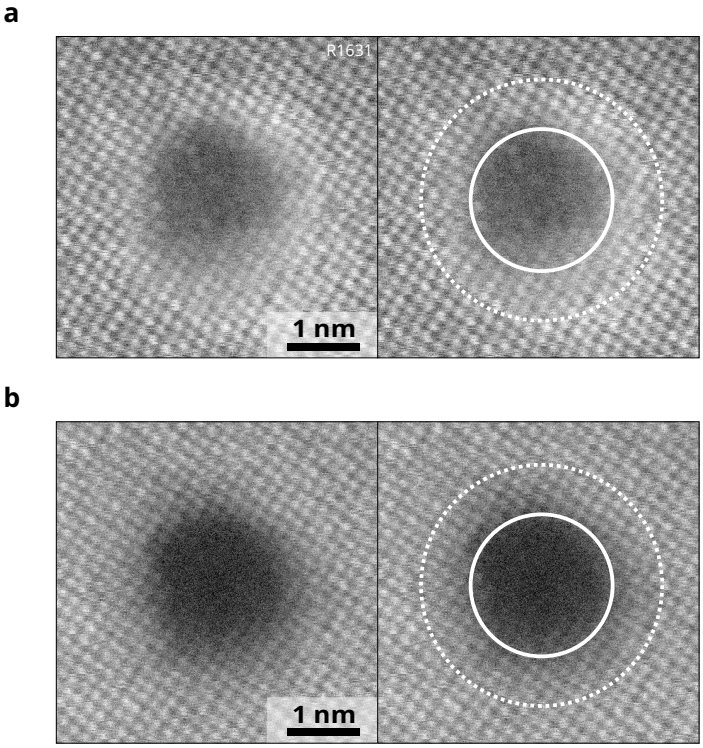

Figure 4.1 | High-resolution plan view STEM images of a sample with $r_{Ge} = 0.08\,\text{Å}\,\text{s}^{-1}$ and $x = 7.3\,\%$ in **a**, LAADF and **b**, HAADF mode. Both images were acquired for the same GeMn cluster string. Right panels are copies of the left panels and contain white circles to mark regions with contrast differing from the Ge matrix contrast. The white halo in the LAADF micrograph of **a** indicates strain.

The presence of local strain confirms a prior work, where the average in-plane strain was quantified to be 2 %.[25] Such strain values are comparable to typical strain values present in lattice-mismatched heterosystems exhibiting self-assembled island formation.[96] Given the short distances between two consecutive GeMn clusters in the [001] growth direction, see Chapter 3, it is very likely that each cluster feels the strain field of its predecessors, as it is known for stacked self-assembled semiconductor islands.[97,98] In these systems, the in-plane positions of self-assembled islands of the first deposited layer serve as seeds for islands in consecutive layers, which by this means experience an effective minimization of their strain energy. In the present GeMn thin film system, the nonequidistant stacking of GeMn clusters is presumably the result of the codeposition of Mn and Ge because thereby the formation and stacking of the clusters follow a dynamic, uncontrolled manner. In order to further confirm that the minimization of strain energy is a driving force for the vertical stacking of GeMn clusters, samples with well-defined distances between the clusters would be helpful. These would also allow to check whether clusters can be stacked over long distances into a string of pearls pattern in GeMn epitaxy. Therefore, we have investigated GeMn/Ge superlattice samples, as outlined in the following.

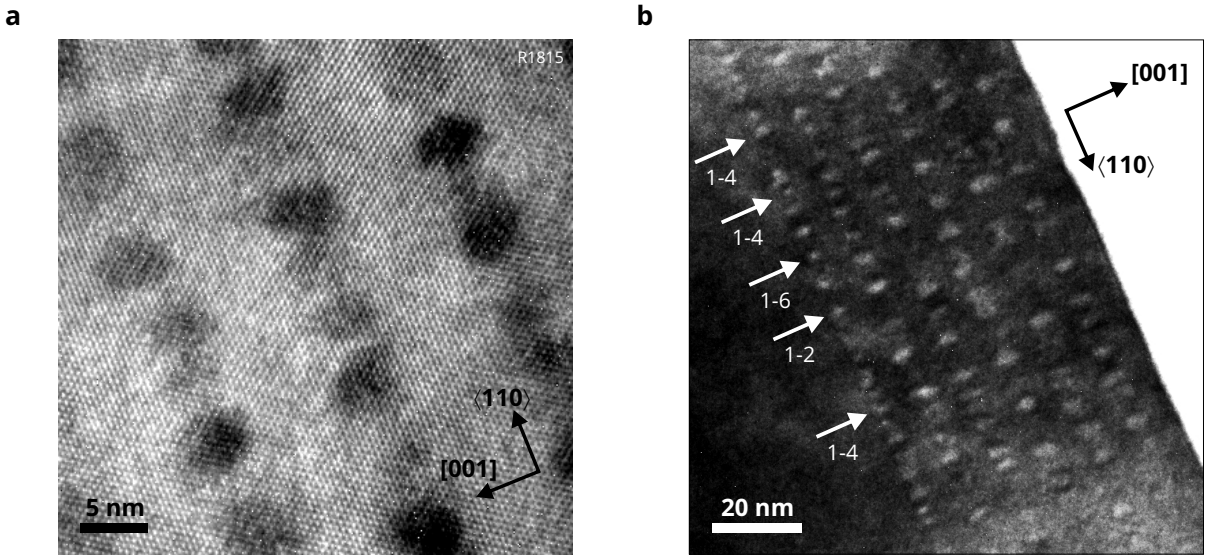

Figure 4.2 | TEM micrographs of a GeMn/Ge superlattice sample with nominally 3 nm-thick GeMn and 6 nm-thick Ge spacer layers. **a**, HRTEM revealing the elongation of GeMn clusters (dark spots) in growth direction with typical dimension of 4 nm in growth and 3 nm in in-plane direction. **b**, BF (000) overview image of the same sample. The arrows exemplary indicate positions in the specimen where a vertical correlation of GeMn clusters (bright spots) can be observed. The numbers denote the first and last layer of the correlation.

4.2 Ge/GeMn superlattices

A test of strain-driven stacking of single GeMn clusters in (Mn,Ge) codeposition can be made by interrupting the deposition of Mn, leaving the growth of pure Ge spacer layers. If the thicknesses of the Ge spacer layers and the GeMn layers in a superlattice thin film with several alternating GeMn/Ge layers are properly adjusted, an investigation of the range of the strain field caused by the formation of only one GeMn cluster is possible. We thus grew a set of samples containing each six GeMn layers separated by five Ge layers. The thickness of the GeMn layers was kept fixed at 3 nm and the Mn concentration of the GeMn alloy set to $x = 7.3\,\%$. The set consisted of five samples with increasing Ge spacer layer thickness of 3 nm, 6 nm, 9 nm, 15 nm, and 30 nm. The last GeMn layer in each sample was capped with 10 nm Ge. The growth rate was set to $r_{\mathrm{Ge}} = 0.08\,\text{Å}\,\mathrm{s}^{-1}$, i.e. the parameters for the growth of the GeMn layers were similar to those of the sample depicted in Fig. 3.1.

Figure 4.2a shows a HRTEM micrograph of the sample with 6 nm-thick Ge spacer layers in cross section. Dark spots in the image confirm the formation of individual GeMn clusters within the nominally 3 nm-thick GeMn layers. Interestingly, the GeMn clusters do not exhibit a sharp interface with the Ge spacer layers, as the growth protocol would imply. In fact, their boundaries in growth direction seem to be washed out to approximately 4 nm in average. With in-plane dimension of about 3 nm this

results in a slightly elliptical shape, similar to that of GeMn clusters in the continuous thin film shown in Fig. 2.1a. We relate this effect either to a segregation process, which is known to be very effective for subsurfactant Mn impurity atoms in [001]-oriented Ge crystals,[20,99] or an interdiffusion process as a first consequence of relief of strain energy accumulation. The latter would be in strong similarity to heteroepitaxial island formation.[100,101] In this context, we remark that the concentration profiles of the GeMn clusters, which were depicted in Fig. 3.3, particularly regarding the rising concentration toward the cluster cores, resemble the distribution of atom species in capped semiconductor islands forming spontaneously in lattice-mismatched heterosystems.[102]

The HRTEM micrograph of Fig. 4.2a already suggests a vertical correlation of individual GeMn clusters in adjacent GeMn layers, an observation that is further evidenced by the overview bright field (BF) TEM image, selecting the directly transmitted (000) electron beam, shown in Fig. 4.2b. In the BF (000) micrograph, GeMn clusters appear as bright spots. The white arrows in Fig. 4.2b exemplary mark positions where GeMn clusters are stacked, the numbers next to the arrows denoting the range of GeMn layers that are involved in this vertical correlation. We observe a cluster correlation that can span all six GeMn layers as well as only two layers. Also, individual apparently nonstacked clusters are present in this sample.

In Fig. 4.3a, a BF TEM image, containing the (000) and diffracted beams, is depicted for the sample with a Ge spacer layer thickness of 30 nm. The image quality is not very good due to a poor specimen quality. Nevertheless, the formation of GeMn clusters can be observed as dark spots in the image. In an effort to enhance the contrast for a better distinguishability of the GeMn clusters from the surrounding Ge matrix, the BF image was digitally post-processed. The result is shown in Fig. 4.3b. Now, an apparent vertical correlation of GeMn clusters becomes visible, as indicated by the double arrows in the figure. The post-processed image thus suggests that, despite the relatively large GeMn layer distance, stacking of GeMn clusters is still possible, very much like in the sample with only 6 nm-thick Ge spacer layers.

4.3 Discussion

From these first observations we infer that the minimization of strain energy is the only reasonable cause for the stacking of GeMn clusters over such large distances. Clearly, this result has to be confirmed in further TEM studies using better prepared specimens and also including the other samples of the series with 3 nm, 9 nm, and 15 nm-thick Ge spacers in order to enhance statistics. Yet, the superlattice studies consistently support our conjectures from the combined APT, TEM, and STEM studies for the occurrence of a string of pearls pattern in continuous GeMn thin films.

The fact that the strain-driven correlation of GeMn clusters of only a few nanometer in extent apparently spans distances of at least up to 30 nm in GeMn/Ge superlattices represents a difference to the well-known stacking phenomenon arising in the heteroepitaxy of lattice-mismatched material systems, such as Ge/Si or InAs/GaAs.

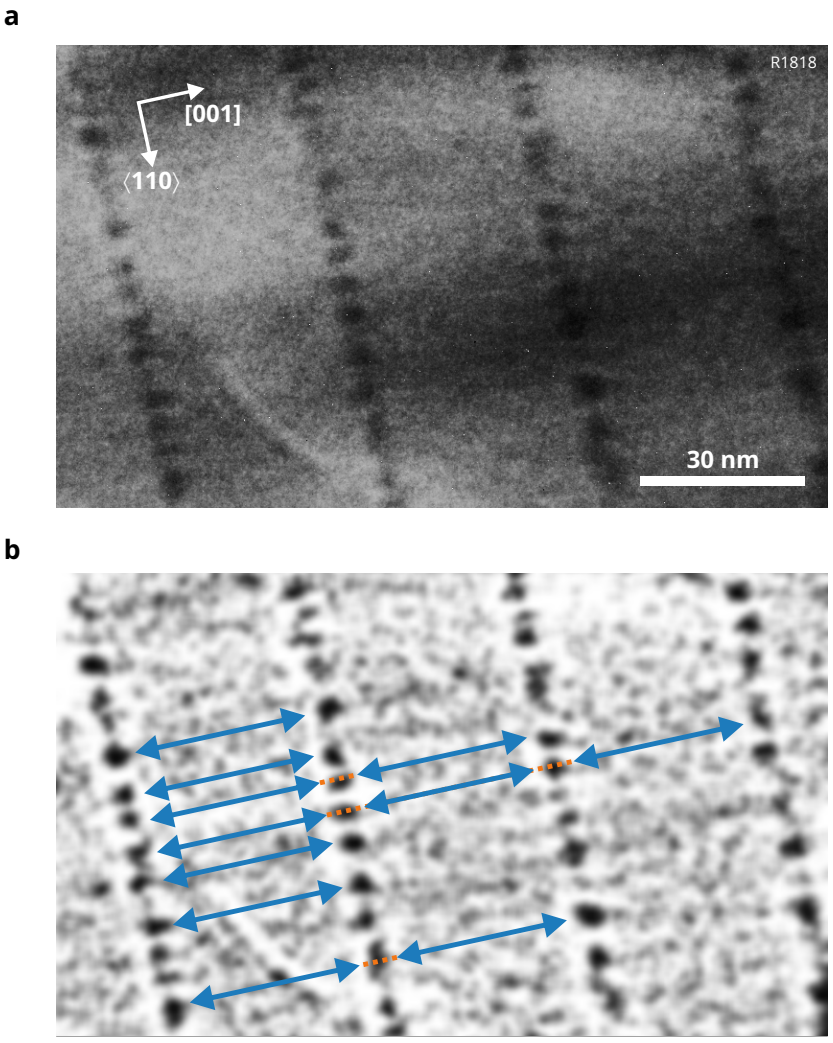

Figure 4.3 | TEM micrographs of a GeMn/Ge superlattice sample with nominally 3 nm-thick GeMn and 30 nm-thick Ge spacer layers. **a**, BF overview image showing the second to fifth GeMn layer. Dark spots indicate the formation of GeMn clusters. **b**, Same image as in **a** after application of digital post-processing filters to enhance contrast fluctuations. Double arrows exemplary mark apparently vertically correlated GeMn clusters.

There, only islands with considerably larger in-plane base diameter can exhibit a strain field strong enough to cause the vertical correlation of islands over such long distances.[98,101,103,104] This implies that in the case of GeMn epitaxy already small minima in the surface strain potential, which are caused by the buried GeMn clusters, are sufficient to trigger the seeding of subsequent GeMn clusters.

For clarification and to avoid confusion regarding the role of strain, we note that the analogy between GeMn/Ge epitaxy and conventional lattice-mismatched heteroepitaxy is limited when it comes to the formation of clusters and islands, respectively. For the latter the formation of 3D islands protruding from the epitaxy plane is the only possible way to reduce the strain energy of deposited layers of the lattice-mismatched material. For GeMn/Ge epitaxy it is not known whether the deposited GeMn would

formally exhibit strain if maintained as such on the Ge substrate surface. If so, due to the miscibility gap of the GeMn material system, it is in principle possible that the deposited layers reduce their overall strain energy by the decomposition into Ge-rich regions completely free of strain and small Mn-rich regions with increased strain. Then, also in this material system, minimization of strain energy would cause the formation of 'islands', yet, not protruding from but embedded in the epitaxy plane. One cannot argue from our observations of a strain field surrounding the Mn-rich GeMn clusters, however, that such a scenario is indeed given for the present GeMn thin films, because these observations mark only the final situation after the decomposition has already taken place. In the early stages, the formation of GeMn clusters could very well be only the consequence of a self-assembly process entirely driven by the chemical energetics, as introduced in Section 2.3. Mn agglomeration, as for example observed in Ref. 20, could act as initial seed for the – subsequently – strain-assisted further development of a GeMn cluster on top.

Regarding the crystalline order, which we presented in Chapter 3, it is unclear as to whether such a seed of a GeMn cluster is already amorphous from the beginning or if it initially adopts the cubic order of the Ge matrix. In (Mn,Ge) codeposition, the first case corresponds to the parallel growth of an amorphous cluster embedded in a crystalline Ge matrix that is seeded by the substrate. In the latter case, the in-plane strain induced by the parallel growth of both the Ge matrix and a cubic GeMn cluster seed would lead to an amorphization of the cluster during the epitaxy of the following layers.

An understanding of the thermodynamic driving forces of the very early stages of the epitaxy, including Mn segregation in (Mn,Ge) codeposition, would be extremely beneficial for the improvement of the control of the self-assembly and the crystallinity of the GeMn clusters. Such control will have direct consequences on the magnetic properties of the material, as we outlined in Chapter 3. Moreover, the degree of crystallinity controls the resulting band structure and thus the electric properties of the material. Tailoring these properties might become of importance in future spintronic applications.

Further understanding of the origin of in-plane strain distribution promises to enhance the control on the homogeneity of the distribution of the GeMn cluster along a string. A dense and very homogeneous stacking of the clusters on a string would increase the probability of magnetic coupling along a stack and could contribute to global ferromagnetism, as for example observed by Jamet *et al.*[16]

5

Interplay of electrical transport properties of GeMn thin films and Ge substrates

DURING the past decade, the intense study of epitaxial GeMn thin films has brought about an increasingly converging picture of their nanostructure, which we partly hinted at in the previous chapters. In contrast, the fingerprint of these thin films in magnetotransport studies lacks such a coherent description. Particularly, GeMn thin films fabricated on Ge substrates exhibit rather versatile magnetotransport properties.[14,16,17,42,67] In this context, it is interesting to note a fact often overlooked and thus rarely addressed in literature on GeMn transport studies: While high-purity substrates of semiconductors such as Si or GaAs exhibit room temperature (RT) resistivities greater than $10^3\,\Omega\,\mathrm{cm}$, this is not the case for Ge substrates. RT resistivities of Ge are intrinsically limited around $50\,\Omega\,\mathrm{cm}$ because intrinsic conduction in Ge, due to its small band gap, already becomes important around RT.[105] This upper limit is already reached with impurity concentrations as low as $10^{13}\,\mathrm{cm}^{-3}$.[106] Substrates with higher purity are commercially not available.

We will show in Section 5.2 that the electrical properties of epitaxial GeMn thin films fabricated by solid-source MBE on such high-purity Ge substrates can severely be influenced by parallel conduction through the substrate. To furthermore demonstrate the effects of parallel conduction, we present in Section 5.3 a system of nonmagnetic, degenerately doped Ge:B epitaxial layers grown on these high-purity Ge substrates. Some of these results have a remarkable resemblance to previously published data on magnetic GeMn thin films,[22,67] although our Ge:B films do not show any sign of magnetism other than common diamagnetism. We will give a two-layer model

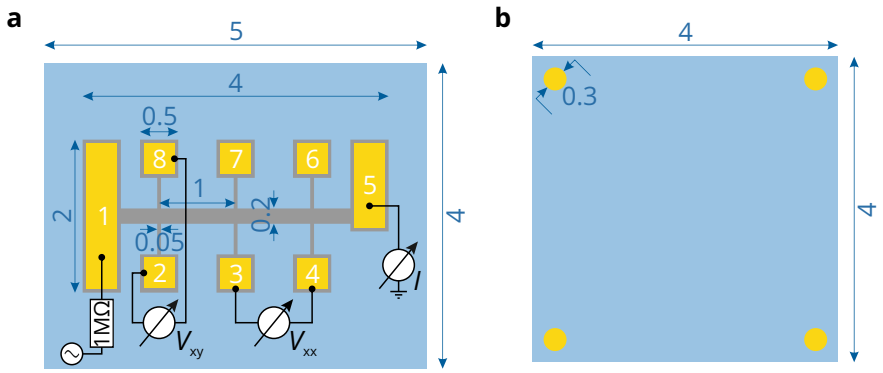

Figure 5.1 | a, Scaled schematic of samples with Hall bar mesa. The setup for measuring the longitudinal (V_{xx}) and Hall (V_{xy}) voltages as well as the total current (I) is also indicated. **b**, Geometry of samples where the van der Pauw method has been employed. Dimensions are given in units of millimeter.

accounting for the parallel conduction through the substrate, which sufficiently well describes the experimental magnetotransport results in those types of thin films. We will briefly address the influence of the sample geometry on the transport behavior within the parallel conduction scheme in Section 5.4 and discuss possible solutions to overcome the parallel conduction in Section 5.5. The contents of this chapter have been published in Ref. 107.

5.1 Experimental

The investigated samples were fabricated with solid-source MBE under ultrahigh vacuum conditions at a base pressure of 5×10^{-11} mbar. We used high-resistivity Ge (001) substrates with a RT resistivity larger than 40 Ω cm and thickness of approximately 500 µm. These substrates are specified to exhibit n-type conduction, due to antimony impurities dissolved into the Ge crystal during its fabrication. However, we would like to note that the vendors specification of this n-type conduction is only true about RT. In fact, the substrate undergoes a transition to p-type conduction below RT. This indicates the presence of a majority of residual acceptorlike impurities. Hence, the substrate may suffer from considerable autocompensation. At RT, the conduction behavior is dominated by intrinsic charge carriers, primarily by electrons due to their smaller effective mass, and is therefore n-type.

Prior to the growth of all thin films a 80 nm-thick, undoped Ge buffer layer was deposited. The GeMn sample was grown by codeposition of Mn and Ge at a Ge growth rate of $r_{Ge} = 0.08\,Å\,s^{-1}$ and at a constant substrate temperature of $T_S = 60\,°C$ in order to avoid the formation of intermetallic secondary phases. The film thickness amounts to 200 nm with a total Mn concentration of $x = 2.8\,\%$. A thorough characterization of the structural and magnetic properties of this sample may be found elsewhere.[15,23]

For comparison we also fabricated a nonmagnetic p-type Ge thin film using a boron effusion cell. This sample was fabricated at $r_{Ge} = 0.3\,\text{Å}\,\text{s}^{-1}$ and $T_S = 360\,°\text{C}$ with a thickness of 200 nm. With $5 \times 10^{19}\,\text{cm}^{-3}$ the B concentration was chosen to be well above the insulator-to-metal transition.[108]

For transport measurements an approximately 450 nm-high Hall bar (HB) mesa was defined by standard lithography methods and wet-chemical etching. Geometrical details are given in Fig. 5.1a. The longitudinal and Hall resistance, R and R_{xy}, were determined by applying a current I along the HB and measuring the longitudinal and Hall voltages, V_{xx} and V_{xy}, in a standard, quasi-dc lock-in setup using an additional $1\,\text{T}\Omega$ input impedance voltage amplifier before the lock-in. As will be introduced in Section 5.4, some samples were also investigated via the van der Pauw method in the geometry shown in Fig. 5.1b.

Temperature-dependent resistance measurements without applied magnetic fields were performed with a heatable sample stick inserted in a liquid helium dewar. The field-dependent measurements were performed in a variable-temperature-insert magnet cryostat, if the shown field range does not exceed 7 T, and in a 300 mK magnet cryostat with a customized, heatable samplestick, if higher fields are shown. The magnetic field was applied perpendicular to the sample surface. Further information on sample processing, realization of ohmic contacts and measurement issues is available in Refs. 109 and 110.

5.2 Nondegenerate GeMn thin films on high-resistivity Ge substrates

Figure 5.2 depicts the sample resistance of the bare high-resistivity Ge substrate sample as a function of temperature T. We can identify the three distinct regions well known for nondegenerate semiconductors, i.e. the freeze-out of extrinsic charge carriers, the extrinsic and the onset of the intrinsic range.

Also shown in Fig. 5.2 is the resistance measurement of the GeMn thin film grown on the high-resistivity Ge substrate. When comparing the two samples, we notice that the resistance of both samples is of the same order of magnitude and has a very similar temperature dependence. This becomes more evident in an Arrhenius plot of the resistance depicted in the inset of Fig. 5.2. Both curves exhibit the same linear slope in the extrinsic freeze-out regime, which corresponds to a thermal activation energy of $E_a = 10.9\,\text{meV}$ for the dopant impurities.[①] This is in good agreement with the activation energy of shallow impurities in Ge.[112,113] It does not correspond to the activation energy of Mn in Ge because Mn is expected to be a two-level, deep band gap acceptor with $E_a = 160\,\text{meV}$ and 370 meV, respectively.[114] It rather seems that in both samples the residual impurities dissolved in the Ge substrate dominate the measurements.

[①] The temperature dependence of the mobility has been neglected. Due to autocompensation we fitted the data with an $e^{(E_a/k_BT)}$ law, see e.g. Blakemore.[111]

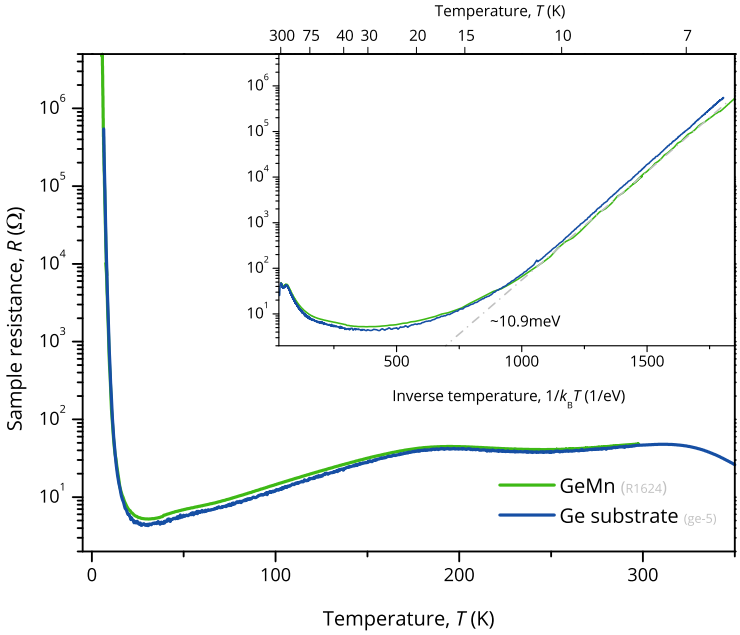

Figure 5.2 | Sample resistance versus temperature for the GeMn sample (green) and the Ge substrate reference (blue). Inset: Same data as function of the inverse temperature $\frac{1}{k_B T}$. A straight line (grey), corresponding to an activation energy of $E_a = 10.9$ meV, can be fitted to the extrinsic freeze-out.

Figure 5.3a shows the MR effect of the GeMn sample versus external magnetic field B for various temperatures, calculated according to the convention

$$\mathrm{MR}\,[\%] = \frac{R(B) - R(0)}{R(0)} \times 100. \tag{5.1}$$

The MR effect is positive and exhibits a paraboliclike dependence for weak fields tending toward a linear dependence at higher fields, without any signs of saturation. For higher temperatures the MR effect gradually decreases in its magnitude. Similar results on the MR effect in GeMn have already been reported.[16]

The orbital MR of the semiclassical Boltzmann transport theory cannot be responsible for the positive MR effect depicted in Fig. 5.3a because the order of magnitude of the MR is too large. In fact, an orbital MR effect would also not explain the nonsaturating character of the observed MR at large fields.[115] A connection of the MR to the magnetic nature of the GeMn epilayer can be ruled out for the same reason because its magnetization saturates at fields about 2 T.[15,23] Jamet *et al.*[16] proposed the occurrence of a geometrically enhanced MR effect[116] to account for the large magnitude and the linear increase at high fields of the MR in their GeMn sample, stemming from the presence of highly conducting Mn-rich inclusions. Described by a resistance network, such an inhomogeneous semiconductor can indeed exhibit extremely large, nonsaturating MR.[117–119] However, we obtain essentially equal results for the magnitude, field and temperature dependence of the MR of the bare Ge substrate, as shown in Fig. 5.3b.

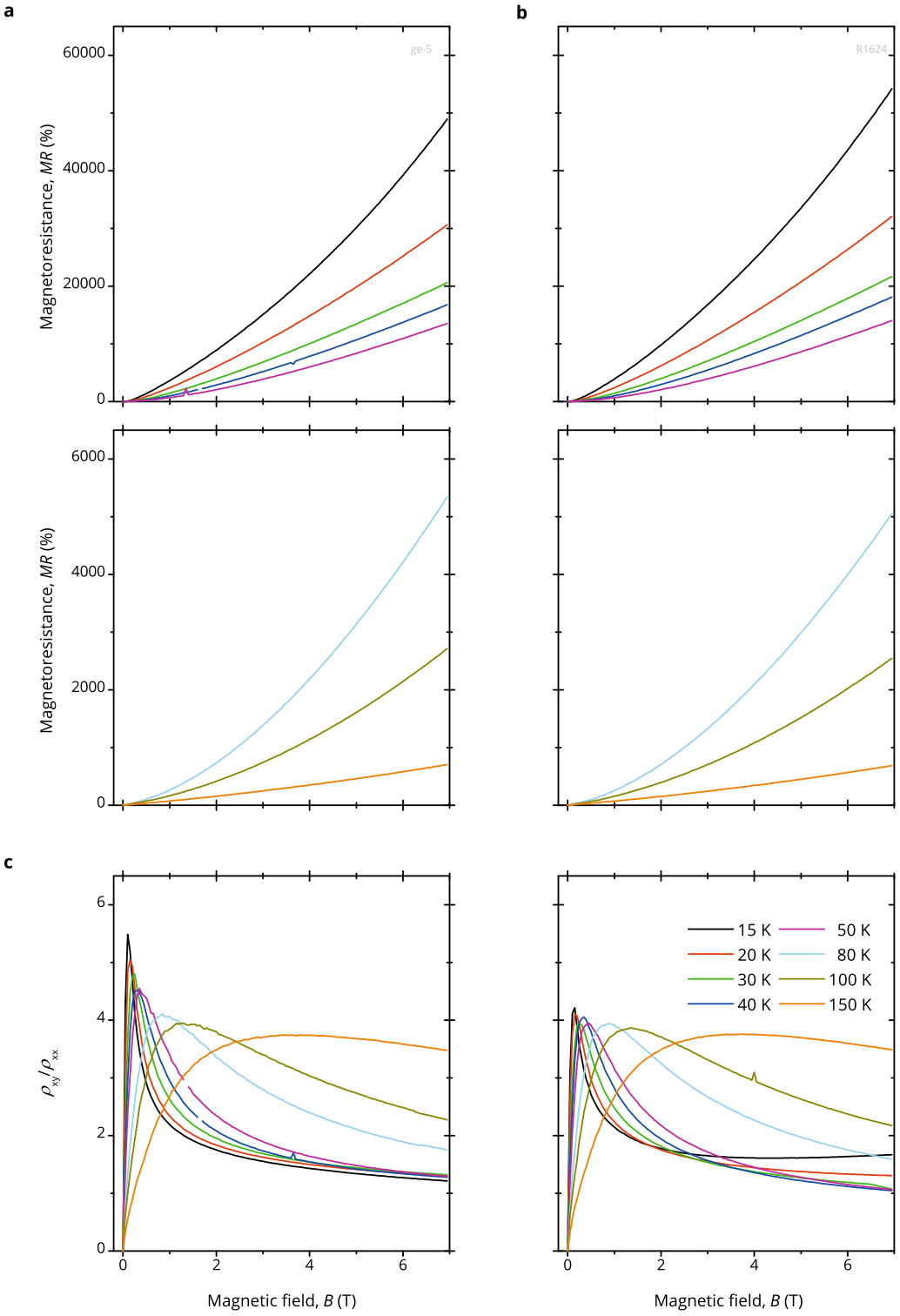

Figure 5.3 | a, MR for various temperatures for the GeMn sample. **b**, MR for the bare high-resistivity Ge substrate. **c**, Tangent of the Hall angle for the GeMn sample (left) and the Ge substrate (right). The color code for the measurement temperatures is the same for all panels.

The left panel in Fig. 5.3c depicts the tangent of the Hall angle of the GeMn sample, defined as ρ_{xy}/ρ_{xx} with ρ_{xy} and ρ_{xx} being the Hall and longitudinal resistivities, respectively. The Hall angle gives a more direct estimate of possible magnetization-induced contributions to the ordinary Hall effect than the common Hall curve. The Hall angle increases steeply with field, tending toward a saturation at higher fields. Similar results were found by other groups for the GeMn material system and were either attributed to a magnetization-induced AHE[16] or related to the multiple Mn acceptor energy states leading to an effective two-band-like conduction.[67] Our undoped, nonmagnetic Ge substrate exhibits the same Hall angle behavior, as can be seen in the right panel of Fig. 5.3c.

The data presented on the GeMn thin film in Figs. 5.2 and 5.3 show a strong similarity to the underlying substrate. This suggests that neither the inhomogeneity, magnetic nature, nor the presence of Mn acceptors in the GeMn thin film leads to the observed transport properties in the present case. We conclude that the transport properties of our GeMn sample do emerge from parallel conduction through the substrate.

This dominating contribution of the substrate can be understood, when one considers the system of an epitaxially fabricated GeMn thin film on top of the high-resistivity Ge substrate as two parallel conducting resistors. For an independent determination of the transport properties of the epilayer without contributions from the substrate layer, the resistance of the GeMn epilayer has to be at least a factor of 10 smaller than that of the substrate. A comparison of the thicknesses of these two layers implicates that the epilayer resistivity then has to be smaller by a factor of 10^4 than the resistivity of the Ge substrate. Considering the RT value of the substrate resistivity of about $40\,\Omega\,\mathrm{cm}$ this in turn means that the GeMn epilayer resistivity has to be in the $10^{-3}\,\Omega\,\mathrm{cm}$ regime. For the present GeMn epitaxial layer, having a hole density around $10^{19}\,\mathrm{cm}^{-3}$ (cf. Section 5.5), but nevertheless being nondegenerate, that would demand RT mobilities on the order of a few $10^2\,\mathrm{cm}\,\mathrm{V}^{-2}\,\mathrm{s}$. Yet, such a high mobility cannot be expected because GeMn thin films exhibit a very inhomogeneous nanostructure, as we outlined in the preceding part of this thesis. In fact, mobilities of that order of magnitude are only reached in conventional p-type-doped Ge with similar hole concentrations, when the dopants are homogeneously diluted in the host matrix.[120] In essence, because of the low conductivity of nondegenerate GeMn thin films, one can not determine the transport properties of the GeMn epilayer in a straightforward manner, when it is fabricated on high-resistivity Ge substrates.

5.3 Degenerate p-type Ge thin films on high-resistivity Ge substrates

We now address whether an electrical transport characterization of degenerately doped, p-type GeMn thin films on high-resistivity Ge substrates, i.e. thin films with carrier concentrations clearly above $10^{19}\,\mathrm{cm}^{-3}$, is feasible. In order to separate phenomena

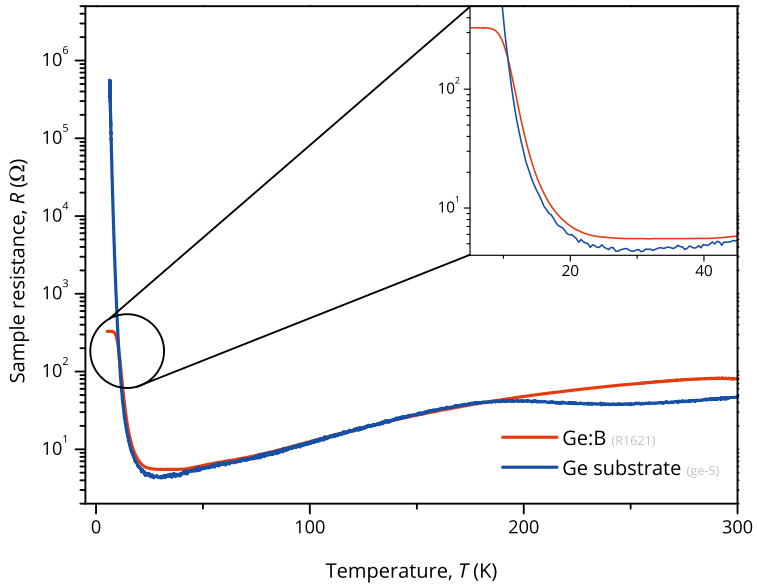

Figure 5.4 | Sample resistance of the Ge:B sample with a doping concentration of $5 \times 10^{19}\,\mathrm{cm}^{-3}$ as function of the temperature. For comparison, the measurement of the bare substrate sample is also depicted. The Ge:B sample is clearly affected by parallel conduction through the substrate. The inset shows a close-up for low temperatures, where the metallic conductance of the Ge:B epilayer is revealed because of the increasing resistance of the substrate.

related to the magnetization or nanostructure from those related to parasitic conduction through the substrate, we explored degenerately doped, nonmagnetic Ge:B epilayers as a model system. Since B opposed to Mn is not a deep but a shallow acceptor in Ge, a doping concentration of $5 \times 10^{19}\,\mathrm{cm}^{-3}$ lies well above the Mott insulator-to-metal transition, and is therefore sufficiently large to deliver thin films with degenerate, metalliclike conduction properties. Figure 5.4 shows the temperature dependence of the resistance of the Ge:B sample. Interestingly, only at temperatures below approximately 10 K the measurements reflect the metallic character of the epilayer, as the resistance enters a constant value regime. Above this temperature the curve quickly traces the measurement of the Ge substrate, which is also depicted for comparison.

The magnetic field dependence of the longitudinal resistance of the Ge:B sample is depicted in Fig. 5.5a for different temperatures. At temperatures below 9 K, the resistance shows little field dependence, yielding a MR effect which does not exceed 3 % at 4.2 K and 7 T. At approximately 9 K, we observe the onset of the decrease of the zero-field resistance with increasing temperature, as already depicted in Fig. 5.4. However, the resistance now rises quickly with increasing magnetic field, hence giving an increased MR effect. Eventually at high fields the resistance tends to saturate at the 4.2 K value. With increasing measurement temperature this saturation is shifted toward higher fields, while at the highest temperatures full saturation is not reached anymore within the investigated field range.

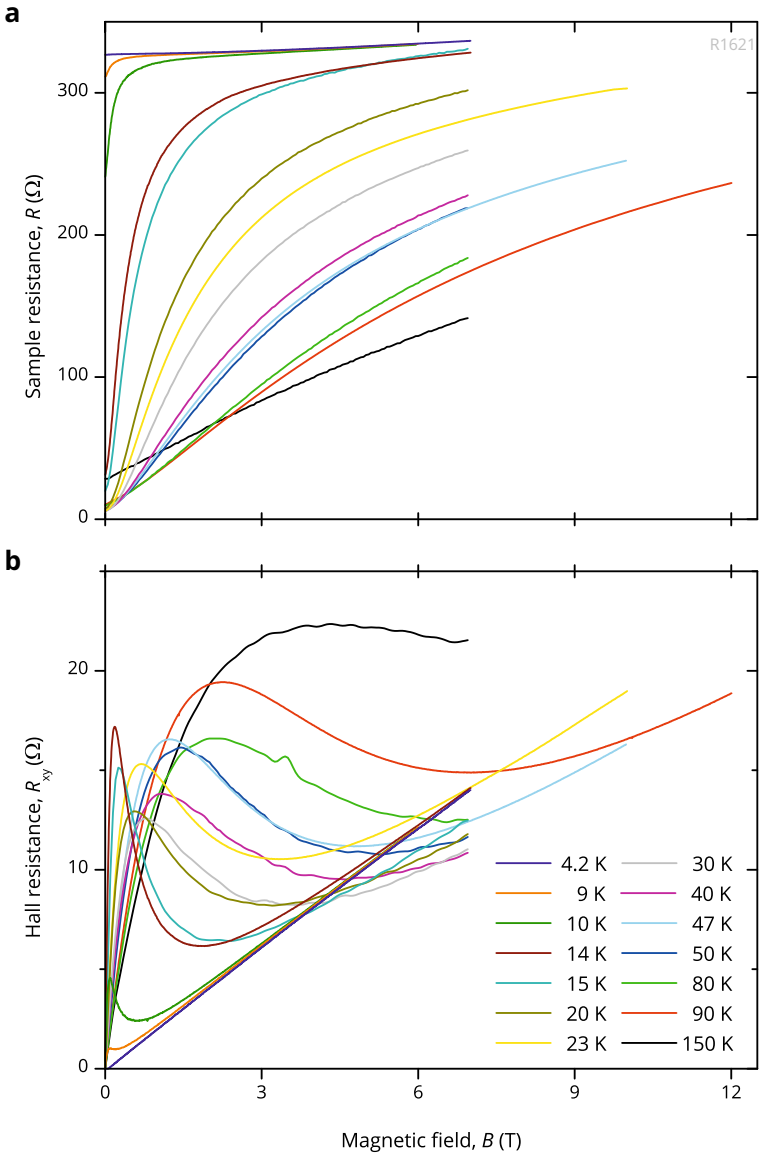

Figure 5.5 | a, Sample resistance R and **b**, Hall resistance R_{xy} versus magnetic field of the Ge:B sample. The dip of R at zero-field in **a** and the peak of R_{xy} at low fields in **b** mark the onset of parallel conduction through the substrate at 9 K. The color code for the measurement temperatures is the same in both panels.

The Hall effect of the Ge:B sample is shown in Fig. 5.5b. Below 9 K we observe a linear Hall effect. At temperatures of 9 K and above, the field dependence drastically changes: For small field values we first observe a strong increase of the Hall slope. Upon increasing the field, the Hall effect shows a peaklike maximum and then approaches the Hall curve measured for 4.2 K asymptotically.

The transport behavior of the Ge:B film, depicted in Figs. 5.4 and 5.5 is not in line with the metallic character of the epilayer. We can rather identify two distinct temperature regimes with different properties below and above 9 K. Similar results for the Hall effect and field dependence of the longitudinal resistivity, which can

be separated into two temperature regimes, were found for degenerate GeMn thin films prepared by ion implantation.[22] They were interpreted in terms of a two-band-like conduction scheme, accounting for possible electronic ground and excited states of Mn in Ge.[67] In contrast, our results in the two distinct regimes are naturally explained by assuming parallel conduction through the substrate: Below 9 K parallel conduction is not present because the substrate resistance gets very large, whereas the resistance of the metallic epilayer does not change. Assuming now that conduction only takes place in the 200 nm-thick Ge:B epilayer, we can extract a hole density of $1.54 \times 10^{19}\,\mathrm{cm}^{-3}$, in fair agreement with the nominal concentration value. Furthermore the carrier mobility amounts to the relatively small value of $\mu = 310\,\mathrm{cm}^2\,\mathrm{V}^{-1}\,\mathrm{s}$. Due to the general proportionality between the orbital MR and carrier mobility, the small MR effect would therefore also be in line with conduction through the metallic Ge:B epilayer. The transport measurements of the Ge:B sample can undoubtedly be attributed solely to the Ge:B epilayer in the temperature regime below 9 K. For temperatures above 9 K we need to include substrate contributions for an interpretation of the magnetotransport data. At low fields, conduction will mostly take place in the substrate because of its smaller resistance. At large fields, conduction through the substrate will quickly cease because its MR gets larger. Then most of the current flows through the epilayer. Thus, in the Hall as well as the MR measurement, we probe the substrate properties at a small magnetic field and the Ge:B epilayer properties at a high field, leading to the described peaking and saturation effects. The decreasing tendency of saturation at a high magnetic field with increasing measurement temperature comes from the weakening of MR of the Ge substrate. The Ge:B sample thus has to be regarded as a system of two conducting layers with different galvanomagnetic responses.

This phenomenological interpretation is supported by a description of the magnetotransport data with a two-layer conduction model. It is based on the assumption that each conducting layer can be described by its individual resistivity tensor, which reduces to a 2×2 matrix in the case where the magnetic field is normal to the plane of carrier motion. Since the two layers are not equally thick, in the following expressions we will give sheet resistivities rather than bulk resistivities to maintain generality. The resulting components of the sheet resistivity tensor of the combined two-layer system have the form

$$\begin{aligned} \rho_{xx} = \rho_{yy} &= \frac{\rho_{1,xx}(\rho_{2,xx}{}^2 + \rho_{2,xy}{}^2) + \rho_{2,xx}(\rho_{1,xx}{}^2 + \rho_{1,xy}{}^2)}{(\rho_{1,xx} + \rho_{2,xx})^2 + (\rho_{1,xy} + \rho_{2,xy})^2} \\ -\rho_{yx} = \rho_{xy} &= \frac{\rho_{1,xy}(\rho_{2,xx}{}^2 + \rho_{2,xy}{}^2) + \rho_{2,xy}(\rho_{1,xx}{}^2 + \rho_{1,xy}{}^2)}{(\rho_{1,xx} + \rho_{2,xx})^2 + (\rho_{1,xy} + \rho_{2,xy})^2}. \end{aligned} \tag{5.2}$$

The quantities with subscripts 1 and 2 correspond to the tensor components of the Ge:B epilayer and the Ge substrate layer, respectively. We restrict ourselves to a semi-empirical application of the above equations for a computation of the Hall and MR effects of the Ge:B sample for different temperatures. The parameters $\rho_{1/2,xx}$ and

$\rho_{1/2,xy}$ entering this computation are taken from measurements: The contributions $\rho_{1,xx}$ and $\rho_{1,xy}$ of the Ge:B epilayer correspond to the 4.2 K measurement curves of the Ge:B sample as were shown in Fig. 5.5a and 5.5b. We assume they do not vary with increasing temperature, which is justified by the metallic character of this epilayer (see also Section 5.5), therefore using them for all temperatures we investigate. The contributions of the Ge substrate, $\rho_{2,xx}$ and $\rho_{2,xy}$, are taken from the measurements depicted in Fig. 5.3b and 5.3c for each corresponding temperature.

Figure 5.6 shows the results of the computation of ρ_{xx} and ρ_{xy}, in the left and right panels, respectively, compared to the measured values for 15 K, 20 K, and 50 K. We also included the $\rho_{1/2,xx}$ and $\rho_{1/2,xy}$ contributions of the Ge:B epilayer and the substrate in the plot. There is good agreement between the two-layer conduction model and the measurements of the Ge:B sample for both the ρ_{xx} and ρ_{xy} components. In particular, the low-field domination of the Ge substrate layer as well as the saturation at the Ge:B epilayer contribution for high fields can be reproduced well by Eqs. (5.2). Thus, the model qualitatively demonstrates that parallel conduction through the substrate is also present in a sample with a degenerate, metallic, well-conducting epilayer in the extrinsic range of the underlying substrate. For the small quantitative differences between the computed and the actual experimental results a major reason can be made out. The model Eqs. (5.2) strictly apply for a two-layer system, where both layers have the same in-plane geometry. Since the HB mesa, however, does not define such a geometry for the substrate conduction channel, differences between theory and experiment will occur.

From the results on the degenerate Ge:B reference sample we infer that in the case of metallic GeMn thin films deposited on the high-resistivity substrate intrinsic properties of the GeMn epilayer may be directly derived in the freeze-out temperature regime of the substrate. For higher temperatures, however, care must be taken to separate the intrinsic properties of GeMn from the aforementioned effects arising due to the two-layer conduction.

We want to make a general note regarding the efforts to explain magnetotransport properties of epitaxial Ge thin films in multi-channel conduction schemes, such like the two-layer scheme presented here or the two-band-like scheme by Zhou *et al.*[67] Essentially, both rely always on the same mathematical formalism and can thus equally be applied to reproduce magnetotransport curves such as the ones presented here. They correspond, however, to a completely different physical interpretation of the measurements. Here, it is interesting to note that very recently another attempt to describe magnetotransport properties of epitaxial GeMn thin films also employed the multi-channel approach in order to model the resistance network picture of GeMn thin films, which we mentioned above.[21] The interpretation in this case is given in terms of well-conducting GeMn inclusions sitting in the poorly-conducting Ge matrix of the thin film. Which of the different interpretations of multi-channel conduction is the correct explanation for experimentally observed magnetotransport curves of the specific GeMn thin film system under investigation can only be judged by a careful weighting of arguments supporting or ruling out either interpretation.

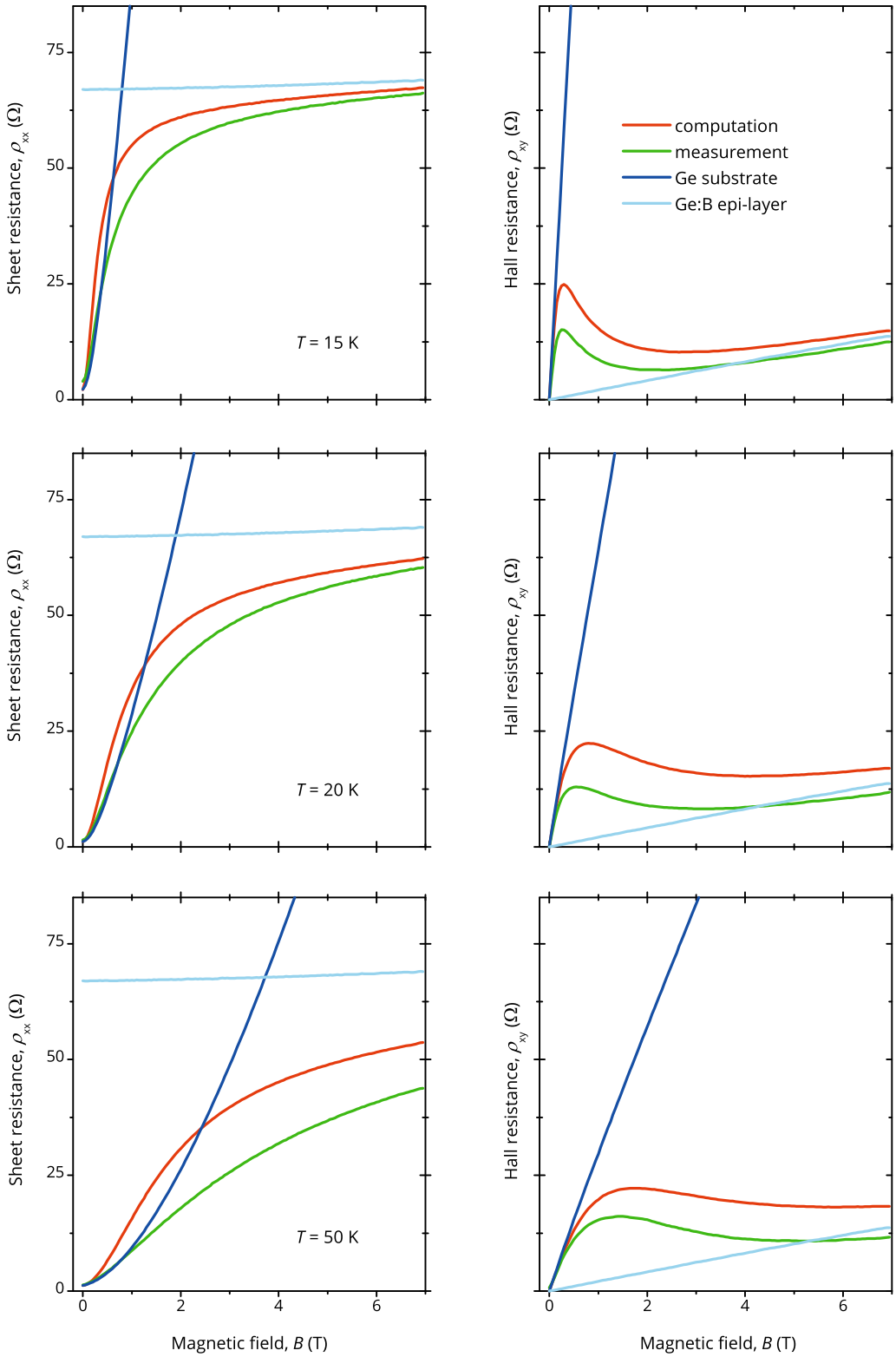

Figure 5.6 | Sheet (left) and Hall resistance (right) of the Ge:B sample versus magnetic field for different temperatures, illustrating the effect of parallel conduction through the substrate. Shown are the measurements, the computations according to Eqs. (5.2), and the individual contributions of the substrate and the metallic Ge:B epilayer.

5.4 Influence of the sample geometry on magnetoresistance measurements

It was previously shown in Fig. 5.3b that the high-resistivity substrate of very pure Ge exhibits an extremely large MR effect up to 50 000 %. However, reports of magnetotransport properties of high-purity Ge show that this large effect is not expected.[121,122] To study the MR effect of the high-resistivity substrate further, we fabricated additional samples using a van der Pauw (vdP) geometry, as depicted in the schematic of Fig. 5.1b. Interestingly, the MR effect of the vdP sample presented in Fig. 5.7 is now more than 30 times smaller than for the corresponding HB sample. Evidently, the large MR effect previously obtained in the HB geometry is not an inherent physical property of the Ge substrate. The measurements taken in vdP geometry agree much better with the above-mentioned magnetotransport studies of Ge.[121,122]

Up to now, we can only speculate about the reasons inducing the large MR effect observed in Fig. 5.3 for the HB samples. Most probably, it is related to a redistribution of the current lines upon applying a magnetic field, similar to the effect observed in Ref. 116. Referring to the sample schematic depicted in Fig. 5.1a the relatively large, metallized voltage probes 2, 3, 4, 6, 7, and 8 have to be considered as effective short circuits within the sample volume if conduction through the substrate is present. In a magnetic field, these short circuits may be diminished as the electric field and therefore the current flow will get tangent to these areas. The result is an artificial increase of the sample resistance. Additionally, the small length-to-width ratio of $l/w \approx 2$, basically given by the separation of contacts 1 and 5 and the width of contact 1, may also favor a considerable Hall-effect-induced contribution to the intrinsic MR.[123,124] Therefore, the large MR effect of up to 50 000 % and with it also the anomalous shape of the Hall angle have to be regarded as a purely extrinsic effects, which strongly rely on the specific HB geometry and the extent of parallel conduction through the substrate. It should be noted that attempts to fit these measurements by a two-carrier-type model, using reasonable parameters for the mobilities and concentrations of the two carrier types were not successful.[①]

We also reinvestigated the GeMn thin film sample in vdP geometry. Upon comparing it with the Ge substrate in Fig. 5.7, we now remark a pronounced difference between the MR measurement above approximately 3 T for temperatures up to 80 K. The MR of the GeMn sample follows a more linear behavior, while the MR of the substrate still increases superlinearly above this field. At 100 K and higher temperatures both samples exhibit the same MR effect. We infer from this behavior that at least below 100 K transport properties of the GeMn epilayer become visible in the measurement. This may be due to the fact that in vdP geometry the volume of the epilayer is not restricted to the in-plane dimensions of the etched HB mesa, but extends over the whole chip area. Therefore the effective volume ratio of the epilayer to the substrate,

[①] In the case of a two-carrier-type model Eqs. (5.2) apply, when the sheet terms are replaced by their respective bulk counterparts, using the well-known standard expressions for $\rho_{1/2,xx}$ and $\rho_{1/2,xy}$.

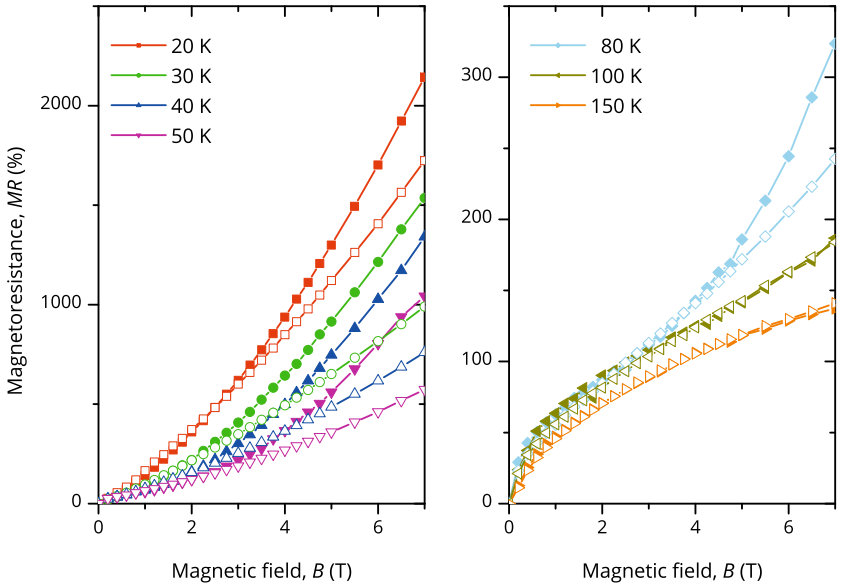

Figure 5.7 | MR for various temperatures for the GeMn sample (open symbols) and the bare Ge substrate (filled symbols) using the VdP measurement geometry.

hence the conductance ratio, is increased in the vdP geometry as compared to the HB geometry.

We thus conclude that a vdP geometry is to be favored over a HB mesa in the GeMn material system with its high probability of parallel conduction through the substrate. By using a vdP geometry the comparison of experimental data with an elaborate, *ab initio* two-layer conduction model, extending the scheme outlined in Section 5.3, may enable a derivation of inherent transport properties of GeMn thin films, in spite of the dominant contribution of the Ge substrate.

5.5 GeMn thin films on *n*-type Ge substrates

The derivation of the transport properties of GeMn thin films would be much easier if the substrate contribution could be further reduced. To this end we fabricated another GeMn sample, which employs a Ge substrate with RT resistivity of 0.13 Ω cm having a well-defined concentration of Sb donors. The build-up of a rectifying interface between the *p*-type GeMn epilayer and the *n*-type substrate would isolate the epilayer electrically from the substrate. The 80 nm-thick GeMn epilayer has a Mn concentration of 10 %. To test the benefit of this concept, we again deposited a metallic Ge:B epilayer on such a substrate. Transport measurements of these samples were made in vdP geometry.

Figure 5.8 displays the temperature-dependent resistance of the second Ge:B sample together with the employed substrate. The curve shape is now in agreement with the metallic character of the Ge:B thin film over the entire temperature range and is clearly different from the substrate behavior. Note that the substrate resistance is

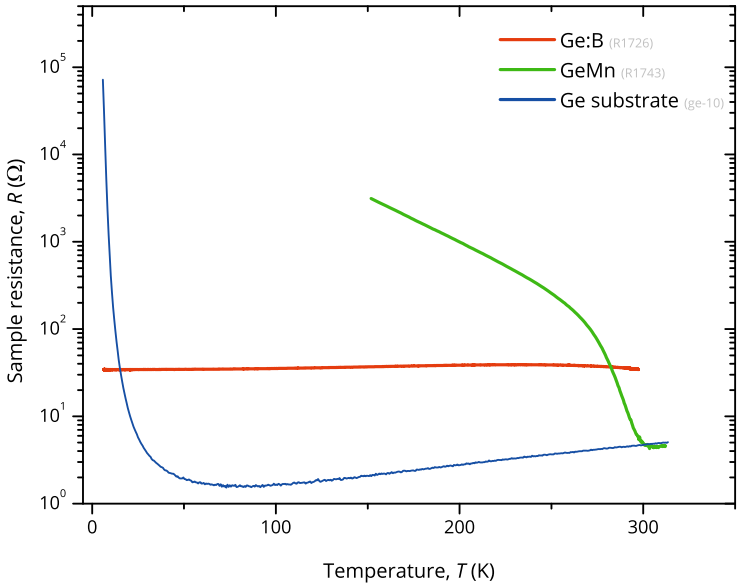

Figure 5.8 | Sample resistance versus temperature for the GeMn sample (green) and the Ge:B sample grown on the *n*-type Ge substrate (blue). The GeMn sample is affected by parallel conduction above 250 K as the *pn*-barrier gets ineffective. The Ge:B sample is not affected by parallel conduction and shows metallic conduction up to RT.

actually a factor of 10 smaller than the resistance of the epilayer for temperatures above 30 K, demonstrating the effectivity of the rectifying *pn*-barrier. The absence of parallel conduction through the substrate is also reflected in Hall measurements (not shown), which in contrast to the measurements depicted in Fig. 5.5 exhibit a linear Hall effect up to RT corresponding to the nominal doping concentration of the thin film.

Also shown in Fig. 5.8 is the resistance curve of the GeMn sample grown on the *n*-type substrate. Reliable measurement data are only available above 150 K because the electrical contacts become nonohmic below this temperature. Nevertheless, in the available temperature range we note a clear difference of the resistance of this sample as compared to that of the substrate. The resistance quickly becomes larger, suggesting the absence of parallel conduction through the substrate. Magnetotransport studies of this sample reveal *p*-type conduction pointing toward the acceptor role of Mn in Ge. Hole concentrations ranging from $5 \times 10^{18}\,\mathrm{cm}^{-3}$ to $1.5 \times 10^{19}\,\mathrm{cm}^{-3}$ for temperatures between 150 K and 210 K could be deduced from the high-field slope of Hall measurements (not shown). We could not identify any signs of a magnetization-induced AHE. This could point toward a negligible contribution of spin-porized holes to the transport at the accessible temperatures above 150 K and would be in line with the fact that the magnetic response of these types of GeMn thin films decreases with increasing temperature.[15,78]

Figure 5.9 depicts the MR of the GeMn sample for three different temperatures. Interestingly, the MR changes only slightly with temperature and does not exceed 3 % for the highest field, in contrast to a value of 120 % for the sample affected by parallel conduction through the substrate, as depicted in Fig. 5.7. While this underlines the

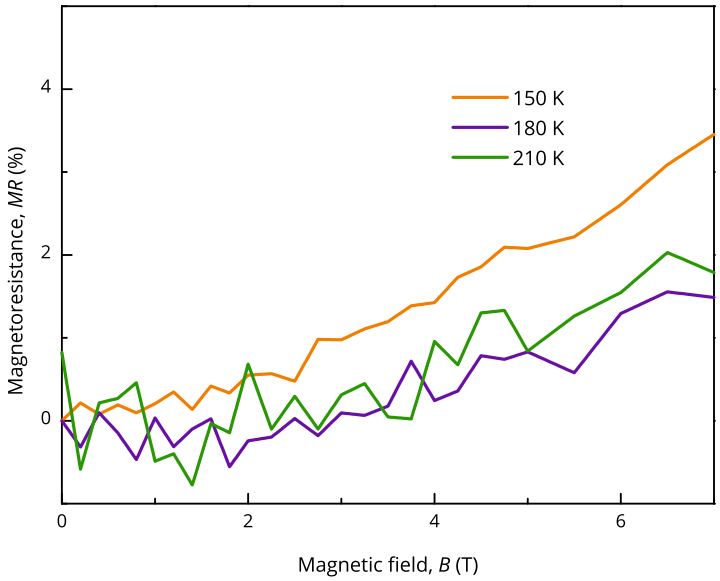

Figure 5.9 | MR for various temperatures for the GeMn sample grown on the *n*-type Ge substrate.

immense influence of the substrate contribution, it also demonstrates that the MR in our GeMn samples is apparently rather small. Its order of magnitude as well as the parabolic curvature could very well originate from the ubiquitous orbital MR in a low-mobility conductor.

The usage of an *n*-type substrate seems to unveil the intrinsic transport characteristics of our GeMn thin film samples. Parallel conduction through the substrate is greatly reduced, compared to thin films fabricated on the high-resistivity Ge substrate. For degenerate epitaxial GeMn thin films a slightly *n*-type-doped Ge substrate seems to be most adequate for transport studies. However, there are several drawbacks from a general, straightforward application of this approach to nondegenerate samples: The *pn*-barrier concept fails for higher temperatures, as indicated by the steep drop of the resistance curve of the GeMn sample in Fig. 5.8 above 250 K. A RT characterization of such devices is impossible because parallel conduction through the substrate will be present.[12] Furthermore, the formation of a space-charge region at the rectifying *pn*-interface leads to a depletion of charge carriers in a certain volume of the epilayer, depending on the carrier concentrations in the *p*- and *n*-type regions. In the present case, conduction in the epilayer is not affected because of the large hole concentration, whereas for lower carrier concentrations or rather thin epilayers, conduction in the epilayer may be quenched. Moreover, a rapid thermal annealing process to obtain ohmic contacts could not be used for these types of samples because this resulted in a direct contact to the substrate that short circuits the *pn*-barrier. A laser-assisted ultrashort-time annealing employed instead, however, did not provide ohmic contacts that work down to cryogenic temperatures.[110] More sophisticated approaches might be explored to overcome this limitation and to also enable low-temperature measurements.

6

Summary and concluding remarks for Part I

In Chapter 3 and Chapter 4 of this thesis, we elucidated some important but so far unanswered questions for the molecular beam epitaxy of GeMn thin films free of intermetallic precipitates, in particular regarding the nature of the nanometer-sized, self-assembled GeMn clusters previously evidenced. We investigated the morphology of these thin films on a nanoscale by state-of-the-art characterization methods.

The combined employment of transmission electron microscopy and atom probe tomography revealed a vertically correlated stacking of GeMn clusters along the growth direction, leading to a string-of-pearls-like arrangement. The 3D chemical mapping of the Mn distribution showed, on the one hand, that the GeMn clusters are built from a nonstoichiometric alloy of Ge and Mn with rising Mn concentration gradient toward the cluster cores and, on the other, that even for close stacking of GeMn clusters these are preserved as smallest structural entity.

Refined transmission electron microscopy studies exposed that the GeMn clusters actually consist of amorphous cluster cores enclosed by strained crystalline shells. Corresponding to this structural core-shell picture, the interpretation of the magnetic properties in a magnetic core-shell picture of the GeMn clusters was done by quantifying the fraction Mn atoms in the disordered and the crystalline GeMn phase with the help of ion beam channeling experiments. The following picture evolved: The Mn impurity atoms contained in the high-concentration cluster core remain magnetically inactive, for which antiferromagnetic coupling of nearest-neighbors Mn-Mn bonds seems most probable. Substitutional or interstitial Mn diluted in the shell is fully magnetically active and conform the superparamagnetic moment of the cluster through ferromagnetic coupling.

Strain occuring together with the presence of the GeMn clusters implied that it plays an important role in the vertical correlation of clusters during the growth of the continuous GeMn thin films. GeMn/Ge superlattices with different thicknesses of the Ge spacer layers further confirmed this conjecture because stacking over distances of at least 30 nm was observed.

From the aforementioned findings a deeper study and understanding of the thermodynamics of the growth of epitaxial GeMn, especially in the early stages when the cluster nucleate, would be valuable to tailor the nanostructure in a controlled manner. For example, the controlled realization of a dense and homogeneous stacking of GeMn clusters might be the key to enhance the probability of global ferromagnetism as observed by Jamet *et al.*[16] Also of interest is the question whether the formation of GeMn clusters with high Mn concentrations is inevitably accompanied by the development of an amorphous phase in the core. Whereas the partially amorphous GeMn clusters may be equally interesting for the experimental integration of selected spintronic applications as completely crystalline material, the realization of the latter is highly desirable to allow a better understanding and modeling of electronic properties of GeMn from a theoretical point of view.

In Chapter 5 we have shown that transport phenomena of nondegenerate GeMn thin films with hole concentrations around 10^{19} cm^{-3} fabricated on high-resistivity Ge substrates are not a consequence of the alloying of Mn with Ge. Instead it was found that the transport studies are severely influenced by parallel conduction through the substrate. This is in essence due to comparable resistances of the individual conducting layers. In this context, findings of extremely large magnetoresistance effects up to 50 000 % are related to an unfavorable measurement geometry. Measurements of a degenerate, *p*-type Ge:B reference sample showed that, despite the well-conducting epilayer, parallel conduction through the substrate is also present, significantly altering Hall and magnetoresistance measurements, which could only be understood in a two-layer conduction model. Parallel conduction through the substrate has been fully suppressed for the degenerate, *p*-type reference and partly for the GeMn thin film sample, by using Sb-doped *n*-type substrates.

Our results on magnetotransport studies emphasize the importance of a thorough characterization of the substrate properties in transport studies of GeMn thin films that are fabricated on Ge substrates. An increasing awareness and proper understanding of this problem may help to rule out possible misinterpretations. Such misinterpretation may *a priori* be avoided by using semi-insulating GaAs substrates with a resistivity larger than $10^3\,\Omega\,$cm, delivering a small lattice mismatch to the Ge diamond lattice structure. A few reports on magnetotransport of various types of GeMn thin films employing GaAs substrates exist,[10,20,32,49] however, out-diffusion of As or Ga is a critical issue.[45,125] It was recently shown that this type of unintentional codoping may actually change the structural and also the magnetic properties of GeMn thin films.[65]

In the past, interest in the GeMn material system was also raised by predictions of half-metallicity.[70,83,126] Half-metallicity is a very interesting property because it

opens the prospect to utilize GeMn as efficient spin-polarizer and consequentially as spin-injector. Naturally, the spin injection from GeMn into Ge comes first to mind. Previous efforts to assess the spin-polarizing potential of GeMn thin films by measurements of the magnetoresistance of a spin-valve-like GeMn/Ge layer-type device in perpendicular transport geometry, however, turned out to be challenging and remained inconclusive.[23] As shown in this thesis, this is in part related to the comparably large intrinsic magnetoresistance effect of Ge itself,[121,122] which potentially conceals the signature characteristic for spin injection/rejection in magnetoresistance measurements of the whole device structure. This problem may be circumvented in different measurement schemes such as nonlocal, lateral probing of spin-diffusion-induced potential differences.[127–129]

We will pursue a different approach for spin injection from GeMn, involving a Si-based device concept. This bears a number of advantages: First, spin injection into a Si-based device is interesting from a technological point of view. Realizing such spin injection via a GeMn spin-polarizing contact would also prove the often-quoted compatibility of both material systems. A Si-based device furthermore opens the possibility to investigate spin-injection by optical means utilizing optically active SiGe heterostructures. Thus for example, the electroluminescence of a light-emitting diode structure was previously employed to verify spin injection from ferromagnetic metal contacts.[130–134]

The basis for the detection of a spin-polarized carrier population in Si and Ge/Si by optical means is a better understanding of optical spin physics in group IV semiconductors. Since this topic is rarely addressed in literature, a first focus of Part II of this thesis will lie on reviewing, discussing, and developing a proper theoretical foundation. Some all-optical experiments will be presented before we eventually come back to the issue of injecting spin-polarized charge carriers from GeMn into Si.

Part II

Optical spin physics in Si, Ge/Si, and GeMn/Si heterostructures

7

Introduction to optical spin injection and detection in Si-based devices

THE fundamental principle of conservation of angular momentum has rendered the method of optical orientation of charge carrier spins by the illumination with circularly polarized light and the subsequent optical investigation of the injected spin population a well-established approach to study various properties of the carrier spins in direct band gap III-V and II-VI material systems. A good introductory survey of the theoretical framework and different experimental schemes is given in a review article by Hermann *et al.*[135] or the book by Meier and Zakharchenya,[136] whereas recent achievements, also for heterostructures made of these materials, are summarized in its sequel by Dyakonov.[137]

Due to unique properties of Si, like the small spin-orbit coupling, the inversion symmetry of the crystal structure and the small nuclear decoherence field, spins in Si are actually far more promising candidates for the implementation of spintronic devices than spins in the III-V and II-VI material systems.[4,5] Despite this fact, the development of a theory for the optical injection and detection of an electronic spin polarization, which would be a key factor to study and understand spin properties in Si by optical means, has not been pursued for a long time, mainly because the unfavorable optical properties of Si made it seemingly unattractive also for optical orientation experiments. The optical investigation of spin physics, however, may form a competitive alternative to electrical experimental schemes. Aside from an earlier approach almost three decades ago,[138] only very recently theoretical work on optical injection and detection of spins in Si emerged,[139,140] owing to the growing interest to take advantage of the optical access. Correspondingly, also lacking this theoretical background, fundamental properties regarding optical spin physics in Si, like polarization-dependent radiative

transition probabilities, have not been experimentally studied in depth – a rather astonishing fact, when one recollects that the very pioneering experimental work of optical spin orientation and foundation to the established experimental schemes for the direct band gap materials was in fact realized for the Si material system already back in 1968 by Lampel.[141]

In **Chapter 8**, we first will shortly recall some general terms regarding optical spin orientation with focus on luminescence experiments, and then develop and discuss Si-specific aspects of spin orientation, which usually are not explicitly or not at all addressed in literature. Based on an existing work on group III-V semiconductors, we will adapt a theory for magnetic-field-induced luminescence polarization to Si by taking the recent findings of Li and Dery[139] for polarization-dependent radiative transitions in bulk Si into account.

In **Chapter 9**, we will compare the theoretical description to our experimental measurements of the field-induced circular polarization of photoluminescence in bulk Si and will be able to give for the first time a quantitative experimental estimate on the validity of Li and Dery's work.

The three-dimensional confinement of charge carriers in nanoscale Ge/Si heterostructures has been discussed during the last years in literature as a possible way to enhance the optical properties of group IV semiconductors.[142] In addition, localized charge carriers within such zero-dimensional, quantum dot structures would form a natural playground for the field of solid-state-based quantum computation, as the electron or hole spin may ultimately act as single, controllable and addressable quantum bit. Optical access to such spin quantum bits has been repeatedly demonstrated by various methods for the direct band gap material heterosystems throughout recent years.[143,144] Although the Ge/Si heterosystem is widely proposed for quantum computational applications due to the aforementioned superior spin properties compared to III-V heterosystems, research on optical access to spin properties of group-IV-based quantum dot structures, however, is still scarce.

In **Chapter 10**, we report first efforts for the resonant and quasi-resonant excitation of circularly polarized photoluminescence in ensembles of Ge quantum dots and discuss the observed peculiarities of the spin-dependent selection rules for the phononless radiative recombination in this system.

The great part of recent experimental work with regard to spin injection into group IV semiconductors focused on the electrical injection of electron spins into Si, which now unequivocally has been demonstrated by a number of research groups using different approaches. They share the concept of injecting spin-polarized electrons into the Si material by using ferromagnetic metals (FM) either as the base in the hot-electron transistor scheme[145–147] or as the injecting contact in the tunneling barrier scheme.[128,129,148–155] The detection of the injected spin polarization in these FM/Si structures is done electrically. Following the success of spin detection schemes in direct band gap materials systems,[156–160] some research groups concerned with the spin injection in FM/Si systems replaced the electrical detection method. Instead,

they established the circular polarization of electroluminescence generated by Si-based light-emitting diode structures, the so-called spin LEDs, as an empiric figure of merit to demonstrate spin injection.[130–134] Being a ferromagnetic semiconductor, GeMn is an alternative candidate as spin-aligning contact. The proof-of-principal demonstrations of FM/Si spin LEDs suggest that a GeMn/Si-based LED may conform an adequate system to investigate the spin-polarizing potentials of GeMn thin films.

In **Chapter 11** we realize a first GeMn/Si-based spin LED device. Preliminary results of electroluminescence experiments of this device, hinting at the successful injection of holes spins into Si, make further efforts in that direction attractive.

8

Theoretical background and Si-specific aspects

In this chapter, general terms important to understand optical spin orientation are outlined. This includes an introductory survey on the formalism known from direct band gap III-V material and additionally a more detailed discussion of aspects specific to Si. With this knowledge, we try to extend the theory on magnetic-field-induced luminescence polarization to Si.

8.1 Degree of electron spin polarization versus degree of luminescence polarization

Charge carriers sitting in the conduction or valence band of a semiconductor exhibit in thermodynamic equilibrium, i.e. in the absence of an external magnetic, applied electric, or irradiating electromagnetic field, no net spin moment. However, any of these perturbations of the equilibrium may give rise to a steady-state nonzero polarization of spins.

First we discuss the situation for electrons at the conduction band minimum because here the spin-orbit coupling – in Si especially because of the small atomic mass, in GaAs due to the *s*-like atomic wave function character of the conduction band – is usually small. The more complicated situation for the valence band is addressed later in Section 8.5.2.

For negligible spin-orbit coupling effects the wave function of a conduction band electron can be written as a Bloch function, i.e. the simple product of a periodic part only depending on the space coordinates and a Pauli spinor describing the spin state

of the electron. Hence, this wave function is an eigenfunction to the spin operator, expressing the fact that the spin quantum number $s = \frac{1}{2}$ of the electron remains a valid eigenvalue. This also allows to quantize the spin into spin-up, $\langle S_z \rangle = +\frac{1}{2}\hbar \equiv \uparrow$, and spin-down, $\langle S_z \rangle = -\frac{1}{2}\hbar \equiv \downarrow$, with respect to an arbitrary axis, meaning the parallel and antiparallel alignment of the spin along this axis, respectively. The projection of the spin quantum number s on this axis is thus either $s_z = \frac{1}{2}$ or $s_z = -\frac{1}{2}$. The quantization axis, for example, can be given by the direction of light propagation in the case where the electrons have been excited by an irradiating light beam or the luminescence of this system is studied, or by the direction of a magnetic field if the system is exposed to such. In either case, we choose this axis to lie along the **z**-direction throughout this thesis. The degree of electron spin polarization P_e will then be defined by

$$P_e = \frac{n_\uparrow - n_\downarrow}{n_\uparrow + n_\downarrow}, \tag{8.1}$$

where $n_\uparrow$ and $n_\downarrow$ denote the number of spin-up and spin-down electrons, respectively. It should be kept in mind that the sign and magnitude of P_e always only refer to the previously defined quantization axis.

For the case when $P_e \neq 0$, upon radiative recombination of the electrons their net angular momentum will be transfered to the luminescence light that propagates along this axis, as a consequence of the conservation of angular momentum.[①] A measurement of this angular momentum is the degree of circular polarization of luminescence P_l, defined by

$$P_l = \frac{I_{\sigma^+} - I_{\sigma^-}}{I_{\sigma^+} + I_{\sigma^-}} = \frac{\Delta I}{I_0}, \tag{8.2}$$

with I_{σ^+} and I_{σ^-} being the intensities of the σ^+- and σ^--polarized components of the luminescence, $\Delta I = I_{\sigma^+} - I_{\sigma^-}$, and $I_0 = I_{\sigma^+} + I_{\sigma^-}$. Here, $\sigma^\pm$ polarization denotes whether the photons carry an angular momentum or spin $S = \pm 1\hbar$ with respect to the given quantization axis. In Appendix B, a detailed explanation on how $\sigma^\pm$ photons are connected to left- and right-circularly polarized light can be found. In principal, by analyzing the luminescence in an experiment it is possible to learn about the spin polarization, if the relation of the two quantities P_e and P_l is known.

8.2 Selection rules of phonon-assisted optical transitions

In order to quantitatively connect the degree of spin polarization P_e with the degree of polarization of luminescence P_l, it is necessary to find the transition probabilities for dipole transitions between the initial conduction band states and the final valence

[①] This actually only holds if finite spin-orbit coupling of the final states is present, which indeed is the case in all realistic applications. Otherwise, the angular momentum is transfered to the final states, whereas the luminescence is not circularly polarized. See also Section 8.4.

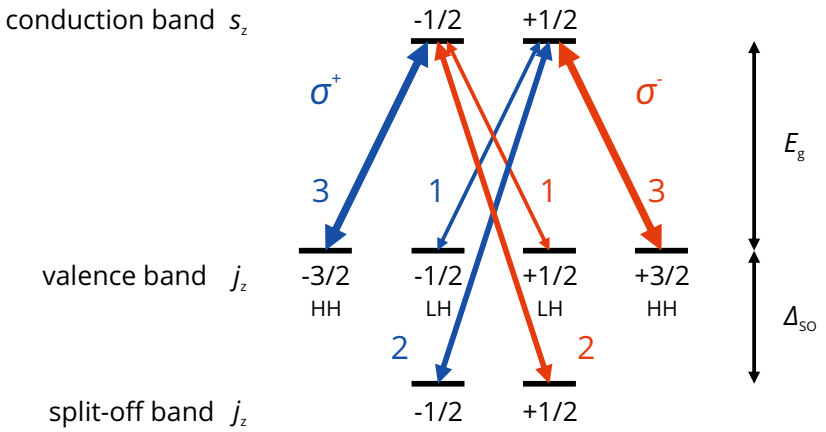

Figure 8.1 | Selection rules of allowed optical dipole transitions involving circularly polarized light for band edge transitions in III-V semiconductors of GaAs type. The numbers next to the arrows indicate the relative intensities of the transitions. The projected angular momentum quantum numbers s_z and j_z are given in the *electron picture*.

band states, which have to obey certain selection rules. It seems productive that we shortly recall these transition probabilities for direct gap semiconductors in order see the differences to Si. For semiconductors like GaAs or InAs, the direct band gap is not only a prerequisite for the efficient conversion of electron-hole pairs into light but furthermore allows a rather straightforward determination of these polarization-dependent transition probabilities by applying Fermi's Golden Rule, the fact that the conduction and valence band states basically behave like atomic levels with angular quantum numbers $s = \frac{1}{2}$ and $j = s + l = \frac{3}{2}$, respectively, and the symmetry properties of these states and the dipole momentum operator.[161]

Figure 8.1 depicts in a schematic the transition probabilities and corresponding photon polarizations for allowed optical dipole transitions between the two degenerate conduction band states and, on the one hand, the fourfold degenerate light-hole (LH) and heavy-hole (HH) valence band states and, on the other, the twofold degenerate split-off (SO) band states of bulk GaAs. A spin polarization of $P_e = 1$, i.e. 100% of the electrons exhibiting spin-up, for example, will lead to the generation of three times more σ^--polarized photons than σ^+-polarized ones if relaxation into the energetically lower lying SO band is neglected. Consequently, according to Eq. (8.2) P_l amounts to $(1-3)/(1+3) = -1/2$ or $-50\,\%$, the absolute value of which is the upper bound for the degree of polarization of luminescence in GaAs-type semiconductors. Thus, for the example of bulk GaAs, the simple relation

$$P_l = -\frac{P_e}{2} \tag{8.3}$$

is valid. A close look at the above equation reveals that, apart from a sign, the polariza-

tion of the luminescence is in fact nothing else than the average spin moment in units of $\hbar$ of an excited electron and thus equals the expectation value of the spin quantum number s_z:

$$P_l = -\langle s_z \rangle . \tag{8.4}$$

For Si the determination of the transition probabilities is not that simple. Si is an indirect band gap semiconductor, with a sixfold conduction band minimum at approximately $\mathbf{k}_0 = 0.85 \times \frac{2\pi}{a_{\mathrm{Si}}} \times \mathbf{e}_{\langle 100 \rangle}$, the so-called Δ-points. a_{Si} is the lattice constant of bulk Si and $\mathbf{e}_{\langle 100 \rangle}$ the unit vectors in the k-space along the $\langle 100 \rangle$ directions of the cubic crystal. The valence band states lie at the Brillouin zone center $\mathbf{k} = 0$, the Γ-point. Hence, to account for the rather large $\mathbf{k}$-momentum mismatch, optical transitions of excited electrons residing in the Δ-valleys into the final states of the valence band maximum have to be accompanied by the emission (or absorption) of a phonon carrying the appropriate $\mathbf{k}$-vector. Fermi's Golden Rule has now to be extended to a second-order perturbation.[162] The three-particle nature of this transition does not directly complicate the determination of the degree of luminescence polarization because phonons do not couple directly to the angular momentum. However, the evaluation of Fermi's Golden Rule based on symmetry arguments gets more complicated than for the direct band gap transitions, since the various phonon types with their different symmetries will couple the initial and final states depending on their symmetry and their spin state in a different manner. Furthermore, multiple pathways for excited electrons to reach the same final state are now possible via the two intermediate states in the valence band at $\mathbf{k}_0$ or the conduction band at $\mathbf{k} = 0$. As highlighted by Li and Dery, this leads to interference effects, meaning that transition amplitudes have to be explicitly summed up in the proper quantum mechanical manner to calculate the transition probabilities.[139] Li and Dery very recently determined the spin-dependent phonon-assisted optical transition probabilities in Si, with focus on the polarization of luminescence, on the basis of pure symmetry arguments, on the one hand, but additionally by applying numerical methods for the inclusion of realistic band structure calculations and phonon mode dispersions, on the other. It should be mentioned that a complimentary work with focus on the optical orientation by light irradiation by Cheng *et al.*[140] has succeeded Li and Dery's study shortly afterwards but will not be outlined in this thesis.

We briefly review some of the key results of Li and Dery, as we will need them later on. As an example, Fig. 8.2 depicts a schematic of the selection rules and transition probabilities in Si derived by symmetry arguments, similar to the one shown in Fig. 8.1 for GaAs. This schematic, however, shows only the possible transitions of spin-up electrons that originate from the four Δ-valleys with axis of revolution perpendicular to $\mathbf{z}$, denoted as x- and y-valleys, and that are accompanied by transverse phonons with wave vector $\mathbf{k}_0$. As indicated in the lower left panel of Fig. 8.2, for example, phonon modes with components that transform like xz give rise to three different relaxation paths, which emit σ^+-polarized light along the $\mathbf{z}$-direction. The relative transition amplitude of the pathway ending in the $+\frac{3}{2}$ HH state ($\Gamma^+_{8,"3/2"}$) is $\sqrt{3}/2$. The two paths

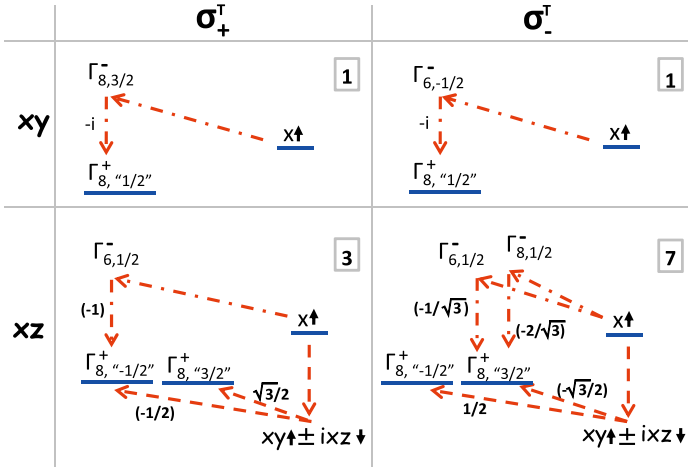

Figure 8.2 | Selection rules of allowed optical dipole transitions involving circularly polarized light for band edge transitions in Si. Only transitions of spin-up electrons originating from the *x*- or *y*-valleys and that are assisted by TA or TO phonons are shown. The left/right-side panels show transitions yielding σ^+- and σ^--polarized photons, respectively, whereas the top/bottom panels show transitions involving phonon modes with components that transform like *xy* and *xz*, respectively. The numbers next to the arrows indicate the relative amplitudes of the transitions. Numbers in brackets correspond to transitions with the same final state and have to be summed up to yield the total transition amplitude. The number in the upper right corner of each panel gives the total relative transition probability resulting from all transitions of the corresponding panel. From Ref. 139.

ending in the $+\frac{1}{2}$ LH state ($\Gamma^+_{8,\text{“}1/2\text{”}}$) have amplitudes of -1 and -1/2, respectively. The latter two transitions interfere constructively. Thus, the total transition probability of the decay channels depicted in this one panel amounts to $(-1-\frac{1}{2})^2+(\frac{\sqrt{3}}{2})^2=3$. Similarly, the other decay channels can be evaluated. Together with the transitions from the two Δ-valleys with axis of revolution parallel to the **z**-direction, the z-valleys (not shown), the polarization of the luminescence accompanied by transverse acoustic (TA) or transverse optical (TO) phonon emission due to an electron polarization of magnitude P_e, only relying on symmetry properties of the electron wave functions and phonon modes, are given by

$$P_{\text{l,TA}} = P_{\text{l,TO}} = -\frac{P_\text{e}}{5} = -\frac{2}{5}\langle s_\text{z}\rangle\,. \tag{8.5}$$

For the longitudinal optical (LO) and longitudinal acoustic (LA) phonon modes

$$P_{\text{l,LA}} = -P_{\text{l,LO}} = -\frac{P_\text{e}}{4} = -\frac{1}{2}\langle s_\text{z}\rangle \tag{8.6}$$

can be found in a similar manner. Interestingly, we see that, according to the work of Li and Dery, in contrast to GaAs not only luminescence with polarization of different magnitude but also of different sign is possible, depending on which phonon is involved in the transition.

The above given expressions were derived by Li and Dery under the approximation that the dipole matrix elements of transitions via the intermediates states at $\mathbf{k} = 0$ and $\mathbf{k}_0$ are exactly the same. The numerical evaluation of Fermi's Golden Rule revealed that this is justified, yet, not precisely accurate because the polarization ratios calculated by this approach slightly deviate from the above given.[139] Table 8.1 shows a complete survey of P_l for transitions between the band edge extrema of excited electrons with $P_\mathrm{e} = 1$, broken down by the individual valleys and phonon modes m = TO, LO, TA and also giving the relative luminescence intensity $I_{0,m}$ for each transition. Thus, Eq. (8.3) has to be generalized for Si as

$$P_{\mathrm{l},m} = \eta_m P_\mathrm{e} = 2\eta_m \langle s_\mathrm{z} \rangle . \tag{8.7}$$

The η_m denote the maximal attainable degrees of luminescence polarization, which are

$$\eta_\mathrm{TO} = -0.188, \tag{8.8}$$
$$\eta_\mathrm{TA} = -0.235, \text{ and} \tag{8.9}$$
$$\eta_\mathrm{LO} = 0.277. \tag{8.10}$$

η_LA is not given because the LA-phonon-assisted transition has negligible intensity. In particular, as one sees the polarization of the TA- and TO-assisted luminescence will not be exactly the same, in contrast to what is expected by symmetry arguments. The TO-related feature will exhibit a slightly smaller, whereas both the TO and LO phonon replica a larger polarization degree than predicted by the symmetry arguments.

The TO and LO phonon replica lie spectrally close together ($E_\mathrm{TO} = 57.8\,\mathrm{meV}$ and $E_\mathrm{LO} = 55.7\,\mathrm{meV}$)[163] and therefore usually cannot be resolved individually.[164,165] In an experiment, where typically the most intense TO feature is studied, the actual polarization will be considerably smaller than the maximum possible value indicated by Eq. (8.8) because the LO-phonon-associated transition will contribute with an opposite sign, albeit with smaller intensity. Furthermore, Li and Dery[139] have shown that especially large p-type doping leads to an additional reduction of the luminescence

Table 8.1 | Light intensities ($I_{0,m}$) and maximum degree of circular polarization (η_m) due to transitions of spin-up electrons ($P_\mathrm{e} = 1$). The light propagates along the **z**-direction. $I_{0,m}$ is normalized with respect to the intensity of the TO-assisted recombination from x- or y-valley electrons. The polarization factors γ_m, attributed to the recombination of $+\frac{3}{2}^\mathrm{hp}$ holes, are also given. See Section 8.5.2 for details on the calculation of the γ_m values. In parts adapted from Ref. 139.

Δ-valley	x, y			z			total		
phonon mode m	TO	LO	TA	TO	LO	TA	TO	LO	TA
$I_{0,m}$	1	0.115	0.086	1.41	0.23	0.092	6.82	0.92	0.53
η_m (%)	−32.3	5.3	−36	0.01	50.1	0.7	−18.8	27.7	−23.5
γ_m (%)	50.0	0	50.0	0	−75.0	0	29.3	−37.5	32.5

polarization. This stems form the increasing admixture of the SO band to the possible hole states involved in the radiative recombination. The polarization ratios taking both these effects into account can be found in Ref. 139.

So far, an independent experimental validation of the above reported selection rules and resulting polarization ratios of luminescence light in Si has not been given and will in part be the scope of Chapter 9.

8.3 Decay of optically oriented electron spins: Radiative lifetime versus spin lifetime

As stated above, in Si a phonon is always involved in the generation of electron-hole pairs by light to conserve **k**-momentum. This transition is a second order process and therefore less likely to occur than the direct *k*-space transitions of first order in direct band gap materials. As immediate consequence, the radiative lifetime τ_r of excited electrons is considerably larger in Si. Table 8.2 lists typical values for radiative lifetimes for intrinsic and doped Si for various temperatures. At room temperature the lifetime spans over several hours in intrinsic Si and drops to a few milliseconds in doped material. A decreasing temperature in general enhances the radiative recombination and thus leads to a decreasing radiative lifetime.

On the other hand, spin lifetimes[①] τ_s are usually much shorter than τ_r. Experimentally measured values of the electron spin lifetime τ_s are also given in Table 8.2. For intrinsic Si the spin lifetimes are always larger than for doped material because mainly momentum scattering by phonons and in smaller extent by impurities contributes to

Table 8.2 | Radiative (τ_r) and spin lifetimes (τ_s) for intrinsic and *n*-type Si for different temperatures.

	300 K			77 K			4.2 K		
	τ_s	τ_r	τ_r/τ_s	τ_s	τ_r	τ_r/τ_s	τ_s	τ_r	τ_r/τ_s
intrinsic Si	10 ns[a]	4.6 h[b]	1.7×10^{12}	1 µs[a]	16.3 min[c]	1×10^9	3 s[d]	1 ms[e]	3×10^{-4}
n-type Si	142 ps[f]	12 µs[g]	8.3×10^4	7.7 ns[h]	250 ns[g]	32	10 µs[i]	100 ns[i]	10

[a] From Cheng *et al.*[166]
[b] From Yu and Cardona.[162]
[c] Extrapolated from the 300 K value, using the temperature dependence of the radiative recombination coefficient *B* by Trupke *et al.*[167]
[d] Single-electron spin T_1 time for a temperature of 143 mK, from Simmons *et al.*[168]
[e] From Hammond and Silver.[165]
[f] From Dash *et al.*,[129] electron concentration $n = 1.8 \times 10^{19}\,\mathrm{cm}^{-3}$.
[g] Calculated from the radiative recombination coefficient *B*,[167] using the relation $\tau_r^{-1} = Bn$.
[h] From Sasaki *et al.*,[154] electron concentration $n = 5 \times 10^{19}\,\mathrm{cm}^{-3}$.
[i] From Jonker *et al.*,[130] electron concentration $n = 2 \times 10^{18}\,\mathrm{cm}^{-3}$.

① In the context of this thesis spin lifetimes are always associated with the T_1 spin relaxation time.

the Elliott-Yafet relaxation mechanism for spins.[4] As a universal trend, the spin lifetime will increase for decreasing temperatures because the phonon scattering processes freeze out.[166]

In an experiment where luminescence is the tool to determine the degree of spin polarization of injected electrons, only those carriers will contribute to the circular polarization of the luminescence which maintain their nonequilibrium spin orientation until they decay. The timescale τ_s should therefore not be much shorter than τ_r, in order to be able to detect the spin polarization. The relation of the initial spin polarization P_i, which is present directly after an optical pumping or electrical injection process, and the final spin polarization P_e at the time of the electron decay is given by Dyakonov and Perel[161] with[①]

$$P_e = P_i \frac{1}{1 + \frac{\tau_r}{\tau_s}}. \tag{8.11}$$

We combine this relation with with Eq. (8.7) to get the degree of circular polarization of luminescence in Si due to an injection processes as

$$P_{l,m} = \eta_m P_i \frac{1}{1 + \frac{\tau_r}{\tau_s}}. \tag{8.12}$$

It is evident that the luminescence due to the recombination of initially spin-polarized electrons will not be polarized for undoped Si at any temperature, because the radiative lifetimes and hereby the ratios $\frac{\tau_r}{\tau_s}$, as given in Table 8.2, are far too large. $P_{l,m}$ will drop to zero. Dopants will decrease both τ_s and τ_r. The reduction of the radiative lifetime τ_r by doping, however, will be more efficient than the decrease of the spin lifetime τ_s. From the values given in Table 8.2 we expect a reasonable trade-off between the two lifetimes of about $\frac{\tau_r}{\tau_s} = 10$ at cryogenic temperatures, which would yield a P_e roughly a factor of ten smaller than P_i. If P_i is not too small, this renders also a finite and measurable $P_{l,m}$ possible.

The initial spin polarization $P_{i,m}$ of the electrons after a photoexcitation process assisted by phonon mode m in principle depends in the same way on the selection rules for carrier recombination stated in Section 8.2, i.e.

$$P_{i,m} = \eta_m P_{inc}, \tag{8.13}$$

where P_{inc} denominates the degree of circular polarization of the incident light beam and usually equals ± 1. Thus, by taking the conversion efficiency of light polarization into electron spin polarization (Eq. (8.13)), the subsequent spin decay (Eq. (8.11)), and eventually the conversion of the spin polarization into luminescence polarization (Eq. (8.7)) into account, we obtain an expression for the degree of circular polarization

[①] Equation (8.11) strictly applies only for p-type material. For n-type material Eq. (8.11) has to be rewritten as $P_e = P_i \frac{1}{1+\frac{n}{G\tau_s}}$, where n is the electron concentration and G the photoexcitation or injection rate.[4] Nevertheless, the subsequent conclusions are also valid from a general point of view.

of luminescence

$$P_{\mathrm{l},m} = \eta_m^2 \frac{P_{\mathrm{inc}}}{1 + \frac{\tau_\mathrm{r}}{\tau_\mathrm{s}}}. \tag{8.14}$$

We can now give a figure of merit of the absolute value of degree of luminescence polarization that can be expected for an all-optical spin injection and detection experiment relying on luminescence, keeping in mind that $\frac{\tau_\mathrm{r}}{\tau_\mathrm{s}} = 10$ and restricting ourselves, for example, to TO-assisted processes:

$$P_{\mathrm{l,TO}} \approx 0.188^2 \cdot 0.1 \approx 0.0035 = 0.35\% \tag{8.15}$$

$P_{\mathrm{l,TO}}$ in this scenario is extremely small. This value should be regarded as an upper bound because $\frac{\tau_\mathrm{r}}{\tau_\mathrm{s}} = 10$ seems appropriate for doped Si, but the polarization factor $\eta_{\mathrm{TO}} = 0.188$ for intrinsic Si has been employed in Eq. (8.15), which in fact is smaller for doped Si. Furthermore, if we also consider competing LO-assisted excitation/recombination processes, which in particular will get important during the excitation because this is usually not phonon-selective, the opposing selection rules for LO-assisted transitions will then lead to an overall reduction of the initial spin polarization. Our considerations lead to the conclusion that it is quite challenging to detect a polarization of luminescence in an experiment where the nonzero spin polarization of electrons has been created optically because basically the squared polarization factor and the large ratio $\frac{\tau_\mathrm{r}}{\tau_\mathrm{s}}$ lead to an immense reduction of $P_{\mathrm{l},m}$ in bulk Si.

8.4 Small spin-orbit coupling in Si

Spin-orbit coupling is another factor with impact on the magnitude of the degree of spin polarization that can be achieved by optical pumping. From a fundamental point of view, as the electromagnetic field of light only affects the orbital motion of an electron by electromagnetic forces and cannot couple directly to the spin angular momentum of an electron, optical spin orientation by an exciting light beam is only possible because of finite spin-orbit interactions.[161] Hence, if the spin-orbit coupling strength becomes negligible with respect to the energy E_{exc} of the exciting light photons, electron spins cannot be oriented by them. A measurement of the spin-obit coupling strength is the energy separation Δ_{SO} of the SO valence band from the LH and HH band at the Brillouin zone center. For simplicity referring to the case of GaAs, we see the consequences of negligible spin-orbit coupling from the spin-dependent transition probabilities depicted in Fig. 8.1: If $E_{\mathrm{exc}} \gg E_\mathrm{g} + \Delta_{\mathrm{SO}}$, where E_g is the energy gap, i.e. if electrons are not only excited from the LH and HH bands but also from the SO band, the resulting initial degree of spin polarization of these excited electrons is zero, $P_\mathrm{i} = (3-1-2)/(3+1+2) = 0$.

For GaAs $\Delta_{\mathrm{SO}} = 340\,\mathrm{meV}$, whereas for Si $\Delta_{\mathrm{SO}} = 44\,\mathrm{meV}$ and is thus far smaller. Optical orientation of electrons in Si thus demands that the exciting laser beam in an experiment is closer to resonance with the fundamental band gap than in GaAs or Ge,

where $\Delta_{SO} = 290\,\mathrm{meV}$. Similarly, recombination processes involving final states in the SO band lead to a reduced luminescence polarization. As stated above, this becomes relevant in heavily p-type-doped Si, since the Fermi energy will get closer to the SO band. It should be noted that P_i does not drop abruptly to zero for $E_\mathrm{exc} \geq E_\mathrm{g} + \Delta_\mathrm{SO}$, but that its energy dependence varies as the joint density of states. Nevertheless, it is important to realize that the property of a weak spin-orbit coupling for Si is one of the main reasons, why the optical orientation of electron spins in Si is difficult.

8.5 Spin polarization in a magnetic field

8.5.1 Luminescence polarization due to oriented electrons

An alternative way to impose an imbalance in the occupation of spin-up and spin-down states on the electronic system is the application of an external magnetic field B. The field lifts the Kramer's degeneracy of the conduction band ground state with energy E_c and defines new ground states with energies $E_\downarrow$ and $E_\uparrow$ for the spin-down and spin-up states, respectively. These energies are shifted by the Zeeman energy $E_\mathrm{Z} = \pm\frac{g_\mathrm{e}\mu_\mathrm{B}B}{2}$ for negatively charged $s_\mathrm{z} = \pm\frac{1}{2}$ particles:

$$E_{\uparrow(\downarrow)} = E_\mathrm{c} + E_\mathrm{Z} = E_\mathrm{c} \pm \frac{g_\mathrm{e}\mu_\mathrm{B}B}{2}. \tag{8.16}$$

μ_B and g_e denote the Bohr magneton and electron g-factor, respectively. In thermodynamic equilibrium these new states are occupied according to the relevant electron distribution function, which for nondegenerate electron systems, as in intrinsic or p-type Si, can be approximated by the Boltzmann distribution at finite temperatures. Hence, the energetically lower lying spin-down states with spin alignment antiparallel to the magnetic field have a larger occupation number than the spin-up states, leading to a field-induced spin polarization.

Under weak-field conditions the polarization-dependent selection rules and transition probabilities for Si will not differ much from the values without field given in Section 8.2, so that in a first approximation it is justified to maintain Eq. (8.7). We then have to find an expression for the mean projection of the electron spin quantum number $\langle s_\mathrm{z}\rangle$ in a magnetic field, in order to give the luminescence polarization. In the scenario described above, $\langle s_\mathrm{z}\rangle$ is equal to that of a paramagnetic $j = \frac{1}{2}$ system of negatively charged particles obeying Boltzmann statistics. The field and temperature dependence of $\langle s_\mathrm{z}\rangle$ is thus given by the Brillouin function $B_j(-x)$, $x = \frac{jg_\mathrm{e}\mu_\mathrm{B}B}{k_\mathrm{B}T}$, the Boltzmann constant k_B, and the temperature T:

$$\begin{aligned}\langle s_\mathrm{z}\rangle = \frac{1}{2}B_{\frac{1}{2}}\left(-\frac{g_\mathrm{e}\mu_\mathrm{B}B}{2k_\mathrm{B}T}\right) &= -\frac{1}{2}\tanh\frac{g_\mathrm{e}\mu_\mathrm{B}B}{2k_\mathrm{B}T} \\ &\approx -\frac{1}{2}\frac{g_\mathrm{e}\mu_\mathrm{B}B}{2k_\mathrm{B}T},\end{aligned} \tag{8.17}$$

where we have made use of the weak-field condition and expanded the hyperbolic tangent in a first-order Taylor series. We can therefore rewrite Eq. (8.7) as[①]

$$\begin{aligned} P_{\mathrm{l},m} &= 2\eta_m \langle s_\mathrm{z} \rangle \\ &\approx -\eta_m \frac{g_\mathrm{e}\mu_\mathrm{B}B}{2k_\mathrm{B}T}. \end{aligned} \tag{8.18}$$

If the recombining electrons already come with a net spin moment along the field direction, the terms in Eq. (8.12) and Eq. (8.18) should be summed up to get the total degree of luminescence polarization

$$P_{\mathrm{l},m} = \eta_m \frac{P_\mathrm{i}}{1+\frac{\tau_\mathrm{r}}{\tau_\mathrm{s}}} - \eta_m \frac{g_\mathrm{e}\mu_\mathrm{B}B}{2k_\mathrm{B}T} \frac{1}{1+\frac{\tau_\mathrm{s}}{\tau_\mathrm{r}}}. \tag{8.19}$$

Following Ref. 170, we have introduced the factor $\frac{1}{1+\frac{\tau_\mathrm{s}}{\tau_\mathrm{r}}}$ in the second term of Eq. (8.19). We thus ensure that for slow spin relaxation the spin orientation of the injected electrons, i.e. the injected nonequilibrium spin polarization, determines the luminescence polarization, whereas for fast spin relaxation only the field-induced component matters, when the injected spins have assumed equilibrium conditions. As it becomes evident, by considering a field-induced spin polarization, a direct access to an experimental validation of η_m is now provided to us, despite a fast spin relaxation or even linearly polarized pump beam ($P_\mathrm{i} = 0$), under the premise of low temperatures or high magnetic fields. Then the Boltzmann factor $\frac{g_\mathrm{e}\mu_\mathrm{B}B}{k_\mathrm{B}T}$ gets large, meaning that $P_{\mathrm{l},m}$ can take larger values by a magnetic field than an initial electron spin polarization by optical pumping would allow. The field-induced polarization therefore opens the way to an easier experimental determination of η_m.

8.5.2 Luminescence polarization due to oriented holes

The role of holes in optical orientation experiments has not been addressed in the preceding. This is due to the fact that the valence band states consist of p-type wave functions and therefore experience considerable spin-orbit coupling effects. Although spin-orbit coupling in Si is comparably small, it will lead to reduced hole spin relaxation times. Unfortunately, reliable data on these relaxation times in bulk Si is not yet present. Nevertheless, as the effect of spin-orbit coupling on holes is more dramatic than on electrons, it can be inferred from Table 8.2 that the ratio of radiative lifetime to spin lifetime for the former is even more unfavorable than for the latter. Thus, optically oriented holes will quickly become unpolarized, explaining why their contribution to a circular polarization of luminescence can be neglected in this context.

[①] A descriptive derivation of Eq. (8.18) is made by taking Eq. (8.7), replacing P_e by Eq. (8.1) and, plugging in $n_{\uparrow(\downarrow)} = n_0 e^{-(E_\mathrm{Z}/k_\mathrm{B}T)}$, as the appropriate terms for the occupation numbers due to a Boltzmann distribution. Here, n_0 is the occupation number without magnetic field. Essentially the same result is also obtained in the work by Dyakonov and Perel, where explicitly the circular polarization in weak magnetic fields of direct band gap semiconductors is theoretically treated.[169]

However, for the reason of their short spin relaxation time, holes will get polarized by a magnetic field quickly after injection. These polarized holes can then also lead to a polarized luminescence when they recombine with electrons. We first want to introduce the situation in direct band gap semiconductors of GaAs type, studied in detail by Dyakonov and Perel,[169] as we later extend their findings to Si. Dyakonov and Perel demonstrated that, in linear approximation in the magnetic field, the origin of polarized luminescence can be regarded as the recombination of polarized electrons (holes) with unpolarized holes (electrons). According to them, both contributions behave additive in the resulting total polarization, i.e.

$$P_1 = \frac{\Delta I}{I_0} = \frac{\Delta I^{\mathrm{e}}}{I_0} + \frac{\Delta I^{\mathrm{h}}}{I_0} = P_1^{\mathrm{e}} + P_1^{\mathrm{h}}. \tag{8.20}$$

It should be mentioned that in the linear field approximation I_0, being the total intensity of the luminescence, equals the intensity without field[169] and in the case of Si is thus still given by the values in Table 8.1. $P_1^{\mathrm{e}} = \frac{\Delta I^{\mathrm{e}}}{I_0}$ denotes the electron contribution to the polarization and is the same as given in Eq. (8.4), which we have shown to be described by Eq. (8.17), in agreement with Dyakonov and Perel's result.[169] For the contribution of holes, they find with

$$P_1^{\mathrm{h}} = \frac{\Delta I^{\mathrm{h}}}{I_0} = \langle j_{\mathrm{z}} \rangle \tag{8.21}$$

an analogous expression as for electrons. Here, $\langle j_{\mathrm{z}} \rangle$ denotes the mean projection of the angular momentum quantum number of the holes in the HH and LH valence band states under the influence of a magnetic field. The mean angular momentum behaves like that of a paramagnetic $j = \frac{3}{2}$ system of negatively charged particles[①] and is thus again described for the nondegenerate case by a Brillouin function:

$$\langle j_{\mathrm{z}} \rangle = \frac{3}{2} B_{\frac{3}{2}} \left(-\frac{3 g_{\mathrm{h}} \mu B}{2 k_{\mathrm{B}} T} \right) \approx -\frac{5}{4} \frac{g_{\mathrm{h}} \mu_{\mathrm{B}} B}{k_{\mathrm{B}} T}. \tag{8.22}$$

In total the degree of circular polarization of luminescence in a weak magnetic field is

$$P_1 = -\langle s_{\mathrm{z}} \rangle + \langle j_{\mathrm{z}} \rangle . \tag{8.23}$$

At this point, we want to highlight an important fact, scarcely addressed in literature: In the case where the g-factor of the conduction and valence band and hereby the mean values $\langle s_{\mathrm{z}} \rangle$ and $\langle j_{\mathrm{z}} \rangle$ have the same sign, the luminescence polarization due to recombination of polarized holes has the opposite sign than that due to electrons. This

[①] The magnetic momentum of a real positively charged elementary particle, like a positron, points in the same direction as its angular momentum. Thus, for a positive field B and hereby positive magnetic momentum, j_{z} would also be positive. The magnetic momentum of a hole in a semiconductor, on the other hand, represents that of the remaining electrons of the valence band. Provided a positive valence band g-factor, the magnetic momentum of these negatively charged particles point opposite to j_{z}, i.e. $j_{\mathrm{z}} < 0$ for $B > 0$, which is the reason to treat holes as 'negatively' charged particles in this context.

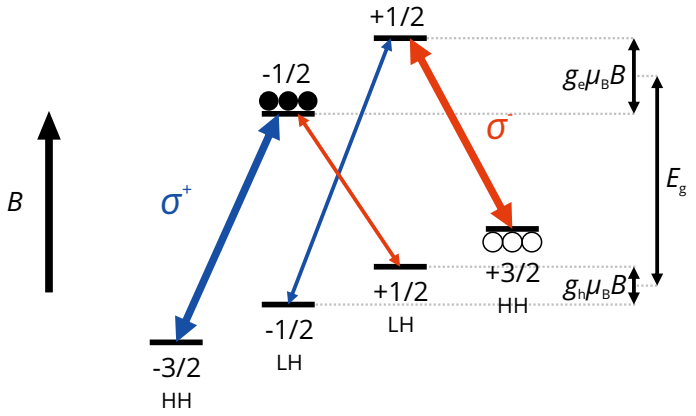

Figure 8.3 | Zeeman-split energy diagram of the conduction and valence band extrema in a magnetic field. A positive g-factor sign is assumed for both bands. Holes, indicated by empty spheres, predominately occupy the electronic $j_z = +3/2$ state and give σ^- light. Electrons, black spheres, mainly populate the energetically favorable $s_z = -1/2$ state and thus recombine with emission of a majority of σ^+-polarized photons. The quantum numbers are given in the *electron picture* for both bands.

is readily explained when we consider the energies of the band extrema in a level structure under the influence of a magnetic field, as shown in Fig. 8.3. Positive g-factors for the valence band and conduction band are assumed. Note, that this scheme does in fact not apply to GaAs where the electron and hole g-factor are negative.[171] Due to the Zeeman exchange interaction the energy bands with positive quantum numbers are shifted toward higher energies, those with negative quantum numbers shifted downward. In the conduction band, thermalized equilibrium electrons mainly sit in the spin-down states, leading to $\langle s_z \rangle < 0$. In the valence band, the states are filled from the bottom with electrons, so that mostly the $+\frac{3}{2}$ states will be left empty. In the *electron picture*, the lack of electrons with a positive quantum number in the valence band corresponds to a negative net moment of the remaining electrons in the valence band. This in turn can be attributed to the moment of the holes, i.e. in the *hole picture*, the occupied states are described with negative quantum numbers. Where it matters, we will introduce the superscript 'hp' to the quantum numbers given in the hole picture, e.g. $+\frac{3}{2}^{\mathrm{hp}}$. In either picture, $\langle j_z \rangle < 0$ holds for the valence band (see also Footnote ① on page 70). Now, the recombination of holes will basically yield σ^- light, the recombination of electrons predominantly σ^+ light, explaining the different signs in Eq. (8.23).

For Si the electron g-factor is positive and lies close to the value for the free electron $g_e = 2$.[172] The hole g-factor of free valence band holes amounts to $g_h = 0.56$[173] and is also positive.① As a general trend, although the selection rules of Si are different from

① The hole g-factor in Si is sometimes given a negative sign in literature,[174,175] using the relation $g_h = 2\kappa$, where κ is one of Luttinger's valence band parameters[176] and has shown to be negative.[173,177] However, this equation is not correct and arises from the imprecise interpretation of κ. Indeed, the design

those indicated in Fig. 8.3, we therefore expect that the above outlined, opposing contributions of polarized electrons and polarized holes to the luminescence polarization will occur for Si.

We now want to adapt Dyakonov and Perel's findings for direct band gap semiconductors, i.e. Eq. (8.20) or Eq. (8.23), to Si. As we have already previously shown, P_l^e is then given by Eq. (8.7). We also have to modify the expression for P_l^h for Si, accounting for the different, more restrictive selection rules in Si compared to GaAs, which will yield a smaller value of P_l^h. With an additional polarization factor γ_m, accounting for this effect and depending on the involved phonon mode m, the contribution of holes writes as

$$P_{l,m}^h = \frac{4}{3}\gamma_m \langle j_z \rangle . \tag{8.24}$$

We attribute γ_m to the maximum attainable difference of the intensities of σ^+- and σ^--polarized light, ΔI_m^h, relative to the total intensity, $I_{0,m}$, that can occur in the recombination of polarized holes. We thus have to consider the extremal case that the angular momentum of the holes is fully oriented in the $+\frac{3}{2}^{hp}$ state. This would be in close analogy to the meaning of η_m as the maximum possible polarization of the PL due to the recombination of polarized electrons that all exhibit $+\frac{1}{2}$ spin. When we deduce γ_m under this assumption from the transition probabilities of GaAs, we get $\gamma_m = \frac{3}{4}$. Thus, we have introduced the additional prefactor $\frac{4}{3}$ in Eq. (8.24), such that it drops back onto Eq. (8.21), which is the valid expression for GaAs. In this sense, the prefactor $\frac{4}{3}$ in Eq. (8.24) for the hole contribution to the luminescence polarization can be understood analogously to the prefactor of 2 for the electron contribution, see Eq. (8.7).

Li and Dery do not explicitly calculate the values of γ_m in their numerical approach to evaluate the spin-dependent transitions probabilities for Si. Hence, in finding these values, we restrict ourselves to derive them from the transition probabilities that Li and Dery established by strict symmetry arguments. Regarding the transverse phonon modes $m = \mathrm{TO}, \mathrm{TA}$, we thus have to refer to Fig. 8.2. As we see, the only transverse-phonon-assisted transition that starts in the $+\frac{3}{2}^{hp}$ state involves the xz components of the phonon mode. With two x- and two y-valleys, it has four possible final states. We obtain the intensity of σ^+-polarized light as $I_{\sigma^+,m}^{h,x} = I_{\sigma^+,m}^{h,y} = \frac{9}{16} I_{0,m}^{x,y}$ and of σ^--polarized light as $I_{\sigma^-,m}^{h,x} = I_{\sigma^-,m}^{h,y} = \frac{1}{16} I_{0,m}^{x,y}$ for each of these four transitions. $I_{0,m}^{x,y}$ denotes the total luminescence intensity due to all transitions depicted in Fig. 8.2 with final states in the x- and y-valleys, respectively. Transitions ending in one of the two z-valleys (not shown) do not originate from the $+\frac{3}{2}^{hp}$ state,[139] and are thus disregarded by us in the context of polarization. Nevertheless, these transition will contribute to the overall

of the Luttinger Hamiltonian of the valence band suggests that κ can be considered as the analogon to a conventional g-factor with the relation $|g_h| = 2|\kappa|$. But, to give the correct sign, one has to account for the fact that Luttinger's original Hamiltonian is not derived in the complete hole picture, i.e. sign inversion of the energy scale and of the angular momentum, but only under sign inversion of the former. Accounting for his convention, $g_h = -2\kappa$ is then the correct form and in fact yields a positive value for g_h.

luminescence with an intensity $I^z_{0,m}$. To give a more accurate value of γ_m, for $I^{x,y}_{0,m}$ and $I^z_{0,m}$ we stick to the numerically derived values of Li and Dery. They are listed in Table 8.2. We thus end up with

$$\begin{aligned}\gamma_{\mathrm{TO}} = \frac{\Delta I^{\mathrm{h},}_{\mathrm{TO}}}{I_{0,\mathrm{TO}}} = \frac{I^{\mathrm{h}}_{\sigma^+,\mathrm{TO}} - I^{\mathrm{h}}_{\sigma^-,\mathrm{TO}}}{I_{0,\mathrm{TO}}} &= \frac{2I^{\mathrm{h},x}_{\sigma^+,\mathrm{TO}} + 2I^{\mathrm{h},y}_{\sigma^+,\mathrm{TO}} - 2I^{\mathrm{h},x}_{\sigma^-,\mathrm{TO}} - 2I^{\mathrm{h},y}_{\sigma^-,\mathrm{TO}}}{4I^{x,y}_{0,\mathrm{TO}} + 2I^{z}_{0,\mathrm{TO}}} \\ &= \frac{4(\frac{9}{16} - \frac{1}{16})}{4 + 2 \cdot 1.41} \\ &= 0.293\end{aligned} \tag{8.25}$$

and likewise with

$$\gamma_{\mathrm{TA}} = \frac{4 \cdot 0.086(\frac{9}{16} - \frac{1}{16})}{4 \cdot 0.086 + 2 \cdot 0.092} = 0.325. \tag{8.26}$$

Similarly, after examining the transition probabilities of LO-assisted recombination processes (not shown),[139] we only have to consider the transitions ending in the two z-valleys. Here, we get $I^{\mathrm{h},z}_{\sigma^+,\mathrm{LO}} = 0$ and $I^{\mathrm{h},z}_{\sigma^-,\mathrm{LO}} = \frac{3}{4} I^z_{0,\mathrm{LO}}$, which yields

$$\gamma_{\mathrm{LO}} = \frac{2 \cdot 0.23(0 - \frac{3}{4})}{4 \cdot 0.115 + 2 \cdot 0.23} = -0.375. \tag{8.27}$$

Combining hole and electron contribution, we obtain as the most general expression for a magnetic-field-induced polarization of luminescence in Si

$$P_{\mathrm{l},m} = 2\eta_m \langle s_{\mathrm{z}} \rangle + \frac{4}{3}\gamma_m \langle j_{\mathrm{z}} \rangle . \tag{8.28}$$

For nondegenerate electron and hole systems, under consideration of Eqs. (8.17) and (8.22), this leads eventually to

$$P_{l,\mathrm{m}} = -\left(\frac{g_{\mathrm{e}}}{2}\eta_m + \frac{5g_{\mathrm{h}}}{3}\gamma_m \right) \frac{\mu_{\mathrm{B}} B}{k_{\mathrm{B}} T}. \tag{8.29}$$

Evidently, $P_{\mathrm{l},m}$ is a linear function of the effective magnetic field $\frac{\mu_{\mathrm{B}} B}{k_{\mathrm{B}} T}$ with a slope of

$$\phi_m = -\left(\frac{g_{\mathrm{e}}}{2}\eta_m + \frac{5g_{\mathrm{h}}}{3}\gamma_m \right). \tag{8.30}$$

As the information about the selections rules is contained in the slope ϕ_m, we get a direct access to them by measuring $P_{\mathrm{l},m}$ in Si as the function of an external magnetic field.

Equation (8.29) has to be modified for strongly n- or p-type-doped Si because either the electrons or holes get degenerate at sufficiently high doping levels, respectively. For such a system, the population of the degeneracy-lifted states with different quantum numbers is not approximated by the Boltzmann distribution anymore but given by the

Fermi-Dirac distribution. The corresponding expressions for the mean of the angular quantum numbers can be derived in the formalism of Pauli paramagnetism of free carriers in paraboliclike bands, which yields

$$\langle s_z \rangle = -\frac{3}{8}\frac{g_e \mu_B B}{E_F^e} \tag{8.31}$$

$$\langle j_z \rangle = -\frac{15}{8}\frac{g_h \mu_B B}{E_F^h}. \tag{8.32}$$

E_F^e and E_F^h are the Fermi energies of the degenerate electron and hole system, respectively. As we show in the following chapter, by using degenerate samples it is also possible to measure η_m and γ_m independently.

9 Field-induced spin polarization in bulk Si

As we showed in the preceding chapter, the application of an external magnetic field will lead to a spin polarization of excited carriers and therefore to a polarization of the recombination luminescence by itself. The measurement of such a field-induced degree of circular polarization of luminescence, according to Eq. (8.28), gives a direct experimental benchmark of the applicability of the selection rules for spin-dependent optical transitions in bulk Si, as they were derived by Li and Dery.[139]

Furthermore, for some experimental schemes the application of an external field is inevitable to demonstrate spin injection in Si. For the example of electrical spin injection, such an external field usually has to be applied if the ferromagnetic, spin-injecting contact does not exhibit a strong remanence magnetization or if its remanent magnetization points to a different direction than the spin quantization axis that is probed by the laboratory framework. In either case, due to the applied field, it is thus possible that the observed degree of luminescence polarization only partly stems from the recombination of the injected, spin-oriented carriers.

9.1 Experimental

In order to optically investigate the spin polarization of Si, photoluminescence (PL) experiments were employed. The experimental setup and measurement procedure are described in detail in Appendix A.4, and only a basic overview to PL measurements is given here. The PL was excited by a diode-pumped solid-state laser emitting at $\lambda_{\mathrm{exc}} = 532\,\mathrm{nm}$ with adjustable power P_{exc}, directed along the sample surface normal.

The polarization state of the incident laser light could be changed between linear polarization (LP), left-circular polarization (LCP), or right-circular polarization (RCP). The PL was collected in backscattering geometry and analyzed with respect to LCP or RCP. A 500 mm focal length spectrograph was used for the subsequent spectral dispersion of the luminescence, which then was detected by a liquid-nitrogen-cooled germanium photo-diode.

The samples were inserted into a magnet cryostat capable of magnetic fields from -7 T to 7 T and temperatures from 1.4 K to 300 K. All measurements were performed in Faraday geometry, i.e. the magnetic field axis was collinear to the light propagation axis. The absolute field direction was carefully determined, which allows to unambiguously attribute the LCP and RCP of the luminescence in the laboratory framework with σ^+ or σ^- polarization of the photons in the physical coordinate system, which is defined by the magnetic field direction (see also Appendix B).

Bulk Si samples with different impurity concentrations are the subject of this chapter. They were all cut from commercially available, single-crystalline, high-quality Si wafers. High-purity Si with impurity concentration below 3×10^{12} cm^{-3}, referred to as intrinsic Si (n-18), degenerately Sb-doped *n*-type Si (n-3), and degenerately B-doped *p*-type Si (p-2) are investigated. Details of these samples are given in Table 9.1. The sample surface normal is directed along the $\langle 001 \rangle$ crystal axis.

sample			impurity	
material	name	resistivity (Ω cm)	atom	concentration (cm^{-3})
intrinsic Si	n-18	$>1.5 \times 10^3$	P	$<3.0 \times 10^{12}$
n-type Si	n-3	$\approx 1.2 \times 10^{-2}$	Sb	$\approx 8.0 \times 10^{18}$
p-type Si	p-2	$\approx 0.5 \times 10^{-2}$	B	$\approx 2.3 \times 10^{19}$

Table 9.1 | Bulk Si samples used in field-dependent photoluminescence experiments.

9.2 Circular polarization of photoluminescence

Intrinsic *n*-type Si

Figure 9.1 contains a normalized PL spectrum as a function of photon energy of the intrinsic Si sample at a temperature of approximately 5 K in the absence of a magnetic field. One can distinguish three individual, well-resolved main luminescence peaks, each of which is accompanied by a broader side peak at the low-energy side. The energetic positions of the main peaks are 1134.8 meV, 1095.7 meV, and 1031.8 meV. They correspond in this order to single-phonon-assisted free-exciton transitions via emission of $\mathbf{k}_0$-TA and -TO phonons, and to a double-phonon-assisted transition via emission of a $\mathbf{k}_0$-TO phonon followed by an optical phonon transition at the Γ-point (TO + O$^\Gamma$).[178,179] From the relative intensities of the spectral features observable

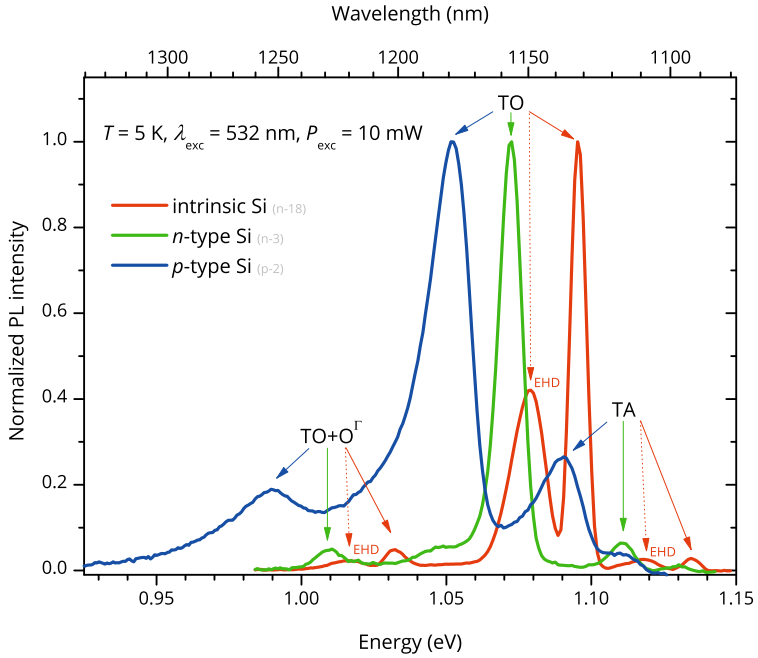

Figure 9.1 | PL spectra of bulk Si of different doping type.

in low-temperature PL spectra in Si, one might expect a fourth prominent peak at approximately 1136.6 meV and 0.15 times in intensity of the TO peak, attributed to the $\mathbf{k}_0$-LO-phonon-assisted transition.[163] This recombination process, however, is missing as an individual peak from the present measurement, which we relate to the fact that the spectral resolution of the setup is apparently not sufficient to resolve the small energetic difference of the TO and LO phonon replica.[164,165] Thus, the TO-denominated peak will contain also the LO-related components, yet in much weaker intensity.

The side peaks, each at approximately 17 meV below its main peak, stem from the recombination of electron-hole pairs that previously have condensed from the gaslike phase of free-excitons into a liquidlike phase of highly correlated charge carriers. The condensate is thus referred to as electron-hole liquid or electron-hole droplet (EHD).[180] The smaller energy of EHD recombination compared to the excitonic luminescence is caused by an effective band gap shrinkage due to strong interactions between the electrons and holes in this high-density droplet.[181]

In Fig. 9.2 two PL spectra of the intrinsic Si sample are shown, obtained under the same excitation conditions, but where the PL was analyzed with respect to its circular polarization. The exciting laser light was linearly polarized for this experiment, meaning that optical spin orientation is excluded. The intensities of the σ^+- and σ^--polarized PL obviously being same is thus expected. These measurements demonstrate that the experimental setup does not introduce any circular dichroism as a constant background to polarization-resolved measurements.

Figure 9.3 depicts the spectra of the σ^+- and σ^--polarized components of the PL of the intrinsic Si sample in the presence of an external magnetic field of $-7\,\mathrm{T}$. The TO-related free-exciton peak clearly shows a circular polarization, the intensity of

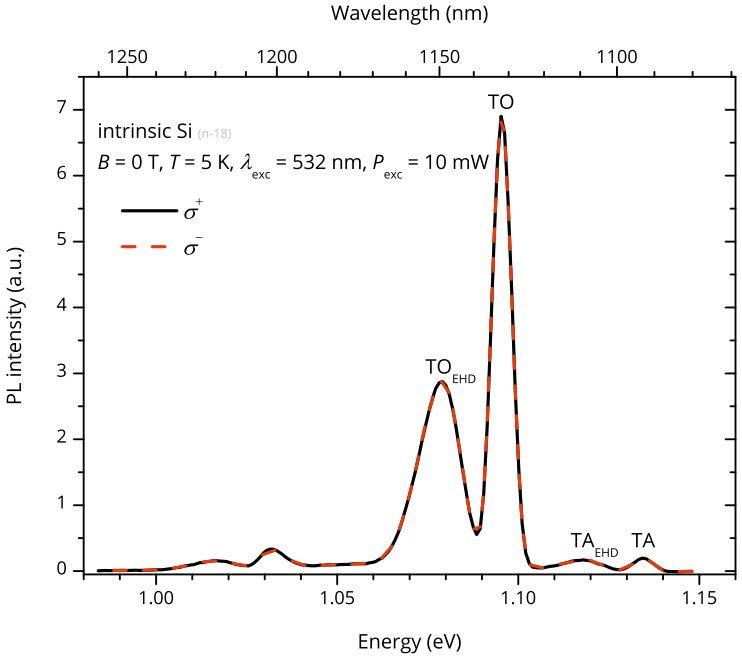

Figure 9.2 | σ^+- and σ^--polarized PL spectra of the intrinsic Si sample without magnetic field and with LP of the exciting laser beam. As expected, a circular polarization is absent.

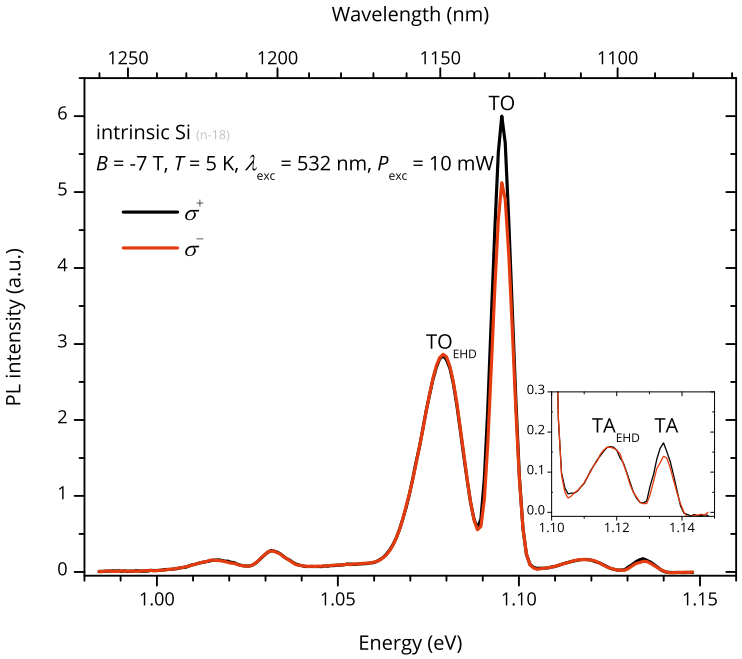

Figure 9.3 | σ^+- and σ^--polarized PL spectra of the intrinsic Si sample in a magnetic field of −7 T. The inset is a close up for the TA-related luminescence. Both the TO and TA free-exciton peaks exhibit a positive circular polarization.

σ^+ being larger than of σ^- light. The same qualitative observation holds for the TA phonon replica, as the close-up in the inset of Fig. 9.3 reveals.

For a quantitative investigation of the degree of polarization P_l of the PL, as defined by Eq. (8.2), and its field dependence, the TO replica will be studied in more detail in the following. The larger signal-to-noise ratio compared to the TA peak allows for a higher accuracy in determining $P_\mathrm{l,TO}$. In principle, $P_\mathrm{l,TO}$ can of course be directly extracted from the type of measurement depicted in Fig. 9.3, where a whole energy spectrum is recorded. However, this is not favorable because of the experimental reasons given in Appendix A.4.4. Instead, the circular polarization was measured multiple times only for the TO peak energy for different magnetic fields in the manner also outlined in Appendix A.4.4.

The resulting field dependence of $P_\mathrm{l,TO}$ is plotted in Fig. 9.4 for a temperature of 5 K. At -7 T, $P_\mathrm{l,TO}$ amounts to a value of approximately 7.9% and then decreases linearly with increasing field, giving a minimum value of -7.9% at the maximum available field of 7 T. Note that at zero-field the circular polarization indeed vanishes, just like depicted in Fig. 9.2. A linear fit to the experimental data yields a slope of $m_\mathrm{int,exp} = -1.14\,\%/\mathrm{T}$.

Degenerate *n*- and *p*-type Si

The PL spectra for heavily *n*- and *p*-type-doped silicon are shown in Fig. 9.1 and slightly differ from the intrinsic case. The three main peaks undergo a red-shift, which is the result of a band structure renormalization and reduction of the band gap due to the large doping concentrations.[182–184] This also leads to the broadening of the luminescence peaks and reflects the degenerate doping character of these sample.[185,186] At these large doping concentrations the recombination peaks are not of excitonic origin because of the strong screening of the attractive Coulomb potential between electrons and holes. Under the present measurement conditions, we attribute them to band-to-band transitions of free carriers, accompanied by TA, TO, and $\mathrm{TO} + \mathrm{O}^\Gamma$ phonon emission.[187] The luminescence peaks of the *p*-type Si sample being broader and more red-shifted than for the *n*-type sample is in line with the higher doping concentration of the former. We note that luminescence of phononless recombinations, the so-called no-phonon (NP) line, can be observed in the *n*-type sample as a separate peak around 1130 meV and in the *p*-type sample as a shoulder to the TA peak around 1111 meV. This is a consequence of the presence of a large number of dopants. The behavior of the circular polarization of the NP PL will be discussed later in Chapter 10 in the context with PL experiments on low-dimensional Ge nanostructures.

The circular polarization $P_\mathrm{l,TO}$ of the TO peak of the heavily doped Si samples as a function of the magnetic field is depicted in Fig. 9.4. $P_\mathrm{l,TO}$ of both samples exhibits a linear dependency on the magnetic field, as it does for intrinsic Si. In contrast to intrinsic Si, however, the gradient of $P_\mathrm{l,TO}$ is positive for the *p*-type Si sample, while it remains negative for the *n*-type sample. It amounts to $m_{p,\mathrm{exp}} = 2.81\,\%/\mathrm{T}$ and $m_{n,\mathrm{exp}} = -0.45\,\%/\mathrm{T}$ for the *p*-type and *n*-type case, respectively. The different signs

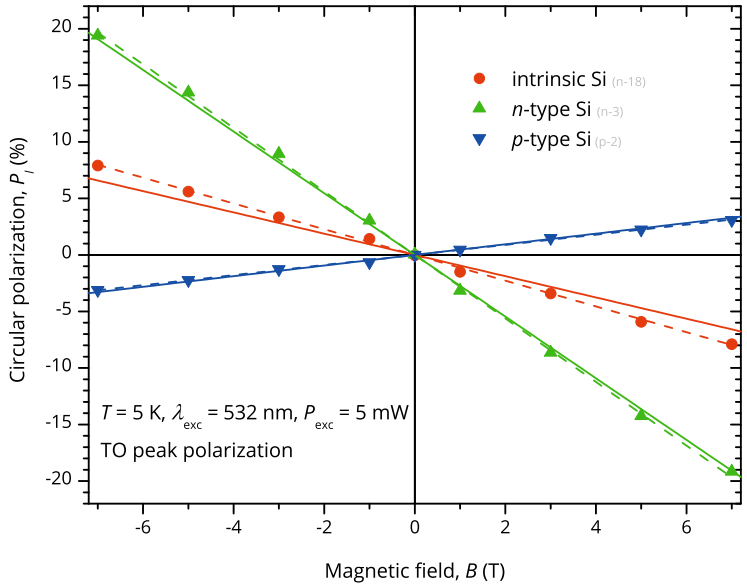

Figure 9.4 | Magnetic field dependence of the degree of circular polarization P_l of the TO-related PL peak of bulk Si of different doping type. The symbols give experimental values. The dashed lines are linear fits to the data, while the solid lines are theoretical calculations.

of the gradients of intrinsic and degenerate n-type Si in comparison to degenerate p-type Si indicate that the predominant polarization mechanism of the luminescence is qualitatively different in these two cases.

9.3 Comparison with theory and discussion

Intrinsic Si

The linear dependence of $P_{l,TO}$ on the magnetic field suggests that we can apply the formalism that we have outlined in Section 8.5 to the present case, i.e. that the weak-magnetic-field approximation for the description of the field-induced polarization is valid and that $P_{l,TO}$ can be decomposed into separate contributions of polarized electrons and holes. For intrinsic Si both contributions have to be considered because the electron as well as the hole system can be profoundly polarized. Hence, $P_{l,TO}$ is described by Eq. (8.29) and it is necessary to find the correct value of the slope $\phi_{TO} = -(\frac{g_e}{2}\eta_{TO} + \frac{5g_h}{3}\gamma_{TO})$ for the TO-related recombination process studied here, where η_{TO} and γ_{TO} represent the electron and hole contribution, respectively. As previously mentioned, the TO-related peak origins in some extent also from LO-phonon-assisted transitions. The PL of spin-polarized carriers that recombine via this relaxation path possesses different polarization factors η_{LO} and γ_{LO}. To account for the LO-induced contribution to $P_{l,TO}$, we determine ϕ_{TO} as an effective $\phi_{\text{“TO”}}$ with effective values $\eta_{\text{“TO”}}$ and $\gamma_{\text{“TO”}}$.

We calculate the effective polarization factor $\eta_{\text{“TO”}}$ by a weighted averaging over the individual polarization factors η_{TO} and η_{LO}. The relative intensities $I_{0,m}$ of the TO and LO peak are taken as weighting factors. For η_{TO}, η_{LO}, $I_{0,\text{TO}}$, and $I_{0,\text{LO}}$ we use the numerical values as given in the theory of Li and Dery,[139] which we have introduced in Section 8.2. These values are listed in Table 8.1. The weighting leads to

$$\eta_{\text{“TO”}} = \frac{\eta_{\text{TO}} I_{0,\text{TO}} + \eta_{\text{LO}} I_{0,\text{LO}}}{I_{0,\text{TO}} + I_{0,\text{LO}}} = \frac{-0.188 \cdot 6.82 + 0.277 \cdot 0.92}{6.82 + 0.92} = -0.133. \tag{9.1}$$

The effective polarization factor $\gamma_{\text{“TO”}}$, attributed to polarized holes, can be obtained by the same weighting procedure. We use the γ_{TO} and γ_{LO} values that we have calculated from the transition probabilities, which Li and Dery established from strict symmetry arguments. The γ_m values are also listed in Table 8.1. We get

$$\gamma_{\text{“TO”}} = \frac{\gamma_{\text{TO}} I_{0,\text{TO}} + \gamma_{\text{LO}} I_{0,\text{LO}}}{I_{0,\text{TO}} + I_{0,\text{LO}}} = 0.285. \tag{9.2}$$

Equations (9.1) and (9.2) can then be inserted in Eq. (8.30) which results in

$$\phi_{\text{“TO”}} = -0.067. \tag{9.3}$$

For intrinsic Si thus the general expression of the field dependence of the degree of circular polarization of PL is

$$P_{\text{l,“TO”}} = -0.067 \cdot \frac{\mu_{\text{B}} B}{k_{\text{B}} T}. \tag{9.4}$$

A straight red line according to this theoretical calculation for a temperature of $T = 5\,\text{K}$ is drawn in Fig. 9.4. The experimental data points lie close to the theoretical prediction, considering the fact that no fitting parameters were used to calculate the latter. The slope of the theoretical curve is $m_{\text{int,theo}} = -0.90\,\%/\text{T}$, which gives a deviation from the slope $m_{\text{int,exp}}$ of the best linear fit of the experimental data as $\frac{m_{\text{int,theo}}}{m_{\text{int,exp}}} = 0.79$. The finding of a negative sign of the slope of $P_{\text{l,“TO”}}$ hints toward the importance of the polarization of the hole angular momentum for intrinsic Si in a magnetic field, which dominates the PL polarization.

Although the polarization of the TA peak has not been studied in detail, the $-7\,\text{T}$ measurement depicted in the inset of Fig. 9.3 implies that it is slightly larger than the corresponding TO polarization. Such an observation is in line with the fact that the exact numerical evaluation of the transition probabilities yield a higher polarization ratio for the TA peak,[139] see Table 8.1.

Degenerate *n*-type Si

The heavy *n*-type doping of Si also leads to a negative, but steeper, slope of the field dependence of the circular polarization of PL compared to the intrinsic case.

This is explained by the degenerate character of the electron system, which now obeys the Fermi-Dirac statistics: Qualitatively, for a degenerate electron gas only the comparatively small fraction of electrons occupying the phase space of energies within $\mu_B B$ around the Fermi energy E_F^e becomes polarized by the external field. As outlined in Section 8.5 the mean spin of the electron system is then given by Eq. (8.31). On the other side, for the holes the Boltzmann statistics still applies, and the expression for their angular momentum does not differ from that of intrinsic Si. The PL polarization in a field writes now as

$$P_{l,\text{“TO”}} = -\frac{3}{4}\frac{g_e \mu_B B}{E_F^e}\eta_{\text{“TO”}} - \frac{5}{3}\frac{g_h \mu_B B}{k_B T}\gamma_{\text{“TO”}}. \tag{9.5}$$

At the present doping concentration of about $N_D = 8 \times 10^{18}\,\text{cm}^{-3}$ and the low measurement temperature, reasonable values for the electron Fermi energy lie around $E_F^e \approx 20\,\text{meV}$,[182] whereas the thermal energy $k_B T = 0.43\,\text{meV}$. Hence, the first term in the summation of Eq. (9.5) is about 50 times smaller than the second, and we can neglect it. For degenerate n-type Si the polarization of PL is therefore only a consequence of the polarization of the excited holes.

Under this premise and taking the same value for $\gamma_{\text{“TO”}}$ as for intrinsic Si, the field dependence of $P_{l,\text{“TO”}}$ is plotted in Fig. 9.4 as a green line with slope $m_{n,\text{theo}} = -2.68\,\%/\text{T}$. The theoretical curve describes the measured field dependence very well and differs from the best fit only as $\frac{m_{n,\text{theo}}}{m_{n,\text{exp}}} = 0.95$.

Degenerate p-type Si

For p-type Si the situation is reversed to the n-type case. Now the hole angular momentum has to be described in the degenerate picture, so that Eq. (8.32) applies and hence

$$P_{l,\text{“TO”}} = -\frac{1}{2}\frac{g_e \mu_B B}{k_B T}\eta_{\text{“TO”}} - \frac{15}{6}\frac{g_h \mu_B B}{E_F^h}\gamma_{\text{“TO”}}. \tag{9.6}$$

Here, the second term is by far smaller than the first, the Fermi energy of the hole gas being likewise in magnitude to that of the degenerate electron gas in the n-type doping case.[183] We can therefore neglect the hole contribution to the luminescence polarization. Additionally, we have to take into account that the polarization factor $\eta_{\text{“TO”}}$ now differs from that of intrinsic Si, because at heavy p-type doping the influence of the SO band increases, owing to its proximity to the Fermi energy. Given the doping concentration of about $N_A = 2.3 \times 10^{19}\,\text{cm}^{-3}$, Li and Dery's numerical treatment of polarized luminescence yields $\eta_{\text{“TO”}} = -0.035$.[139]

The blue straight line in Fig. 9.4 marks our calculation based on above considerations. In accordance with the experiment, the slope $m_{p,\text{theo}} = 0.47\,\%/\text{T}$ is now positive, revealing the dominant contribution of the spin-polarized electrons. Its deviation from the linear fit of the experimental data points is only as small as $\frac{m_{p,\text{theo}}}{m_{p,\text{exp}}} = 1.04$.

Discussion and Summary

Each sample being studied, intrinsic, degenerate *n*-type, and degenerate *p*-type Si, shows a very good quantitative agreement between the magnetic field dependence of the degree of circular polarization derived by experiment and that predicted by our respective calculation, particularly keeping in mind that no fitting parameters were used in the calculations. This evidences that the spin-dependent selection rules and resulting transition probabilities given by Li and Dery[139] are accurate. Our measurements can be considered as the first experimental verification of spin-dependent transition probabilities in Si. Although Li and Dery derived their theory in the absence of a magnetic field, our approach to use their results in our adaptation of a magnetic-field-dependent description of the circular polarization of luminescence seems justified. The consistency between experiment and theory in the presence of a weak external field thus suggests that merely the band population depending on the angular momentum is changed by the field, whereas the matrix elements of the dipole and the phonon-assisted transitions between the individual bands, which mainly rely only on the band symmetries, are not affected.

Doping plays a vital role for the magnitude of the field-induced polarization effect. The cases of strong *p*- and *n*-type degeneracy, studied here, should be considered as the extremal points. We could completely disregard either holes or electrons in the analysis of the data because of their relatively large Fermi energies. Moderate doping concentrations about the Mott transition, however, may lead to significant contributions of the corresponding carrier type to the field-induced circular polarization. Therefore we can imagine doping concentrations for which the electron and hole contribution to the polarization may cancel out. For a large doping range, well below the Mott transition, in which the carrier population is only governed by Boltzmann statistics, the results obtained for intrinsic Si can be considered as representative.

As we showed, the absolute value of the luminescence polarization, depending on the doping intensity, roughly varies as 0.5 %/T to 3 %/T near liquid He temperatures. Accordingly, considerable values of luminescence polarization are obtained in moderate fields. Equation (8.19) shows that this forms an additive contribution to the luminescence polarization due to the injection of spin-polarized electrons. Hence, in Si-based spin injection experiments that utilize luminescence as a quantitative verification of the degree of spin injection and that are performed in a similar temperature regime, one has to take care in the interpretation of the data, if a magnetic field is present.

In this context, we want to compare the results at hand with available data in literature, among them the spin LED experiment by Jonker *et al.*[130] being the most prominent. The electroluminescence that was studied in their paper stemmed from spin-polarized electrons that were recombining with holes in the heavily *p*-type-doped substrate with $N_A \gtrsim 1 \times 10^{19}\,\mathrm{cm}^{-3}$,[139] and had been injected from a ferromagnetic Fe contact. A magnetic field was applied to orient the Fe magnetization and hereby the electron spins in the proper direction. Thus, similar conditions were present as for the degenerate *p*-type sample investigated by us. Jonker *et al.*, however, quote a

value of only about 0.1 %/T for the field-induced circular polarization at a temperature of 5 K, which is more than a factor of four smaller than the value found in this thesis. In principle, since the field-induced polarization scales inversely with temperature, a profoundly increased, nonequilibrium carrier temperature might explain the reduced polarization in their experiment. The temperature needed for such a situation, as high as about 20 K, however, seems very unlikely. We cannot resolve this disagreement at this point. As Jonker *et al.* also performed their measurements for temperatures as high as 80 K, where the field-induced contribution is strongly suppressed, the general conclusions of their work and the possibility to efficiently inject electron spins into Si, should not be questioned.

It is interesting to note that the luminescence of the EHD that has formed in the intrinsic Si sample does not show any signs of a circular polarization up to the available fields of 7 T. This can be seen in Fig. 9.3. The EHD is a high-density condensate of correlated electrons and holes and thus obeys Fermi-Dirac statistics. The base width of the EHD peak is a good measure for the sum of the two quasi-Fermi levels of the electrons and holes. It can roughly be extracted from the spectra as ≈ 25 meV. The quasi-Fermi energy of the holes accounts for approximately two third of this value, due to their larger effective density of states mass.[188] That means both electrons and holes in the droplet experience comparable conditions to the degenerate *n*- and *p*-type samples, respectively. Hence, both species of the droplet do not exhibit a relevant angular momentum polarization in the magnetic field if spin relaxation is fast enough to establish equilibrium conditions, after electrons and holes have been captured in the droplet from the polarized excitons and before radiative decay occurs. This condition is likely fulfilled: The radiative decay time in the droplet will be of the same order as that in highly doped *n*-type Si, i.e. about 0.1 ms according to Table 8.2. The spin relaxation time of electrons in the droplet, however, can be expected to be even shorter than that of electrons in *n*-type-doped material and of the order of the hole spin relaxation time. This is due to the simultaneous presence of a large number of electrons and holes within the droplet, such that mutual spin-flips by the Bir-Aronov-Pikus mechanism[4,189] are very efficient in reducing the electron spin relaxation time.

10

Optical spin detection by Ge quantum dot ensembles

OPTICAL processes in bulk group IV semiconductors are inefficient in terms of the conversion of photons into electron-hole pairs and also of photon spins into angular momentum of the created carriers. As outlined in Chapter 8, the main cause for this inefficiency is the need of phonons that enable radiative transitions by conserving **k**-momentum. Consistent with Noether's theorem, the **k**-momentum conservation through phonons is, however, partly relaxed in structures with broken translational symmetry. In a semiconductor, symmetry breaking of the periodic lattice can occur due to impurities, compositional fluctuations in alloys, or heterostructure interfaces.

In this chapter we pursue the latter approach of a heterosystem to achieve phonon-less radiative recombinations in a Si-compatible material system. As we discuss later, such a system seems to be more feasible than bulk material for gaining an optical access to spin physics in group-IV-based devices. Ge islands of only a few nanometer in spatial extent that are embedded in a crystalline Si matrix are subject to this chapter.

10.1 Introduction to Ge quantum dots in Si

The Ge/Si samples that we used for our purposes had been previously fabricated at the WSI by solid-source MBE. The growth, morphology, composition, and electronic band structure of these specific samples are documented in detail in Ref. 190. For general properties on Ge islands the reader is also referred to the aforementioned work and the literature referenced therein. We give only a brief summary on the properties important to us.

Growth and morphology of Ge hut-clusters

The fabrication was realized by the deposition of nominally 8 monolayers of pure Ge on [001]-oriented Si substrates at a temperature of around 310 °C. During the pseudomorphic growth phase the mismatch of the lattice constants of the Ge and Si crystal causes compressive strain of the Ge layer. In order to reduce the strain energy of the pseudomorphic grown Ge material, the formation of well-defined, faceted pyramids with a rectangular base is favored after a thin wetting layer has established. This self-assembly process leads to a densely packed ensemble of pyramids, which are rather uniform in size and shape with typical base-edge lengths of about 15 nm to 20 nm and heights of about 2 nm. Owing to its shape, such a pyramid is commonly called *hut-cluster*. In the present sample, 80 Ge hut-cluster layers were fabricated, each overgrown by 25 nm-thick Si spacers. Only minor intermixing of Si and Ge within the Ge hut-clusters occurs, leaving a Ge hut-cluster core that consists of at least 80 % Ge.

Carrier confinement in Ge quantum dots

Ge has a smaller band gap as compared to Si. Heterostructures of these two materials therefore exhibit a band edge offset at the Ge/Si interface. The band edge alignment of the present Ge/Si heterostructure is of type-II, i.e. both the conduction and valence band edge offsets point in the same direction. Both have a positive sign, whereas the offset of the valence band edge is much larger than of the conduction band edge. Due to the arising potential well, holes are repelled by the surrounding Si matrix and confined to the Ge volume. The 3D confinement within that volume of very small spatial extent leads to a quantization of the hole energies. Therefore, we will denote a hut-cluster also as *quantum dot* (QD). In the context of this thesis, both nomenclatures are utilized interchangeably. Contrarily to holes, electrons are pushed off by and are not confined within the Ge QDs. Detailed calculations of the electronic band structure in consideration of the structural and compositional properties and thereby accompanying strain effects, however, showed that electrons can still be weakly confined within a triangular potential well formed in the Si matrix at the Ge hut-cluster apex. Such a calculation is depicted in Fig. 10.1. Tensile in-plane strain of the Si material at the hut-cluster apex lifts the sixfold degeneracy of the Δ conduction band minimum in Si within growth direction. The emerging $\Delta(2)$ band is shifted down in energy and forms the weakly confining potential well for electrons. The attractive character of this potential extents roughly 6 nm to 7 nm into the Si matrix.

Luminescence of Ge quantum dots

Figure 10.2 depicts a typical PL spectrum of the Ge hut-clusters for continuous wave illumination with the 514 nm line of an Ar-ion laser. At this excitation energy, which lies above the Si band gap, electron-hole pairs are most likely created in the Si spacer layers or in parts of the Si substrate due to their larger volume. In addition to the PL

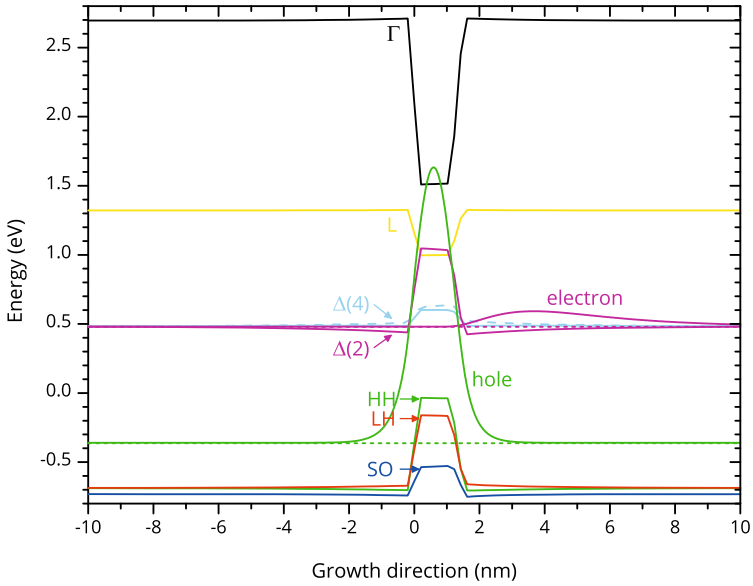

Figure 10.1 | next**nano**++ simulation of the band edge alignment of a 20 nm × 15 nm base diameter, {105}-faceted Ge hut-cluster with Ge content of 80 % embedded in a Si matrix, including a 3-monolayer-thick, 80 % Ge wetting layer beginning at 0 nm. Shown is the 1D energy diagram along the [001] growth direction through the center of the hut-cluster. The probability densities for the electron and hole ground state are also given.

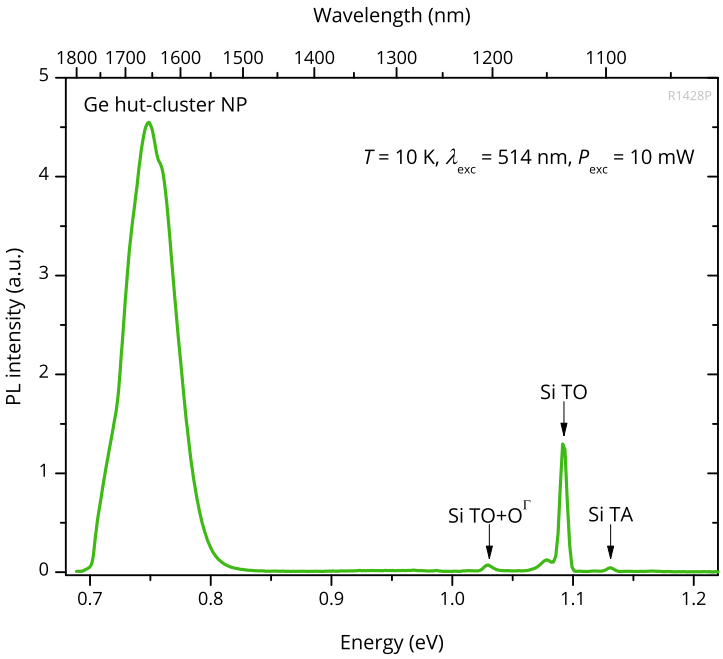

Figure 10.2 | PL spectrum of a sample containing 80 layers of Ge hut-clusters, each separated by 25 nm-thick Si spacers. The strong luminescence around 750 meV is due to the recombination of electron-hole pairs that are bound to the Ge QDs.

phonon replica peaks of Si around 1050 meV, we observe a clear PL signal centered around 750 meV. It stems from excitonic recombinations of electrons that are trapped within the shallow confining potentials of the Si spacer layers and holes that are trapped within the confining potentials of the hut-cluster cores. The inhomogeneous broadening of the excitonic recombination line is attributed to a multimodal size variation of the hut-clusters within the ensemble.

10.2 Radiative and spin lifetimes in Ge quantum dots

In the following we want to review and discuss the radiative and spin lifetimes associated with Ge QDs in more detail because these quantities are of particular interest in the context of optical spin orientation.

Radiative lifetimes

PL from low-dimensional Ge/Si heterostructures is argued to be predominately arising from NP recombinations of photoexcited electrons and holes.[191–195] The fundamental physical reason behind NP recombinations always lies in the breaking of translational symmetry. Several aspects of this symmetry breaking may be employed separately to explain the possibility of a phononless transition, yet, the picture drawn by Fukatsu *et al.*[192] is probably the most adequate for the present case of 3D confinement of carriers: The localization in real space is synonymous with the description of the carrier wave function as standing wave, which has to be built from multiple Fourier components of the k-space. This means that for the corresponding quantum-confined state the description by a single $\mathbf{k}$-vector cannot be valid, and thus $\mathbf{k}$-momentum is not a good quantum number. For this reason, in contrast to the bulk energy spectrum, the quantized energy levels in fact intrinsically lack any $\mathbf{k}$-momentum dispersion. This allows the seeming violation of $\mathbf{k}$-momentum conservation and hence NP recombinations. Radiative transitions between the initial and final states in Fukatsu *et al.*'s picture simply reduce from a second-order to a first-order process. The corresponding matrix element W of such a transition is simply of the form

$$W \propto \langle \psi_\mathrm{v} \, | \hat{\mathbf{p}} | \, \psi_\mathrm{c} \rangle \, . \tag{10.1}$$

Here, $\hat{\mathbf{p}}$ denotes the quantum mechanical dipole operator. ψ_c and ψ_v are the wave functions that form the confined states of the electron and hole, respectively. The hole state is built from the valence band wave functions belonging to the $\Gamma_8^+ \equiv \psi_\mathrm{v}$ representation (under negligence of contributions from SO valence band states) with p-symmetry, whereas the electron state is built from wave functions that are members of the $\Delta_1 \equiv \psi_\mathrm{c}$ representation with partial s-symmetry. It is worthwhile noting that in this description we expect the selection rules of spin-dependent radiative transitions for Ge QDs to tend toward those of GaAs-like semiconductors, because in GaAs radiative

transitions are similarly described by a first-order process between states with *s*- and *p*-like symmetry.

In the present case of type-II alignment of the band edge offsets for Ge QDs, the supposed enhancement of the radiative recombination rate due to the reduction of the recombination mechanism to a first-order process, however, comes at the price of spatial separation of the electron-hole pair comprising the recombining exciton. The spatial separation leads to a small overlap integral of the electron and hole wave functions, which can drastically impair the transition matrix element and cause prolonged radiative recombination times. The available studies on the PL decay dynamics in Ge/Si-based heterostructures containing 3D nanostructures do not allow to give definite conclusions on whether the radiative recombination times are enhanced or diminished compared to the values possible for bulk Si and Ge.[192,196–199] This ambiguity is caused by the fact that for low-dimensional structures of indirect band gap semiconductors, just as for the bulk material, the time dependence of transient PL data cannot be assigned to the radiative recombination due to the presence of competing decay mechanism like the Auger recombination[200] or the Shockley-Read-Hall recombination. The latter is of particular importance in Ge/Si heterostructures where a considerable amount of crystal defects was introduced during fabrication.[201,202] Based on the findings of Refs. 192, 197, and 199, we nevertheless want to give an order of magnitude for the excitonic radiative lifetimes in Ge QDs around liquid He temperatures with

$$\tau_\mathrm{r} \approx 10\,\mu\mathrm{s}. \tag{10.2}$$

It should be mentioned that the radiative lifetime may actually decrease for experimental conditions such as increased temperature or large excitation power, because a quasi-type-I spatially direct exciton recombination can then be induced.[203–205] This affects especially the high-energy tail of PL light, where it leads to $\tau_\mathrm{r} \approx 0.2 - 1\,\mu\mathrm{s}$.[197,199] In any case, the aforementioned values indicate a smaller radiative lifetime in Ge QDs compared to undoped bulk Si and Ge and match those of strongly doped material, as shown in Table 8.2.

Spin lifetimes

The growing interest within the past decade to exploit the spin degree of freedom of electrons or holes confined in self-assembled heterostructure QDs as spin quantum bits has brought about considerable progress in the determination of the spin dynamics of confined carriers. Theoretical and experimental work consistently showed that the 3D confinement leads to enhanced spin relaxation and spin coherence times compared to the bulk material.[143,144,206–209] However, this statement is actually restricted to be intensively proven only for the well-studied material class of group III-V QDs, which took most research efforts due to their natural suitability for optical experiments. We want to point out here that it cannot *a priori* be generalized to the group-IV-based Ge/Si QD systems, because the premises for a particular relaxation mechanism that was

being investigated and shown to be diminished by quantum confinement in a III-V system may be absent or less pronounced in the Ge/Si material system, as remarked by Khaetskii and Nazarov.[210] For example, an increase of the spin lifetime that relies on the reduction of the consequences of bulk-inversion-asymmetry-induced spin-orbit interactions of the Dresselhaus type does not apply to Si. On the other hand, spin relaxation related to the randomness of spin-orbit coupling of Bychkov-Rashba type in III-V heterostructures with structural inversion asymmetry may be equally or even more significant for group IV heterostructures.[211]

Studies explicitly focusing on the spin dynamics of electrons and holes confined at Ge QDs are only recently evolving. Electron spin resonance experiments for strain-confined electrons yield spin lifetimes at liquid He temperatures of about[212,213]

$$\tau_s^e \approx 10 - 20\,\mu s. \tag{10.3}$$

These spin lifetimes are much shorter than those observed for donor states[172] or for electrons in electrostatically defined single QDs,[168] and are of the order of spin lifetimes of doped bulk Si. This difference has been related to a weaker spatial confinement of the electrons to the self-assembled Ge QDs.[213] Specifically, it was proposed that the large density of dots may allow tunnel-hopping processes of the electrons to neighboring QDs. The asymmetric structure of the Ge QDs then causes the electrons to experience an effective, fluctuating Bychkov-Rashba field during a sequence of tunneling processes, which in turn leads to an increased spin-flipping rate.[214]

Concerning holes confined within Ge QDs, no experimental data on spin lifetimes is available yet. Some theoretical aspects determining the hole spin lifetime for III-V QD systems, however, have a general validity also for Ge QDs, irrespective of the precise spin relaxation mechanism. Most important among these is the fact that the relatively large out-of-plane quantum confinement due to the small QD size in growth direction lifts the degeneracy of the HH and LH band states very efficiently in Ge QDs. This lifting can further be promoted by strain. As a consequence, the spin-orbit-coupling-mediated mixing of HH and LH states is very weak,[215] leaving a ground state that is predominately built from the HH states, and excited states that have increasing admixtures from LH and SO states.[190] Spin-flip transitions between these states are now strongly suppressed because the spin-flipping mechanism has to obey energy conservation. Explicit theoretical investigations for Ge QDs show that the small admixture of LH states to the QD ground state is responsible for hole spin lifetimes of at least a few milliseconds if only single-phonon-mediated spin relaxation processes are considered.[216] However, this value should be regarded as an upper bound because in dense QD ensembles, similar to electrons, a tunnel-coupling-based spin relaxation is also applicable to the holes and limits the hole spin lifetime to comparable magnitudes of about[217]

$$\tau_s^h \approx 10\,\mu s. \tag{10.4}$$

This smaller value would still be a profound increase compared to the hole spin relaxation time in bulk Ge, which was recently found to be of the order of 100 ps.[218]

As we outlined, the hole and electron spin lifetimes in Ge QDs, see Eqs. (10.3) and (10.4), can be expected to be very similar to the excitonic radiative lifetimes, see Eq. (10.2). Thus, in optical spin injection and detection experiments with Ge QDs, contrary to bulk material, the hole spin may not be neglected for resonant excitation conditions, i.e. if the hole is created within the confining Ge QD potential. The hole spin may then still be preserved upon radiative recombination, which would promote a larger circular polarization of luminescence light.

To summarize, the favorable ratios of spin lifetimes of electrons and holes to the radiative lifetimes in Ge QD structures should *a priori* render the optical injection and subsequent detection of a spin population possible, at least from the viewpoint of spin decay. Furthermore, from the NP nature of the recombination of excited electron-hole pairs we can expect an enhancement of the conversion efficiency of the spin polarization into circular polarization of PL as compared to bulk material. The spin-dependent selection rules will presumably tend to be similar to those of a direct band gap III-V semiconductor material.

In this context, the quantization of hole energies in the Ge QDs becomes of particular interest. For bulk III-V material the opposite polarization of photons stemming from recombinations with the degenerate HHs and LHs limits the degree of PL polarization to 50 %, as has been derived in Eq. (8.3). As we mentioned before, the confinement effect in Ge QDs, however, leads to a hole ground state that is mostly built from the HH valence band states, whereas the next excited state with a considerable LH contribution of about 30 % lies already 60 meV higher in energy.[190] Accordingly, for excitonic recombination, which mainly takes places between the electron and hole ground states, the circular polarization can reach much higher values than 50 %.

10.3 Circular polarization of phononless radiative recombination

Before we turn to the actual optical orientation experiments for Ge QD ensembles, we first investigate the circular polarization of Ge QD PL caused by a magnetic-field-induced spin population. The analogous measurements of the circular polarization of bulk Si PL of TO-phonon-assisted transitions have been outlined in the preceding Chapter 9. From the direct comparison we can thus qualitatively discuss the consequences of the NP character of the Ge QD luminescence on the spin-dependent selection rules and test whether these rules indeed behave similar to those of direct band gap III-V semiconductor radiative transitions.

The experimental scheme was in principle similar to the one introduced in Chapter 9 and outlined in detail in Appendix A.4. The PL was excited with the 514 nm line of an Ar-ion laser. The incident laser beam had LP, and the circular polarization of the resulting PL with respect to the quantization axis defined by the positive magnetic field direction was analyzed. The measurements were carried out at a temperature of 10 K.

Figure 10.3a and 10.3b depict the polarization-resolved PL spectra of the Ge QD sample in a magnetic field of 7 T and -7 T, respectively. There is a clear difference of the intensities of the σ^+- and σ^--polarized components of the luminescence. We note that the sign of the slope of the polarization $P_l(B) = \frac{I_{\sigma^+} - I_{\sigma^-}}{I_{\sigma^+} + I_{\sigma^-}}$ of the PL is negative. Because of the small signal-to-noise ratio, we deduce the magnitude of the degree of circular polarization from the difference of the peak amplitude of two Gaussian curves that were fitted to the data sets of both polarizations. This yields a figure of merit of about $P_l(\pm 7\,\mathrm{T}) = \mp(10.2 \pm 1.1)\,\%$.

For an interpretation of the negative slope of $P_l(B)$ for the Ge QDs, we recall the formalism derived in Section 8.5 for field-induced luminescence polarization for bulk Si and specifically Eq. (8.28). Hence, we have to determine the signs of $\langle s_z \rangle$, $\langle j_z \rangle$, η_m, and γ_m.

It is reasonable to assume that the field-induced spin polarization of both electrons and holes contributes to the polarization of PL and neither of them can be neglected, because the present sample is nominally not doped. The electrons that are taking part in the recombination are localized in Si, and hence their g-factor and hereby field-induced spin polarization $\langle s_z \rangle$ are similar to those of bulk Si. For the holes, on the contrary, we must account for the fact that they are localized within the Ge hut-clusters, the cores of which are a $Si_{1-x}Ge_x$ alloy with $x = 0.8$.[190] The hole g-factor of bulk Ge was shown to have a negative sign,[177,219] and thus has the opposite sign to that of Si (see also Footnote ① on page 72).

Two effects, however, should be addressed to give an estimate on the sign of the hole g-factor in low-dimensional Ge structures. These are the alloying of Ge with Si and the quantum confinement of the holes. Studies show that both effects can in principle lead to an increase of the hole g-factor, which could result in a sign change from negative to positive.[220,221] Nevertheless, given the parameters of the present Ge QD structures, we believe that the increase is only of minor importance and thus the hole g-factor still remains a negative quantity. We note that no experimental verification on the hole ground state g-factor of Ge hut-clusters is at hand, but experiments on larger GeSi islands indeed suggest the negative g-factor.[222] Hence, while the electron spin orientation in a magnetic field of the Ge QDs behaves similar to that of pure bulk Si, the hole spin orientation is reversed in comparison to Si. In other words, for a positive field we maintain the negative sign for $\langle s_z \rangle$, whereas we get a positive for $\langle j_z \rangle$.

The magnitudes and signs of η_m and γ_m follow from the spin-dependent probabilities of NP transitions in Ge QDs. So far, calculations of these do not exist. As we highlighted in Section 10.2, the matrix element $\langle \Gamma_8^+ | \hat{\mathbf{p}} | \Delta_1 \rangle$ may be used as a starting point to qualitatively determine the selection rules for Ge QDs. The Γ_8^+ valence and Δ_1 conduction band states in the Ge/Si QD system share, at least partly, the same p- and s-symmetries as the valence and conduction band states in GaAs-like semiconductors. Hence, the selection rules for GaAs-like radiative recombinations might qualitatively apply to the Ge QDs. These are similar to those of Si TO recombinations in the sense that both predict that the photon spin predominantly points in the opposite direction as

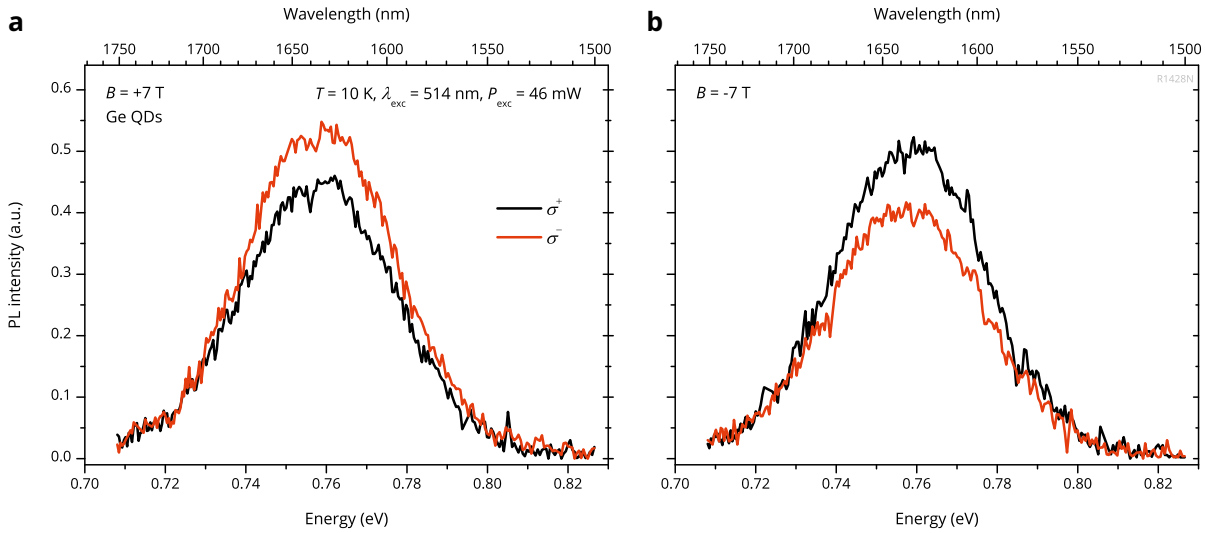

Figure 10.3 | a, Circular-polarization-resolved PL spectra of a sample containing 80 layers of Ge hut-clusters each separated by 25 nm Si. The spectra were acquired in a magnetic field of 7 T and at a temperature of about 10 K. **b**, Same as in **a** but in a field of −7 T. The quantization axis is defined by the positive magnetic field direction.

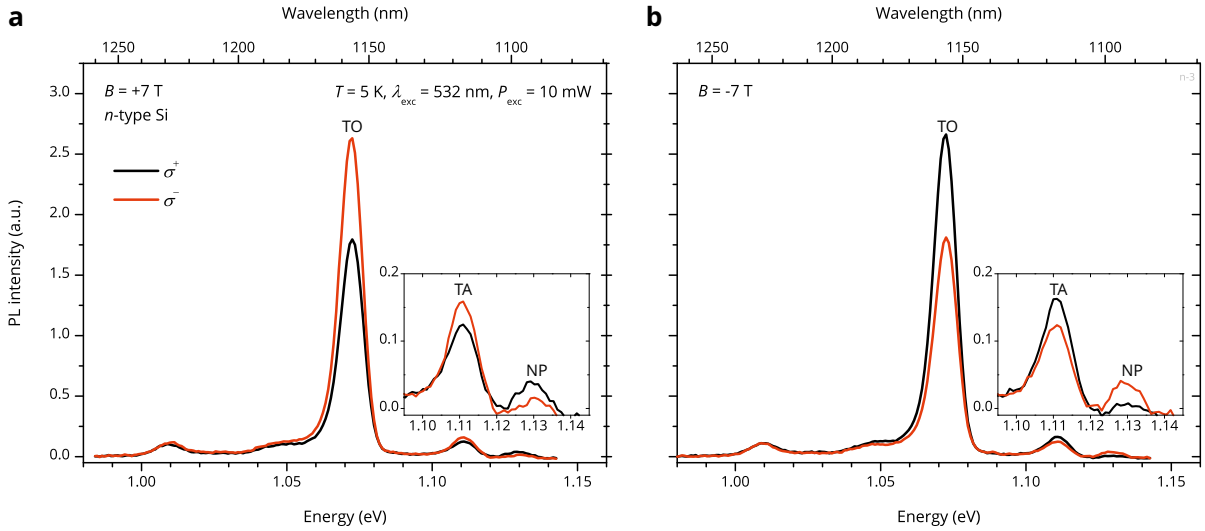

Figure 10.4 | a, Circular-polarization-resolved PL spectra of an *n*-type-doped Si sample. The spectra were acquired in a magnetic field of 7 T and at a temperature of about 5 K. **b**, Same as in **a** but in a field of −7 T. The quantization axis is defined by the positive magnetic field direction. The insets in **a**, **b** are close-ups of the high-energy regions of the spectra, containing the TA peak around 1110 meV and the NP peak at 1130 meV. The NP peak has an opposite polarization compared to the TA and TO peak.

the predominant electron spin orientation and in the same direction as the predominant hole spin orientation. That is, NP recombinations would correspond to a negative value for η_m and a positive for γ_m. Under this premise and also taking our considerations regarding the signs of $\langle s_z \rangle$ and $\langle j_z \rangle$ into account, we come to the conclusion that from Eq. (8.28) a positive slope of the degree of polarization of the Ge QD PL as a function of the external magnetic field is expected. The measurements shown in Fig. 10.3, however, contrarily yield a negative slope.

Further evidence for the unexpected behavior of NP luminescence in indirect band gap materials comes from PL measurements of doped bulk Si. Figure 10.4a and 10.4b depict the polarization-resolved PL spectra of heavily doped n-type Si in a magnetic field of 7 T and -7 T, respectively. The field dependence of the circular degree of polarization for the TO luminescence line was studied in detail in Chapter 9. In accordance with the transition probabilities for TO recombinations in bulk Si, we were able to quantitatively describe the magnitude and sign of the polarization of this recombination pathway. Here, we want to highlight the NP luminescence feature, which lies approximately at 1130 meV. Despite the bulk character of this Si sample, NP luminescence becomes possible due to the large number of impurities in the sample, which provides breaking of the translational symmetry on a local scale. Interestingly, the sign of the degree of polarization of the NP line is different from that of the transverse-phonon-related luminescence features, which can readily be seen for both magnetic field directions by a close-up of the NP luminescence region depicted in the insets of Fig. 10.4. This behavior is consistent with our finding of the inverted sign of the polarization of the NP luminescence of the Ge QDs.

In consequence, we infer from our experimental facts that the selection rules governing spin-dependent dipole transitions of NP recombinations have to be distinctively different from that of GaAs-like direct band gap recombinations. A possible explanation may lie in the quantum confinement of the electron wave function ψ_c within the Si material. Fukatsu *et al.*[192] suggested that for the electrons the short-range confining potential can in principle lead to an admixture of the Γ_6^- states of the Brillouin zone center to the Δ_1 states that form ψ_c. Γ_6^- states in Si, however, have a predominant p-symmetry, other than the corresponding states in GaAs of s-symmetry. Now, Nastos *et al.*[223] have recently highlighted in a theoretical work that for this reason the role of σ^- and σ^+ light for spin-dependent transitions of the form $\langle \Gamma_8^+ | \hat{\mathbf{p}} | \Gamma_6^- \rangle$ at the direct band gap is inverted in Si in comparison to the same transitions in GaAs.

Thus, if the admixture of the Γ_6^- states to ψ_c is large enough, it can lead to the counterintuitive sign of the polarization that we observe. A prerequisite for this scenario is that the coupling of the Γ_6^- and Δ_1 band is not impaired too much by the energy difference of both bands. Also, the dipole matrix element $\langle \Gamma_8^+ | \hat{\mathbf{p}} | \Gamma_6^- \rangle$ has to be sufficiently large. Whether or not an admixture of different bands to the electron wave function is really responsible for our peculiar observations for NP luminescence can thus only be answered by the precise modeling of the electron and hole wave functions in the presence of a confinement potential. The next**nano**++ tool is not suited for this task because its 8-band $\mathbf{k} \cdot \hat{\mathbf{p}}$ algorithm cannot couple the Δ_1 with the Γ_6^- band.

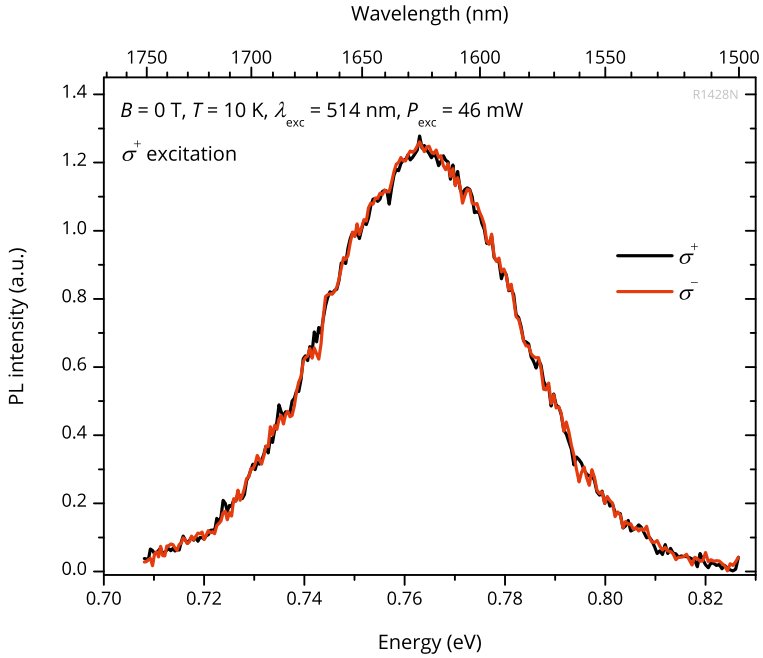

Figure 10.5 | Circular-polarization-resolved PL spectra of a sample containing 80 layers of Ge hut-clusters each separated by 25 nm Si at a temperature of about 10 K. The RCP of the exciting laser beam corresponds to σ^+-polarized photons. The hut-cluster PL does not exhibit a detectable circular polarization.

10.4 Optical orientation of spins in Ge quantum dots

In the following, we will discuss our efforts to impose an imbalance to the spin population of the electron and hole systems of Ge QD ensembles by optical orientation and to detect it by the circular polarization of the QD PL. For these all-optical spin orientation experiments, without applied magnetic field, the exciting laser beam always had RCP. The measurements were carried out at a temperature of 10 K.

10.4.1 Nonresonant excitation

In a first attempt, we used the 514 nm Ar-ion laser line to excite the PL. Figure 10.5 shows the circular-polarization-resolved NP PL spectra of the Ge QD sample. The propagation direction of the exciting light beam is now chosen to define the quantization axis, and with respect to this direction the RCP of the incident light corresponds to σ^+-polarized photons. The intensities of the σ^+- and σ^--polarized components of the PL are obviously similar within the signal-to-noise ratio.[①] We would have expected

[①] For accuracy we note that for the present experimental conditions, as depicted in Fig. A.4, the quantization axis, now given by the propagation direction of the incident laser light, lay antiparallel to the quantization axis of the field-dependent measurements presented before. Hence, the terms σ^+ and σ^- are reversed for the two opposite polarization directions probed by the fixed laboratory framework. See also Appendix B.

the σ^--polarized component to have a larger intensity than the σ^+ component because in principle the same selection rules as observed for the NP recombination in the field-dependent case should apply.

The absence of any circular polarization in the PL suggests that these selection rules and hereby spin-dependent phenomena cannot be probed by the employed excitation wavelength of 514 nm equivalent to a photon energy of about 2.41 eV. This excitation energy lies considerably above the indirect band gap of Si. Hence, spatially direct creation of electron-hole pairs within the Si spacer layers is likely to occur. As we pointed out in Section 8.4, the small spin-orbit coupling in Si then makes the optical injection of electron spins impossible. In fact, Cheng *et al.*[140] demonstrated very recently in a theoretical work that the degree of electron spin polarization is already negligible for excitation energies only as low as 300 meV above the indirect band gap. Due to the fundamental conservation of angular momentum, the spins of the incident circularly polarized photons then have to be transferred solely to angular momentum of the holes created in the Si spacer layers. The absence of any circular polarization of the QD luminescence indicates that the relaxation of the angular momentum of these holes in the Si layers takes place on a faster timescale than both the capture of the holes by the confining potential of Ge QDs and the subsequent radiative recombination. The initial spin information is thus lost and missing from the PL. The conclusion we can draw from our observations is that the optical injection of neither spin-polarized electrons nor holes into the Ge QDs is possible for the present nonresonant, high-energy excitation.

10.4.2 Quasi-resonant excitation

By *quasi-resonant* excitation we understand sufficiently small photon energies E_{exc} that do not allow excitation from the SO valence bands of Si. For cryogenic temperatures and transitions via the excitation of a TO phonon this corresponds to $E_{\mathrm{exc}} < E_{\mathrm{g}} + \Delta_{\mathrm{SO}} + E_{\mathrm{TO}} = (1170 + 44 + 58)\mathrm{meV} = 1272\,\mathrm{meV}$ or wavelengths $\lambda_{\mathrm{exc}} > 975\,\mathrm{nm}$. We chose an infra-red wavelength of $\lambda_{\mathrm{exc}} = 1464\,\mathrm{nm}$ or $E_{\mathrm{exc}} = 847\,\mathrm{meV}$ emitted from a single-mode fiber-coupled, diode-pumped solid state laser with a maximum output power of 150 mW. The laser photon energy is so small that excitations over the fundamental band gap of Si cannot occur. Hence, only electrons from the quantum-confined hole states of the Ge QDs, which lie within the fundamental Si band gap, can be excited into the conduction band states of Si. The relatively large spin-orbit coupling energy in Ge of about $\Delta_{\mathrm{SO}} = 290\,\mathrm{meV}$ now guarantees that states with a profound fraction from the SO valence band do not contribute to the excitation process. In fact, quantum calculations show that transitions from up to the seventh excited hole state are possible, for which the admixture of the SO band is only as low as 15 %.[190] Furthermore, all the contributing hole states are primarily built from HH valence band states. Thus, in the same way as the magnitude of the degree of polarization of luminescence profits from the quantum-confined nature of the hole states, as described at the end of Section 10.1, also the optical spin injection efficiency for quasi-resonant excitation may as well.

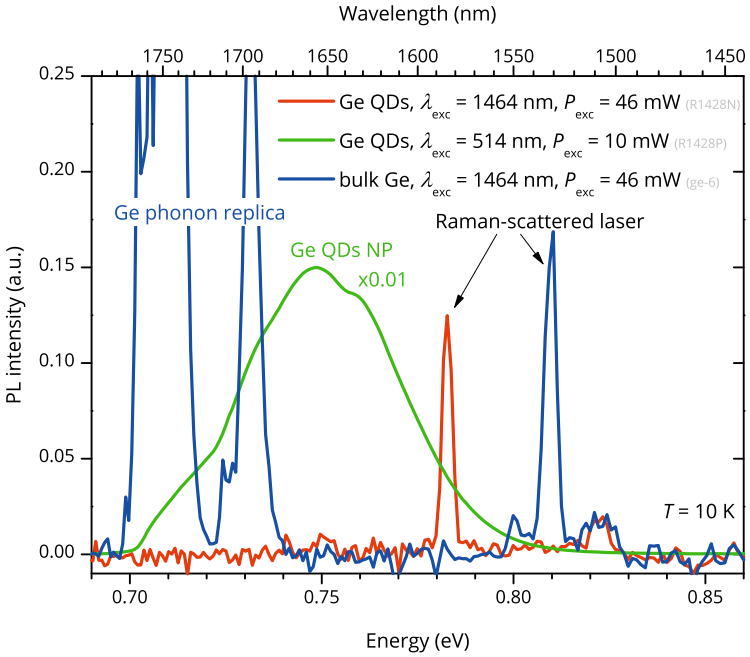

Figure 10.6 | PL spectra of the Ge QD sample for quasi-resonant (red) and nonresonant (green) excitation. For comparison a PL spectrum of an intrinsic bulk Ge sample (blue) is given for quasi-resonant excitation.

The PL spectrum of the Ge QD sample for quasi-resonant excitation is depicted in Fig. 10.6. For comparison a spectrum for an intrinsic bulk Ge sample is shown, obtained under the same illumination conditions. A PL spectrum of the Ge QDs obtained for Ar-ion laser excitation is included Fig. 10.6 to indicate the spectral range in which a PL signal can be expected. The bulk Ge sample clearly shows various phonon replica PL lines around 710 meV and 730 meV (the peak maxima lie out of the axis scale). The Ge QDs do not exhibit any PL signal in the expected spectral range above the noise level. The peak at 782 meV corresponds to laser light that has Raman-scattered at Si phonons of the Brillouin zone center and does not reflect any PL. This absence of a PL signal indicates that the integral absorption of the incident laser light power in the Ge QD sample is by far smaller than in the bulk Ge sample. From the near infra-red absorption edge around $E_{\mathrm{exc}} = 847$ meV we can estimate the penetration depth of the laser beam to be about $\alpha^{-1} = 400\,\mu$m in the Ge bulk sample.[224] Since the sample thickness d is of the same order of magnitude, practically the entire laser power that has not been reflected at the sample surface is absorbed within the volume of the bulk specimen and can thus excite the PL. If we take a value of 0.025 a.u. of the detector signal in Fig. 10.6 as a conveniently detectable lower limit, we can estimate from the peak height of the Ge phonon replica PL that we still could detect PL from up to 100 times thinner pieces of such a bulk Ge crystals. In other words, for materials with different absorption coefficients and thicknesses we should obey the relation $\alpha \cdot d \gtrsim 0.01$ as a lower-limit figure of merit in order to be able to detect a finite PL signal with our present setup. Approximating a single Ge QD layer as a slim, homogeneous 3D layer, all 80 layers of

Ge material forming QDs in the Ge QD sample roughly sum up to a total thickness of only $d = 100\,\mathrm{nm}$. Employing our figure of merit, the absorption coefficient of the Ge QD sample should therefore be around $\alpha = 10^3\,\mathrm{cm}^{-1}$. We should keep in mind, however, that this value is already a very optimistic approximation, given the fact that the optically active region in the Ge QD sample, due to the type-II band alignment and the resulting spatially indirect creation of electron-hole pairs, may actually be considerably less than 100 nm. If we assume a ten times smaller optically active length, we end up with $\alpha = 10^4\,\mathrm{cm}^{-1}$ as the minimum absorption coefficient needed. This is already in the order of magnitude of the absorption coefficient at the direct band gap of GaAs,[225] for example. It is doubtful that, although the radiative lifetime in the present Ge QD sample can be expected to be decreased in comparison with bulk Ge, such a high absorption coefficient is reached.

In order to be able to access PL with sufficient resolution to carry out polarization experiments, the setup has to be technically enhanced or light absorption/extraction in the Ge QD sample improved. Enhancements of the setup could be: Using a microscope objective as focusing lens to increase the power density of the incident laser beam and also the collection efficiency of the PL. This, however, requires major reconstructions of the used magnet cryostat itself; Laser sources with higher output powers than 150 mW could also be an option but are hardly commercially available for the necessary near infra-red wavelength region; Although we consider the Ge photo-diode detector to be quite sensitive, alternatively InGaAs photomultiplier tubes may be tried.

Improvements of the QD samples itself seem only hardly feasible. Structuring of waveguides or even photonic crystal cavities to the sample may enhance light absorption/extraction but will in the end have direct consequences on the polarization of the luminescence and do not help in understanding optical orientation in Ge QDs from a fundamental point of view. Growth of samples with a considerably increased number of Ge QD layers is not possible with our MBE machine.

A completely alternative approach to spin orientation experiments lies in methods like Faraday and Kerr rotation, which use the measurement of spin-dependent absorption. These type of measurements could get rid of the long timescale of radiative transitions that is an obstacle in PL experiments of group IV materials. In addition, Faraday and Kerr rotation are usually employed in such an experimental way that they deliver a direct differential measurement of the spin polarization and are thus inherently more sensitive. In the past, especially ultrafast Faraday spectroscopy has been an important tool to investigate spin properties of III-V and II-VI semiconductors and also to get direct access to their spin dynamics.[226] The Ge QD sample discussed in this chapter is currently studied by Faraday rotation in a collaboration with the group of M. Betz, Technische Universität Dortmund.

11

Spin injection from GeMn into Si – spin light-emitting diodes

In the preceding chapters of Part II of this thesis, we have concentrated on laying the foundation for the comprehension of the optical injection and detection of spin-polarized charge carriers in bulk Si and Ge/Si-based heterostructures. We have demonstrated the general potential to optically verify a spin-polarized carrier population with these group IV materials. In this chapter, we try to utilize the optical detection to examine the spin-polarizing potential of the semiconducting GeMn thin films, addressed in Part I of this thesis, with their promising magnetic properties. To this end, we study GeMn thin films acting as electrical contacts to inject possibly spin-polarized carriers into a SiGe quantum well (QW) embedded in a Si-based *pin* diode structure. By measuring the circular polarization of the resulting electroluminescence (EL) upon carrier recombination in the QW, a spin polarization of the injected carriers can be detected.

This so-called spin light-emitting diode (LED) is well established as a detection tool of spin-polarized electron currents injected from a ferromagnetic metal (FM) into optically active, direct band gap semiconductor materials[156–160] and has also recently been applied to verify spin injection from FMs into Si-based devices.[130–134] In general, however, it is not possible to directly inject a spin-polarized electrical current from a spin-polarized material of high conductivity, like a FM, into a material of small conductivity, like a semiconductor, over useful length scales. This fact, firstly highlighted by Schmidt *et al.*[227] and known in literature as the *conductivity mismatch problem*, is further promoted if the weakly conducting material exhibits long spin relaxation times or large spin scattering lengths, as it is the case for Si.[227] Hence, in spin LED studies it is common practice that the FM is not directly deposited onto the

semiconductor heterostructure. Instead, a nanometer-thin, highly insulating oxide layer is inserted between the interface of the FM contact and the semiconductor. The oxide layer acts as tunneling barrier and thus forms, by the nature of the quantum mechanical tunneling process, a spin-dependent, high in-series resistance for charge carriers crossing the junction. As proposed by Rashba,[228] this junction type meets the necessary properties to overcome the conductivity mismatch problem and allows the spin injection from a highly conducting into a poorly conducting material over length scales of more than a few nanometer.

In our case, the incorporation of an additional oxide layer will not be necessary because the GeMn thin films are not metallic. The conductivities of these, still semiconducting, layers can be tuned by conventional doping and will be matched to the conductivity of the Si structure, as will be outlined below. In fact, regarding spin injection, this is one of the key benefits of a ferromagnetic semiconductor over a FM contact. It should be mentioned that due to the *p*-type nature of the GeMn thin films, hole spin injection rather than the usual electron spin injection is investigated here.

11.1 Growth and characterization of GeMn/Si-based spin LED structures

11.1.1 Molecular beam epitaxy of spin LEDs

We utilized a MBE-grown $Si_{0.7}Ge_{0.3}$ QW embedded in the middle of the intrinsic region of a Si-based *pin* diode as the optically active region of the spin LED. A very similar structure was recently used to successfully detect spin injection from the remanent state of a ferromagnetic Co/Pt contact.[133] Despite the fact that epitaxy of high-grade SiGe QWs is very well documented in literature and has also a long history in the Abstreiter group at the WSI,[229–231] the fabrication of reliable, optically active samples took a lot of effort. The optimization process of growth parameters is in part comprised in Appendix C.1. Here, we present only the final sample structure. A highly Sb-doped, [001]-oriented Si wafer was used as the substrate. The substrate forms the *n*-region of the diode and acts at the same time as the back contact of the final device. 30 nm-thick undoped Si was grown as the first intrinsic spacer layer. Subsequently, nominally 40 monolayers of a $Si_{0.7}Ge_{0.3}$ alloy were deposited at a substrate temperature of about $T_S = 615\,^{\circ}C$, forming the fully strained, pseudomorphic, 5.6 nm-thick QW. This step was succeeded by the growth of again 30 nm intrinsic Si material as the second spacer layer, before 100 nm of B-doped, *p*-type Si with a B concentration of about $5 \times 10^{18}\,cm^{-3}$ were deposited. For the final GeMn contact layer, the growth was interrupted and the substrate temperature was reduced to $T_S = 60\,^{\circ}C$, in order to match the growth conditions of the thin films presented in Part I. At a total growth rate of $r_{Ge} = 0.25\,\text{Å}\,s^{-1}$, a $Ge_{0.88}Mn_{0.12}$ thin film of 80 nm thickness was grown by codeposition of Ge and Mn, which from hereon shall be denoted only as GeMn thin film for brevity. The GeMn thin film was simultaneously codoped with B at a concentration of $5 \times 10^{18}\,cm^{-3}$.

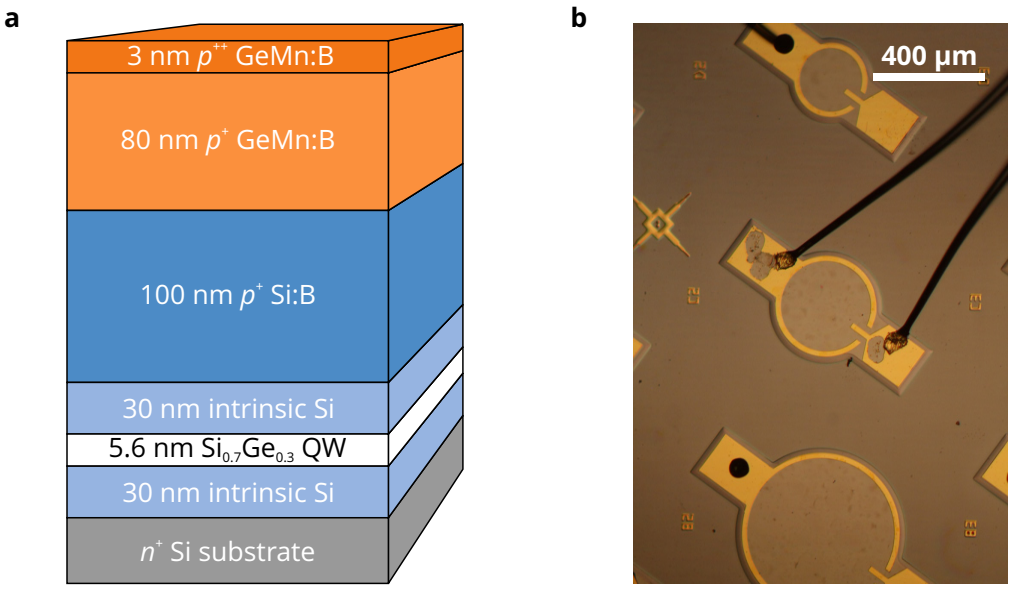

Figure 11.1 | a, Layer scheme for the GeMn contact spin LED. In a reference sample, the GeMn layers were replaced by corresponding *p*-type Ge:B layers. **b**, Microscope image of the actual device.

Eventually, in a 3 nm-thick capping layer the B concentration in the GeMn alloy was raised to 3×10^{19} cm^{-3} to allow for an easy electrical contacting. The sample design is schematically depicted in Fig. 11.1a. A reference sample, similar in the layout but with omission of Mn, was also fabricated.

11.1.2 Magnetism of spin LEDs

The pseudomorphic growth of high-content Ge layers on Si is only possible for a very limited thickness, due to the rapid accumulation of strain energy in thick Ge layers. The GeMn film thickness of 80 nm clearly exceeds the critical thickness for which plastic relaxation of the strained epilayer occurs. Hence, the morphology and structural quality of GeMn layers grown on top of a Si structure can be expected to be different from that of GeMn grown on Ge substrates. A recent study of heteroepitaxial growth of low-temperature GeMn on Si substrates has shown that despite a large number of point and line defects, which are introduced at the interface between the Si substrate and GeMn, and an overall increased surface roughness, the growth of GeMn clusters embedded in a crystalline Ge matrix that is known from the homoepitaxial growth is not affected.[59,60]

In order to verify that the structural properties of the GeMn thin film have not changed in such an extent that the ferromagnetic properties of the GeMn clusters in the contact layer are absent, we conducted magnetization measurements in the out-of-plane sample geometry. The magnetization versus external applied field for different measurement temperatures is plotted in Fig. 11.2. We find a weakly remanent magnetization for temperatures below approximately 15 K and an unblocked super-

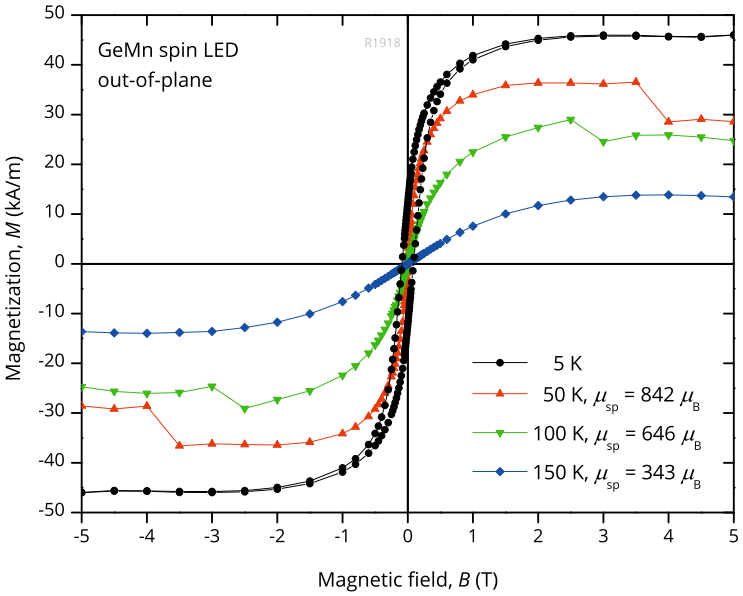

Figure 11.2 | Measurement of the sample magnetization versus external magnetic field. The magnetic field was applied along the out-of-plane direction. The supermoments μ_{sp} obtained from fits of simple Langevin curves to the data for 50 K, 100 K, and 150 K are given in the legend. The full measurement loop for 5 K clearly exhibits a hysteresis. Note that the offsets in the curves for 50 K and 100 K around 4 T and 3 T, respectively, are measurement artifacts.

paramagnetism for higher temperatures, in accordance with our prior findings for GeMn films grown on Ge substrates and both representative for the presence of the ferromagnetic clusters.[15,23] The supermoments μ_{sp} we obtained from simple Langevin fits to the measurement curves (see the legend of Fig. 11.2), are roughly by a factor of two larger than those of thin films grown on Ge substrates. Also in agreement with the prior findings for the chosen growth conditions of the GeMn contact layer is the absence of any signature of the ferromagnetic Mn_5Ge_3 secondary phase in field-cooled magnetization measurement versus temperature (not shown). Hence, we conclude from the magnetization measurements that GeMn growth on Si substrates delivers the expected magnetic features.

11.2 Device fabrication and electroluminescence experiments

The LED devices for EL measurements were obtained in a first step by photolithographic definition of roundly shaped mesas and subsequent wet chemical etching of the sample. In a second lithography step, areas for the top contacts were defined to parts of the mesas, leaving circular windows in the mesa centers for the extraction of the luminescence. The top contacts were fabricated by deposition of 5 nm Ti succeeded by 100 nm Au. The specimen was mounted with conductive silver paint to a chip

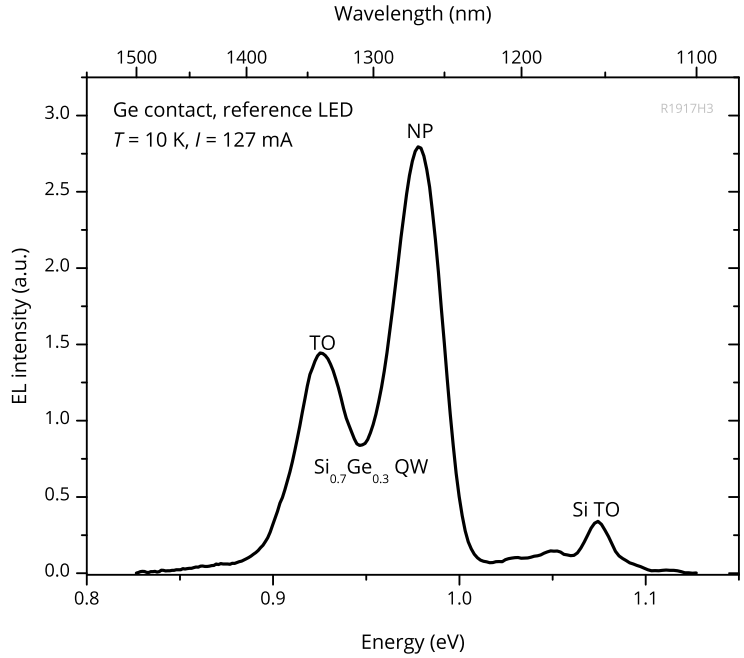

Figure 11.3 | EL spectrum of the Ge contact reference LED showing distinct NP and TO luminescence features of the QW.

carrier, such that the degenerate *n*-type backside of the substrate could act as a global back contact of the device. Individual, ultrasonic ball-bonding of the top contacts made the selection of different mesas as active light emitters possible. The experiments presented in the following were conducted for the mesa with a base diameter of 400 µm and a window diameter of 360 µm. Details of the fabrication process are given in Appendix C.2. A picture of the final device is shown in Fig. 11.1b.

The EL was excited by applying a 50/50 duty cycle, square-waveform, ac voltage to the spin LED sample, alternating between 0 V and a peak voltage in forward direction of about 4.3 V. The corresponding peak current density was approximately 62 A cm^{-2}. The same magnet cryostat setup as used for the PL measurements shown in the previous chapters was employed for the EL measurements. Magnetic-field-dependent measurements were carried out in Faraday geometry with the sample surface normal being parallel to the field axis. Details of the setup are described in Appendix A.4.

Figure 11.3 depicts an EL spectrum of the reference LED sample at a temperature of 10 K. In addition to the small EL peak at 1075 meV, which is a signal arising from electron-hole recombinations in bulk Si, we can distinguish two separate peaks at the low-energy side of the Si luminescence. These belong to recombination processes attributed to the $Si_{0.7}Ge_{0.3}$ QW. The peak around 977 meV corresponds to NP recombinations, while the red-shifted peak at 925 meV stems from TO-phonon-assisted recombinations. In the following we concentrate on the study of the spectral region of the QW luminescence.

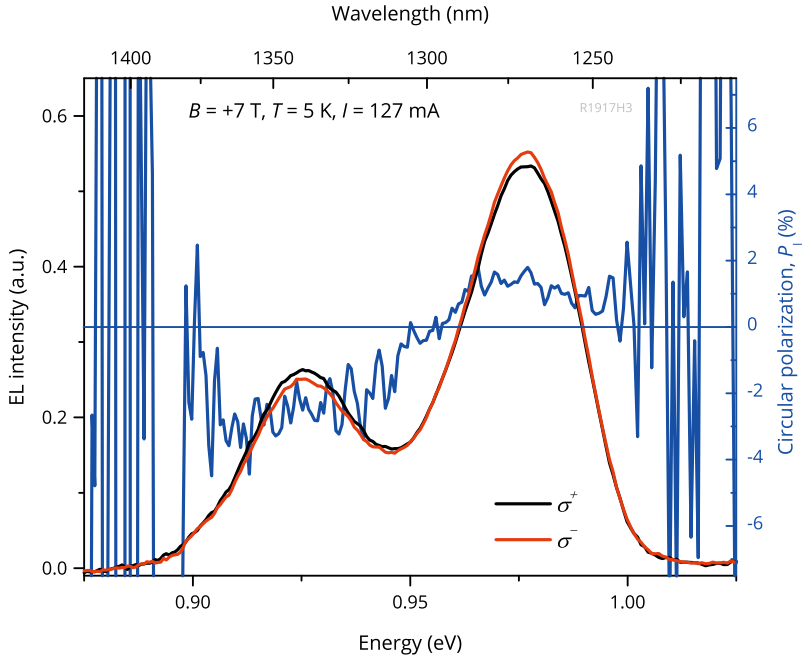

Figure 11.4 | (left axis) EL spectra of the Ge contact reference LED in a magnetic field of 7 T for the σ^+- and σ^--polarized component. (right axis) Spectrally resolved degree of circular polarization P_l. A change of sign of P_l occurs for the NP and TO recombination line. The large-amplitude polarizations at the peak tails are artifacts due to the small signal-to-noise ratio.

11.3 Circularly polarized electroluminescence – an outlook to spin injection

As can be seen from Fig. 11.2, the remanent magnetization of the GeMn thin film does not exceed the order of 20 % of the saturation magnetization. Thus, in order to maximize the circular polarization of the luminescence stemming from the possibly spin-polarized injected holes, we measure the EL in an external field to fully orient the magnetization of the GeMn thin film. As we learned in the preceding chapters the applied field, however, inevitably leads to a circular polarization of luminescence of bulk Si and Ge QDs by itself. We can see in Fig. 11.4, where the polarization-resolved EL of the reference sample in a field of 7 T and at temperature of 5 K is depicted, that this also holds for the luminescence of the $Si_{0.7}Ge_{0.3}$ QW.

At this stage, we briefly remark that the sign of the degree of polarization of the NP luminescence of the QW is not the same as of the TO luminescence. We easily see this in Fig. 11.4 from the spectrally resolved degree of circular polarization (blue curve, right axis), which crosses the zero-line for an energy in between the TO and NP part of the EL spectra. This fact is in line with the observations for bulk Si NP and Ge QD NP luminescence and supports the implication of qualitatively different selection rules for NP and TO transitions as discussed at the end of Chapter 10.

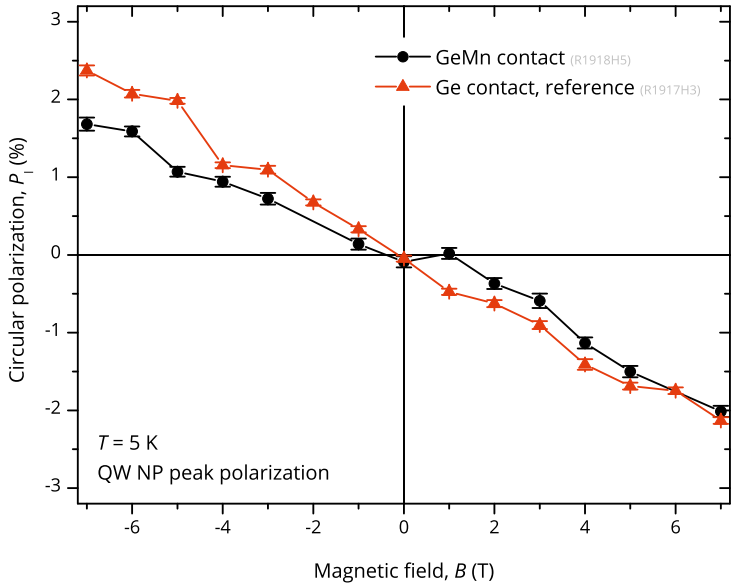

Figure 11.5 | Degree of circular polarization of the NP EL versus magnetic field for both the Ge contact reference LED and the GeMn contact spin LED.

The field dependence of the degree of circular polarization of both the sample with the reference Ge and GeMn contact was recorded for the peak energies of the respective NP EL signals and for the down-sweep direction of the magnetic field. The results are depicted in Fig. 11.5. Every data point is an average of 100 readings of the detector output signal. This procedure was pursued primarily to reduce the noise arising in the signal acquisition process. Corresponding error bars, assuming a Gaussian noise distribution, are also indicated in Fig. 11.5. We want to note, however, that a larger form of error is introduced to the measurements by an ubiquitous, nonmonotonic drift of the EL signal, the reasons of which are not completely understood.

We can see in Fig. 11.5 that the degree of circular polarization of the LED sample with the reference Ge contact exhibits a linear dependence on the magnetic field with a negative slope. A similar behavior and the same order of magnitude is found for the degree of circular polarization of the EL of the GeMn contact spin LED, although it is apparently a little smaller for negative field values and larger for positive field values than that of the reference sample. The observation of an entirely field-induced EL polarization for the reference sample suggests that in the case of the GeMn spin LED such a polarization will form an additive background contribution to a possible polarization stemming from injected spin-polarized carriers. In Fig. 11.6 we thus plot the polarization curve of the GeMn contact spin LED after point-by-point subtraction of the polarization curve of the reference Ge contact LED. The figure also includes the corresponding 5 K out-of-plane magnetization curve. If spin-polarized carriers were successfully injected into the QW, due to the orientation of the magnetization of the GeMn layer by the external field, the spin LED polarization should track the Langevin-like s-shaped magnetization curve. Despite the widely scattered data points, we are inclined to identify this s-shaped curvature in the remaining polarization curve of the

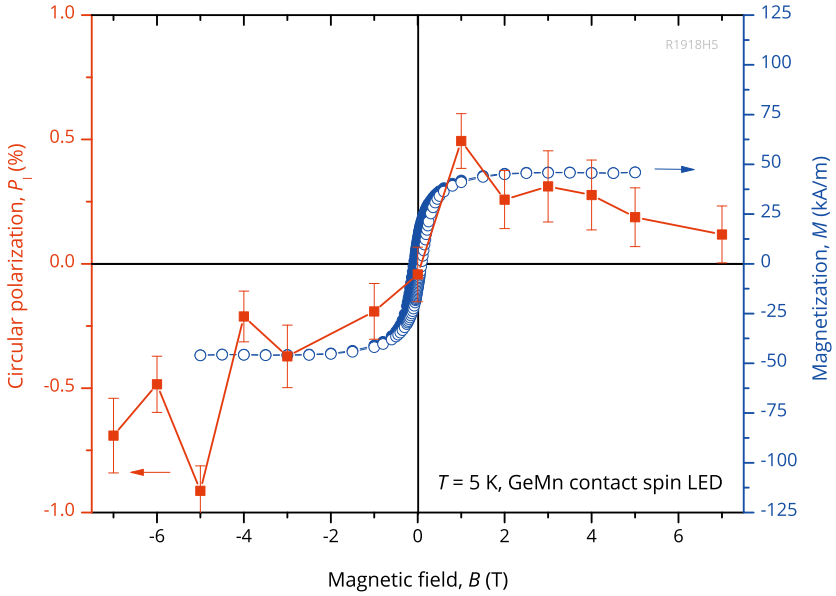

Figure 11.6 | (left axis, red) Degree of circular polarization of EL versus magnetic field of the GeMn contact spin LED after subtraction of the reference data. (right axis, blue) For comparison the corresponding magnetization loop is also plotted.

spin LED EL because, at least in part, it resembles the plotted magnetization. We can consider this observation a first indication for the injection of holes that indeed have a predominant, nonequilibrium alignment of their angular momentum, and therefore must have been polarized within the GeMn contact layer.

For final conclusions, however, several control experiments are necessary: First of all, the same kind of EL measurement should be carried out with higher magnetic field resolution, in order to verify that the field dependence of the EL polarization is really described by the magnetization curve. Particularly, it should also exhibit a hysteresis. In context with the drifting EL signal described above, this seems only productive after a further modification of the experimental setup to reduce errors. Then it has to be checked that the circular polarization of the luminescence is not just artificially introduced by a possible magnetic circular dichroism (MCD) of the GeMn layer while the photons cross the GeMn contact window. To this end, recombination of nonpolarized carriers injected into the QW has to be investigated, for which two approaches seem adequate. On the one hand, there is the excitation of PL in the QW. First attempts to excite the QW PL from the topside with an Ar-ion laser were unsuccessful, which we connect to the strong absorption of the exciting laser light within the 80 nm-thick GeMn layer. Note that excitation from the topside may in general not be ultimately conclusive, because the exciting light beam might itself undergo dichroic absorption in the GeMn layer. Thus, exciting the PL from the backside of the sample while observing it from the topside should be favored, which however would require extreme thinning of the specimen. Alternatively, using EL as proof or disproof of an MCD effect, one could try to inject nonpolarized carriers by selectively contacting the highly doped p-type Si layer, which lies in between the GeMn layer and

the QW, in a refined lithography process. Upon current injection the holes would then not pass the GeMn layer, while photons still have to exit through the GeMn layer. Of course, stand-alone experiments for the quantification of the MCD of GeMn thin films may also be helpful.

In addition to the necessary, further experimental efforts to investigate the possibly successful hole spin injection from GeMn into Si, it is necessary to highlight some aspect of this problem by theory, too. Two mayor topics come to mind here. On the one hand, the spin coupling mechanism of itinerant holes with the magnetic moments within the GeMn layers has to be investigated in more detail. This determines the direction of the angular momentum of holes that are injected into the Si part of the spin LED. Our preliminary results suggest that their angular momentum alignment is opposite to the field-induced alignment in the QW, because the absolute value of the degree of polarization is reduced for the GeMn spin LED in comparison to the reference sample. Such a study has to account for the real nanostructure, the resulting electronic band structure, and origins of ferromagnetism of the GeMn thin film. In large extents, these factors are themselves still not satisfactorily or not at all treated by theory. The other point, also relying on an improved and realistic theoretical description of the properties of the GeMn material system, is a detailed investigation of the conductivity mismatch between the ferromagnetic GeMn clusters, the surrounding Ge matrix, and the optically active Si-based device. Although we tried to equalize the global charge carrier density in the GeMn layer and the Si *p*-type side of the diode by doping, this does not automatically guarantee that the conductivity of the GeMn clusters for the possibly spin-polarized holes is actually matched to the conductivity of the Ge matrix or the Si material. Numerical estimates on the consequences of the conductivity mismatch on the spin diffusion length have to make assumptions on the spin relaxation times or spin scattering lengths of the involved materials.[227] For realistic estimates of the conductivity mismatch problem, theory thus also has to take the presumably large number of crystal defects in the present GeMn contact layer into account because such defects are known to act as a source of additional spin scattering.[130] We remind that for the present GeMn spin LED hole spin injection into Si is studied. Hole spin relaxation, also for Si, is in general faster than electron spin relaxation and thus may be obstructive to spin injection from GeMn into Si over wide distances. From a realistic treatment of this device by theorists, including above mentioned factors, we would extremely benefit in judging whether the observed polarization of the spin LED luminescence is a true consequence of spin injection.

12

Summary and concluding remarks for Part II

Part II comprised our multifaceted approach to optically detect a carrier spin polarization in group-IV-based semiconductor materials. As a first focus, we sketched a way to study spin-dependent transition probabilities in bulk Si. To this end, the possibility to optically detect a magnetic-field-induced spin polarization was illuminated. The field-induced polarization can basically be traced back to the Boltzmann distributed population of Zeeman-split conduction and valence bands. For sufficiently low temperatures or high fields the imbalance in the spin population is large enough to be observable in luminescence experiments. We derived a formal description for the resulting degree of circular polarization of the photoluminescence as a function of the applied field and temperature by including recent theory on the spin-dependent selection rules of phonon-assisted radiative transitions in bulk Si. The importance to account for both an electron- and a hole-induced luminescence polarization was outlined.

Experiments on field-induced photoluminescence polarization were presented for intrinsic, degenerate *n*-type, and degenerate *p*-type Si. The obtained results were in excellent agreement with our theory, the photoluminescence showing a linear dependence of its degree of circular polarization on the magnetic field. In bulk Si the effect of doping is crucial to explain the reversed sign of the slope of this field-induced luminescence of polarization upon comparison of intrinsic or *n*-type Si with *p*-type Si. In the former two, the polarized luminescence is mainly due to the recombination of field-polarized holes, whereas the contribution of electrons is only marginal. The opposite is true for *p*-type Si. In general our findings confirm the recent theoretical predictions of the selection rules and the magnitudes of the corresponding transition

probabilities for phonon-assisted spin-dependent radiative transitions in Si, including the effect of doping on these theoretical quantities. Thus, one might consider our study as their first experimental verification.

We also investigated the field-induced photoluminescence polarization of phononless luminescence features provided by quasi-zero-dimensional Ge quantum dots embedded in Si and revealed a remarkable and so far not documented property: We found a sign reversal of the degree of photoluminescence polarization for these spin-dependent phononless radiative transitions compared to the transverse-phonon-assisted transitions of Si type or the direct transitions of GaAs type. Independent confirmation of this observation came from similar results on phononless transitions in degenerate *n*-type Si as well as SiGe quantum wells. This points to a generic property of the phononless transitions in Si-based structures. We proposed that it may be related to the confined character of the electron wave function. The hereby possibly resulting admixture of direct to indirect band gap states might lead to a qualitative change of the spin-dependent selection rules. Further input, particularly from the theory side, is needed to resolve the exact origins of the observed effect.

Moreover, it was discussed that the direct optical injection of electron spins in bulk Si in the absence of a magnetic field and the subsequent optical detection via luminescence experiments are very challenging, basically because of the long radiative recombination times that lead to the decay of any spin information long before carrier recombination. A rather optimistic estimate showed that no more than 0.35 % of circular polarization can be expected in an all-optical injection and detection experiment. Such an all-optical approach seems more feasible when the phononless optical transitions of Ge quantum dots are utilized. The exitonic radiative lifetimes and the electron/hole spin lifetimes are expected to be of comparable orders of magnitude. Yet, we have shown that spin injection of carriers confined to the Ge quantum dots is not possible for an excitation energy, 2.41 eV in our case, well above the indirect band gap of Si. For such nonresonant excitation wavelengths electrons and holes are both created first in the Si material surrounding the quantum dots and not within the confining potentials of the dots. Due to the small spin-orbit coupling of Si, upon this carrier injection the photon spin polarization is expected to be transferred in large parts to the hole system. However, this information seems to be lost during the capture of the holes by the quantum dots' confining potentials because the resulting luminescence was completely unpolarized.

We presented also efforts to excite electron-hole pairs quasi-resonantly, i.e. creating carriers within the confining potentials attributed to the quantum dots. An excitation energy of 847 meV was employed, whereas the ground state excitonic luminescence lines of the quantum dots in the ensemble were centered around 755 meV. Unfortunately, there is no conclusive result whether the quasi-resonant spin injection yields a finite polarization of photoluminescence because its intensity has been too weak to be observed by the current measurement setup. Although improvements of the setup are conceivable, it seems equally instructive to study spin injection in Ge quan-

tum dots by the complementary technique of Faraday rotation. In collaboration with M. Betz, Technische Universität Dortmund, we have started first experiments in this direction by measuring the transient sample absorption in a pump-probe setup for quasi-resonant excitation. So far, only two-photon absorption for zero delay time of pump and probe beam is observed indicating an extremely small absorption of the sample in this wavelength range.

Enclosing this thesis, we finally tested the functionality of a superparamagnetic GeMn layer as spin-injecting electrical contact. To this end, an group IV all-semiconductor spin light-emitting diode was fabricated by depositing a layer of *p*-type GeMn on a *pin* Si diode with embedded SiGe quantum well as optical emitter. Although further experimental confirmation is needed, the first result of the field-dependent electroluminescence curve tracking the sample magnetization curve seems to indicate the successful injection of spin-polarized holes.

Appendices

A Experimental techniques

THIS appendix details information about the experimental techniques that have been used in the course of this thesis, a part of which employed in collaboration with coworkers. Also background information on certain techniques is given.

A.1 Transmission electron microscopy

TEM was done in collaborations with S. Stemmer and J. M. LeBeau, Materials Department, University of California, Santa Barbara, USA, for the STEM and HRTEM micrographs depicted in Figs. 3.5, 3.6 and 4.1, with A. Trampert, Paul-Drude-Institut für Festkörperelektronik, Berlin, Germany, for the DFTEM micrograph shown in Fig. 3.1, and with J. Zweck, Universität Regensburg, Regensburg, Germany for the BFTEM micrographs depicted in Figs. 4.2 and 4.3.

Samples were prepared by standard wedge polishing techniques followed by Ar ion milling. An FEI Titan 80–300 kV S/TEM operating at 300 kV was used for STEM and HRTEM imaging. STEM in HAADF mode was done with a ring-detector at inner semiangle of 65 mrad, for the LAADF mode the inner semiangle was 23 mrad. For DFTEM a Jeol 3010 microscope operating at 300 kV with a spatial resolution of 0.18 nm was employed.

A.2 Atom probe tomography

The pulsed-laser APT study was carried out in collaboration with A. Cerezo and D. W. Saxey, Department of Materials, University of Oxford, Oxford, U.K. The initial

preparation of APT specimen needles was kindly performed by V. Lang in a cooperation with H. Cerva, Siemens AG, Corporate Technology MM 7, Munich, Germany.

A.2.1 Background

Pulsed-laser local-electrode APT is a method suitable to project spatial atomic positions of a sample specimen in form of a sharp needle layer-by-layer onto a large-scale detector. Spatial resolution on the atomic scale is reached because the magnification in APT essentially relies only on the ratio of the radius of curvature of the needle and its distance to the detector. The basic principle is as follows: A large electric field is applied between the specimen needle and a local electrode placed near the tip of the needle. With the help of a laser pulse the topmost atomic layer of the specimen is sequentially evaporated, whereas the evaporated atoms are ionized during this process. In each evaporation step, the ions are accelerated through the applied electric field to a velocity that corresponds to their individual mass-to-charge ratio. By time-of-flight mass spectrometry the ion species can thus be distinguished during their flight to a position-sensitive detector. Here, events of arriving ions are recorded in a sequential data stream. Accounting for the geometry of the experiment, the data is reconstructed to a 3D spatial distribution map of atom species in the needle. Detailed reviews on this experimental technique can be found in Refs. 79 and 80.

Figure A.1a depicts a scanning electron microscopy (SEM) image of a prefabricated Si micropost, which acts as the base for APT specimen needles. In a first preparation step, an approximately 100 nm-thick layer of Ni followed by 1 µm Pt was deposited onto the sample in situ of a focused ion beam chamber. Such a metal capping serves by default as a protective layer against ion implantation during subsequent processing steps. Then, a lamella was cut from the sample wafer with the help of a dual beam focused ion beam and lifted out. The roughly 3 µm × 3 µm × 8 µm-sized piece of the sample attached to the micropost is shown in Fig. A.1b. Prior to the APT analysis the needle was sharpened by Ga ion milling, as depicted in Fig. A.1c. With a second, low-energy milling process, usually intended to form a smooth shape and needle surface, the complete Pt/Ni cap was purposely removed, see Fig. A.1d. This turned out to be necessary because first runs of APT revealed that field evaporation through the Ni layer causes the fraction of the specimen.

A.2.2 Experimental

APT was conducted using an Imago LEAP 3000X HR instrument[232] in a pulsed-laser mode. The laser had a wavelength of 532 nm and a beam spot diameter at the specimen of less than 10 µm. The laser pulse repetition rate was 100 kHz with a pulse duration of a few picoseconds and pulse energy of approximately 0.1 nJ. The average field evaporation rate was controlled at 0.005 ions per pulse. Specimens were held at a temperature of 23 K during the acquisitions in order to avoid surface diffusion of atoms prior to field evaporation. Evidence of surface diffusion on the specimen tip was

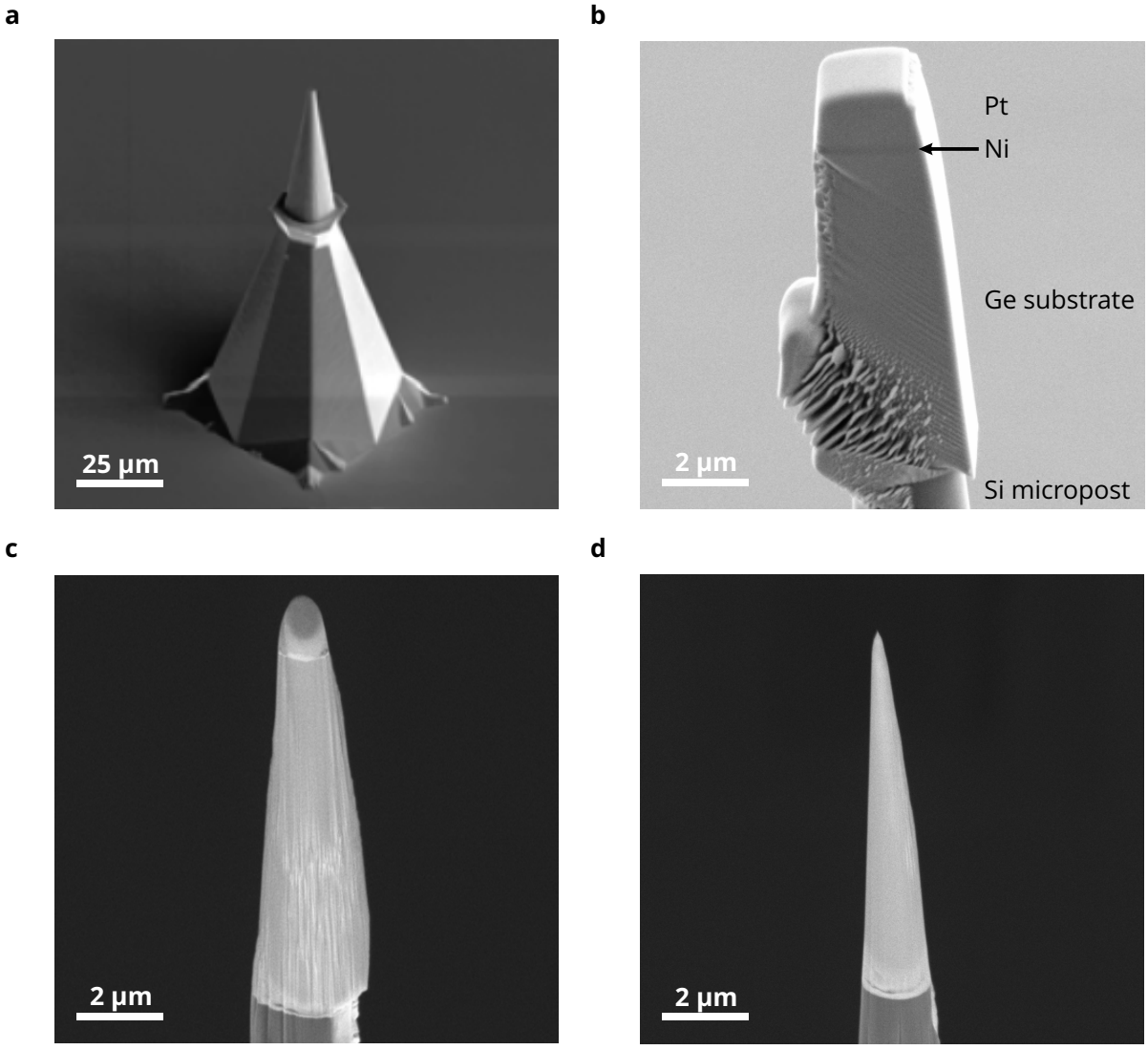

Figure A.1 | SEM micrographs taken at different stages of the processing of APT needles. **a**, Bare Si micropost serving as base for the specimen needle. **b**, Unshaped specimen lamella attached to the post. The Pt and Ni layers are clearly visible, while the GeMn/Ge interface cannot be resolved with SEM. **c**, Sharpened specimen after the first ion milling with the metal layers still lying on top. **d**, Final specimen after the low-energy, second milling.

observed when performing the analysis at temperatures above 23 K and at higher laser energies. The known thickness of the epitaxial layers was used to correctly scale the reconstructed data.

A.3 Ion beam channeling

The channeling RBS and PIXE analysis was kindly performed by K. M. Yu, Materials Sciences Division, Lawrence Berkeley National Laboratory, Berkeley, USA.

A.3.1 Background

In RBS a sample specimen is bombarded with a beam of high-energetic, positively charged ions of a light element, usually H or He. The kinetic energy of these ions is typically in the MeV range. If these ions come close to the atomic cores of the specimen, they are scattered by the strong Coulomb interaction. As Rutherford observed, the scattering angle in principle only depends on the energy of the ion beam, the atomic species of the beam, and that of the scatterer. Hence, by placing an energy-sensitive ion detector at a given detection angle one can deduce a chemical information about the specimen from the peak-like energy spectrum of the scattered beam and identify, for example, impurities in a semiconductor crystal. If the impurity atom is heavier than the host atom, the ions scattered at the impurity have larger energies than ions scattered at the host. The opposite is true for lighter impurity atoms. For thick specimens, however, the incident ions can undergo multiple scattering events and hereby lose energy before they are scattered back to the detector. Therefore, in reality, the peak-like energy spectrum at the detector is often convoluted with a depth information. Particularly identifying light impurity elements in a heavy-atom host, such as Mn impurities in Ge, is then not easy. In order to do this, PIXE can be employed. In addition to being scattered, the incident ion beam can also excite electrons from the inner atomic shells to higher-order shells. The resulting X-ray emission is specific to the scattering atom species and does not depend on the energy of the incident ion beam, as long as it has enough energy to excite the electrons. A PIXE spectrum thus always contains well-defined element-specific X-ray emission lines.

A.3.2 Channeling

Channeling RBS/PIXE is a very useful tool to characterize defects in a crystalline host material. A good introduction to the channeling technique can be found in Ref. 233, for example. In channeling ion beam analysis one exploits the phenomenon that if the ion beam is incident parallel to a high-symmetry axis of a crystalline host, Ge in our case, the scattering of ions at the host atoms is highly suppressed. Only the host atoms in the first layer of the specimen can contribute to scattering events, whereas the host atoms in underlying layers are shadowed by the first atomic layer. Hence, along high-symmetry axes the majority of the crystal appears 'empty' to the ion beam, i.e. only a small area surrounding the host atoms, mainly given by the atomic radius, has a finite scattering cross section with the beam. The larger part of the area facing the beam, given by the interatomic distances, has zero scattering cross section. The ion beam is said to be channeled by the atomic columns or planes. For a beam direction that is parallel to the $\langle hkl \rangle$-axes of high symmetry, the yield of backscattered ions or X-ray emission $Y_{\mathrm{min,Ge}}^{\langle hkl \rangle}$ is minimal. In contrast, tilting the beam to a random orientation with respect to the specimen results in a maximum yield $Y_{\mathrm{r,Ge}}$. In a first approximation,

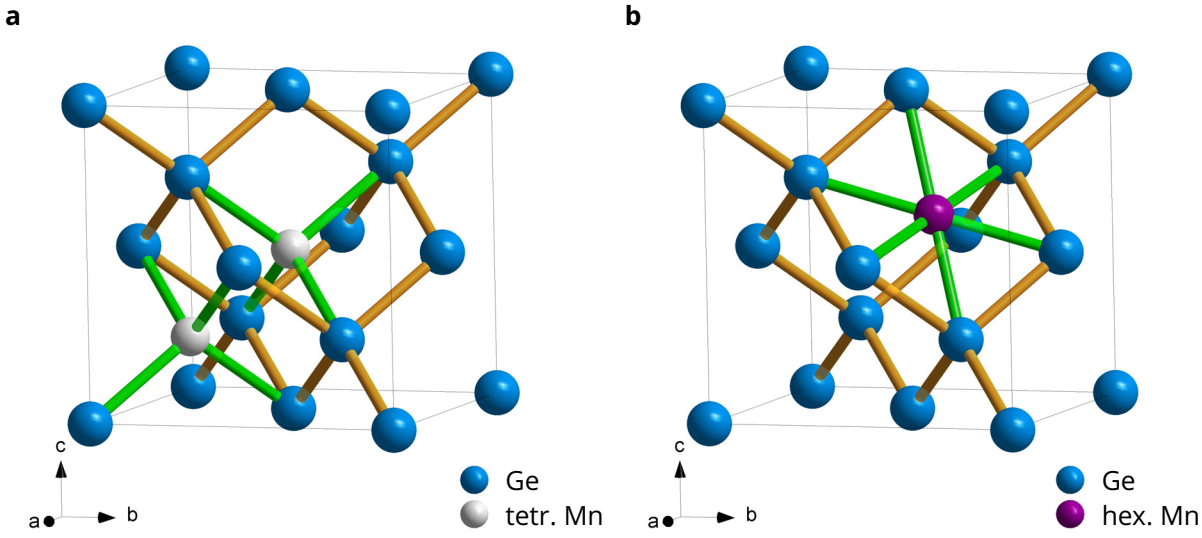

Figure A.2 | Schematic of the different interstitial sites in a Ge lattice. **a**, Two (equivalent) tetrahedrally coordinated interstitials. **b**, Hexagonally coordinated interstitial.

the quantity

$$\chi^{\langle hkl\rangle}_{\mathrm{min,Ge}} \equiv \frac{Y^{\langle hkl\rangle}_{\mathrm{min,Ge}}}{Y_{\mathrm{r,Ge}}}, \tag{A.1}$$

referred to as the normalized minimum yield, depends only on the specimen material and is of the order of only a few percent for high-quality crystals of Ge.[233] Every perturbation of the perfect crystal periodicity leads to an increase of $\chi^{\langle hkl\rangle}_{\mathrm{min,Ge}}$.

Because of the element-specificity of RBS/PIXE, the normalized minimum yield of impurity atoms that are incorporated in the host crystal, Mn in our case, can be determined separately. If these impurities are incorporated in a random manner in the crystal, i.e. neither on a substitutional nor interstitial site, $\chi^{\langle hkl\rangle}_{\mathrm{min,Mn}}$ will always be larger than $\chi^{\langle hkl\rangle}_{\mathrm{min,Ge}}$ because the Mn atoms are not shadowed. On the other hand, if they sit on interstitial sites, the value of $\chi^{\langle hkl\rangle}_{\mathrm{min,Mn}}$ depends on the orientation of the crystal with respect to the ion beam because in certain directions these interstitials are shadowed, in other directions not. There are two possible, tetrahedrally and hexagonally coordinated, interstitial sites in the Ge lattice, as depicted in Fig. A.2a and A.2b, respectively. In the following we assume only tetrahedrally coordinated interstitials.

In Fig. A.3 the three main channeling directions, $\langle 100\rangle$, $\langle 111\rangle$, and $\langle 110\rangle$, for diamond-lattice-type crystals, such as Ge, are depicted. Also shown is a multitude of tetrahedrally coordinated interstitial Mn atoms. For channeling along the $\langle 100\rangle$ and $\langle 111\rangle$ directions the tetrahedral Mn interstitials are shadowed by the Ge host atoms, as one can see in Fig. A.3a and A.3b, respectively. Of course, the same holds for substitutional Mn. Thus, an increase of $\chi^{\langle 100\rangle}_{\mathrm{min,Mn}}$ or $\chi^{\langle 111\rangle}_{\mathrm{min,Mn}}$ must be to due randomly

incorporated Mn atoms. For both these directions one defines now the quantity

$$f_{\mathrm{nr}} \equiv \frac{1-\chi_{\mathrm{min,Mn}}^{\langle hkl\rangle}}{1-\chi_{\mathrm{min,Ge}}^{\langle hkl\rangle}} \tag{A.2}$$

as the nonrandom fraction of Mn atoms and correspondingly

$$f_{\mathrm{r}} = 1 - f_{\mathrm{nr}} \tag{A.3}$$

as the random fraction of Mn atoms.

It is now possible to distinguish the nonrandom fraction f_{nr} further into a substitutional, f_{s}, and interstitial, f_{i}, fraction of Mn atoms. This is can be done by channeling along the $\langle 110\rangle$ directions, as shown in Fig. A.3c. Here, the interstitials are completely visible to the beam and contribute to scattering effects. They cause an increase of $\chi_{\mathrm{min,Mn}}^{\langle 110\rangle}$, whereas substitutional Mn atoms are still shadowed. The increase of $\chi_{\mathrm{min,Mn}}^{\langle 110\rangle}$, however, is not solely due to the presence of interstitials but in part also due to the so-called flux-peaking effect. The flux-peaking effect describes the fact that because of the channeling of the ion beam by the atomic columns, its flux density is increased in the center of a channel and, in turn, decreased nearby the atomic columns. Thus, the tetrahedral interstitial Mn atoms, which sit near the center of the channel, experience a higher beam current than substitutional Mn atoms would. For a correct quantification of f_{i}, one includes this effect by a numerical parameter F, which is empirically derived or calculated from simulations of the flux distribution.[233] The connection between the $\chi_{\mathrm{min,Mn}}^{\langle 110\rangle}$, f_{i}, and f_{s} is then given by[234,235]

$$\chi_{\mathrm{min,Mn}}^{\langle 110\rangle} = f_{\mathrm{r}} + f_{\mathrm{s}} \cdot \chi_{\mathrm{min,Ge}}^{\langle 110\rangle} + f_{\mathrm{i}} \cdot F. \tag{A.4}$$

On the other hand, Eq. (A.3) has to be modified to the new relation

$$f_{\mathrm{r}} + f_{\mathrm{s}} + f_{\mathrm{i}} = 1. \tag{A.5}$$

Now, Eq. (A.4) and Eq. (A.5) allow to independently solve for f_{s} and f_{i}.

A.3.3 Experimental

For the present analysis a He ion beam with primary ion energy of 2 MeV was used. The RBS and PIXE detectors were located at 165° and 135° with respect to the ion beam, respectively. $\chi_{\mathrm{min,Ge}}^{\langle hkl\rangle}$ was determined from the region in the RBS spectra corresponding to the expected main peak for Ge, whereas $\chi_{\mathrm{min,Mn}}^{\langle hkl\rangle}$ was quantified from PIXE scans of the $\mathrm{Mn}_{\mathrm{K}\alpha}$ line. The nonrandom fraction f_{nr} is calculated as the average of the values obtained from $\langle 100\rangle$ and $\langle 111\rangle$ channeling scans. A flux peaking effect of $F = 1.5$ was assumed in Eq. (A.4). In order to distinguish between tetrahedral and hexagonal interstitials, careful angular scans around the different axial channels would have been

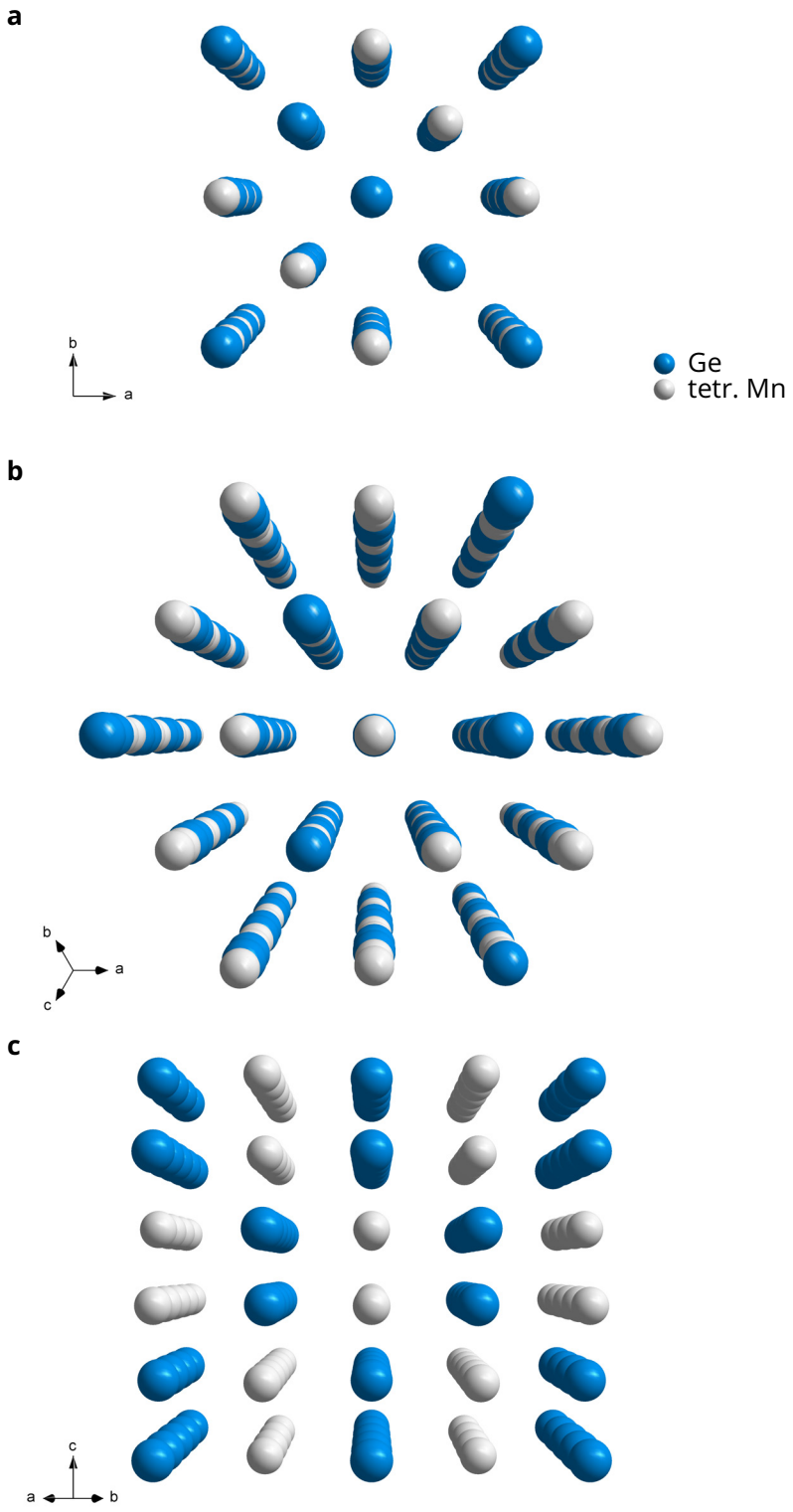

Figure A.3 | a, ⟨100⟩, **b**, ⟨111⟩, and **c**, ⟨110⟩ channeling directions for a Ge lattice with tetrahedral Mn interstitials. The interstitials are shadowed in the ⟨100⟩ and ⟨111⟩ directions but exposed in the ⟨110⟩ direction.

necessary, but were not conducted. Thus, the measurement results only evidence the presence of Mn atoms at some interstitial position. $F = 1.5$ accounts for something in between the two possible sites.[235] The results of this study are summarized in Table A.1.

A.4 Photo- and electroluminescence spectroscopy

A.4.1 Basic setup

For luminescence measurements we employed the experimental setup schematically depicted in Fig. A.4. The samples were inserted in an Oxford Instruments SM4000-8 split-coil magnet cryostat where magnetic fields ranging from $-7\,\mathrm{T}$ to $7\,\mathrm{T}$ and temperatures between $1.4\,\mathrm{K}$ and $300\,\mathrm{K}$ are available. The setting of a positive value for the magnetic field at the magnet power supply corresponded to the field direction indicated in Fig. A.4. For field-dependent measurements this direction was chosen as quantization axis, for optical orientation, i.e. circularly polarized excitation, the quantization axis was given by the propagation axis of the incident light. In the latter case, for an alignment as shown in Fig. A.4 the finite angle θ_{inc} between the incident and the luminescence light generally reduces the detectable circular polarization of the luminescence. The degree of the polarization scales with $\cos\theta_{\mathrm{t}}$, where θ_{t} is the angle between the luminescence beam and the incident beam transmitted into the sample. In small-angle approximation, $\cos\theta_{\mathrm{t}} \approx \cos\left(\theta_{\mathrm{inc}}/n_{\mathrm{Si}}\right) = 0.998$, where $\theta_{\mathrm{inc}} = 12°$ and the refractive index of Si $n_{\mathrm{Si}} = 3.4$ were used. Thus, the small θ_{inc} is without any consequences here.

PL was excited in the visible spectrum either with an Ar-ion laser or 532 nm diode-pumped solid-state (DPSS) laser. For excitation in the infra-red spectrum, a high-power 1464 nm DPSS with a maximum output power of approximately 150 mW was used. The cw-laser beam was chopped with a 50/50 duty cycle chopper in order to allow detection of the PL by lock-in technique. A chopping frequency of 66 Hz was chosen. This is high enough to avoid jitter annoying the experimenter and at the same time low enough for the response time of the detector. The laser powers P_{exc} given throughout this thesis were determined for the unchopped cw-beam in the beam path directly before the cryostat.

Table A.1 | Results of the channeling RBS/PIXE analysis of the GeMn thin film sample with $r_{\mathrm{Ge}} = 0.08\,\text{Å}\,\mathrm{s}^{-1}$ and $x = 7.3\,\%$.

sample	Mn conc.		$\chi_{\mathrm{min,Ge}}$			$\chi_{\mathrm{min,Mn}}$			f_{r}	f_{s}	f_{i}
	SIMS[a]	RBS[b]	⟨100⟩	⟨111⟩	⟨110⟩	⟨100⟩	⟨111⟩	⟨110⟩			
R1631	7.3 %	6.0 %	0.103	0.11	0.093	0.88	0.89	1.02	0.88	0.09	0.03

[a] Quantified by secondary ion mass spectrometry (SIMS).
[b] Estimated from the PIXE signal intensity and the sample thickness as deduced from the RBS spectrum.

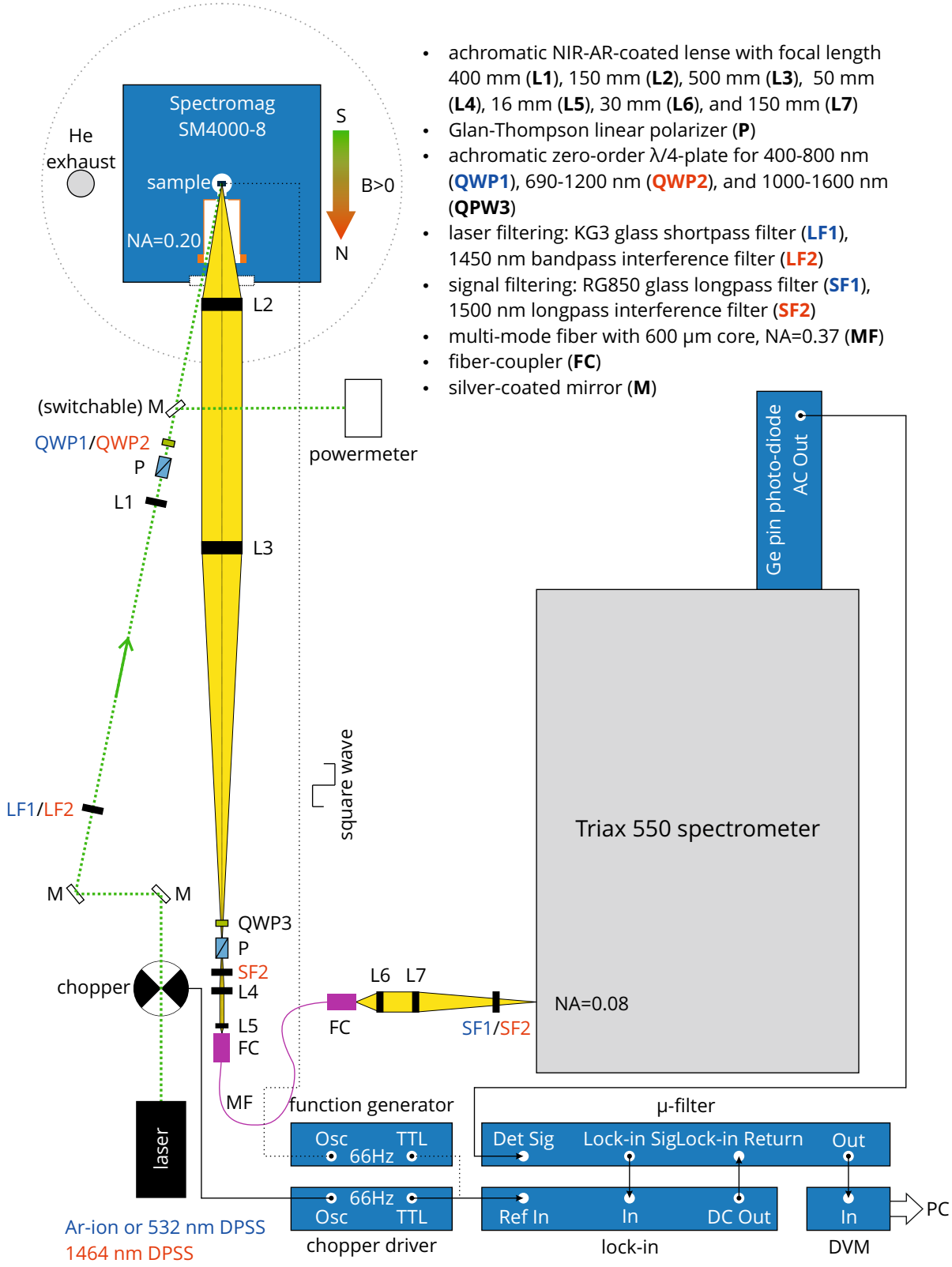

- achromatic NIR-AR-coated lense with focal length 400 mm (**L1**), 150 mm (**L2**), 500 mm (**L3**), 50 mm (**L4**), 16 mm (**L5**), 30 mm (**L6**), and 150 mm (**L7**)
- Glan-Thompson linear polarizer (**P**)
- achromatic zero-order λ/4-plate for 400-800 nm (**QWP1**), 690-1200 nm (**QWP2**), and 1000-1600 nm (**QPW3**)
- laser filtering: KG3 glass shortpass filter (**LF1**), 1450 nm bandpass interference filter (**LF2**)
- signal filtering: RG850 glass longpass filter (**SF1**), 1500 nm longpass interference filter (**SF2**)
- multi-mode fiber with 600 μm core, NA=0.37 (**MF**)
- fiber-coupler (**FC**)
- silver-coated mirror (**M**)

Figure A.4 | Schematic of the experimental layout for PL and EL measurements

Similarly, a 50/50 duty cycle square-wave voltage was applied to the sample for measurements of EL. Using an ac voltage to excite the EL of the spin LEDs instead of a dc voltage followed by chopping of the EL was favored in order to reduce the heat load to the cryostat. Thus the liquid helium consumption during the very helium-consuming low-temperature measurements is reduced.

The adjustment of the circular polarization of the excitation in PL and of the polarization analysis of the detection path in both PL and EL were done by a combination of Glan-Thompson linear polarizers and achromatic zero-order quarter-wave retardation plates. To switch between RCP and LCP, the quarter-wave plate was manually rotated. The precise relative alignment of the optical axes of these polarization optics had been previously determined in an independent setup in Faraday isolator geometry.

The luminescence was spectrally dispersed in a Jobin-Yvon Triax 550 spectrometer by a motorized 600 lines/mm grating blazed at 1500 nm. The spectrometer slits were maximally opened to 2 mm to allow for large signals, which were more important than high resolution for the measurements presented here. For the large-bandwidth spectral scans shown in this thesis, rotation steps of the grating nominally corresponding to 1 nm or 2 nm resolution were typically employed. The luminescence was detected with a single-channel, liquid-nitrogen-cooled North Coast EO-817 Ge photo-diode. The luminescence-induced ac voltage output signal of the Ge diode was recovered and transformed to a dc signal by a lock-in amplifier.

A.4.2 Signal filtering

Due to cosmic-rays penetrating the detector area, the output of a Ge diode generally contains sharp, large-amplitude voltage spikes.[236] In our experiments, these overlaid to the actual luminescence-induced signal and drastically reduce the spectrum quality. To remove these spikes, the lock-in-recovered dc voltage signal was electronically filtered in a so-called muon-filter, which is an electronic trigger-sample-hold circuit. The spikes in the raw ac voltage output of the Ge detector work as a trigger for an adjustable hold time period, during which the lock-in dc signal is replaced by a matched sample voltage generated by muon-filter. The filtered signal is then further smoothed in an integration circuit and the so-processed signal is output by the muon-filter. It is actually this signal that is read with a digital voltmeter (DVM) and digitally recorded. Typically, a hold time of 300 ms and an integration time of 1000 ms was chosen for the muon-filter. The trigger threshold was adjusted to a setting of 30 dB, which corresponds to a spike amplitude of 30 mV that had to be exceeded for a trigger event to occur. It is important to set the lock-in integration time constant shorter than the hold time of the muon-filter to allow an effective filtering. Otherwise, the voltage spikes in the lock-in-recovered signal are smeared out in time and exceed the hold time of the muon-filter. Usually, a time constant of 30 ms was set for the lock-in.

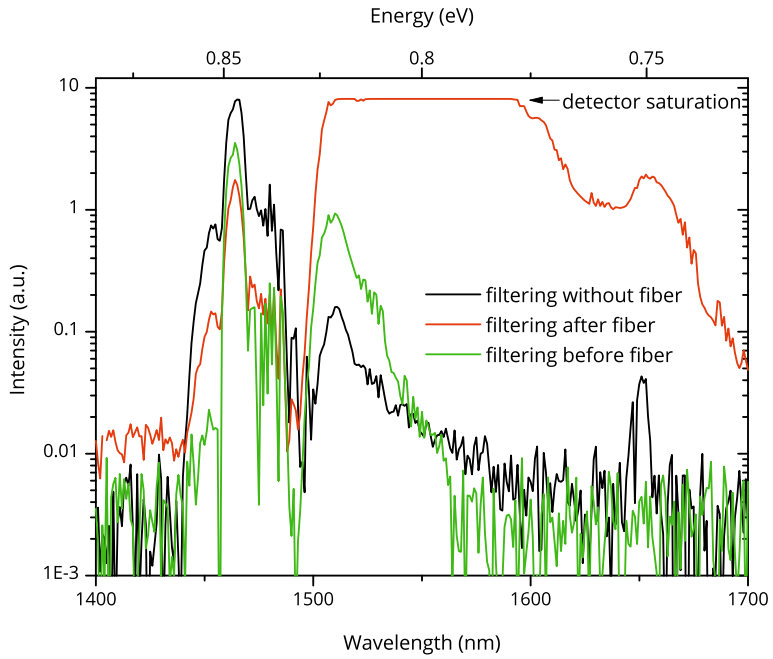

Figure A.5 | Longpass filtering of the infra-red 1464 nm laser by an interference filter with 1500 nm cut-on frequency. Filtering after the silica fiber (red) allows the laser to undergo Raman scattering in the fiber, which is drastically reduced by filtering before the fiber (green). For comparison a laser spectrum without using any fiber (black) to guide the light to the spectrometer is given. Note that for these test measurements the intensity of laser light incident on the fiber was much higher than in actual PL measurements.

A.4.3 Laser filtering

Particularly for excitation with the infra-red 1464 nm laser diode, it was important in our experiments with Ge hut-clusters to filter the laser light from the luminescence. As indicated in Fig. A.4, this was done, on the one hand, by removing sidebands of the laser well exceeding 1464 nm from the excitation spectrum by bandpass filtering and, on the other, by blocking light with wavelengths above 1500 nm from entering the spectrometer by longpass filtering. Here, it was important to not only put longpass filters directly before the spectrometer but also at least one additional before the multi-mode silica fiber. Otherwise, the 1464 nm laser excited the very broad Raman band of the silica material and was dispersed to wavelengths up to 1700 nm, which cannot be distinguished from the typical wavelengths of Ge hut-cluster PL. This phenomenon is illustrated in Fig. A.5.

A.4.4 Field sweep measurements

Spectral scans of the luminescence were acquired in a stepwise manner, i.e. a starting wavelength was set, the PL data recorded for this wavelength, the next wavelength set according to the chosen resolution width, the data recorded, and so on. The adjustable wait time between these steps has a minimum value of approximately 300 ms, limited

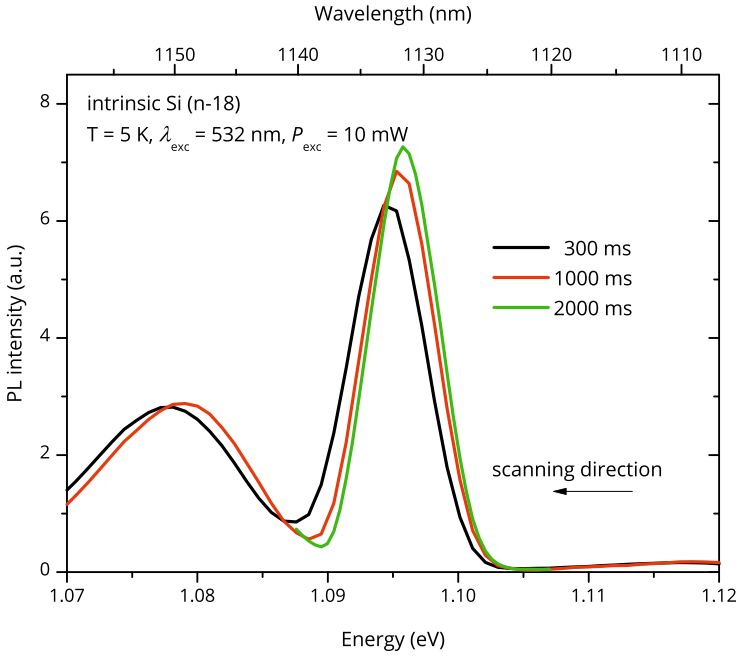

Figure A.6 | Influence of the wait time between scanning steps on the shape of spectral scans of the luminescence.

by the cumulated setup response time of one acquisition step. The choice of the wait time has direct consequences on the shape of the PL spectra. Figure A.6 depicts a comparison of Si TO PL spectra acquired with three different wait times. Clearly, for the shortest wait time the PL peak is smeared out and its energetic position shifted into the scanning direction. A precise spectrum is only achieved for wait times of 2000 ms and above, given a setting of 1000 ms for the integration time of the muon-filter.

Thus, for an accurate determination of the energetic position and intensity of sharp luminescence peaks, which is necessary to determine the degree of polarization in polarization-resolved measurements, quick scanning is not desirable. On the other hand, for these kind of measurements long wait times are also not an option because they prolong the overall acquisition time of one spectrum. Determining the field-dependence of so-measured polarization ratios then takes several hours. Due to drifts in the luminescence signal (see below), the comparability of polarization ratios for the different field values is impaired and in general of bad statistical significance. For field-dependent measurements we recorded only one luminescence spectrum in high resolution and with sufficient wait time to determine the energetic position of the peak maximum. Then, at this photon energy the PL signal for one field value and one polarization direction was typically measured 50 or 100 times in intervals of 1000 ms to increase the signal-to-noise-ratio. Subsequently, the opposite polarization sense was analyzed before the next magnetic field value was approached and the switching/measurement procedure repeated. The degree of circular polarization is determined from the statistically averaged values. The error bars in Fig. 11.5 are determined assuming a Gaussian distribution of the measured values.

Particularly EL signals undergo a nonmonotonic drift on the minute time scale, the origin of which is not completely clear. It might be related to Eddy currents arising in the samplestick during the field sweeps and causing micrometer movements of the sample. Indeed, we believe this drift makes already the larger error than statistical fluctuations of the measured value, such that longer averaging and thus smaller statistical error bars would not be of help to obtain cleaner measurements.

An improvement of the setup may lie in an automatic, motorized switching of the polarization analysis. This would allow to change between the two circular polarization states on a time scale shorter than the drift time scale, while it would maintain the possibility to reduce noise by a multiply repeating of the switching procedure. In this context, we want to note that the experience with standard liquid-crystal variable wave retarders were highly discouraging because of their strong chromatic aberration and poor polarization characteristics.

B

Circular polarization of light

HERE we specify the meaning of the terms right-circularly, left-circularly, σ^+-, and σ^--polarized light wave or photon that we adopt throughout this thesis. We do so because there is, firstly, a differing convention for the usage of the terms right-circular polarization (RCP) and left-circular polarization (LCP) to describe the polarization sense of light in the field of wave optics, on the one hand, and quantum optics, on the other. Moreover, RCP and LCP are often used as synonyms for σ^+- and σ^--polarized photons, which is incorrect in the general case.

In the framework of this thesis, RCP and LCP denote whether the **x**-**y**-plane projection of the electric field vector of a circularly polarized light wave at a fixed point in space *as seen from the light source* describes a clockwise or counterclockwise rotation, respectively, around the light propagation direction **k** as time progresses. Within this convention, the electric field vectors $\mathbf{E}_{\mathrm{RCP}}$ and $\mathbf{E}_{\mathrm{LCP}}$ for these two cases, given that the wave travels in positive **z**-direction with a frequency ω and an electric field amplitude E, are parameterized by

$$\mathbf{E}_{\mathrm{RCP}}(z,t) = \frac{E}{\sqrt{2}} \begin{pmatrix} 1 \\ +i \end{pmatrix} e^{i(kz-\omega t)} \quad \text{and} \tag{B.1}$$

$$\mathbf{E}_{\mathrm{LCP}}(z,t) = \frac{E}{\sqrt{2}} \begin{pmatrix} 1 \\ -i \end{pmatrix} e^{i(kz-\omega t)}. \tag{B.2}$$

These two polarization states are depicted in Fig. B.1a and B.1b, respectively. RCP and LCP denote the circular polarization states with respect to a laboratory framework and are directly adjustable/measurable with our experimental setup once the polarization optics have been properly adjusted. Yet, RCP and LCP cannot be related to any physics without further knowledge of the experimental conditions.

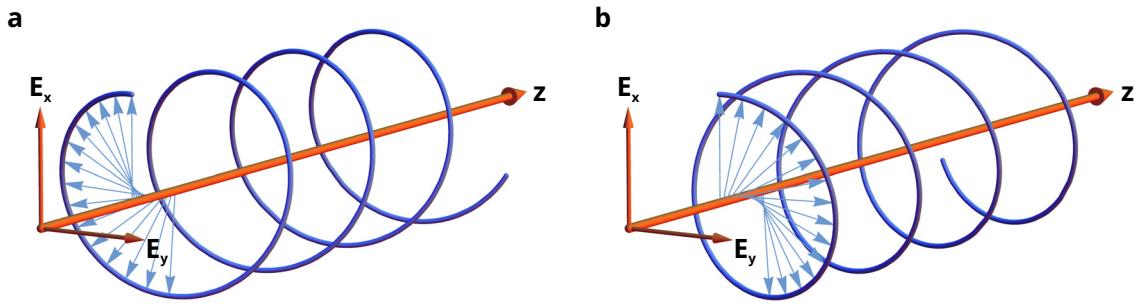

Figure B.1 | Evolution of the electric field vector of a light wave with **a**, RCP and **b**, LCP as defined by Eq. (B.1) and Eq. (B.2), respectively, for a fixed time and propagation along the positive **z**-direction.

In contrast, σ^+ and σ^- polarization of a photon indicate the value of the projection of the photon spin onto a quantization axis. For a value of $+1\,\hbar$ we speak of a σ^+-polarized photon and, accordingly, of a σ^--polarized photon for a projected value of $-1\,\hbar$. If the spin quantization axis is given by the propagation direction $\mathbf{k}$ of the photon, the spin of a σ^+-polarized photon points into the same direction as $\mathbf{k}$. In conformity with particle physics, the photon is called right-handed, which by definition corresponds to a light wave with RCP. Analogously, a σ^--polarized photon is then left-handed and corresponds to LCP. The spin quantization axis can coincide but has not to coincide with the propagation direction of the photon. For example, when one is interested in the mutual relationship between the magnetic-field-oriented or optically oriented spin of an electron and that of a photon created upon the electron recombination, it is sensible to choose the direction of the magnetic field $\mathbf{B}$ or propagation direction of the incident light beam $\mathbf{k}_{\text{inc}}$ as the physically relevant quantization axis. That is, 'σ^+-polarized' or 'σ^--polarized' is actually the significant nomenclature of polarization and does not dependent on a laboratory framework. In Table B.1 we comprise the relationship of σ^+/σ^--polarized photons to RCP/LCP for the different alignments of $\mathbf{k}$, $\mathbf{k}_{\text{inc}}$ and $\mathbf{B}$ that are of practical relevance in experiments.

Table B.1 | Relation between RCP/LCP of a light wave in the laboratory framework, as defined in the text, and σ^+/σ^--polarized photons in the physical framework. The physical framework is either given by $\mathbf{B}$ or $\mathbf{k}_{\text{inc}}$. $\mathbf{k}$ is the propagation direction of the observed light, e.g. luminescence. Their relative alignment is indicated by the arrows, (↑↑) meaning parallel and (↑↓) antiparallel alignment. Black and red color code correspond to the observation of a σ^+- and σ^--polarized photon, respectively.

		B		$\mathbf{k}_{\text{inc}}$	
		↑	↓	↑	↓
k	↑	RCP	LCP	RCP	LCP
		LCP	RCP	LCP	RCP
	↓	LCP	RCP	LCP	RCP
		RCP	LCP	RCP	LCP

C Light-emitting diodes

THE way to the fabrication of reliable SiGe QW emitters embedded in LED structures is sketched in the following, including the processing recipes for the preparation of LED devices.

C.1 Growth optimization

C.1.1 Temperature issues

In the beginning of our spin LED study, we had to recover the knowledge about the growth of optically active SiGe QWs, exhibiting distinct TO and NP luminescence lines. We aimed at growing a nominally 40-monolayer-thick, single $Si_{0.7}Ge_{0.3}$ QW, sandwiched between 30 nm-thick intrinsic Si barriers. 40 monolayers of this pseudomorphic alloy correspond to approx. 5.6 nm. In analogy to a similar, multi-QW structure that was previously fabricated in the Abstreiter group, we chose a growth temperature around $T_S = 615\,^{\circ}C$ as measured by the thermocouple on the wafer manipulator of the MBE machine.[230] In a first try, we directly integrated this sandwich into a *nip* Si diode structure (R1840), as depicted in Fig. C.1a. The growth of a SiGe alloy on nonrotating wafers results in a concentration gradient due to the asymmetric position of our Si and Ge electron beam sources with respect to the wafer center. Consequently, the actual composition of the QW and hereby the luminescence energies change with wafer position, whereas the nominal composition is only valid for the center (cf. Ref. 237). We thus characterized many pieces of this first sample taken from different positions of the wafer. In what follows, the nomenclature of the positions of these pieces is always identical and is indicated in the wafer map depicted in Fig. C.1b.

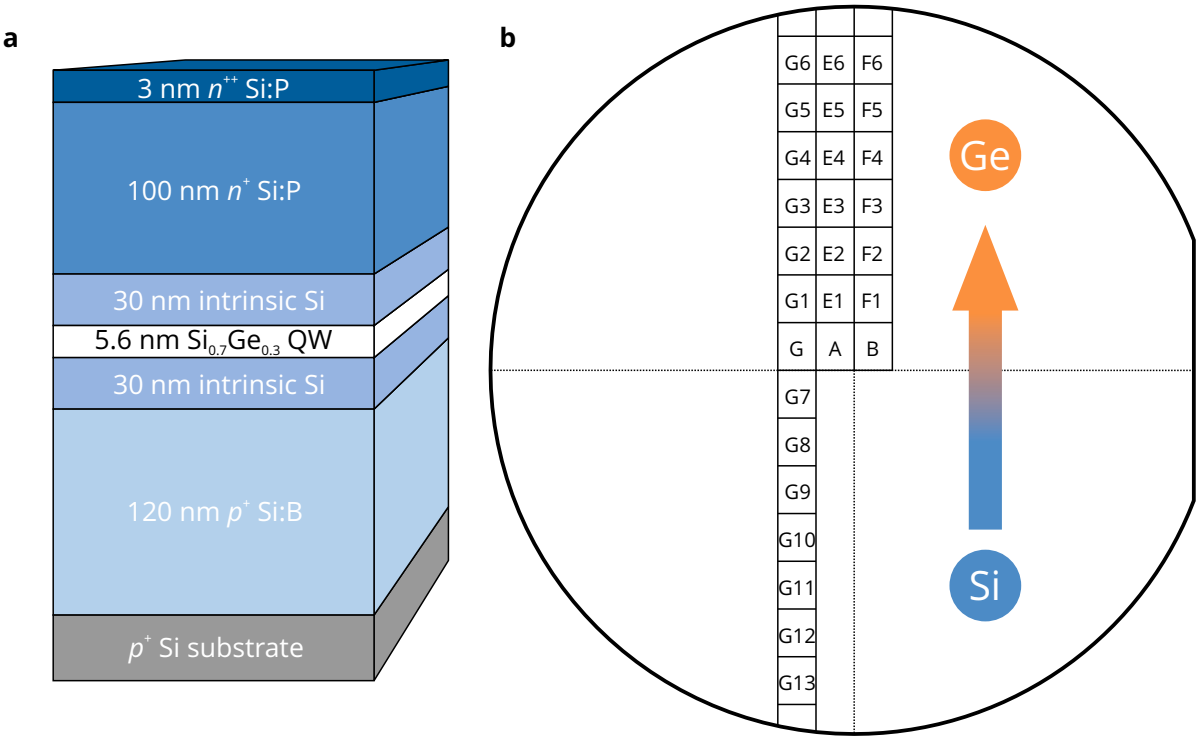

Figure C.1 | a, Schematic of the first layout of *nip* diodes. **b**, Wafer map indicating the SiGe concentration gradient.

The corresponding PL measurements are shown in Fig. C.2. Several features can be noted: The wafer pieces G3–6 and G9–13 exhibit distinctive QW NP and TO luminescence. As expected, for increasing Ge content these features become red-shifted. On the other hand, the pieces B, F1–6, and E1–3 do not exhibit these two distinct luminescence lines but only one very broad red-shifted feature, encircled in the figure. These features lie at energies that are *a priori* not in line with the recombination of electron-hole pairs that were quantum-confined within a 5.6 nm-thick QW. The broad feature is furthermore antisymmetric, exhibiting a low-energy tail. The remaining wafer pieces exhibit a mixture of both the QW luminescence and the broad feature. Note that the NP line of wafer piece A and its associated TO line have a large and unexpected blue shift.

By the fabrication of control samples we excluded that the origin of the broad feature is a consequence of the growth on *p*-type substrates (R1843), *p*-type buffers (R1850), or the capping with *n*-type Si layers (R1858). Particularly for the center of the wafers, all control samples shared the absence of QW luminescence. Furthermore, also a sample where the $Si_{0.7}Ge_{0.3}$ was replaced by 25-monolayer-thick (3.4 nm) $Si_{0.8}Ge_{0.2}$ QW (R1871) exhibited QW luminescence only away from the wafer center.

We fabricated another $Si_{0.7}Ge_{0.3}$ reference sample (R1866), omitting all capping layers of the QW. The surface topography of this sample was characterized by atomic force microscopy (AFM). Two AFM scans for a 10 µm × 10 µm pane and a 1 µm × 1 µm

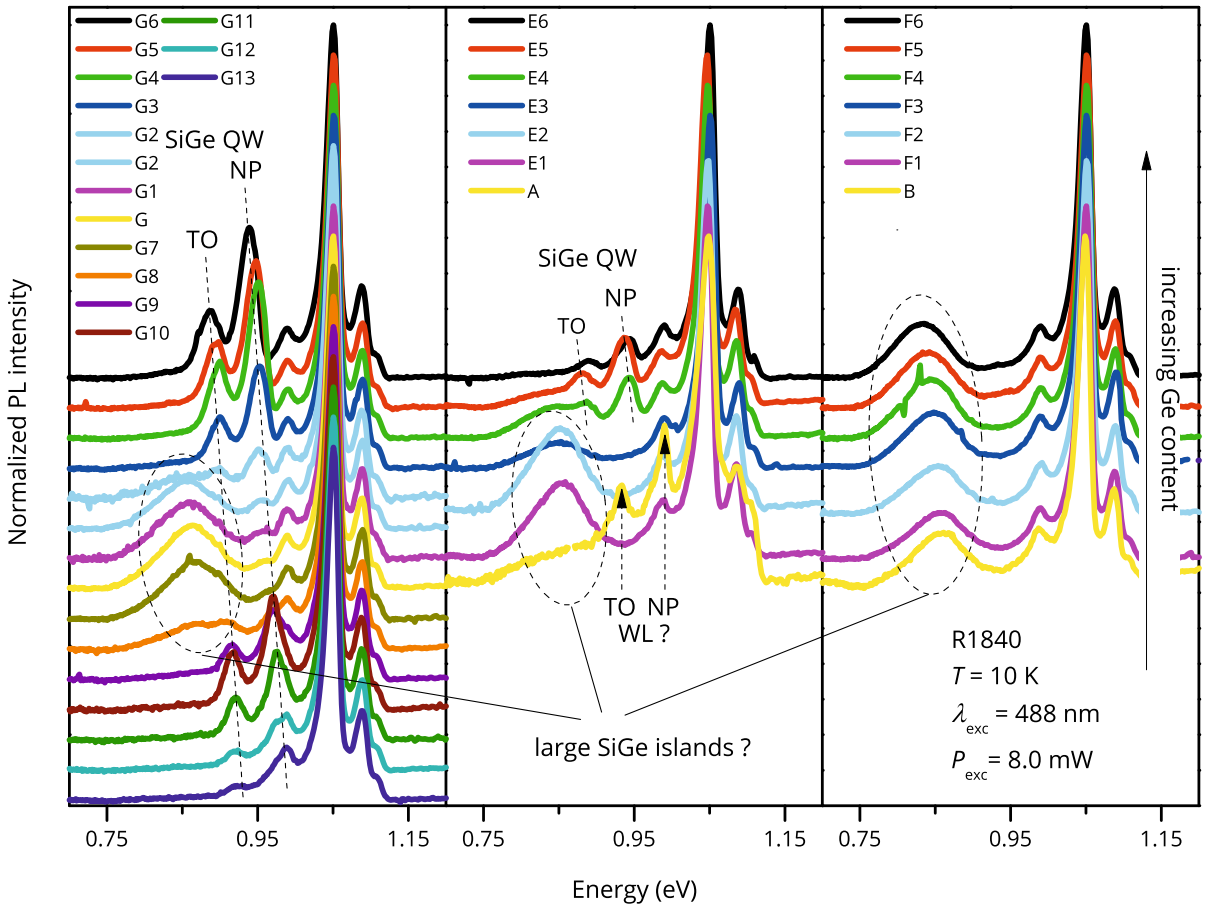

Figure C.2 | PL spectra of different wafer pieces of a sample containing a nominal $Si_{0.7}Ge_{0.3}$ QW. The QW NP and TO luminescence are indicated by the dotted lines, red-shifting with increasing Ge content. Possible PL features of a wetting layer are marked with arrows, whereas possible PL from large SiGe islands is encircled.

close-up are shown in Fig. C.3a and C.3b, respectively. Surprisingly, AFM evidences the formation of well-defined, well-ordered pyramids, oriented parallel to the ⟨100⟩ crystal directions. The height of these pyramids is on the 30 nm to 50 nm scale.

The uncapped sample cannot directly be compared to the overgrown samples. However, particularly if the temperature during the overgrowth is not sufficient to allow interdiffusion of subsequently deposited Si and hereby flattening of the surface, it is reasonable to assume that the pyramidal features are in some extent preserved in overgrown samples. This may very well be the case due to two facts: At substrate temperatures around 600 °C, a distinctively darker glow of the center of 3-inch wafers is clearly visible during the growth in the MBE machine, hinting at a cold spot in the wafer center. Additionally, with the intent to diminish dopant segregation in the *n*-type Si layer, for all QWs discussed up to here the growth protocol contained a rather rapid temperature drop directly after the QW layer, corresponding to a power decrease of the manipulator heater from 53 % to 36 % in 90 s.

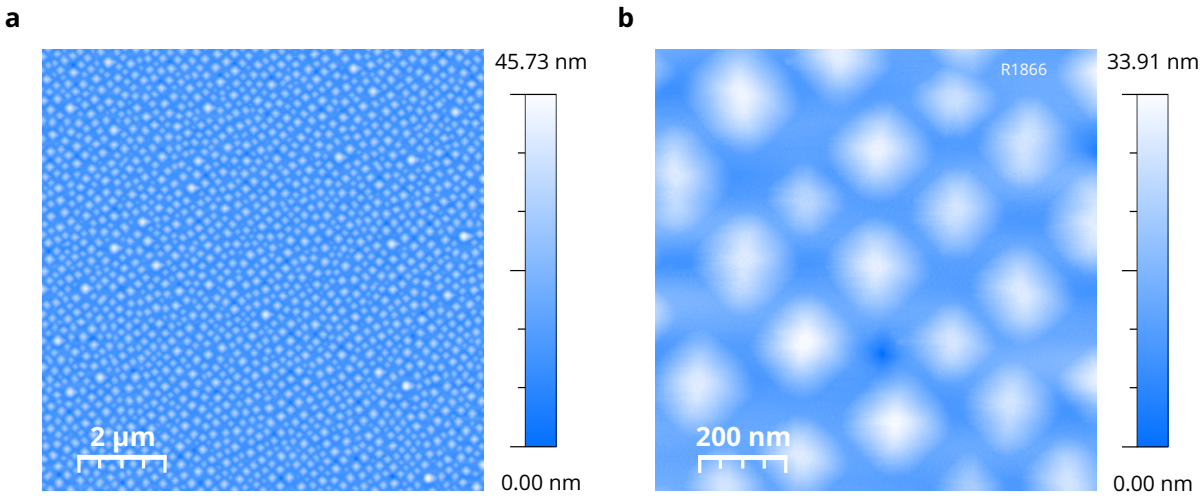

Figure C.3 | AFM topography of 40 monolayers of a $Si_{0.7}Ge_{0.3}$ alloy deposited at a temperature around 615 °C on a Si (001) surface.

Thus, we believe that the broad luminescence is connected to the pyramidal SiGe islands which apparently are still present in nominal QW samples. The red-shift might be caused by their large dimensions and the thus resulting reduction of quantum confinement effects. The asymmetric shape of this feature could be the consequence of a merging NP and TO line. Finally, the blue-shifted luminescence peaks of piece A in Fig. C.2 might arise from a narrow wetting layer. These conjectures suggest that a continuous QW as such is not realized for the present growth conditions and that the observed QW luminescence is rather due to flattened islands acting as 'QW' segments.

The above describe preliminary observations, particularly regarding the occurrence of well-ordered SiGe island arrays, are currently investigated in more detail in the course of the dissertation of T. Zabel, WSI.[238]

In order to obtain a better and more reliable yield of QW-like luminescence for our spin LED experiments, we adapted the growth protocol and introduced a smooth temperature ramp during a slower growth of the intrinsic Si layer that followed the QW. The power decrease of the heater in this new protocol was only 53 % to 36 % in 580 s.

C.1.2 Phosphorus segregation

After the realization of working *nip* LEDs, we turned to the fabrication of *pin* LEDs, i.e. diodes with a *p*-type capping, because these were necessary to integrate the *p*-type GeMn on top for the final spin LEDs. In our first attempt, we basically inverted the structure shown in Fig. C.1a. Figure C.4 shows PL scans for different wafer pieces of this first *pin* sample (R1907). Aside from luminescence peaks of the *n*-type Si substrate, neither QW nor island luminescence could be observed. This effect is possibly related to the P-doped Si buffer layer that was included in the sample structure.

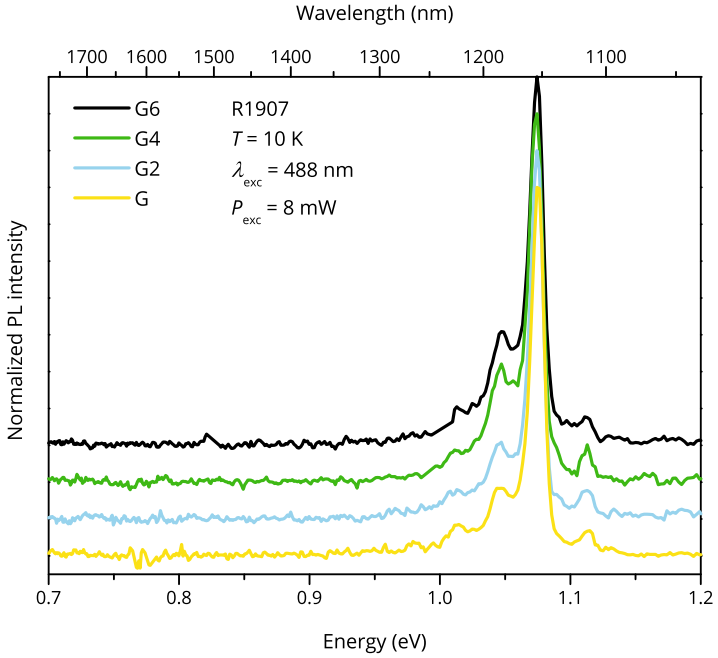

Figure C.4 | PL spectra of different wafer pieces of a sample containing a $Si_{0.7}Ge_{0.3}$ QW embedded in a *pin* diode structure. Only PL signals from the *n*-type Si substrate are visible. The QW PL is quenched, most likely due to P segregation.

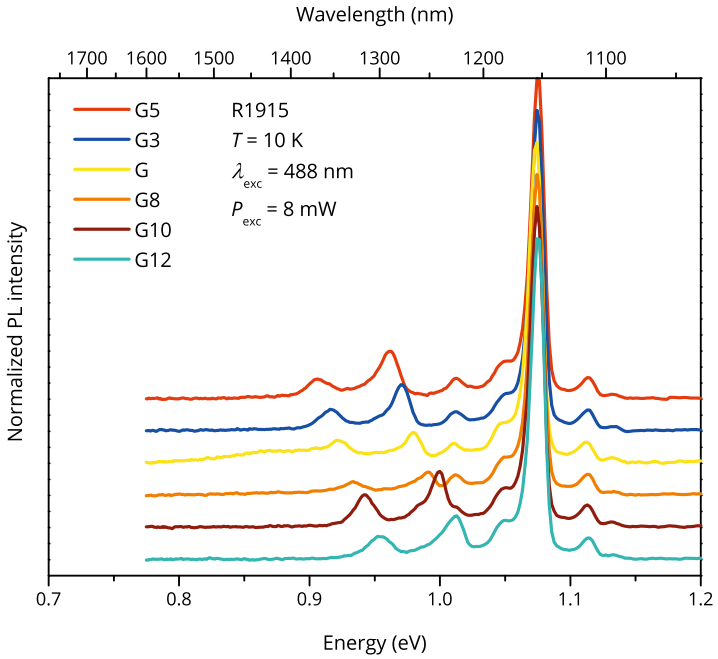

Figure C.5 | PL spectra of different wafer pieces of a sample containing a $Si_{0.7}Ge_{0.3}$ QW embedded in a *pin* diode structure. No *n*-type buffer layer was grown in this structure. QW luminescence is clearly visible.

The buffer was grown at moderate temperatures around 320 °C, but the QW growth made a strong increase of the substrate temperature during the following 30 nm of intrinsic Si necessary. It is known that the segregation of h is promoted by increasing temperatures.[239] We believe that such segregation of P atoms into the QW leads to the quenching of PL, probably due to an enhancement of nonradiative decay mechanisms.

In the final sample layout, which we also used to implement the spin LEDs, the growth of a buffer layer was omitted. The first 30 nm-thick intrinsic Si layer was directly deposited onto the substrate, after the usual deoxidization step. As shown in Fig. C.5, QW PL is present, also in pieces cut from the center of the wafer (R1915).

C.2 Process technology

For device processing we always used 4 mm × 5 mm-shaped wafer pieces as dies.

Sample cleaning In order to remove dust from the chip surface, they were cleaned in an ultrasonic acetone bath, while manually wiping the surface with a Q-tip. The sample pieces were removed from the bath in a constant flush of isopropanol and subsequently blown dry with nitrogen. Immediately before spinning of the photoresist in each photolithography step an additional cleaning step was carried out directly in the spinner:

- spinning at 4000 rpm, 0 s acceleration, 30 s duration
- 10 s rinsing in acetone
- smooth transition to 10 s rinsing in isopropanol
- drying with nitrogen

Photolithography of mesas In lack of a photoresist with larger spinning thickness, the spinning and soft-bake procedure was carried out three times:

- photoresist Microposit S1818, in order to completely cover the samples edges 2–3 drops were used
- spinning at 4000 rpm, 0 s acceleration, 40 s duration
- soft-bake: 2 min at 115 °C on a hotplate, samples lay on a clean microscope slide
- exposure: 40 s in hard-contact mode, 380 W lamp
- development: 30 s in AZ351 developer (1:5 DI water), stopping in DI water, drying with nitrogen
- hard-bake: 3 h at 120 °C in an oven

Mesa etching First attempts to employ reactive ion etching to define the mesa were unsatisfactory. The etch rates were not reproducible and highly sample-dependent. In addition, already the etching on a single die was extremely inhomogeneous. We thus switched to conventional wet-chemical etching:

- etchant: 20 parts of 0.5 % HF and 90 parts of 69 % HNO_3
- etch-time: 10 min

Usually the etching of Ge or GeMn in above given etchant was very fast, whereas the Si material needed distinctively longer etching times. For the sample structure depicted in Fig. 11.1a, 10 min etching resulted in the removal of approx. 600 nm material.

Photolithography of contacts The photolithography mask for the metallized contacts consisted of a guard-ring-like metallized area circumventing the mesa window and including an attached bond pad area. In the same lithography step another bond pad area with a small bar extending into the mesa window was created. This second bond pad would have allowed selective contacting of a circular contact centered on the mesa window that could optionally be defined and which was intended to deposit a transparent contact. This option was not used for the devices presented here.

- sample-cleaning (see above)
- photoresist Microposit S1818, 2–3 drops
- spinning at 4000 rpm, 0 s acceleration, 40 s duration
- soft-bake: 10 min at 90 °C in an oven
- exposure: 10 s in hard-contact mode
- development: 20 s in AZ351 developer (1:5 DI water), stopping in DI water, drying with nitrogen
- soft-bake: 10 min at 90 °C in an oven, primary purpose of the second-soft bake was to fix the samples with photoresist to a microscope slide

Evaporation of contacts The metal contact were fabricated by thermal evaporation in a vacuum chamber:

- adhesion layer: 5 nm Ti
- contact layer: 100 nm Au

Direct ultrasonic ball-bonding to these contacts was possible on a day-to-day as well as sample-to-sample basis. Also, a Cr/Ti/Au layer structure was tried as contact, yet, without any benefit for bonding. The exact Au layer thickness was not crucial to provide working contacts. As the optional transparent contact window was not deposited, both pads were held at the same potential for EL measurements. The highly conducting *n*-type substrate was exploited as the back contact of the finished device. To this end, the processed die was glued onto a conducting chip carrier with silver conductive paint.

Bibliography

[1] G. Binasch, P. Grünberg, F. Saurenbach, and W. Zinn. *Enhanced magnetoresistance in layered magnetic structures with antiferromagnetic interlayer exchange.* **Phys. Rev. B 39,** 4828 (1989).

[2] M. N. Baibich, J. M. Broto, A. Fert, F. N. Van Dau, F. Petroff, P. Etienne, G. Creuzet, A. Friederich, and J. Chazelas. *Giant magnetoresistance of (001)Fe/(001)Cr magnetic superlattices.* **Phys. Rev. Lett. 61,** 2472 (1988).

[3] S. A. Wolf, D. D. Awschalom, R. A. Buhrman, J. M. Daughton, S. von Molnar, M. L. Roukes, A. Y. Chtchelkanova, and D. M. Treger. *Spintronics: A spin-based electronics vision for the future.* **Science 294,** 1488 (2001).

[4] I. Žutić, J. Fabian, and S. Das Sarma. *Spintronics: Fundamentals and applications.* **Rev. Mod. Phys. 76,** 323 (2004).

[5] J. Fabian, A. Matos-Abiague, C. Ertler, P. Stano, and I. Žutić. *Semiconductor spintronics.* **Acata Phys. Slovaca 57,** 565 (2007).

[6] C. Chappert, A. Fert, and F. N. Van Dau. *The emergence of spin electronics in data storage.* **Nature Mater. 6,** 813 (2007).

[7] D. D. Awschalom and M. E. Flatte. *Challenges for semiconductor spintronics.* **Nature Phys. 3,** 153 (2007).

[8] T. Dietl and H. Ohno. *Engineering magnetism in semiconductors.* **Mater. Today 9,** 18 (2006).

[9] H. Ohno, A. Shen, F. Matsukura, A. Oiwa, A. Endo, S. Katsumoto, and Y. Iye. *(Ga,Mn)As: A new diluted magnetic semiconductor based on GaAs.* **Appl. Phys. Lett. 69,** 363 (1996).

[10] Y. D. Park, A. T. Hanbicki, S. C. Erwin, C. S. Hellberg, J. M. Sullivan, J. E. Mattson, T. F. Ambrose, A. Wilson, G. Spanos, and B. T. Jonker. *A group-IV ferromagnetic semiconductor: Mn_xGe_{1-x}.* **Science 295,** 651 (2002).

[11] F. Tsui, L. He, L. Ma, A. Tkachuk, Y. Chu, K. Nakajima, and T. Chikyow. *Novel germanium-based magnetic semiconductors.* **Phys. Rev. Lett. 91,** 177203 (2003).

[12] N. Pinto, L. Morresi, M. Ficcadenti, R. Murri, F. D'Orazio, F. Lucari, L. Boarino, and G. Amato. *Magnetic and electronic transport percolation in epitaxial $Ge_{1-x}Mn_x$ films.* **Phys. Rev. B. 72,** 165203 (2005).

[13] A. P. Li, J. Shen, J. R. Thompson, and H. H. Weitering. *Ferromagnetic percolation in Mn_xGe_{1-x} dilute magnetic semiconductor.* **Appl. Phys. Lett. 86,** 152507 (2005).

[14] A. P. Li, J. F. Wendelken, J. Shen, L. C. Feldman, J. R. Thompson, and H. H. Weitering. *Magnetism in Mn_xGe_{1-x} semiconductors mediated by impurity band carriers.* **Phys. Rev. B. 72,** 195205 (2005).

[15] D. Bougeard, S. Ahlers, A. Trampert, N. Sircar, and G. Abstreiter. *Clustering in a precipitate-free GeMn magnetic semiconductor.* **Phys. Rev. Lett. 97,** 237202 (2006).

[16] M. Jamet, A. Barski, T. Devillers, V. Poydenot, R. Dujardin, P. Bayle-Guillemaud, J. Rothman, E. Bellet-Amalric, A. Marty, J. Cibert, R. Mattana, and S. Tatarenko. *High-Curie-temperature ferromagnetism in self-organized $Ge_{1-x}Mn_x$ nanocolumns.* **Nat. Mater. 5,** 653 (2006).

[17] A. P. Li, C. Zeng, K. van Benthem, M. F. Chisholm, J. Shen, S. V. S. N. Rao, S. K. Dixit, L. C. Feldman, A. G. Petukhov, M. Foygel, and H. H. Weitering. *Dopant segregation and giant magnetoresistance in manganese-doped germanium.* **Phys. Rev. B. 75,** 201201 (2007).

[18] A. Bonanni, A. Navarro-Quezada, T. Li, M. Wegscheider, Z. Matěj, V. Holý, R. T. Lechner, G. Bauer, M. Rovezzi, F. D'Acapito, M. Kiecana, M. Sawicki, and T. Dietl. *Controlled aggregation of magnetic ions in a semiconductor: An experimental demonstration.* **Phys. Rev. Lett. 101,** 135502 (2008).

[19] S. Kuroda, N. Nishizawa, K. Takita, M. Mitome, Y. Bando, K. Osuch, and T. Dietl. *Origin and control of high-temperature ferromagnetism in semiconductors.* **Nature Mater. 6,** 440 (2007).

[20] C. Zeng, Z. Zhang, K. van Benthem, M. F. Chisholm, and H. H. Weitering. *Optimal doping control of magnetic semiconductors via subsurfactant epitaxy.* **Phys. Rev. Lett. 100,** 066101 (2008).

[21] I.-S. Yu, M. Jamet, A. Marty, T. Devillers, A. Barski, C. Beigné, P. Bayle-Guillemaud, and J. Cibert. *Modeling magnetotransport in inhomogeneous (Ge,Mn) films.* **J. Appl. Phys. 109,** 123906 (2011).

[22] O. Riss, A. Gerber, I. Y. Korenblit, A. Suslov, M. Passacantando, and L. Ottaviano. *Magnetization-driven metal-insulator transition in strongly disordered Ge:Mn magnetic semiconductors.* **Phys. Rev. B 79,** 241202 (2009).

[23] S. Ahlers. *Magnetic and electrical properties of epitaxial GeMn.* Dissertation (Walter Schottky Institut, Technische Universität München, 2009).

[24] S. Ahlers, D. Bougeard, N. Sircar, G. Abstreiter, A. Trampert, M. Opel, and R. Gross. *Magnetic and structural properties of Ge_xMn_{1-x} films: Precipitation of intermetallic nanomagnets.* **Phys. Rev. B. 74,** 214411 (2006).

[25] V. Holý, R. T. Lechner, S. Ahlers, L. Horák, T. H. Metzger, A. Navarro-Quezada, A. Trampert, D. Bougeard, and G. Bauer. *Diffuse x-ray scattering from inclusions in ferromagnetic $Ge_{1-x}Mn_x$ layers.* **Phys. Rev. B 78,** 144401 (2008).

[26] S. Ahlers, P. R. Stone, N. Sircar, E. Arenholz, O. D. Dubon, and D. Bougeard. *Comparison of the magnetic properties of GeMn thin films through Mn L-edge x-ray absorption.* **Appl. Phys. Lett. 95,** 151911 (2009).

[27] S. Ahlers. *Ferromagnetische Eigenschaften Mn-dotierter Ge-Nanostrukturen.* Diplomarbeit (Walter Schottky Institut, Technische Universität München, 2004).

[28] E. S. Demidov, Y. A. Danilov, V. V. Podol'skii, V. P. Lesnikov, M. V. Sapozhnikov, and A. I. Suchkov. *Ferromagnetism in epitaxial germanium and silicon layers supersaturated with managanese and iron impurities.* **J. Exp. Theor. Phys. Lett. V83,** 568 (2006).

[29] Y. X. Chen, S. Yan, Y. Fang, Y. F. Tian, S. Q. Xiao, G. L. Liu, Y. H. Liu, and L. M. Mei. *Magnetic and transport properties of homogeneous Mn_xGe_{1-x} ferromagnetic semiconductor with high Mn concentration.* **Appl. Phys. Lett. 90,** 052508 (2007).

[30] S.-K. Kim, J. Y. Son, Y.-H. Shin, M.-H. Jo, S. Park, T. E. Hong, and K. J. Yee. *Structural and magnetic properties of $Ge_{0.7}Mn_{0.3}$ thin films.* **Thin Solid Films 518,** 2665 (2010).

[31] C. G. Zeng, S. C. Erwin, L. C. Feldman, A. P. Li, R. Jin, Y. Song, J. Thompson, and H. H. Weitering. *Epitaxial ferromagnetic Mn_5Ge_3 on Ge(111).* **Appl. Phys. Lett. 83,** 5002 (2003).

[32] C. Zeng, Y. Yao, Q. Niu, and H. H. Weitering. *Linear magnetization dependence of the intrinsic anomalous Hall effect.* **Phys. Rev. Lett. 96,** 037204 (2006).

[33] S. G. Cho, S. Choi, S. C. Hong, Y. Kim, J. B. Ketterson, B. J. Kim, Y. C. Kim, and J. H. Jung. *Ferromagnetism in Mn-doped Ge.* **Phys. Rev. B. 66,** 033303 (2002).

[34] E. Biegger, L. Staheli, M. Fonin, U. Rudiger, and Y. S. Dedkov. *Intrinsic ferromagnetism versus phase segregation in Mn-doped Ge.* **J. Appl. Phys. 101,** 103912 (2007).

[35] L. Ottaviano, M. Passacantando, S. Picozzi, A. Continenza, R. Gunnella, A. Verna, G. Bihlmayer, G. Impellizzeri, and F. Priolo. *Phase separation and dilution in implanted Mn_xGe_{1-x} alloys.* **Appl. Phys. Lett. 88,** 061907 (2006).

[36] L. Ottaviano, M. Passacantando, A. Verna, R. Gunnella, E. Principi, A. D. Cicco, G. Impellizzeri, and F. Priolo. *Direct structural evidences of Mn dilution in Ge.* **J. Appl. Phys. 100,** 063528 (2006).

[37] L. Ottaviano, P. Parisse, M. Passacantando, S. Picozzi, A. Verna, G. Impellizzeri, and F. Priolo. *Nanometer-scale spatial inhomogeneities of the chemical and electronic properties of an ion implanted Mn-Ge alloy.* **Surf. Sci. 600,** 4723 (2006).

[38] L. Ottaviano, M. Passacantando, A. Verna, P. Parisse, S. Picozzi, G. Impellizzeri, and F. Priolo. *Microscopic investigation of the structural and electronic properties of ion implanted Mn-Ge alloys.* **Phys. Status Solidi A 204,** 136 (2007).

[39] M. Passacantando, L. Ottaviano, F. D'Orazio, F. Lucari, M. De Biase, G. Impellizzeri, and F. Priolo. *Growth of ferromagnetic nanoparticles in a diluted magnetic semiconductor obtained by Mn^+ implantation on Ge single crystals.* **Phys. Rev. B. 73,** 195207 (2006).

[40] J. Chen, K. L. Wang, and K. Galatsis. *Electrical field control magnetic phase transition in nanostructured Mn_xGe_{1-x}.* **Appl. Phys. Lett. 90,** 012501 (2007).

[41] S. Zhou, A. Shalimov, K. Potzger, N. M. Jeutter, C. Baehtz, M. Helm, J. Fassbender, and H. Schmidt. *Memory effect of Mn_5Ge_3 nanomagnets embedded inside a Mn-diluted Ge matrix.* **Appl. Phys. Lett. 95,** 192505 (2009).

[42] S. Zhou, D. Bürger, A. Mücklich, C. Baumgart, W. Skorupa, C. Timm, P. Oesterlin, M. Helm, and H. Schmidt. *Hysteresis in the magnetotransport of manganese-doped germanium: Evidence for carrier-mediated ferromagnetism.* **Phys. Rev. B 81,** 165204 (2010).

[43] W. Yin, L. He, M. C. Dolph, J. Lu, R. Hull, and S. A. Wolf. *Modulation of the magnetism in ion implanted Mn_xGe_{1-x} thin films by rapid thermal anneal.* **J. Appl. Phys. 108,** 093919 (2010).

[44] S. Decoster, S. Cottenier, U. Wahl, J. G. Correia, L. M. C. Pereira, C. Lacasta, M. R. D. Silva, and A. Vantomme. *Diluted manganese on the bond-centered site in germanium.* **Appl. Phys. Lett. 97,** 151914 (2010).

[45] Y. D. Park, A. Wilson, A. T. Hanbicki, J. E. Mattson, T. Ambrose, G. Spanos, and B. T. Jonker. *Magnetoresistance of Mn:Ge ferromagnetic nanoclusters in a diluted magnetic semiconductor matrix.* **Appl. Phys. Lett. 78,** 2739 (2001).

[46] N. Pinto, L. Morresi, R. Gunnella, R. Murri, F. D'Orazio, F. Lucari, S. Santucci, P. Picozzi, M. Passacantando, and A. Verna. *Growth and magnetic properties of MnGe films for spintronic application.* **J. Mater. Sci.: Mater. El. 14,** (2003).

[47] F. D'Orazio, F. Lucari, N. Pinto, L. Morresi, and R. Murri. *Toward room temperature ferromagnetism of Ge:Mn systems.* **J. Magn. Magn. Mater. 272-76,** 2006 (2004).

[48] S. Sugahara, K. L. Lee, S. Yada, and M. Tanaka. *Precipitation of amorphous ferromagnetic semiconductor phase in epitaxially grown Mn-doped Ge thin films.* **Jpn. J. Appl. Phys. 44,** L1426 (2005).

[49] H. Li, Y. Wu, Z. Guo, P. Luo, and S. Wang. *Magnetic and electrical transport properties of $Ge_{1-x}Mn_x$ thin films.* **J. Appl. Phys. 100,** 103908 (2006).

[50] J.-P. Ayoub, L. Favre, I. Berbezier, A. Ronda, L. Morresi, and N. Pinto. *Morphological and structural evolutions of diluted $Ge_{1-x}Mn_x$ epitaxial films.* **Appl. Phys. Lett. 91,** 141920 (2007).

[51] L. Morresi, J. Ayoub, N. Pinto, M. Ficcadenti, R. Murri, A. Ronda, I. Berbezier, F. D'Orazio, and F. Lucari. *Structural, magnetic and electronic transport properties of Mn_xGe_{1-x}/Ge(001) films grown by MBE at 350°C.* **Surf. Sci. 601,** 2632 (2007).

[52] C. Bihler, C. Jäger, T. Vallaitis, M. Gjukic, M. Brandt, E. Pippel, J. Woltersdorf, and U. Gosele. *Structural and magnetic properties of Mn_5Ge_3 clusters in a dilute magnetic germanium matrix.* **Appl. Phys. Lett. 88,** 112506 (2006).

[53] P. De Padova, J.-P. Ayoub, I. Berbezier, J.-M. Mariot, A. Taleb-Ibrahimi, M. C. Richter, O. Heckmann, A. M. Testa, D. Fiorani, B. Olivieri, S. Picozzi, and K. Hricovini. *Mn_xGe_{1-x} thin layers studied by TEM, X-ray absorption spectroscopy and SQUID magnetometry.* **Surf. Sci. 601,** 2628 (2007).

[54] P. De Padova, L. Favre, I. Berbezier, B. Olivieri, A. Generosi, B. Paci, V. Rossi Albertini, P. Perfetti, C. Quaresima, J.-M. Mariot, A. Taleb-Ibrahimi, M. Richter, O. Heckmann, F. D'Orazio, F. Lucari, and K. Hricovini. *Structural and magnetic properties of Mn_5Ge_3 nanoclusters dispersed in Mn_xGe_{1-x}/Ge(001)2×1 diluted magnetic semiconductors.* **Surf. Sci. 601,** 4370 (2007).

[55] P. De Padova, J.-P. Ayoub, I. Berbezier, P. Perfetti, C. Quaresima, A. M. Testa, D. Fiorani, B. Olivieri, J.-M. Mariot, A. Taleb-Ibrahimi, M. C. Richter, O. Heckmann, and K. Hricovini. *$Mn_{0.06}Ge_{0.94}$ diluted magnetic semiconductor epitaxially grown on Ge(001): Influence of Mn_5Ge_3 nanoscopic clusters on the electronic and magnetic properties.* **Phys. Rev. B. 77,** 045203 (2008).

[56] Y. Wang, J. Zou, Z. Zhao, X. Han, X. Zhou, and K. L. Wang. *Direct structural evidences of $Mn_{11}Ge_8$ and Mn_5Ge_2 clusters in $Ge_{0.96}Mn_{0.04}$ thin films.* **Appl. Phys. Lett. 92,** 101913 (2008).

[57] L. Zeng, J. X. Cao, E. Helgren, J. Karel, E. Arenholz, L. Ouyang, D. J. Smith, R. Q. Wu, and F. Hellman. *Distinct local electronic structure and magnetism for Mn in amorphous Si and Ge.* **Phys. Rev. B 82,** 165202 (2010).

[58] F. Xiu, Y. Wang, K. Wong, Y. Zhou, X. Kou, J. Zou, and K. L. Wang. *MnGe magnetic nanocolumns and nanowells.* **Nanotechnology 21,** 255602 (2010).

[59] Y. Wang, F. Xiu, J. Zou, K. L. Wang, and A. P. Jacob. *Tadpole shaped $Ge_{0.96}Mn_{0.04}$ magnetic semiconductors grown on Si.* **Appl. Phys. Lett. 96,** 051905 (2010).

[60] Y. Wang, F. Xiu, Y. Wang, H. Xu, D. Li, X. Kou, K. L. Wang, A. P. Jacob, and J. Zou. *Effect of Mn concentration and growth temperature on nanostructures and magnetic properties of $Ge_{1-x}Mn_x$ grown on Si.* **J. Cryst. Growth 312,** 3034 (2010).

[61] A. Jain, M. Jamet, A. Barski, T. Devillers, I.-S. Yu, C. Porret, P. Bayle-Guillemaud, V. Favre-Nicolin, S. Gambarelli, V. Maurel, G. Desfonds, J. F. Jacquot, and S. Tardif. *Structure and magnetism of Ge_3Mn_5 clusters.* **J. Appl. Phys. 109,** 013911 (2011).

[62] T. Devillers, M. Jamet, A. Barski, V. Poydenot, R. Dujardin, P. B. Guillemaud, J. Rothman, E. B. Amalric, J. Cibert, R. Mattana, and S. Tatarenko. *Structural and magnetic properties of GeMn layers; High Curie temperature ferromagnetism induced by self organized GeMn nano-columns.* **Phys. Status Solidi A 204,** 130 (2007).

[63] M. Rovezzi, T. Devillers, E. Arras, F. d'Acapito, A. Barski, M. Jamet, and P. Pochet. *Atomic structure of Mn-rich nanocolumns probed by x-ray absorption spectroscopy.* **Appl. Phys. Lett. 92,** 242510 (2008).

[64] S. Tardif, S. Cherifi, M. Jamet, T. Devillers, A. Barski, D. Schmitz, N. Darowski, P. Thakur, J. C. Cezar, N. B. Brookes, R. Mattana, and J. Cibert. *Exchange bias in GeMn nanocolumns: The role of surface oxidation.* **Appl. Phys. Lett. 97,** 062501 (2010).

[65] I.-S. Yu, M. Jamet, T. Devillers, A. Barski, P. Bayle-Guillemaud, C. Beigné, J. Rothman, V. Baltz, and J. Cibert. *Spinodal decomposition to control magnetotransport in (Ge,Mn) films.* **Phys. Rev. B 82,** 035308 (2010).

[66] J. X. Deng, Y. F. Tian, S. M. He, H. L. Bai, T. S. Xu, S. S. Yan, Y. Y. Dai, Y. X. Chen, G. L. Liu, and L. M. Mei. *Strong anisotropy of magnetization and sign reversion of ordinary Hall coefficient in single crystal $Ge_{1-x}Mn_x$ magnetic semiconductor films.* **Appl. Phys. Lett. 95,** 062513 (2009).

[67] S. Zhou, D. Bürger, M. Helm, and H. Schmidt. *Anomalous Hall resistance in Ge:Mn systems with low Mn concentrations.* **Appl. Phys. Lett. 95,** 172103 (2009).

[68] T. Fukushima, K. Sato, H. Katayama-Yoshida, and P. H. Dederichs. *Spinodal decomposition under layer by layer growth condition and high Curie temperature quasi-one-dimensional nano-structure in dilute magnetic semiconductors.* **Jpn. J. Appl. Phys. 45,** L416 (2006).

[69] S. Zheng, W. Zhu, Y. F. Gao, G. M. Stocks, and Z. Zhang. *Kinetic Monte Carlo simulations of nanocolumn formation in two-component epitaxial growth.* **Appl. Phys. Lett. 96,** 071913 (2010).

[70] A. Continenza, G. Profeta, and S. Picozzi. *Transition metal impurities in Ge: Chemical trends and codoping studied by electronic structure calculations.* **Phys. Rev. B 73,** 035212 (2006).

[71] A. Continenza, G. Profeta, and S. Picozzi. *Transition metal doping and clustering in Ge.* **Appl. Phys. Lett. 89,** 202510 (2006).

[72] T. Dietl, T. Andrearczyk, A. Lipinska, M. Kiecana, M. Tay, and Y. Wu. *Origin of ferromagnetism in $Zn_{1-x}Co_xO$ from magnetization and spin-dependent magnetoresistance measurements.* **Phys. Rev. B. 76,** 155312 (2007).

[73] T. Devillers, M. Jamet, A. Barski, V. Poydenot, P. Bayle-Guillemaud, E. Bellet-Amalric, S. Cherifi, and J. Cibert. *Structure and magnetism of self-organized $Ge_{1-x}Mn_x$ nanocolumns on Ge(001).* **Phys. Rev. B. 76,** 205306 (2007).

[74] S. Tardif, V. Favre-Nicolin, F. Lançon, E. Arras, M. Jamet, A. Barski, C. Porret, P. Bayle-Guillemaud, P. Pochet, T. Devillers, and M. Rovezzi. *Strain and correlation of self-organized $Ge_{1-x}Mn_x$ nanocolumns embedded in Ge (001).* **Phys. Rev. B 82,** 104101 (2010).

[75] K. Binder and P. Fratzl. *Spinodal decomposition.* In *Phase Transformations in Materials,* 409 (Wiley-VCH Verlag GmbH & Co. KGaA, Weinberg, 2005).

[76] P. N. Hai, S. Yada, and M. Tanaka. *Phase decomposition diagram of magnetic alloy semiconductor.* **J. Appl. Phys. 109,** 073919 (2011).

[77] R. Wagner, R. Kampmann, and P. W. Voorhees. *Homogeneous second-phase precipitation.* In *Phase Transformations in Materials,* 309 (Wiley-VCH Verlag GmbH & Co. KGaA, Weinberg, 2005).

[78] D. Bougeard, N. Sircar, S. Ahlers, V. Lang, G. Abstreiter, A. Trampert, J. M. LeBeau, S. Stemmer, D. W. Saxey, and A. Cerezo. *$Ge_{1-x}Mn_x$ clusters: Central structural and magnetic building blocks of nanoscale wire-like self-assembly in a magnetic semiconductor.* **Nano Lett. 9,** 3743 (2009).

[79] T. F. Kelly and M. K. Miller. *Atom probe tomography.* **Rev. Sci. Instrum. 78,** 031101 (2007).

[80] D. N. Seidman. *Three-dimensional atom-probe tomography: Advances and applications.* **Annu. Rev. Mater. Res. 37,** 127 (2007).

[81] S. Stemmer. Private communication (2009).

[82] T. C. Schulthess and W. H. Butler. *Electronic structure and magnetic interactions in Mn doped semiconductors.* **J. Appl. Phys. 89,** 7021 (2001).

[83] A. Stroppa, S. Picozzi, A. Continenza, and A. J. Freeman. *Electronic structure and ferromagnetism of Mn-doped group-IV semiconductors.* **Phys. Rev. B. 68,** 155203 (2003).

[84] J. Zhao, P. Mahadevan, and A. Zunger. *Practical rules for orbital-controlled ferromagnetism of 3d impurities in semiconductors.* **J. Appl. Phys. 98,** 113901 (2005).

[85] H. Weng and J. Dong. *First-principles investigation of transition-metal-doped group-IV semiconductors: R_xY_{1-x} (R=Cr,Mn,Fe; Y=Si,Ge).* **Phys. Rev. B 71,** 035201 (2005).

[86] G. Liu and B.-G. Liu. *Tight-binding study of the magnetic properties of Mn-doped Ge.* **Phys. Rev. B 73,** 045209 (2006).

[87] H. Chen, W. Zhu, E. Kaxiras, and Z. Zhang. *Optimization of Mn doping in group-IV-based dilute magnetic semiconductors by electronic codopants.* **Phys. Rev. B 79,** 235202 (2009).

[88] A. Stroppa, G. Kresse, and A. Continenza. *Revisiting Mn-doped Ge using the Heyd-Scuseria-Ernzerhof hybrid functional.* **Phys. Rev. B 83,** 085201 (2011).

[89] Y. J. Zhao, T. Shishidou, and A. J. Freeman. *Ruderman-Kittel-Kasuya-Yosida-like ferromagnetism in Mn_xGe_{1-x}.* **Phys. Rev. Lett. 90,** 047204 (2003).

[90] J. Kudrnovský, I. Turek, V. Drchal, F. Máca, P. Weinberger, and P. Bruno. *Exchange interactions in III-V and group-IV diluted magnetic semiconductors.* **Phys. Rev. B 69,** 115208 (2004).

[91] X. Huang, A. Makmal, J. R. Chelikowsky, and L. Kronik. *Size-dependent spintronic properties of dilute magnetic semiconductor nanocrystals.* **Phys. Rev. Lett. 94,** 236801 (2005).

[92] K. N. Trohidou, X. Zianni, and J. A. Blackman. *Magnetic behavior of antiferromagnetic and composite ferro-antiferromagnetic nanoparticles.* **Phys. Status Solidi A 189,** 305 (2002).

[93] M. Bañobre-López, C. Vázquez-Vázquez, J. Rivas, and M. A. López-Quintela. *Magnetic properties of chromium (III) oxide nanoparticles.* **Nanotechnology 14,** 318 (2003).

[94] S. Mørup, D. E. Madsen, C. Frandsen, C. R. H. Bahl, and M. F. Hansen. *Experimental and theoretical studies of nanoparticles of antiferromagnetic materials.* **J. Phys.: Condens. Mat. 19,** 213202 (2007).

[95] R. H. Kodama, S. A. Makhlouf, and A. E. Berkowitz. *Finite size effects in antiferromagnetic NiO nanoparticles.* **Phys. Rev. Lett. 79,** 1393 (1997).

[96] D. J. Eaglesham and M. Cerullo. *Dislocation-free Stranski-Krastanow growth of Ge on Si(100).* **Phys. Rev. Lett. 64,** 1943 (1990).

[97] K. Brunner. *Si/Ge nanostructures.* **Rep. Prog. Phys. 65,** 27 (2002).

[98] J. Tersoff, C. Teichert, and M. G. Lagally. *Self-organization in growth of quantum dot superlattices.* **Phys. Rev. Lett. 76,** 1675 (1996).

[99] W. Zhu, H. H. Weitering, E. G. Wang, E. Kaxiras, and Z. Zhang. *Contrasting growth modes of Mn on Ge(100) and Ge(111) surfaces: Subsurface segregation versus intermixing.* **Phys. Rev. Lett. 93,** 126102 (2004).

[100] S. A. Chaparro, J. Drucker, Y. Zhang, D. Chandrasekhar, M. R. McCartney, and D. J. Smith. *Strain-driven alloying in Ge/Si(100) coherent islands.* **Phys. Rev. Lett. 83,** 1199 (1999).

[101] O. G. Schmidt and K. Eberl. *Multiple layers of self-asssembled Ge/Si islands: photoluminescence, strain fields, material interdiffusion, and island formation.* **Phys. Rev. B 61,** 13721 (2000).

[102] P. H. Tan, K. Brunner, D. Bougeard, and G. Abstreiter. *Raman characterization of strain and composition in small-sized self-assembled Si/Ge dots.* **Phys. Rev. B 68,** 125302 (2003).

[103] Q. Xie, A. Madhukar, P. Chen, and N. P. Kobayashi. *Vertically self-organized InAs quantum box islands on GaAs(100).* **Phys. Rev. Lett. 75,** 2542 (1995).

[104] O. Kienzle, F. Ernst, M. Rühle, O. G. Schmidt, and K. Eberl. *Germanium quantum dots embedded in silicon: Quantitative study of self-alignment and coarsening.* **Appl. Phys. Lett. 74,** 269 (1999).

[105] F. J. Morin and J. P. Maita. *Conductivity and Hall effect in the intrinsic range of germanium.* **Phys. Rev. 94,** 1525 (1954).

[106] M. B. Prince. *Drift mobilities in semiconductors. I. Germanium.* **Phys. Rev. 92,** 681 (1953).

[107] N. Sircar, S. Ahlers, C. Majer, G. Abstreiter, and D. Bougeard. *Interplay between electrical transport properties of GeMn thin films and Ge substrates.* **Phys. Rev. B 83,** 125306 (2011).

[108] H. Fritzsche and K. Lark-Horovitz. *Effect of minority impurities on impurity conduction in p-type germanium.* **Phys. Rev. 113,** 999 (1959).

[109] N. Sircar. *Electrical characterisation of germanium and germanium manganese thin films.* Diplomarbeit (Walter Schottky Institut, Technische Universität München, 2006).

[110] C. Majer. *Transportuntersuchungen an Germanium und dünnen Schichten von Germanium-Mangan.* Diplomarbeit (Walter Schottky Institut, Technische Universität München, 2008).

[111] J. Blakemore. *Semiconductor Statistics* (ed. H. Henisch) (Pergamon Press, New York, 1962).

[112] Collaboration: Authors and Editors of the volumes III/22b-41A2a. *Germanium (Ge), shallow donor transition energies.* In *Landolt-Börnstein - Group III Condensed Matter. Numerical Data and Functional Relationships in Science and Technology* (eds. O. Madelung, U. Rössler, and M. Schulz) chap. Germanium (Ge) (SpringerMaterials - The Landolt-Börnstein Database, 2011).

[113] Collaboration: Authors and Editors of the volumes III/22b-41A2a. *Germanium (Ge), shallow single acceptor transition energies.* In *Landolt-Börnstein - Group III Condensed Matter. Numerical Data and Functional Relationships in Science and Technology* (eds. O. Madelung, U. Rössler, and M. Schulz) chap. Germanium (Ge) (SpringerMaterials - The Landolt-Börnstein Database, 2011).

[114] H. H. Woodbury and W. W. Tyler. *Properties of germanium doped with manganese.* **Phys. Rev. 100,** 659 (1955).

[115] C. M. Hurd. *The Hall effect in metals and alloys* (Plenum Press, New York, 1972).

[116] S. A. Solin, T. Thio, D. R. Hines, and J. J. Heremans. *Enhanced room-temperature geometric magnetoresistance in inhomogeneous narrow-gap semiconductors.* **Science 289,** 1530 (2000).

[117] M. M. Parish and P. B. Littlewood. *Classical magnetotransport of inhomogeneous conductors.* **Phys. Rev. B 72,** 094417 (2005).

[118] M. M. Parish and P. B. Littlewood. *Non-saturating magnetoresistance in heavily disordered semiconductors.* **Nature 426,** 162 (2003).

[119] J. Hu, M. M. Parish, and T. F. Rosenbaum. *Nonsaturating magnetoresistance of inhomogeneous conductors: Comparison of experiment and simulation.* **Phys. Rev. B 75,** 214203 (2007).

[120] O. A. Golikova, B. Y. Moizhes, and L. S. Stil'bans. *Hole mobility of germanium as a function of concentration and temperature.* **Soviet Phys. - Solid State 3,** 2259 (1962).

[121] C. Goldberg and R. E. Davis. *Weak-field magnetoresistance of n-type germanium.* **Phys. Rev. 102,** 1254 (1956).

[122] J. W. Gallagher and W. F. Love. *Transverse magnetoresistance in n-type germanium.* **Phys. Rev. 161,** 793 (1967).

[123] R. F. Wick. *Solution of the field problem of the germanium gyrator.* **J. Appl. Phys. 25,** 741 (1954).

[124] H. H. Jensen and H. Smith. *Geometrical effects in measurements of magnetoresistance.* **J. Phys. C: Solid State 5,** 2867 (1972).

[125] R. Tsuchida, J. T. Asubar, Y. Jinbo, and N. Uchitomi. *MBE growth and properties of GeMn thin films on (001) GaAs.* **J. Cryst. Growth 311,** 937 (2009).

[126] S. Picozzi, F. Antoniella, A. Continenza, A. MoscaConte, A. Debernardi, and M. Peressi. *Stabilization of half metallicity in Mn-doped silicon upon Ge alloying.* **Phys. Rev. B 70,** 165205 (2004).

[127] X. Lou, C. Adelmann, S. A. Crooker, E. S. Garlid, J. Zhang, K. S. M. Reddy, S. D. Flexner, C. J. Palmstrøm, and P. A. Crowell. *Electrical detection of spin transport in lateral ferromagnet-semiconductor devices.* **Nature Phys. 3,** 197 (2007).

[128] O. M. J. van 't Erve, A. T. Hanbicki, M. Holub, C. H. Li, C. Awo-Affouda, P. E. Thompson, and B. T. Jonker. *Electrical injection and detection of spin-polarized carriers in silicon in a lateral transport geometry.* **Appl. Phys. Lett. 91,** 212109 (2007).

[129] S. P. Dash, S. Sharma, R. S. Patel, M. P. de Jong, and R. Jansen. *Electrical creation of spin polarization in silicon at room temperature.* **Nature 462,** 491 (2009).

[130] B. T. Jonker, G. Kioseoglou, A. T. Hanbicki, C. H. Li, and P. E. Thompson. *Electrical spin-injection into silicon from a ferromagnetic metal/tunnel barrier contact.* **Nature Phys. 3,** 542 (2007).

[131] G. Kioseoglou, A. T. Hanbicki, R. Goswami, O. M. J. van 't Erve, C. H. Li, G. Spanos, P. E. Thompson, and B. T. Jonker. *Electrical spin injection into Si: A comparison between Fe/Si Schottky and Fe/Al_2O_3 tunnel contacts.* **Appl. Phys. Lett. 94,** 122106 (2009).

[132] C. H. Li, G. Kioseoglou, O. M. J. van 't Erve, P. E. Thompson, and B. T. Jonker. *Electrical spin injection into Si(001) through a SiO_2 tunnel barrier.* **Appl. Phys. Lett. 95,** 172102 (2009).

[133] L. Grenet, M. Jamet, P. Noe, V. Calvo, J.-M. Hartmann, L. E. Nistor, B. Rodmacq, S. Auffret, P. Warin, and Y. Samson. *Spin injection in silicon at zero magnetic field.* **Appl. Phys. Lett. 94,** 032502 (2009).

[134] R. Jansen, B. C. Min, S. P. Dash, S. Sharma, G. Kioseoglou, A. T. Hanbicki, O. M. J. van 't Erve, P. E. Thompson, and B. T. Jonker. *Electrical spin injection into moderately doped silicon enabled by tailored interfaces.* **Phys. Rev. B 82,** 241305 (2010).

[135] C. Hermann, G. Lampel, and V. I. Safarov. *Optical pumping in semiconductors.* **Ann. Phys. Fr. 10,** 1117 (1985).

[136] *Optical Orientation* (eds. F. Meier and B. Zakharchenya) (North-Holland Physics Publishing, Amsterdam, 1984).

[137] *Spin Physics in Semiconductors* (ed. M. I. Dyakonov) (Springer-Verlag, Berlin-Heidelberg, 2008).

[138] A. V. Efanov and M. V. Entin. *Optical orientation and polarized luminescence in silicon.* **Phys. Status Solidi B 118,** 63 (1983).

[139] P. Li and H. Dery. *Theory of spin-dependent phonon-assisted optical transitions in silicon.* **Phys. Rev. Lett. 105,** 037204 (2010).

[140] J. L. Cheng, J. Rioux, J. Fabian, and J. E. Sipe. *Theory of optical spin orientation in silicon.* **Phys. Rev. B 83,** 165211 (2011).

[141] G. Lampel. *Nuclear dynamic polarization by optical electronic saturation and optical pumping in semiconductors.* **Phys. Rev. Lett. 20,** 491 (1968).

[142] L. Tsybeskov, E.-K. Lee, H.-Y. Chang, D. Lockwood, J.-M. Baribeau, X. Wu, and T. Kamins. *Silicon-germanium nanostructures for on-chip optical interconnects.* **Appl. Phys. A - Mater. 95,** 1015 (4 2009).

[143] M. Kroutvar, Y. Ducommun, D. Heiss, M. Bichler, D. Schuh, G. Abstreiter, and J. J. Finley. *Optically programmable electron spin memory using semiconductor quantum dots.* **Nature 432,** 81 (2004).

[144] D. Heiss, S. Schäck, H. Hübl, M. Bichler, G. Abstreiter, J. J. Finley, D. V. Bulaev, and D. Loss. *Observation of extremely slow hole spin relaxation in self-assembled quantum dots.* **Phys. Rev. B 76,** 241306 (2007).

[145] D. J. Monsma, J. C. Lodder, T. J. A. Popma, and B. Dieny. *Perpendicular hot electron spin-valve effect in a new magnetic field sensor: The spin-valve transistor.* **Phys. Rev. Lett. 74,** 5260 (1995).

[146] D. J. Monsma, R. Vlutters, and J. C. Lodder. *Room temperature-operating spin-valve transistors formed by vacuum bonding.* **Science 281,** 407 (1998).

[147] I. Appelbaum, B. Huang, and D. J. Monsma. *Electronic measurement and control of spin transport in silicon.* **Nature 447,** 295 (2007).

[148] B.-C. Min, K. Motohashi, C. Lodder, and R. Jansen. *Tunable spin-tunnel contacts to silicon using low-work-function ferromagnets.* **Nature Mater. 5,** 817 (2006).

[149] B. Huang, D. J. Monsma, and I. Appelbaum. *Coherent spin transport through a 350 micron thick silicon wafer.* **Phys. Rev. Lett. 99,** 177209 (2007).

[150] B. Huang, H.-J. Jang, and I. Appelbaum. *Geometric dephasing-limited Hanle effect in long-distance lateral silicon spin transport devices.* **Appl. Phys. Lett. 93,** 162508 (2008).

[151] H.-J. Jang, J. Xu, J. Li, B. Huang, and I. Appelbaum. *Non-ohmic spin transport in n-type doped silicon.* **Phys. Rev. B 78,** 165329 (2008).

[152] Y. Ando, K. Hamaya, K. Kasahara, Y. Kishi, K. Ueda, K. Sawano, T. Sadoh, and M. Miyao. *Electrical injection and detection of spin-polarized electrons in silicon through an Fe_3Si/Si Schottky tunnel barrier.* **Appl. Phys. Lett. 94,** 182105 (2009).

[153] H.-J. Jang and I. Appelbaum. *Spin polarized electron transport near the Si/SiO_2 interface.* **Phys. Rev. Lett. 103,** 117202 (2009).

[154] T. Sasaki, T. Oikawa, T. Suzuki, M. Shiraishi, Y. Suzuki, and K. Noguchi. *Temperature dependence of spin diffusion length in silicon by Hanle-type spin precession.* **Appl. Phys. Lett. 96,** 122101 (2010).

[155] R. Jansen, B.-C. Min, and S. P. Dash. *Oscillatory spin-polarized tunnelling from silicon quantum wells controlled by electric field.* **Nature Mater. 9,** 133 (2010).

[156] R. Fiederling, M. Keim, G. Reuscher, W. Ossau, G. Schmidt, A. Waag, and L. W. Molenkamp. *Injection and detection of a spin-polarized current in a light-emitting diode.* **Nature 402,** 787 (1999).

[157] Y. Ohno, R. Terauchi, T. Adachi, F. Matsukura, and H. Ohno. *Spin relaxation in GaAs(110) quantum wells.* **Phys. Rev. Lett. 83,** 4196 (1999).

[158] A. T. Hanbicki, B. T. Jonker, G. Itskos, G. Kioseoglou, and A. Petrou. *Efficient electrical spin injection from a magnetic metal/tunnel barrier contact into a semiconductor.* **Appl. Phys. Lett. 80,** 1240 (2002).

[159] B. T. Jonker, A. T. Hanbicki, Y. D. Park, G. Itskos, M. Furis, G. Kioseoglou, A. Petrou, and X. Wei. *Quantifying electrical spin injection: Component-resolved electroluminescence from spin-polarized light-emitting diodes.* **Appl. Phys. Lett. 79,** 3098 (2001).

[160] B. T. Jonker, Y. D. Park, B. R. Bennett, H. D. Cheong, G. Kioseoglou, and A. Petrou. *Robust electrical spin injection into a semiconductor heterostructure.* **Phys. Rev. B 62,** 8180 (2000).

[161] M. I. Dyakonov and V. I. Perel. *Theory of optical spin orientation.of electrons and nuclei in semiconductors.* In *Optical Orientation,* 11 (eds. F. Meier and B. Zakharchenya) (North-Holland Physics Publishing, Amsterdam, 1984).

[162] P. Y. Yu and M. Cardona. *Fundamentals of Semiconductors. Physics and Material Properties* (Springer-Verlag, Berlin-Heidelberg-New York, 2005).

[163] R. Corkish and M. A. Green. *Band edge optical absorption in intrinsic silicon: Assessment of the indirect transition and disorder models.* **J. Appl. Phys. 73,** 3988 (1993).

[164] G. Davies. *The optical properties of luminescence centres in silicon.* **Phys. Rep. 176,** 83 (1989).

[165] R. B. Hammond and R. N. Silver. *Temperature dependence of the exciton lifetime in high-purity silicon.* **Appl. Phys. Lett. 36,** 68 (1980).

[166] J. L. Cheng, M. W. Wu, and J. Fabian. *Theory of the spin relaxation of conduction electrons in silicon.* **Phys. Rev. Lett. 104,** 016601 (2010).

[167] T. Trupke, M. A. Green, P. Wurfel, P. P. Altermatt, A. Wang, J. Zhao, and R. Corkish. *Temperature dependence of the radiative recombination coefficient of intrinsic crystalline silicon.* **J. Appl. Phys. 94,** 4930 (2003).

[168] C. B. Simmons, J. R. Prance, B. J. Van Bael, T. S. Koh, Z. Shi, D. E. Savage, M. G. Lagally, R. Joynt, M. Friesen, S. N. Coppersmith, and M. A. Eriksson. *Tunable spin loading and T_1 of a silicon spin qubit measured by single-shot readout.* **Phys. Rev. Lett. 106,** 156804 (2011).

[169] M. I. Dyakonov and V. I. Perel. *Circular polarization of recombination radiation of semiconductors in weak magnetic field.* **Soviet Phys. - Solid State 14,** 1245 (1972).

[170] R. I. Dzhioev, B. P. Zakharchenya, and V. G. Fleisher. *Investigation of semiconductor paramagnetism using luminescence polarization in a weak magnetic field.* **J. Exp. Theor. Phys. Lett. 17,** 174 (1973).

[171] I. Saïdi, S. B. Radhia, and K. Boujdaria. *Band parameters of GaAs, InAs, InP, and InSb in the 40-band $k \cdot p$ model.* **J. Appl. Phys. 107,** 043701 (2010).

[172] G. Feher. *Electron spin resonance experiments on donors in silicon. I. Electronic structure of donors by the electron nuclear double resonance technique.* **Phys. Rev. 114,** 1219 (1959).

[173] K. Suzuki, M. Okazaki, and H. Hasegawa. *Effective-mass theoretical approach to optical and microwave phenomena in semiconductors I. Zeeman effect of acceptors in Si and Ge.* **J. Phys. Soc. Jpn. 19,** 930 (1964).

[174] G. L. Bir, E. I. Butekov, and G. E. Pikus. *Spin and combined resonance on acceptor centres in Ge and Si type crystals–I: Paramagnetic resonance in strained and unstrained crystals.* **J. Phys. Chem. Solids 24,** 1467 (1963).

[175] H. Neubrand. *ESR from boron in silicon at zero and small external stress I. Line positions and line structure.* **Phys. Status Solidi B 86,** 269 (1978).

[176] J. M. Luttinger. *Quantum theory of cyclotron resonance in semiconductors: General theory.* **Phys. Rev. 102,** 1030 (1956).

[177] J. J. Stickler, H. J. Zeiger, and G. S. Heller. *Quantum effects in Ge and Si. I.* **Phys. Rev. 127,** 1077 (1962).

[178] P. J. Dean, J. R. Haynes, and W. F. Flood. *New radiative recombination processes involving neutral donors and acceptors in silicon and germanium.* **Phys. Rev. 161,** 711 (1967).

[179] M. A. Vouk and E. C. Lightowlers. *Two-phonon assisted free exciton recombination radiation from intrinsic silicon.* **J. Phys. C: Solid State 10,** 3689 (1977).

[180] L. V. Keldysh. *The electron-hole liquid in semiconductors.* **Contemp. Phys. 27,** 395 (1986).

[181] R. B. Hammond, T. C. McGill, and J. W. Mayer. *Temperature dependence of the electron-hole-liquid luminescence in Si.* **Phys. Rev. B 13,** 3566 (1976).

[182] W. P. Dumke. *Comparison of band-gap shrinkage observed in luminescence from n^+-Si with that from transport and optical absorption measurements.* **Appl. Phys. Lett. 42,** 196 (1983).

[183] W. P. Dumke. *Band-gap narrowing from luminescence in p-type Si.* **J. Appl. Phys. 54,** 3200 (1983).

[184] S. C. Jain and D. J. Roulston. *A simple expression for band gap narrowing (BGN) in heavily doped Si, Ge, GaAs and Ge_xSi_{1-x} strained layers.* **Solid-State Electron. 34,** 453 (1991).

[185] J. Wagner and L. Viña. *Radiative recombination in heavily doped p-type germanium.* **Phys. Rev. B 30,** 7030 (1984).

[186] P. E. Schmid, M. L. W. Thewalt, and W. P. Dumke. *Photoluminescence in heavily doped Si:B and Si:As.* **Solid State Commun. 38,** 1091 (1981).

[187] R. R. Parsons. *On the origin of photoluminescence in heavily-doped silicon.* **Solid State Commun. 29,** 763 (1979).

[188] P. Vashishta, S. G. Das, and K. S. Singwi. *Thermodynamics of the electron-hole liquid in Ge, Si, and GaAs.* **Phys. Rev. Lett. 33,** 911 (1974).

[189] G. L. Bir, A. G. Aronov, and G. E. Pikus. *Spin relaxation of electrons due to scattering by holes.* **J. Exp. Theor. Phys. 69,** 1382 (1975).

[190] D. Bougeard. *Spektroskopische Charakterisierung von Germanium-Quantenpunkten in Silizium.* Dissertation (Walter Schottky Institut, Technische Universität München, 2005).

[191] G. Abstreiter, P. Schittenhelm, C. Engel, E. Silveira, A. Zrenner, D. Meertens, and W. Jäger. *Growth and characterization of self-assembled Ge-rich islands on Si.* **Semicond. Sci. Technol. 11,** 1521 (1996).

[192] S. Fukatsu, H. Sunamura, Y. Shiraki, and S. Komiyama. *Phononless radiative recombination of indirect excitons in a Si/Ge type-II quantum dot.* **Appl. Phys. Lett. 71,** 258 (1997).

[193] S. Fukatsu, H. Sunamura, Y. Shiraki, and S. Komiyama. *Suppression of phonon replica in the radiative recombination of an MBE-grown type-II Ge/Si quantum dot.* **Thin Solid Films 321,** 65 (1998).

[194] M. W. Dashiell, U. Denker, and O. G. Schmidt. *Photoluminescence investigation of phononless radiative recombination and thermal-stability of germanium hut clusters on silicon(001).* **Appl. Phys. Lett. 79,** 2261 (2001).

[195] L. Tsybeskov and D. J. Lockwood. *Silicon-germanium nanostructures for light emitters and on-chip optical interconnects.* **PIEEE 97,** 1284 (2009).

[196] B. V. Kamenev, L. Tsybeskov, J.-M. Baribeau, and D. J. Lockwood. *Coexistence of fast and slow luminescence in three-dimensional $Si/Si_{1-x}Ge_x$ nanostructures.* **Phys. Rev. B 72,** 193306 (2005).

[197] B. V. Kamenev, E.-K. Lee, H.-Y. Chang, H. Han, H. Grebel, L. Tsybeskov, and T. I. Kamins. *Excitation-dependent photoluminescence in Ge/Si Stranski-Krastanov nanostructures.* **Appl. Phys. Lett. 89,** 153106 (2006).

[198] L. Nataraj, N. Sustersic, M. Coppinger, L. F. Gerlein, J. Kolodzey, and S. G. Cloutier. *Structural and optoelectronic properties of germanium-rich islands grown on silicon using molecular beam epitaxy.* **Appl. Phys. Lett. 96,** 121911 (2010).

[199] B. Julsgaard, P. Balling, J. L. Hansen, A. Svane, and A. N. Larsen. *Luminescence decay dynamics of self-assembled germanium islands in silicon.* **Appl. Phys. Lett. 98,** 093101 (2011).

[200] E.-K. Lee, D. J. Lockwood, J.-M. Baribeau, A. M. Bratkovsky, T. I. Kamins, and L. Tsybeskov. *Photoluminescence dynamics and Auger fountain in three-dimensional Si/SiGe multilayer nanostructures.* **Phys. Rev. B 79,** 233307 (2009).

[201] W. M. Chen, I. A. Buyanova, A. Henry, W.-X. Ni, G. V. Hansson, and B. Monemar. *Nonradiative defects in Si and SiGe/Si heterostructures grown by molecular beam epitaxy.* **Appl. Phys. Lett. 68,** 1256 (1996).

[202] I. A. Buyanova, W. M. Chen, G. Pozina, B. Monemar, W.-X. Ni, and G. V. Hansson. *Mechanism for thermal quenching of luminescence in SiGe/Si structures grown by molecular beam epitaxy: Role of nonradiative defects.* **Appl. Phys. Lett. 71,** 3676 (1997).

[203] M. L. W. Thewalt, D. A. Harrison, C. F. Reinhart, J. A. Wolk, and H. Lafontaine. *Type II band alignment in $Si_{1-x}Ge_x/Si(001)$ quantum wells: The ubiquitous type I luminescence results from band bending.* **Phys. Rev. Lett. 79,** 269 (1997).

[204] M. Larsson, A. Elfving, W.-X. Ni, G. V. Hansson, and P. O. Holtz. *Growth-temperature-dependent band alignment in Si/Ge quantum dots from photoluminescence spectroscopy.* **Phys. Rev. B 73,** 195319 (2006).

[205] B. Adnane, K. F. Karlsson, G. V. Hansson, P. O. Holtz, and W.-X. Ni. *Spatially direct and indirect transitions of self-assembled GeSi/Si quantum dots studied by photoluminescence excitation spectroscopy.* **Appl. Phys. Lett. 96,** 181107 (2010).

[206] A. V. Khaetskii and Y. V. Nazarov. *Spin relaxation in semiconductor quantum dots.* **Phys. Rev. B 61,** 12639 (2000).

[207] A. V. Khaetskii. *Spin relaxation in semiconductor mesoscopic systems.* **Physica E 10,** 27 (2001).

[208] L. M. Woods, T. L. Reinecke, and Y. Lyanda-Geller. *Spin relaxation in quantum dots.* **Phys. Rev. B 66,** 161318 (2002).

[209] D. V. Bulaev and D. Loss. *Spin relaxation and decoherence of holes in quantum dots.* **Phys. Rev. Lett. 95,** 076805 (2005).

[210] A. V. Khaetskii and Y. V. Nazarov. *Spin-flip transitions between Zeeman sublevels in semiconductor quantum dots.* **Phys. Rev. B 64,** 125316 (2001).

[211] E. Y. Sherman and D. J. Lockwood. *Spin relaxation in quantum dots with random spin-orbit coupling.* **Phys. Rev. B 72,** 125340 (2005).

[212] A. F. Zinovieva, A. V. Dvurechenskii, N. P. Stepina, A. I. Nikiforov, A. S. Lyubin, and L. V. Kulik. *Direct measurements of spin relaxation times of electrons in tunnel-coupled Ge/Si quantum dot arrays.* **Phys. Rev. B 81,** 113303 (2010).

[213] F. Lipps, F. Pezzoli, M. Stoffel, C. Deneke, J. Thomas, A. Rastelli, V. Kataev, O. G. Schmidt, and B. Büchner. *Electron spin resonance study of Si/SiGe quantum dots.* **Phys. Rev. B 81,** 125312 (2010).

[214] A. F. Zinovieva, A. V. Nenashev, and A. V. Dvurechenskii. *Spin relaxation mechanism of hopping transport in a 2D asymmetric quantum dot array.* **J. Exp. Theor. Phys. 105,** 388 (2 2007).

[215] C. Lü, J. L. Cheng, and M. W. Wu. *Hole spin relaxation in semiconductor quantum dots.* **Phys. Rev. B 71,** 075308 (2005).

[216] A. F. Zinovieva, A. V. Nenashev, and A. V. Dvurechenskii. *Hole spin relaxation in Ge quantum dots.* **J. Exp. Theor. Phys. Lett. 82,** 302 (2005).

[217] A. F. Zinovieva, A. V. Nenashev, and A. V. Dvurechenskii. *Hole spin relaxation during the tunneling between coupled quantum dots.* **Phys. Rev. B 71,** 033310 (2005).

[218] C. Hautmann, B. Surrer, and M. Betz. *Ultrafast optical orientation and coherent Larmor precession of electron and hole spins in bulk germanium.* **Phys. Rev. B 83,** 161203 (2011).

[219] J. C. Hensel and K. Suzuki. *Anisotropy of the g factor of the free hole in Ge and conduction-band spin-orbit splitting.* **Phys. Rev. Lett. 22,** 838 (1969).

[220] N. Fraj, I. Saidi, S. B. Radhia, and K. Boujdaria. *Band structures of AlAs, GaP, and SiGe alloys: A 30 $\boldsymbol{k} \cdot \boldsymbol{p}$ model.* **J. Appl. Phys. 102,** 053703 (2007).

[221] A. V. Nenashev, A. V. Dvurechenskii, and A. F. Zinovieva. *Wave functions and g factor of holes in Ge/Si quantum dots.* **Phys. Rev. B 67,** 205301 (2003).

[222] G. Katsaros, P. Spathis, M. Stoffel, F. Fournel, M. Mongillo, V. Bouchiat, F. Lefloch, A. Rastelli, O. G. Schmidt, and S. De Franceschi. *Hybrid superconductor-semiconductor devices made from self-assembled SiGe nanocrystals on silicon.* **Nature Nanotechnol. 5,** 458 (2010).

[223] F. Nastos, J. Rioux, M. Strimas-Mackey, B. S. Mendoza, and J. E. Sipe. *Full band structure LDA and $k \cdot p$ calculations of optical spin-injection.* **Phys. Rev. B 76,** 205113 (2007).

[224] G. G. Macfarlane, T. P. McLean, J. E. Quarrington, and V. Roberts. *Fine structure in the absorption-edge spectrum of Ge.* **Phys. Rev. 108,** 1377 (1957).

[225] M. D. Sturge. *Optical absorption of gallium arsenide between 0.6 and 2.75 eV.* **Phys. Rev. 127,** 768 (1962).

[226] M. W. Wu, J. H. Jiang, and M. Q. Weng. *Spin dynamics in semiconductors.* **Phys. Rep. 493,** 61 (2010).

[227] G. Schmidt, D. Ferrand, L. W. Molenkamp, A. T. Filip, and B. J. van Wees. *Fundamental obstacle for electrical spin injection from a ferromagnetic metal into a diffusive semiconductor.* **Phys. Rev. B. 62,** R4790 (2000).

[228] E. I. Rashba. *Theory of electrical spin injection: Tunnel contacts as a solution of the conductivity mismatch problem.* **Phys. Rev. B. 62,** R16267 (2000).

[229] U. Menczigar. *Optische Eigenschaften von Si/SiGe Heterostrukturen und Si_mGe_n Übergittern.* Dissertation (Walter Schottky Institut, Technische Universität München, 1993).

[230] J. Brunner. *Herstellung und optische Charakterisierung von Si/SiGe Heterostrukturen.* Dissertation (Walter Schottky Institut, Technische Universität München, 1995).

[231] M. Gail. *Optische Interbandübergänge in Si/Ge Heterostrukturen.* Dissertation (Walter Schottky Institut, Technische Universität München, 1996).

[232] T. F. Kelly, T. T. Gribb, J. D. Olson, R. L. Martens, J. D. Shepard, S. A. Wiener, T. C. Kunicki, R. M. Ulfig, D. R. Lenz, E. M. Strennen, E. Oltman, J. H. Bunton, and D. R. Strait. *First data from a commercial local electrode atom probe (LEAP).* **Microsc. Microanal. 10,** 373 (2004).

[233] L. C. Feldman, J. W. Mayer, and S. T. Picraux. *Materials Analysis by Ion Channeling: Submicron Crystallography* (Academic Press, New York, 1982).

[234] K. M. Yu, W. Walukiewicz, L. Y. Chan, R. Leon, E. E. Haller, J. M. Jaklevic, and C. M. Hanson. *Effects of rapid quenching on the impurity site location in Zn-diffused InP.* **J. Appl. Phys. 74,** 86 (1993).

[235] K. M. Yu. Private communication (2011).

[236] A. T. Collins and T. Jeffries. *Circuits to eliminate the voltage spikes caused by cosmic rays in germanium PIN-diode infrared detectors.* **J. Phys. E: Sci. Instrum. 15,** 712 (1982).

[237] J. Sailer. *Materials and devices for quantum information processing in Si/SiGe.* Dissertation (Walter Schottky Institut, Technische Universität München, 2010).

[238] T. Zabel. *Manuscript draft.* Unpublished (2011).

[239] J. F. Nützel and G. Abstreiter. *Segregation and diffusion on semiconductor surfaces.* **Phys. Rev. B 53,** 13551 (1996).

List of publications

[1] N. Sircar and D. Bougeard. *Manuscript draft on spin-dependent transition probabilities of phonon-assisted and phononless transitions in bulk Si and Ge/Si quantum dots.* In preparation (2011).

[2] N. Sircar, S. Ahlers, C. Majer, G. Abstreiter, and D. Bougeard. *Interplay between electrical transport properties of GeMn thin films and Ge substrates.* **Phys. Rev. B 83,** 125306 (2011).

[3] D. Bougeard, N. Sircar, S. Ahlers, V. Lang, G. Abstreiter, A. Trampert, J. M. LeBeau, S. Stemmer, D. W. Saxey, and A. Cerezo. *$Ge_{1-x}Mn_x$ clusters: Central structural and magnetic building blocks of nanoscale wire-like self-assembly in a magnetic semiconductor.* **Nano Lett. 9,** 3743 (2009).

[4] S. Ahlers, P. R. Stone, N. Sircar, E. Arenholz, O. D. Dubon, and D. Bougeard. *Comparison of the magnetic properties of GeMn thin films through Mn L-edge x-ray absorption.* **Appl. Phys. Lett. 95,** 151911 (2009).

[5] S. Ahlers, D. Bougeard, N. Sircar, G. Abstreiter, A. Trampert, M. Opel, and R. Gross. *Magnetic and structural properties of Ge_xMn_{1-x} films: Precipitation of intermetallic nanomagnets.* **Phys. Rev. B. 74,** 214411 (2006).

[6] D. Bougeard, S. Ahlers, A. Trampert, N. Sircar, and G. Abstreiter. *Clustering in a precipitate-free GeMn magnetic semiconductor.* **Phys. Rev. Lett. 97,** 237202 (2006).

— When you can't see the angles no more, you're in trouble, maybe. You're in trouble. —

Carlito Brigante

Danksagungen

Die zurückliegende Zeit, die ich zur Anfertigung dieser Dissertation am WSI zugebracht habe, wird mir wohl immer in unvergesslicher und guter Erinnerung bleiben. Dies hat nicht zuletzt damit zu tun, dass ich hierbei eine Reihe von Leuten kennenlernen durfte, deren freundschaftliche, oft tatkräftige, manchmal nur moralische, auf jeden Fall aber immer kollegiale Unterstützung ich erfahren habe und denen ich an dieser Stelle danken möchte:

Gerhard Abstreiter gilt mein Dank für die Überlassung des Dissertationthemas und die exzellenten Arbeitsbedingungen, die er hier im WSI nicht nur für seine Arbeitsgruppe durch seinen unermüdlichen Einsatz schafft. Ihm ist es auch zu verdanken, dass ich mich beim Studium der Physik an der TUM von Anfang an gut aufgehoben fühlte, da ich meine ersten Vorlesungen zur Mechanik bei ihm hören durfte und seine Art, komplexe Zusammenhänge mit bayerischer Gelassenheit zu erklären, immer geschätzt habe.

Ganz besonders danke ich **Dominique Bougeard**, über den ich nur uneingeschränkt Positives sagen kann. Auf seinen Rat konnte ich jederzeit zählen und habe in ergiebigen Diskussionen immer wieder von seiner klaren und direkten Art profitiert, auch davon, Dinge eher kritisch zu hinterfragen. Zudem war es immer erfrischend, ganz besonders während meiner Zeit in Santa Barbara, in ihm einen Betreuer gehabt zu haben mit dem ich auch mal über andere Themen als Physik reden konnte, vorzugsweise über europäischen Spitzenfußball.

Die Zusammenarbeit mit meinem ehemaligen Mitstreiter **Stefan Ahlers** war immer erfreulich, und in vielerlei Hinsicht sehr wertvoll für diese Arbeit. Ich verdanke ihm unter anderem, in die hohe Kunst der eigentlichen Laborarbeit inklusive der effizienten Auswertung und effektvollen Präsentation („Style-God Ahlers") von Messdaten eingeführt worden zu sein.

Beim reibungslosen Betrieb im Optiklabor und an der MBE war der fast beiläufige Austausch über Fortschritte aber auch über manches Problem mit meinem Mitbenutzer **Thomas Zabel** immer hilfreich. Vermissen werde ich besonders die vielen Weißwurstfrühstücke, Leberkasessen und Fußballspiele, die er initiiert hat. Ihm wünsche ich, am Ende seiner eigenen Dissertation mal „Es ward Licht!" sagen zu können.

Ganz besonders danken möchte ich den beiden langjährigen Mitinsassen von S104, die das Büroleben abwechslungsreich und lustig gestaltet haben: Mit **Hubert Riedel** hatte ich das Glück einen äußerst versierten und zuvorkommenden Techniker im wahrsten Sinne des Wortes an meiner Seite zu haben. Als Sitznachbar diente ihm mein Schreibtisch zwar ab und zu als erweiterte Ablagefläche, diese räumliche Nähe bot jedoch den unschätzbaren Vorteil, selten länger als fünf Minuten auf seine Hilfe zu warten müssen.

Mein Gegenüber **Jürgen Sailer** hatte trotz oder vielleicht gerade wegen des von vier Monitoren behinderten Sichtkontakts immer ein offenes Ohr für einen wissenschaftlichen oder nicht-wissenschaftlichen Plausch. Mit seiner schwäbischen Gründlichkeit war er stets engagiert, meinen etwaigen Problemen, insbesondere beim Transport, auf den Grund zu gehen. Mittlerweile muss ich sogar zugeben, dass die Beschallung mit seiner elektronischen Musik garnicht so übel war.

Bleiben noch die letzten beiden Mitglieder der aussterbenden SiGe-Gruppe am WSI zu nennen, denen ich noch viel Erfolg mit ihren Quantenpunkten wünsche: **Andreas Wild** möchte ich für seine wirklich gut fundierten physikalischen Kenntnisse loben, die mir in dem einen oder anderen Gespräch viel Einsicht verschafft haben. Bei hartnäckigen IT-Problemen stand seine Tür sowieso immer offen.

Johannes Kierig war mit seiner lockeren Art eine echte Bereicherung für unsere Gruppe und hatte immer interessante Geschichten, vorzugsweise beim Mittagessen, zu berichten.

Beim Pendeln zwischen S104 und dem ZNN-Neubau hatte **Peter Weiser** immer wieder Neuigkeiten vom Kampf mit störrischen Handwerkern und Planern im Gepäck, die aufgrund ihres zum Teil abenteuerlichen Inhaltes bei mir oft genug ein Schmunzeln hervorgerufen haben.

Claudia Majer ist hervorzuheben für ihren unermüdlichen Elan, den sie bei den Transportmessungen an vielen und zum Teil sehr widerspenstigen GeMn Proben immer wieder aufs Neue an den Tag legte.

Volker Lang hat seinerzeit den wertvollen Kontakt nach Oxford hergestellt. Seine Verbundenheit mit der Siemens Technologie Abteilung sowie sein persönliches Engagement waren von großen Wert für meine Forschung.

Natürlich wäre da noch **Max Bichler** zu nennen, der mit seiner Expertise aushelfen konnte, wann immer Hubert mal nicht griffbereit war, und der ganz allgemein mit seiner angenehmen Art ein gerne willkommener Gast in S104 war.

Irmgard Neuner war mir eine große Hilfe bei sämtlichen organisatorischen Dingen. Vielmehr schätze ich jedoch ihre herzliche und freundliche Art die in kleinen Gesten und Gesprächen zum Tragen kam.

Diese habe ich auch gerne mit **Claudia Paulus** geführt. Auch wenn ich nur ab und zu davon profitiert habe, ist es ihrem Engagement zu verdanken, dass die

Arbeitsqualität in der oberen Technologie in den letzten Jahren deutlich zugenommen hat.

Mario Bamesreiter ist zwar kein WSI'ler, dennoch thematisch wohl am ehesten als mein Nachfolger zu bezeichen. Er hat sich mit seiner Unterstützung bei einigen Magnetotransportmessungen hervorgetan. Ihm wünsche ich viel Erfolg bei allem, was er in Zukunft noch so mit GeMn anfangen will.

Genauso danke ich **Richard Geiger** für die eine oder andere Last-Minute Messung, die er trotz eigenem Termindruck noch irgendwie untergekriegt hat.

Die Türen von **Peter Vogl**, **Martin Brandt**, **Jon Finley** und **Thomas Eissfeller** waren immer geöffnet, um unkompliziert an Detailwissen zu gelangen.

Genauso angenehm wie die Arbeitsatmosphäre im WSI waren Unternehmungen mit WSI'lern außerhalb des Instituts. Dazu haben insbesondere **Ying Xiang**, **Vase** und **Dance Jovanov**, **Ilaria Zardo**, **Michael Kaniber** und **Daniel Rudolph** beigetragen.

Große Teile dieser Arbeit hätten niemals ohne die vielseitige Unterstützung von außerhalb des WSI zustande kommen können. Mit **Bele Boeddinghaus** war am SQUID in der Chemie jederzeit eine freundliche Ansprechpartnerin zur Stelle, die mir dort ein reibungsloses Arbeiten ermöglicht hat.

Achim Trampert und **Astrid Pfeiffer** haben mir in Berlin die Geheimnisse der Elektronenmikroskopie bzw. Probenpräparation nähergebracht.

Am anderen Ende von München sind **Markus Döblinger** und **Steffen Schmidt** ebenfalls für die nette Zusammenarbeit bei den TEM Studien zu nennen, genau wie **Josef Zweck** an der Universität Regensburg.

Die APT Expertise von **Alfred Cerezo** und **David W. Saxey** aus Oxford waren ebenso von unschätzbarem Wert für Teile meiner Arbeit wie die RBS Messungen von **Kin Man Yu** aus Berkeley.

Auch von der Zusammenarbeit mit **Susanne Stemmer** und **James M. LeBeau**, entstanden während Dominiques und meiner Zeit in Santa Barbara, habe ich profitiert. An dieser Stelle ist ein ganz besonderer Dank an **David D. Awschalom** zu richten, der mir erst die Möglichkeit bot, Optikexperimente in seinen Laboren an diesem wundervollen Fleck Erde näher kennenzulernen.

Der normale Forschungsalltags kann natürlich auch mal etwas zäh werden, weshalb ich immer froh war, in **Marcio da Silva Lima** einen guten Freund aus Schulzeiten zu haben, mit dem man die kuriosesten und lustigsten Dinge erleben kann.

Am Ende bleibt mir nur noch **meinen Eltern** und meinen beiden Geschwistern **Ishani** und **Krishnan** für die grenzenlose Rückendeckung, die sie mir über all die vergangenen Jahre geboten haben, den größten Dank auszusprechen!

In der Schriftenreihe des Walter Schottky Instituts der Technischen Universität München sind bisher folgende Bände erschienen:

Vol. 1
Cornelia Engel
Si/SiGe basierende Phototransistoren
131 Seiten
ISBN 3-932749-01-4

Vol. 2
Peter Schittenhelm
Selbst-Organisation und Selbst-Ordnung in Si/SiGe-Heterostrukturen
151 Seiten
ISBN 3-932749-02-2

Vol. 3
Andreas Nutsch
Selektive Epitaxie von (GaIn)(AsP) Schichtstrukturen
129 Seiten
ISBN 3-932749-03-0

Vol. 4
Peter Baumgartner
Optische und elektronische Eigenschaften lasergeschriebener GaAs-Nanostrukturen
180 Seiten
ISBN 3-932749-04-9

Vol. 5
Walter Franz Rieger
Untersuchung der elektronischen und strukturellen Eigenschaften von GaNAlN und deren Legierungen
158 Seiten
ISBN 3-932749-05-7

Vol. 6
Markus Hauser
Oberflächenemittierende Laserdioden mit Mehrfachepitaxie
148 Seiten
ISBN 3-932749-06-5

Vol. 7
Markus Sexl
Verspannte und gitterrelaxierte In(GaAl)As Heterostrukturen
144 Seiten
ISBN 3-932749-07-3

Vol. 8
Christian Obermüller
Photolumineszenszspektroskopie mit optischen Nahfeldmethoden an GaAs-Nanostrukturen
140 Seiten
ISBN 3-932749-08-1

Vol. 9
Edilson Silveira
Inelastische Lichtstreuung an niedrig-dimensionalen Halbleiterstrukturen
104 Seiten
ISBN 3-932749-09-X

Vol. 10
Eberhard Christian Rohrer
Photoleitungs-Spektroskopie von Diamant
153 Seiten
ISBN 3-932749-10-03

Vol. 11
Thomas Wimbauer
Magnetische Resonanz-Untersuchungen an modernen Halbleitermaterialien
125 Seiten
ISBN 3-932749-11-1

Vol. 12
Herbert Verhoeven
Thermische Eigenschaften von CVD-Diamantschichten
154 Seiten
ISBN 3-932749-12-X

Vol. 13
Hans-Christoph Ostendorf
Trennung von Volumen- und Oberflächenrekombination in Silizium
128 Seiten
ISBN 3-932749-13-8

Vol. 14
Martin Städele
Dichtefunktionaltheorie mit exaktem Austausch für Halbleiter
202 Seiten
ISBN 3-932749-14-6

Vol. 15
Helmut Angerer
Herstellung von Gruppe III-Nitriden mit Molekularstrahlepitaxie
144 Seiten
ISBN 3-932749-15-4

Vol. 16
Wolfgang Heller
Spektroskopie einzelner Quantenpunkte in magnetischen und elektrischen Feldern
128 Seiten
ISBN 3-932749-16-2

Vol. 17
Molela Moukara
Pseudopotentiale mit exaktem Austausch
117 Seiten
ISBN 3-932749-17-0

Vol. 18
Ralph Oberhuber
Elektronische Struktur und Transport in verspannten Halbleiterschichtsystemen
110 Seiten
ISBN 3-932749-18-9

Vol. 19
Reiner Pech
High-Energy Boron-Implantation into Different Silicon Substrates
158 Seiten
ISBN 3-932749-19-7

Vol. 20
Christoph Martin Engelhardt
Zyklotronresonanz zweidimensionaler Ladungsträgersysteme in Halbleitern, Effekte der Elektron-Elektron-Wechselwirkung und Lokalisierung
317 Seiten
ISBN 3-932749-20-0

Vol. 21
Eduard Neufeld
Erbium-dotierte Si/SiGe-Lichtemitter und -Wellenleiter
136 Seiten
ISBN 3-932749-21-9

Vol. 22
Gert Schedelbeck
Optische Eigenschaften von Halbleiternanostrukturen hergestellt durch Überwachsen von Spaltflächen
154 Seiten
ISBN 3-932749-22-7

Vol. 23
Jürgen Zimmer
Optoelektronisches Verhalten von Dünnschichtbauelementen aus amorphem und mikrokristallinem Silizium
171 Seiten
ISBN 3-932749-23-5

Vol. 24
Berthold Schmidt
Leistungsoptimierung abstimmbarer InGaAsP/InP Halbleiterlaser
85 Seiten
ISBN 3-932749-24-3

Vol. 25
Jianhong Zhu
Ordering of self-assembled Ge and SiGe nanostructures on vicinal Si surfaces
120 Seiten
ISBN 3-932749-25-1

Vol. 26
Gerhard Groos
Herstellung und Charakterisierung von Silizium-Nanostrukturen
168 Seiten
ISBN 3-932749-26-X

Vol. 27
Uwe Hansen
Theorie der Reaktionskinetik an Festkörperoberflächen
119 Seiten
ISBN 3-932749-27-8

Vol. 28
Roman Dimitrov
Herstellung und Charakterisierung von AlGaN/GaN-Transistoren
196 Seiten
ISBN 3-932749-28-6

Vol. 29
Martin Eickhoff
Piezowiderstandsmechanismen in Halbleitern mit großer Bandlücke
151 Seiten
ISBN 3-932749-29-4

Vol. 30
Nikolai Wieser
Ramanspektroskopie an Gruppe III-Nitriden
161 Seiten
ISBN 3-932749-30-8

Vol. 31
Rainer Janssen
Strukturelle und elektronische Eigenschaften amorpher Silizium-Suboxide
275 Seiten
ISBN 3-932749-31-6

Vol. 32
Martin W. Bayerl
Magnetic resonance investigations of group III-nitrides
155 Seiten
ISBN 3-932749-32-4

Vol. 33
Martin Rother
Elektronische Eigenschaften von Halbleiternanostrukturen hergestellt durch Überwachsen von Spaltflächen
196 Seiten
ISBN 3-932749-33-2

Vol. 34
Frank Findeis
Optical spectroscopy on single self-assembled quantum dots
156 Seiten
ISBN 3-932749-34-0

Vol. 35
Markus Ortsiefer
Langwellige Vertikalresonator-Laser-dioden im Materialsystem InGaAlAs/InP
152 Seiten
ISBN 3-932749-35-9

Vol. 36
Roland Zeisel
Optoelectronic properties of defects in diamond and AlGaN alloys
140 Seiten
ISBN 3-932749-36-7

Vol. 37
Liwen Chu
Inter- und Intraband Spektroskopie an selbstorganisierten In(Ga)As/GaAs Quantenpunkten
124 Seiten
ISBN 3-932749-37-5

Vol. 38
Christian Alexander Miesner
Intra-Valenzbandspektroskopie an SiGe-Nanostrukturen in Si
100 Seiten
ISBN 3-932749-38-3

Vol. 39
Szabolcs Kátai
Investigation of the nucleation process of chemical vapour deposited diamond films
178 Seiten
ISBN 3-932749-39-1

Vol. 40
Markus Arzberger
Wachstum, Eigenschaften und Anwendungen selbstorganisierter InAs-Quantenpunkte
236 Seiten
ISBN 3-932749-40-5

Vol. 41
Markus Oliver Markmann
Optische Eigenschaften von Erbium in $Si/Si_{1-x}C_x$, $Si/Si_{1-x}Ge_x$ und Si/SiO_x Heterostrukturen
182 Seiten
ISBN 3-932749-41-3

Vol. 42
Rainer Alexander Deutschmann
Two dimensional electron systems in atomically precise periodic potential
210 Seiten
ISBN 3-932749-42-1

Vol. 43
Uwe Karrer
Schottky-Dioden auf Galliumnitrid: Eigenschaften und Anwendungen in der Sensorik
182 Seiten
ISBN 3-932749-43-X

Vol. 44
Günther Anton Johann Vogg
Epitaxial thin films of Si and Ge based Zintl phases and sheet polymers
169 Seiten
ISBN 3-932749-44-8

Vol. 45
Christian Strahberger
Vertikaler Transport und extreme Magnetfelder in Halbleitern
167 Seiten
ISBN 3-932749-45-6

Vol. 46
Jan Schalwig
Feldeffekt-Gassensoren und ihre Anwendung in Abgasnachbehandlungssystemen
125 Seiten
ISBN 3-932749-46-4

Vol. 47
Christopher Eisele
Novel absorber structures for Si-based thin film solar cells
126 Seiten
ISBN 3-932749-47-2

Vol. 48
Stefan Hackenbuchner
Elektronische Struktur von Halbleiter-Nanobauelementen im thermodynamischen Nichtgleichgewicht
213 Seiten
ISBN 3-932749-48-0

Vol. 49
Andreas Sticht
Herstellung und Charakterisierung von dünnen Silizium/Siliziumoxid-Schichtsystemen
166 Seiten
ISBN 3-932749-49-9

Vol. 50
Giuseppe Scarpa
Design and fabrication of Quantum Cascade Lasers
193 Seiten
ISBN 3-932749-50-2

Vol. 51
Jörg Frankenberger
Optische Untersuchungen an zweidimensionalen Ladungsträgersystemen
158 Seiten
ISBN 3-932749-51-0

Vol. 52
Doris Heinrich
Wavelength selective optically induced charge storage in self-assembled semiconductor quantum dots
144 Seiten
ISBN 3-932749-52-9

Vol. 53
Nicolaus Ulbrich
Entwurf und Charakterisierung von Quanten-Kaskadenlasern und Quantenpunktkaskaden
133 Seiten
ISBN 3-932749-53-7

Vol. 54
Lutz Carsten Görgens
Analyse stickstoffhaltiger III-V Halbleiter-Heterosysteme mit hochenergetischen schweren Ionen
116 Seiten
ISBN 3-932749-54-5

Vol. 55
Andreas Janotta
Doping, light-induced modification and biocompatibility of amorphous silicon suboxides
180 Seiten
ISBN 3-932749-55-3

Vol. 56
Sebastian Tobias Benedikt Gönnenwein
Two-dimensional electron gases and ferromagnetic semiconductors: materials for spintronics
198 Seiten
ISBN 3-932749-56-1

Vol. 57
Evelin Beham
Photostromspektroskopie an einzelnen Quantenpunkten
186 Seiten
ISBN 3-932749-57-X

Vol. 58
Po-Wen Chiu
Towards carbon nanotube-based molecular electronics
116 Seiten
ISBN 3-932749-58-8

Vol. 59
Tobias Graf
Spin-spin interactions of localized electronic states in semiconductors
194 Seiten
ISBN 3-932749-59-6

Vol. 60
Stefan Klein
Microcrystalline silicon prepared by hot wire CVD: preparation and characterisation of material and solar cells
157 Seiten
ISBN 3-932749-60-X

Vol. 61
Markus Krach
Frequenzverdreifacher mit Anti-Seriellem Schottky-Varaktor für den Terahertzbereich
156 Seiten
ISBN 3-932749-61-8

Vol. 62
Ralph Thomas Neuberger
AlGaN/GaN-Heterostrukturen als chemische Sensoren in korrosiven Medien
153 Seiten
ISBN 3-932749-62-6

Vol. 63
Sonia Perna
Wasserstoff-Passivierung von trikristallinem Silizium durch hydrogenisiertes Siliziumnitrid
136 Seiten
ISBN 3-932749-63-4

Vol. 64
Oliver Schumann
Einfluss von Stickstoff auf das Wachstum und die Eigenschaften von InAs-Quantenpunkten
148 Seiten
ISBN 3-932749-64-2

Vol. 65
Gerhard Rösel
Entwicklung und Charakterisierung von Typ-II-Heterostrukturen für die Abstimmregion in abstimmbaren Laserdioden
101 Seiten
ISBN 3-932749-65-0

Vol. 66
Angela Link
Zweidimensionale Elektronen- und Löcher-Gase in GaN/AlGaN Heterostrukturen
156 Seiten
ISBN 3-932749-66-9

Vol. 67
Matthias Sabathil
Opto-electronic and quantum transport properties of semiconductor nanostructures
156 Seiten
ISBN 3-932749-67-7

Vol. 68
Frank Fischer
Growth and electronic properties of two-dimensional systems on (110) oriented GaAs
139 Seiten
ISBN 3-932749-68-5

Vol. 69
Robert Shau
Langwellige oberflächenemittierende Laserdioden mit hoher Ausgangsleistung und Modulationsbandbreite
198 Seiten
ISBN 3-932749-69-3

Vol. 70
Andrea Baumer
Structural and electronic properties of hydrosilylated silicon surfaces
163 Seiten
ISBN 3-932749-70-7

Vol. 71
Andreas Florian Kreß
Manipulation of the Light-Matter-Interaction in Photonic Crystal Nanocavities
185 Seiten
ISBN 3-932749-71-5

Vol. 72
Markus Grau
Molekularstrahlepitaktische Herstellung von antimonidischen Laserdioden für die Gassensorik
138 Seiten
ISBN 3-932749-72-3

Vol. 73
Karin Buchholz
Microprocessing of silicon on insulator substrates and biofunctionalisation of silicon dioxide surfaces for sensing applications in fluids
170 Seiten
ISBN 3-932749-73-1

Vol. 74
Dominique Bougeard
Spektroskopische Charakterisierung von Germanium-Quantenpunkten in Silizium
154 Seiten
ISBN 3-932749-74-X

Vol. 75
Jochen Bauer
Untersuchungen zum kontrollierten Wachstum von InAs-Nanostrukturen auf Spaltflächen
140 Seiten
ISBN 3-932749-75-8

Vol. 76
Ingo Bormann
Intersubband Spektroskopie an Silizium-Germanium Quantenkaskadenstrukturen
124 Seiten
ISBN 3-932749-76-6

Vol. 77
Hubert Johannes Krenner
Coherent quantum coupling of excitons in single quantum dots and quantum dot molecules
160 Seiten
ISBN 3-932749-77-4

Vol. 78
Ulrich Rant
Electrical manipulation of DNA-layers on gold surfaces
249 Seiten
ISBN 3-932749-78-2

Vol. 79
René Todt
Widely tunable laser diodes with distributed feedback
152 Seiten
ISBN 3-932749-79-0

Vol. 80
Miroslav Kroutvar
Charge and spin storage in quantum dots
150 Seiten
ISBN 3-932749-80-4

Vol. 81
Markus Maute
Mikromechanisch abstimmbare Laser-Dioden mit Vertikalresonator
170 Seiten
ISBN 3-932749-81-2

Vol. 82
Frank Ertl
Anisotrope Quanten-Hall-Systeme, Vertikale Ultrakurzkanal- und Tunneltransistoren
170 Seiten
ISBN 3-932749-82-0

Vol. 83
Sebastian M. Luber
III-V semiconductor structures for biosensor and molecular electronics applications
212 Seiten
ISBN 978-3-932749-83-4

Vol. 84
Claudio Ronald Miskys
New substrates for epitaxy of group III nitride semiconductors: challenges and potential
207 Seiten
ISBN 978-3-932749-84-1

Vol. 85
Sebastian Friedrich Roth
n- and p-type transport in (110) GaAs substrates, single- and double-cleave structures
138 Seiten
ISBN 978-3-932749-85-8

Vol. 86
Mario Gjukic
Metal-induced crystallization of silicon-germanium alloys
309 Seiten
ISBN 978-3-932749-86-5

Vol. 87
Tobias Zibold
Semiconductor based quantum information devices: Theory and simulations
151 Seiten
ISBN 978-3-932749-87-2

Vol. 88
Thomas Jacke
Weit abstimmbare Laserdiode mit vertikal integriertem Mach-Zehnder-Interferometer
165 Seiten
ISBN 978-3-932749-88-9

Vol. 89
Nenad Ocelić
Quantitative near-field phonon-polariton spectroscopy
174 Seiten
ISBN 978-3-932749-89-6

Vol. 90
Kenji Arinaga
Control and manipulation of DNA on gold and its application for biosensing
111 Seiten
ISBN 978-3-932749-90-2

Vol. 91
Hans-Gregor Hübl
Coherent manipulation and electrical detection of phosphorus donor spins in silicon
162 Seiten
ISBN 978-3-932749-91-9

Vol. 92
Andrea Friedrich
Quanten-Kaskaden-Laser ohne Injektorbereiche
140 Seiten
ISBN 978-3-932749-92-6

Vol. 93
Oliver Dier
Das Materialsystem (AlGaIn) (AsSb): Eigenschaften und Eignung für GaSb-basierte Vertikalresonator-Laserdioden
174 Seiten
ISBN 978-3-932749-93-3

Vol. 94
Georg Steinhoff
Group III-nitrides for bio- and electrochemical sensors
197 Seiten
ISBN 978-3-932749-94-0

Vol. 95
Stefan Harrer
Next-generation nanoimprint lithography: Innovative approaches towards improving flexibility and resolution of nanofabrication in the sub-15-nm region
161 Seiten
ISBN 978-3-932749-95-7

Vol. 96
Stefan Ahlers
Magnetic and electrical properties of epitaxial GeMn
184 Seiten
ISBN 978-3-932749-96-0

Vol. 97
Emanuele Uccelli
Guided self-assembly of InAs quantum dots arrays on (110) surfaces
172 Seiten
ISBN 978-3-932749-97-1

Vol. 98
Shavaji Dasgupta
Growth optimization and characterization of high mobility two-dimensional electron systems in AlAs quantum wells
152 Seiten
ISBN 978-3-932749-98-8

Vol. 99
Werner Hofmann
InP-based long-wavelength VCSELs and VCSEL arrays for high-speed optical communication
142 Seiten
ISBN 978-3-932749-99-5

Vol. 100
Robert Lechner
Silicon nanocrystal films for electronic applications
227 Seiten
ISBN 978-3-941650-00-8

Vol. 101
Nebile Işık
Investigation of Landau level spin reversal in (110) oriented p-type GaAs quantum wells
114 Seiten
ISBN 978-3-941650-01-5

Vol. 102
Andreas Florian Härtl
Novel concepts for biosensors using diamond-based field effect transistors
255 Seiten
ISBN 978-3-941650-02-2

Vol. 103
Felix Florian Georg Hofbauer
Realization of electrically tunable single quantum dot nanocavities
160 Seiten
ISBN 978-3-941650-03-9

Vol. 104
Dominic F. Dorfner
Novel photonic biosensing based on silicon nanostructures
169 Seiten
ISBN 978-3-941650-04-6

Vol. 105
Till Andlauer
Optoelectronic and spin-related properties of semiconductor nanostructures in magnetic fields
157 Seiten
ISBN 978-3-941650-05-3

Vol. 106
Christoph Bihler
Magnetic semiconductors
190 Seiten
ISBN 978-3-941650-06-0

Vol. 107
Michael Huber
Tunnel-Spektroskopie im Quanten-Hall-Regime
164 Seiten
ISBN 978-3-941650-07-7

Vol. 108
Philipp Achatz
Metal-insulator transition and super-Conductivity in heavily boron-doped diamond and related materials
151 Seiten
ISBN 978-3-941650-08-4

Vol. 109
Sebastian Strobel
Nanoscale contacts to organic molecules based on layered semiconductor substrates
140 Seiten
ISBN 978-3-941650-09-1

Vol. 110
Ying Xiang
Semiconductor nanowires and templates for electronic applications
152 Seiten
ISBN 978-3-941650-10-7

Vol. 111
Michael Kaniber
Non-classical light generation in photonic crystal nanostructures
177 Seiten
ISBN 978-3-941650-11-4

Vol. 112
Martin Hermann
Epitaktische AlN-Schichten auf Saphir und Diamant
216 Seiten
ISBN 978-3-941650-12-1

Vol. 113
Dominik Heiss
Spin storage in quantum dot ensembles and single quantum dots
196 Seiten
ISBN 978-3-941650-13-8

Vol. 114
Tillmann Christoph Kubis
Quantum transport in semiconductor nanostructures
253 Seiten
ISBN 978-3-941650-14-5

Vol. 115
Lucia Steinke
Magnetotransport of coupled quantum Hall edges in a bent quantum well
194 Seiten
ISBN 978-3-941650-15-2

Vol. 116
Christian Lauer
Antimonid-basierte Vertikalresonator-Laserdioden für Wellenlängen oberhalb 2 μm
180 Seiten
ISBN 978-3-941650-16-9

Vol. 117
Simone Maria Kaniber
Optoelektronische Phänomene in hybriden Schaltkreisen aus Kohlenstoffnanoröhren und dem Photosystem I
136 Seiten
ISBN 978-3-941650-17-6

Vol. 118
Martin Heiß
Growth and properties of low-dimensional III-V semiconductor nanowire heterostructures
172 Seiten
ISBN 978-3-941650-18-3

Vol. 119
Sandro Francesco Tedde
Design, fabrication and characterization of organic photodiodes for industrial and medical applications
277 Seiten
ISBN 978-3-941650-19-0

Vol. 120
Danche Spirkoska Jovanov
Fundamental properties of self-catalyzed GaAs nanowires and related heterostructures
200 Seiten
ISBN 978-3-941650-20-6

Vol. 121
Jürgen Sailer
Materials and devices for quantum Information processing in Si/SiGe
158 Seiten
ISBN 978-3-941650-21-3

Vol. 122
Ilaria Zardo
Growth and raman spectroscopy studies of gold-free catalyzed semiconductor nanowires
184 Seiten
ISBN 978-3-941650-22-0

Vol. 123
Andre Rainer Stegner
Shallow dopants in nanostructured and in isotopically engineered silicon
185 Seiten
ISBN 978-3-941650-23-7

Vol. 124
Andreas J. Huber
Nanoscale surface-polariton spectroscopy by mid- and far-infrared near-field microscopy
144 Seiten
ISBN 978-3-941650-24-4

Vol. 125
Marco Andreas Höb
Funktionalisierung von Gruppe IV-Halbleitern
186 Seiten
ISBN 978-3-941650-25-1

Vol. 126
Daniel Claudio Pedone
Nanopore analytics – electro-optical studies on single molecules
114 Seiten
ISBN 978-3-941650-26-8

Vol. 127
Casimir Richard Simeon Katz
Multi-alloy structures for injectorless Quantum Cascade Lasers
131 Seiten
ISBN 978-3-941650-27-5

Vol. 128
Barbara Annemarie Kathrin Baur
Functionalization of group III-nitrides for biosensor applications
215 Seiten
ISBN 978-3-941650-28-2

Vol. 129
Arne Laucht
Semiconductor quantum optics with tailored photonic nanostructures
232 Seiten
ISBN 978-3-941650-29-9

Vol. 130
Jia Chen
Compact laser-spectroscopic gas sensors using Vertical-Cavity Surface-Emitting Lasers
150 Seiten
ISBN 978-3-941650-30-5

Vol. 131
Hans Leonhard Prechtel
Ultrafast Photocurrents and Terahertz Radiation in Gallium Arsenide and Carbon Based Nanostructures
160 Seiten
ISBN 978-3-941650-31-2

Vol. 132
Roland Enzmann
Technologieentwicklung für eine Einzelphotonenquelle
142 Seiten
ISBN 978-3-941650-32-9

Vol. 133
Alexander Bachmann
Antimonide-Based Vertical-Cavity Surface-Emitting Lasers
144 Seiten
ISBN 978-3-941650-33-6

Vol. 134
Markus Andreas Mangold
Two-Dimensional Gold Nanoparticle Arrays – A Platform for Molecular Optoelectronics
140 Seiten
ISBN 978-3-941650-34-3

Vol. 135
Stefan Birner
Modeling of semiconductor nanostructures and semiconductor–electrolyte interfaces
227 Seiten
ISBN 978-3-941650-35-0

Vol. 136
Christian Claus Jäger
Polycrystalline Silicon Thin Films for Electronic Applications
202 Seiten
ISBN 978-3-941650-36-7

Vol. 137
Gunther Christian Jegert
Modeling of Leakage Currents in High-κ Dielectrics
170 Seiten
ISBN 978-3-941650-37-4

Vol. 138
Shamsul Arafin
Electrically-Pumped GaSb-Based Vertical-Cavity Surface-Emitting Lasers
126 Seiten
ISBN 978-3-941650-38-1

Vol. 139
Norman Hauke
Enhanced spontaneous emission from silicon-based photonic crystal nanostructures
208 Seiten
ISBN 978-3-941650-39-8

Vol. 140
Christoph Schindler
Quantum spin transport in semiconductor nanostructures
175 Seiten
ISBN 978-3-941650-40-4

Vol. 141
Narayan Sircar
Group IV all-semiconductor spin-tronics: Materials aspects and optical spin selection rules
163 Seiten
ISBN 978-3-941650-41-1

ISBN 978-3-941650-41-1

(€ 15,00)